

This item was submitted to Loughborough's Institutional Repository (<https://dspace.lboro.ac.uk/>) by the author and is made available under the following Creative Commons Licence conditions.



**CC creative commons**  
COMMONS DEED

**Attribution-NonCommercial-NoDerivs 2.5**

**You are free:**

- to copy, distribute, display, and perform the work

**Under the following conditions:**

**BY:** **Attribution.** You must attribute the work in the manner specified by the author or licensor.

**Noncommercial.** You may not use this work for commercial purposes.

**No Derivative Works.** You may not alter, transform, or build upon this work.

- For any reuse or distribution, you must make clear to others the license terms of this work.
- Any of these conditions can be waived if you get permission from the copyright holder.

**Your fair use and other rights are in no way affected by the above.**

This is a human-readable summary of the [Legal Code \(the full license\)](#).

[Disclaimer](#) 

For the full text of this licence, please go to:  
<http://creativecommons.org/licenses/by-nc-nd/2.5/>



**Microwave Assisted Processing of  
Nanocrystalline Barium Titanate based  
Capacitor Devices**

**By**

**Vinothini Venkatachalam**

**A Doctoral Thesis submitted in partial fulfilment of the requirements for the award of Doctor of  
Philosophy of Loughborough University**

**May 2011**

**© by Vinothini Venkatachalam 2011**

*To my dear Jay & our Parents*

---



## **ACKNOWLEDGMENTS**

First, I would like to express my sincere gratitude to my supervisor Dr.B.Vaidhyanathan for the faith on me giving this project and driving me constantly with motivating guidance throughout the course of this work. I am very much grateful for his immense help, moral support, and timely suggestions at various stages of the project work. I am very much thankful to the science faculty and EPSRC/TSB for providing the financial & research support.

I am thankful to Prof. Jon Binner for his continuous encouragement and for the valuable suggestions during weekly research team meetings.

I am thankful to Syfer Technology Ltd., for helping with MLCC fabrication. My special thanks to Mr. Howard Ingleson, Mr. John Shreeve, Ms. Angie Ellmore and Mr. Rob Wiley for their support during the project

I take this opportunity to thank, Dr. David Ross and Dr. Sandier Dan for XRD characterization; Mr. John Bates for Electron microscopy, Mr. Bryan Dennis, Raman spectroscopy; Mrs.Jayshree Bhuptani, Particle size analysis; Dr. Gisueppe Forte, DSC; Dr.David Granby, Thermal analysis; Dr.George Dimitrakis, Dielectric properties measurements.

I would like to thank Mr. Andrew Lau, for being very friendly, kind, creating good environment for work and being very helpful at many difficult situations and Mr. Ray Owens for his help at various stages of my work.

Here is also an occasion for me to thank my friends at Loughborough University Dr. Annapoorani Keetharam, Dr.Bala Ragupathy, Dr.Anish Paul, Dr. Sina Saremi, Ms. Minnah Tong, Ms. Saranya Venugopal, Mr. Aravind Mullah, Ms. Sherry.G, Ms. Sherry Liu, Ms. Sharon Huang, Mr. Prabhu Ramalingam, Mr. Yifei & Mr. Nakro. Thanks to Geoffrey and Oliver Pearman for working with me during the project.

My special thanks to Mrs. Pat Storer and Ms.June Lennie and all the staffs in the department for their kindness.

Finally, I pay my indebt thanks to my family members for their tolerances, inspiration, support and prayers without which I am incomplete.



# TABLE OF CONTENTS

TABLE OF CONTENTS .....	IV
ABSTRACT .....	X
FIGURE CAPTIONS.....	XII
LIST OF TABLES.....	XX
CHAPTER 1: INTRODUCTION.....	1
CHAPTER 2: LITERATURE REVIEW.....	7
2.1. Capacitors.....	7
2.1.1. Types of Capacitors.....	8
2.1.2. Multilayered ceramic capacitors (MLCCs) .....	10
(i) <i>Effect of thickness of the ceramic layer on the capacitance of the capacitor...</i>	12
2.1.3. Ceramic capacitor materials .....	13
(i) <i>Titanate based materials .....</i>	13
2.2. Barium titanate (BT) .....	13
2.2.1. Crystal structure and Polymorphs of BT .....	14
2.2.2. Effect of particle and grain size on dielectric properties.....	15
2.2.3. Variation of dielectric properties with temperature and frequency .....	17
2.2.4. Effect of density / porosity on dielectric properties .....	18
2.2.5. Effect of compositional modifications on dielectric properties of BT ...	19
(i) <i>'Ba' Site Substituents.....</i>	21
(ii) <i>'Ti' Site Substituents .....</i>	23
(iii) <i>Aliovalent substitution.....</i>	25
2.2.6. Effect of microstructure on dielectric properties.....	26
2.3. Electrode materials used in MLCCs.....	28
2.3.1. Use of cheaper metal electrodes in MLCCs .....	29
2.3.2. Processing issues during co-sintering of metals and ceramics .....	31

<b>2.4.</b>	<b>Nanocrystalline ceramics .....</b>	<b>32</b>
2.4.1.	Different ways of producing nanopowders of BT .....	33
	(i) Alkoxide derived precursors method .....	33
	(ii) Oxalate process.....	34
	(iii) Co-Precipitation process .....	34
	(iv) Hydrothermal synthesis .....	34
	(v) Sol gel derived process .....	35
	(vi) Polymeric precursor method.....	35
2.4.2.	Synthesis of compositionally modified BT nanopowders .....	38
2.4.3.	Difficulties in producing nano BT powders.....	38
<b>2.5.</b>	<b>Processing of nanocrystalline powders.....</b>	<b>39</b>
2.5.1.	Control of agglomeration .....	39
2.5.2.	Difficulties in dry processing of nanopowders.....	40
2.5.3.	Challenges in the wet processing of BT nanopowders .....	41
	(i) Dispersability of nanopowders.....	41
	(ii) Aqueous processing .....	44
	(iii) Non-aqueous processing:.....	46
<b>2.6.</b>	<b>Fabrication of multilayered capacitor devices.....</b>	<b>46</b>
2.6.1.	Solvents:.....	47
2.6.2.	Dispersants: .....	48
2.6.3.	Binders: .....	48
2.6.4.	Milling operations:.....	50
2.6.5.	Ink Rheology: .....	50
2.6.6.	Tape casting:.....	54
2.6.7.	Screen-printing: .....	54
<b>2.7.</b>	<b>Sintering of BT ceramics: .....</b>	<b>56</b>
2.7.1.	Types of sintering: .....	60
	(i) Solid state sintering .....	60
	(ii) Liquid phase/Reactive liquid sintering .....	61
2.7.2.	Grain growth in BT ceramics .....	62

(i)	<i>Normal grain growth</i> .....	62
(ii)	<i>Abnormal grain growth (AGG)</i> .....	62
<b>2.8.</b>	<b>Approaches for nano BT sintering</b> .....	<b>65</b>
2.8.1.	Sintering aid/ Flux additions during BT sintering .....	66
(i)	<i>Flux additions:</i> .....	66
(ii)	<i>Glass compositions:</i> .....	67
2.8.2.	Reduced atmosphere .....	68
2.8.3.	Novel sintering techniques .....	69
(i)	<i>Rapid rate sintering</i> .....	69
(ii)	<i>Spark plasma sintering</i> .....	69
(iii)	<i>Laser sintering</i> .....	70
(iv)	<i>Microwave sintering</i> .....	71
<b>2.9.</b>	<b>Microwave assisted heating</b> .....	<b>71</b>
2.9.1.	Microwave vs. Conventional heating .....	71
2.9.2.	Characteristics of microwaves .....	72
2.9.3.	Interaction of microwaves with materials .....	73
2.9.4.	Mechanism of microwave heating .....	76
2.9.5.	Limitations of microwave heating .....	79
2.9.6.	Microwave/ conventional hybrid heating.....	80
<b>2.10.</b>	<b>Microwave assisted processing of nanocrystalline BT ceramics</b>	<b>81</b>
<b>2.11.</b>	<b>Scope of the present project</b> .....	<b>82</b>
<b>CHAPTER 3:</b>	<b>EXPERIMENTAL WORK</b> .....	<b>84</b>
<b>3.1.</b>	<b>Overall Methodology</b> .....	<b>84</b>
<b>3.2.</b>	<b>Synthesis of nano BT based formulations</b> .....	<b>85</b>
3.2.1.	Raw materials used .....	85
3.2.2.	Synthesis procedure (wet chemical procedure used) .....	85

3.2.3.	Heating methodologies employed (Conventional vs. Microwave vs. Hybrid)	88
	.....	88
(i)	Conventional heating.....	88
(ii)	Microwave heating.....	88
(iii)	Hybrid heating.....	90
3.2.4.	Characterization related to the synthesis of BT .....	92
(i)	Thermal analysis.....	92
(ii)	XRD .....	92
(iii)	Micro-Raman spectroscopy.....	93
(iv)	Transmission electron microscopy .....	94
(v)	BET surface area analysis.....	95
(vi)	Malvern Mastersizer .....	96
(vii)	High frequency dielectric property measurements .....	96
<b>3.3.</b>	<b>Processing of the nano BT powders to make green bodies.....</b>	<b>99</b>
3.3.1.	Dry processing .....	99
(i)	Compaction of the nano BT powders to form pellets .....	99
3.3.2.	Wet processing.....	99
(i)	Nano BT ink/slip formulation.....	100
(ii)	Nano ink rheology optimization .....	102
(iii)	FOG Tests .....	103
(iv)	Screen printing of the nano ink.....	104
3.3.3.	Characterization of the green bodies.....	106
(i)	Density measurements.....	106
(ii)	Optical microscopy .....	106
(iii)	Field Emission Gun -Scanning Electron Microscopy.....	106
<b>3.4.</b>	<b>Sintering of the green bodies to make components .....</b>	<b>106</b>
3.4.1.	Dilatometer studies.....	107
3.4.2.	Characterization of the sintered bodies .....	108
(i)	Density measurements:.....	108
(ii)	Microstructure and Grain size measurements:.....	109
(iii)	Electrical property measurements .....	109

<b>CHAPTER 4: RESULTS AND DISCUSSION.....</b>	<b>111</b>
<b>4.1. BT nanopowder synthesis.....</b>	<b>111</b>
4.1.1. Characterization of the starting precursor.....	111
(i) Thermal analysis of the precursor.....	111
(ii) Dielectric properties of the BT precursors.....	113
4.1.2. Characterization of the calcined powders.....	114
(i) Phase analysis.....	114
(ii) Particle size analysis.....	118
4.1.3. Effect of microwaves on hexagonal phase suppression.....	119
4.1.4. Effect of microwaves on nano t-BT phase evolution.....	120
4.1.5. Possible mechanism of microwave heating during nano BT synthesis.....	124
4.1.6. Synthesis of Zr substituted BT nanopowders.....	131
4.1.7. Synthesis of Sr substituted BZT nanopowders.....	137
<b>4.2. Nano BT Processing.....</b>	<b>140</b>
4.2.1. Powder characteristics.....	140
4.2.2. Nano BT ink formulation.....	142
(i) Effect of dispersant concentration.....	142
(ii) Maximum solid loading.....	146
(iii) Optimizaion of PVB:EC ratio.....	148
(iv) Influence of molar mass of EC.....	151
(v) Effect of total binder concentration.....	154
(vi) Temperature characteristics of the optimized nano BT ink.....	156
(vii) Printability of the nano BT ink.....	158
4.2.3. Characterization of green samples.....	159
<b>4.3. Nano BT sintering and electrical performance optimization.....</b>	<b>161</b>
4.3.1. Dilatometer studies of Nano BT chip.....	161
4.3.2. Sintering of n-S-BT chips.....	162
4.3.3. Electrical properties of the n-S-BT powder.....	165
<b>4.4. Effect of dopants on sintering and electrical performance.....</b>	<b>168</b>

4.4.1.	Characteristics of the dopants .....	168
4.4.2.	Effect of dopants on the sintering kinetics .....	169
4.4.3.	Optimising the amount of dopants .....	170
4.4.4.	Sintering of nano MLCCs .....	174
4.4.5.	Electrical properties of the n-S-BT powder with dopants .....	176
<b>4.5.</b>	<b>Effect of glass frits addition .....</b>	<b>177</b>
4.5.1.	Glass frit composition and properties .....	179
4.5.2.	Optimization of glass frit amount .....	182
4.5.3.	Sintering of n-S-BT with glass frits.....	183
4.5.4.	Electrical properties of the n-S-BT with glass frits addition.....	184
<b>CHAPTER 5: CONCLUSIONS .....</b>		<b>186</b>
<b>CHAPTER 6: FUTURE WORK.....</b>		<b>189</b>
6.1.	<b>Synthesis:.....</b>	<b>189</b>
6.2.	<b>Green processing.....</b>	<b>190</b>
6.3.	<b>Sintering.....</b>	<b>191</b>
<b>APPENDIX-1 .....</b>		<b>192</b>
<b>APPENDIX-2 .....</b>		<b>199</b>
<b>REFERENCES .....</b>		<b>195</b>

## ABSTRACT

Interest towards fabrication of nanostructured electro ceramic devices has witnessed exponential growth in recent years, owing to the requirements of miniaturization, multifunctionality and improved reliability. The major hurdle in realising the full potential of nano ceramics is preventing the unwanted grain growth whilst achieving high densification during conventional high temperature processing. In this project, a detailed study was performed on the fabrication of nanostructured barium titanate based X7R multilayer ceramic capacitors (MLCCs) using microwave assisted heating. The main processing stages involved in MLCC manufacture were;

- (i) nano BT powder synthesis,
- (ii) making nano BT ink formulations suitable for screen printing,
- (iii) sintering of components using conventional, microwave, hybrid heating methods and
- (iv) performance evaluation of the end products

In the first stage, using a microwave-assisted polymeric precursor approach nanocrystalline  $\text{BaTiO}_3$ ,  $\text{Ba}(\text{Zr}_x\text{Ti}_{1-x})\text{O}_3$  ( $x = 0.1-0.3$ ) and  $(\text{Ba}_{1-y}\text{Sr}_y)(\text{Zr}_{0.1}\text{Ti}_{0.9})\text{O}_3$  ( $y = 0.1-0.4$ ) compositions with tetragonal structure were synthesised at less demanding processing conditions (at  $700^\circ\text{C}/30\text{min}$ ;  $\langle\text{crystallite size}\rangle = 20\text{ nm}$ , against a conventional heating profile of  $900^\circ\text{C}/5\text{hrs}$ ;  $\langle\text{crystallite size}\rangle = 50-150\text{ nm}$ ). The role played by microwaves during the rapid synthesis was elucidated by subjecting the samples to identical thermal history at different microwave power levels in a hybrid furnace. The activation energy was found to be  $40 \pm 2\text{ kJ/mol}$  for microwave assisted synthesis with  $1000\text{ W}$  of microwave power, compared to  $92 \pm 1\text{ kJ/mol}$  in conventional method. Thus, the activation energy has been reduced by more than half when microwaves were used for nano BT synthesis.

In addition, co-existence of hexagonal BT phase at power levels of  $< 200\text{ W}$ , initiation of tetragonal phase nucleation at  $\geq 200\text{ W}$  and single phase t-BT formation with  $\geq 1200\text{ W}$  were observed at the same thermodynamic conditions of temperature-time-pressure. This provided an entirely new possibility of controlling/altering phase evolution during nanoceramics synthesis with microwave power.

The synthesized nano BT powders were found not to be suitable for wet processing (an industrially preferred option), due their poor dispersion characteristics. Hence a commercially procured nano BT powder ( $100\text{ nm}$  particle size), suitable for wet

processing was identified for the fabrication of nano MLCCs. The optimum amount of dispersant required for achieving well dispersed nano BT dispersion was identified as 0.75 wt%. The total binder content of 3 wt% with 2:3 ratio of poly vinyl butyral to ethyl cellulose having 1:1:1 ratio of N4:N10:N22 ethyl cellulose with different molecular weights was found to be desirable for achieving screen printable ink. Using the optimised nano BT ink formulation with 62 wt% solid loading, multilayer ceramic capacitor devices were fabricated, with and without internal electrodes.

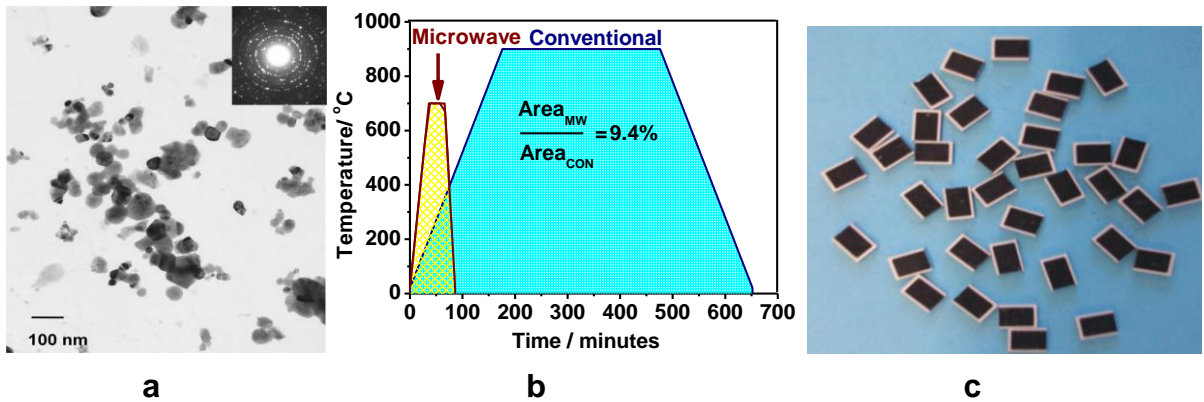


Figure: (a) Microstructure of the nano BT synthesized by microwave heating, (b) Comparison of the conventional and microwave time-temperature profiles used for nano BT synthesis, (c) Fabricated nano BT MLCCs devices

The resultant nanocrystalline BT chips were sintered using conventional, microwave and hybrid heating profiles. Based on the dilatometer studies, the n-BT showed a 100°C reduction in onset sintering temperature compared to the  $\mu$ -BT and the onset temperature of n-BT was further lowered by an additional 50°C when microwave power was used. Microwave assisted sintering of the n-BT chips at 1150°C for 1 h resulted in 97% densification without abnormal grain growth. The proprietary dopants were added to the ink to form core shell structure, which is responsible for temperature stable characteristics of the capacitors (X7R). A maximum density of 98% T.D was achieved for doped MLCC devices at 1120°C using microwave heating. Addition of glass frits further helped to achieve high density at 1050°C itself, a 300°C reduction in processing temperature compared to micron BT. This significant reduction in processing temperature enabled the use of low Pd containing electrode material leading to significant cost savings (~40%) during MLCCs production.



## FIGURE CAPTIONS

Figure 2.1: Symbolic representation of different types of capacitors.....	8
Figure 2.2: Different kinds of ceramic capacitors .....	9
Figure 2.3: Typical surfaces mount components on a Flash drive circuit board.....	9
Figure 2.4: Schematic representation of the MLCC cross sectional view .....	10
Figure 2.5: The typical BT crystal structure above its Curie temperature.....	14
Figure 2.6: The polymorphic transformations of BT at different temperatures .....	14
Figure 2.7: Reported dielectric permittivity of BT as a function of grain size .....	16
Figure 2.8: The typical variation of BT dielectric permittivity with temperature and frequency .....	18
Figure 2.9: Typical variation of BT dielectric permittivity with sample porosity .....	19
Figure 2.10: Variation of the transition temperatures for different amount of isovalent substituent .....	21
Figure 2.11: Schematic diagram of defect perovskite formation .....	27
Figure 2.12: Schematic representation of the core shell structure in a BT ceramic .....	28
Figure 2.13: Equilibrium oxygen pressure of metal/metal oxides at higher temperature .....	30
Figure 2.14: The intermediate structure of the BT chelate .....	37
Figure 2.15: (a) Schematic representation of agglomerates in the nanopowders (b) Typical pore size distribution of the agglomerated nanoceramics powders .....	40
Figure 2.16: Schematic illustration of the interaction potential energy and relevant length scales for (a) electrostatic, (b) steric, and (c) structural contributions, where $k^{-1}$ is the effective double-layer thickness, $\delta$ the adlayer thickness, and $\sigma$ the characteristic size of species resulting in ordering within the inter particle gap.....	43
Figure 2.17: Schematic representation of $Ba^{2+}$ dissolution during aqueous processing .....	45

Figure 2.18: Flow chart showing fabrication steps involved during multilayered device manufacturing.....	47
Figure 2.19: Dependence of shear viscosity on average molar mass (M) of the polymeric binders.....	49
Figure 2.20: Two plate model .....	50
Figure 2.21: Typical (a) viscosity curve and (b) flow curve of shear thinning behaviour .....	51
Figure 2.22: Typical thixotropic behaviour in a 3 interval rotational test.....	51
Figure 2.23: (a) Dash pot model; (b) Spring model.....	52
Figure 2.24: Maxwell model .....	53
Figure 2.25: Schematic diagram showing the tape casting procedure.....	54
Figure 2.26: Schematic picture showing the ink deposition during screen printing technique.....	55
Figure 2.27: Schematic representation of various steps involved in screen printing process.....	55
Figure 2.28: Rate versus Temperature. ....	58
Figure 2.29: Arrhenius plot of rates of densification and grain growth .....	60
Figure 2.30: Abnormal grain growth in BT ceramics sintered at 1300°C.....	63
Figure 2.31: Microstructure of BT sintered with (a) TiO <sub>2</sub> excess-showing abnormal elongated grains and twin defects at 1215°C, (b) BaO excess- showing intergranular cracks at 1250°C .....	64
Figure 2.32: The typical heating mechanism of conventional, hybrid and microwave heating .....	72
Figure 2.33: The electromagnetic spectrum.....	73
Figure 2.34: Interaction of microwaves with material. ....	74
Figure 2.35: Schematic representation of a potential barrier for an atom (●)to exchange its lattice site with a vacancy (□) (a) without an external electric field; (b) With an external electric field (Reproduced from reference ) .....	78
Figure 3.1: Flow chart of overall experimental work.....	84

Figure 3.2: Flow chart for synthesis of BT and compositionally modified BT using citrate polymeric precursor method .....	87
Figure 3.3: Microwave cavity at Loughborough used for BT powder synthesis and sintering .....	88
Figure 3.4: Sample arrangements in the microwave cavity.....	89
Figure 3.5: Sample arrangements in the hybrid microwave furnace at Loughborough used for BT powder synthesis and sintering .....	90
Figure 3.6: Sample arrangements for micro Raman spectroscopy technique.....	94
Figure 3.7: Sample arrangements for BET surface area analysis.....	95
Figure 3.8: High frequency dielectric measurements facility used courtesy: Nottingham University .....	97
Figure 3.9: FOG testing kit used for the present work.....	104
Figure 3.10: Screen printing facility at Loughborough University .....	105
Figure 3.11: The dilatometer in the hybrid furnace and schematic diagram of the dilatometer. ....	107
Figure 3.12: Equivalent circuit diagram for parallel and series capacitance measurements .....	110
Figure 4.1: Thermal analysis of BT precursor .....	112
Figure 4.2: Loss tangent Vs Temperature for BT precursor produced using barium carbonate source at 2.45 GHz using cavity perturbation method.....	113
Figure 4.3: The room temperature X-Ray diffraction patterns of the precursor calcined in Conventional heating .....	115
Figure 4.4: The room temperature X-Ray diffraction patterns of the precursor calcined in microwave heating .....	115
Figure 4.5: The room temperature Raman spectra of the precursor calcined between 600 and 900°C for 5 hrs in conventional heating.....	117
Figure 4.6: The room temperature Raman spectra of the precursor calcined between 550 and 700°C for 1 h in microwave heating.....	117
Figure 4.7: The TEM microstructure and SAED pattern of the powders calcined at (a) 900°C /5 h in conventional heating and (b) 700°C/ 30 min in microwave heating .....	118

Figure 4.8: Particle size distribution of the BT powders synthesized using conventional (900°C/ 5 h) and microwave heating (700°C/ 30 min).....	119
Figure 4.9: Representative Conventional power Vs Time Profiles during hybrid heating with different microwave power levels used. ....	121
Figure 4.10: The room temperature Raman spectra of the precursor calcined at 700°C /30 min in hybrid heating with different microwave power levels.....	121
Figure 4.11: Temperature distribution across the sample during nano BT synthesis under identical thermal history using hybrid furnace .....	123
Figure 4.12: Optimised Time-Temperature profiles for conventional and microwave heating experiments.....	124
Figure 4.13: Percentage tetragonal BT (t-BT) formation with soaking time in conventional, microwave and hybrid heating for same temperature at 700°C.....	125
Figure 4.14: Percentage tetragonal BT (t- BT) formation with temperature in conventional, microwave and hybrid heating at a constant soaking time, 30 min .....	126
Figure 4.15: Arrhenius plot of the tetragonal BT (t-BT) formation as a function of reciprocal of temperature at various microwave power levels.....	127
Figure 4.16: The percentage of t-BT formation and change in activation energy with different microwave powers in hybrid heating at 700°C/ 30 min .....	127
Figure 4.17: The room temperature Raman spectra of BT precursors prepared at 400°C & 500°C and then calcined at 700°C/ 30 min/ 1 kW .....	129
Figure 4.18: The room temperature Raman spectra of the BT precursors produced using different barium sources and calcined at 700°C/ 30 min/ 1 kW in hybrid heating.....	129
Figure 4.19: Schematic diagram on effect of microwaves on diffusion enhancement .....	130
Figure 4.20: Room temperature XRD patterns of the BT, BZT-10 and BZT-20 precursors calcined at 900°C for 5 hours using conventional heating .....	132
Figure 4.21: Room temperature magnified view of (110) peak shift of the BT, BZT-10 and BZT-20 precursors calcined at 900°C for 5 hours using conventional heating.....	132

Figure 4.22: Room temperature Raman spectra of BT, BZT-10, BZT-20 and BZT-30 precursors calcined at 900°C for 5 hours in conventional heating.....	133
Figure 4.23: Room temperature XRD patterns of BT, BZT-10, BZT-20 and BZT-30 precursors calcined at 700°C for 30 minutes in microwave heating.....	133
Figure 4.24: Room temperature Raman spectra of BT, BZT-10, BZT-20 and BZT-30 precursors calcined at 700°C for 30 minutes in microwave heating.....	134
Figure 4.25: TEM images of the BZT-20 powders calcined at a) 900°C for 5 hours using conventional heating and b) 700°C for 30 minutes using microwave heating.....	135
Figure 4.26: Typical DSC of the BZT10 composition.....	136
Figure 4.27: Room temperature XRD patterns of BSZT-10/10, BSZT-20/10, BSZT 30/10 and BSZT 40/10 calcined at 700°C for 30 min in microwave heating.....	137
Figure 4.28: Room temperature Raman spectra of BSZT-10/10, BSZT-20/10, BSZT 30/10 and BSZT 40/10 calcined at 700°C for 30 min in microwave heating.....	138
Figure 4.29: TEM images of the BSZT-30/10 powders calcined at a) 900°C for 5 hrs using conventional heating and b) 700°C for 30 min using microwave heating.....	139
Figure 4.30: XRD pattern of the nano Lboro, Sakai BT and micron BT powders.....	140
Figure 4.31: TEM image of the (a) micron-Fischer, (b) nano-Sakai BT powders and refer Figure 4.7 for TEM of nano- Lboro synthesized BT powders.....	141
Figure 4.32: Particle size distribution of the nano Sakai BT powders.....	141
Figure 4.33: Viscosity curves of n-S-BT (55 wt%) suspension with varying amount of dispersants.....	143
Figure 4.34: Viscosity curves of n-LU-BT (55 wt%) suspension with varying amount of dispersants.....	143
Figure 4.35: Viscosity curves for $\mu$ -BT (64 wt%) suspension with 0.35 wt% and 0.75 wt% dispersant.....	145

Figure 4.36: Viscosity curves of the n-S-BT powder suspensions with 0.75 wt% dispersant and increasing solid content .....	146
Figure 4.37: Viscosity curves of the $\mu$ -BT nanopowder suspensions with 0.75 wt% dispersant and increasing solid content .....	147
Figure 4.38: Viscosity curves for the different binders used.....	148
Figure 4.39: Shear rate thixotropy of the different binders used .....	149
Figure 4.40: Viscosity curve of 62 wt% n-S-BT ink with 3 wt% total binder content - at different PVB: EC ratio .....	149
Figure 4.41: Shear rate thixotropy loop of 62 wt% n-S-BT ink with 3 wt% total binder content – at different PVB: EC ratio .....	150
Figure 4.42: Viscosity curves of 62 wt% n-S-BT ink with 3 wt% total binder content and PVB:EC-2:3-effect of EC-N4:N10:N22 ratio on viscosity .....	152
Figure 4.43: Schematic diagram of polymer molecules behaviour under shear force.....	153
Figure 4.44: Shear rate thixotropy loop of 62 wt% n-S-BT ink with 3 wt% total binder content and PVB: EC-2:3-at different EC-N4:N10:N22 ratios .....	153
Figure 4.45: Viscosity curves of 62 wt% nano n-S-BT ink with PVB: EC-2:3, EC-N4:N10:N22-1:1:1 –varying the total binder content .....	155
Figure 4.46: Shear rate thixotropy loop of 62 wt% nano n-S-BT ink with PVB: EC-2:3, N4:N10:N22-1:1:1 –effect of variation in total binder content.....	155
Figure 4.47: The stress sweep of the nano BT ink with varying binder content .....	156
Figure 4.48: Temperature characteristics of the nano BT inks.....	157
Figure 4.49: Optical picture of the n-S-BT ink prints (a) Top surface of the MLCC, (b) cross section of MLCC with electrodes.....	159
Figure 4.50: BET surface area analysis of the n-S-BT and $\mu$ -BT chip .....	160
Figure 4.51: SEM micrograph on top surface of the (a) n-S-BT, (b) $\mu$ -BT chip .....	160
Figure 4.52: Linear shrinkage Vs Temperature of n-S-BT and $\mu$ -BT chip .....	161
Figure 4.53: Variation of density and grain size of the n-S-BT chips at various heating rate .....	163

Figure 4.54: Density of the sintered n-S-BT chip at various temperatures for 4 h and 2 h using 0 and 1kW of microwave power levels in hybrid heating .....	164
Figure 4.55: Temperature change of capacitance (with reference to room temperature) of n-S-BT chip sintered using conventional, microwave and hybrid conditions .....	167
Figure 4.56: SEM micrograph of the dopants (a) as received and (b) after 5 min of micronization.....	168
Figure 4.57: Agglomerate size distribution of the (a) as received & (b) after 5 min of micronization .....	168
Figure 4.58: Shrinkage Vs Temperature of the n-S-BT with 2.5 wt% of dopants (MW-Microwave power) .....	169
Figure 4.59: Microstructures of the surface of n-S-BT sintered with varying amount of dopants using different type of heating .....	171
Figure 4.60: Temperature change of capacitance (with reference to room temperature) of the n-S-BT with different dopant concentrations sintered at 1120°C for 1 h using microwave heating.....	173
Figure 4.61: (a) Picture of nano MLCCs made (b) Optical micrograph of the nano MLCCs.....	174
Figure 4.62: Elemental mapping of the binder removed nano MLCCs.....	174
Figure 4.63: Optical micrographs of the nano MLCCs sintered using different types of heating at 1120°C and 1150°C.....	175
Figure 4.64: Elemental mapping of the nano MLCC sintered at 1120°C for 1 h using microwave heating .....	176
Figure 4.65: Temperature change of capacitance (TCC) for nano MLCCs sintered using different heating methods .....	177
Figure 4.66: Time-Temperature profile used for dilatometer studies of the doped n-S-BT with 1.5 wt% of six different glass frits compositions .....	179
Figure 4.67: Linear shrinkage Vs Temperature of the doped n-S-BT with 1.5wt% of six different glass frit compositions .....	179
Figure 4.68: Linear shrinkage Vs Temperature of the doped n-S-BT with 1.5 wt% GF2 using different microwave power. ....	181

Figure 4.69: Variation of sintered density with different amount of glass frits (GF1, GF2 and GF4), sintered at 1050°C for 1 hour using microwave heating. ....	182
Figure 4.70: Microstructures of the doped n-S-BT with 1.5 wt% GF2 glass frit, sintered surface at (a) 1050°C for 2 h using conventional heating and (b) 1050°C for 1 h using microwave heating .....	183
Figure 4.71: Temperature change in capacitance (TCC) (with reference to room temperature) of the n-S-BT with 2.5 wt% dopants and 1.5 wt% of different glass frits.....	184
Figure 4.72: Optical micrograph of the new n-S-BT doped capacitor device .....	185



## LIST OF TABLES

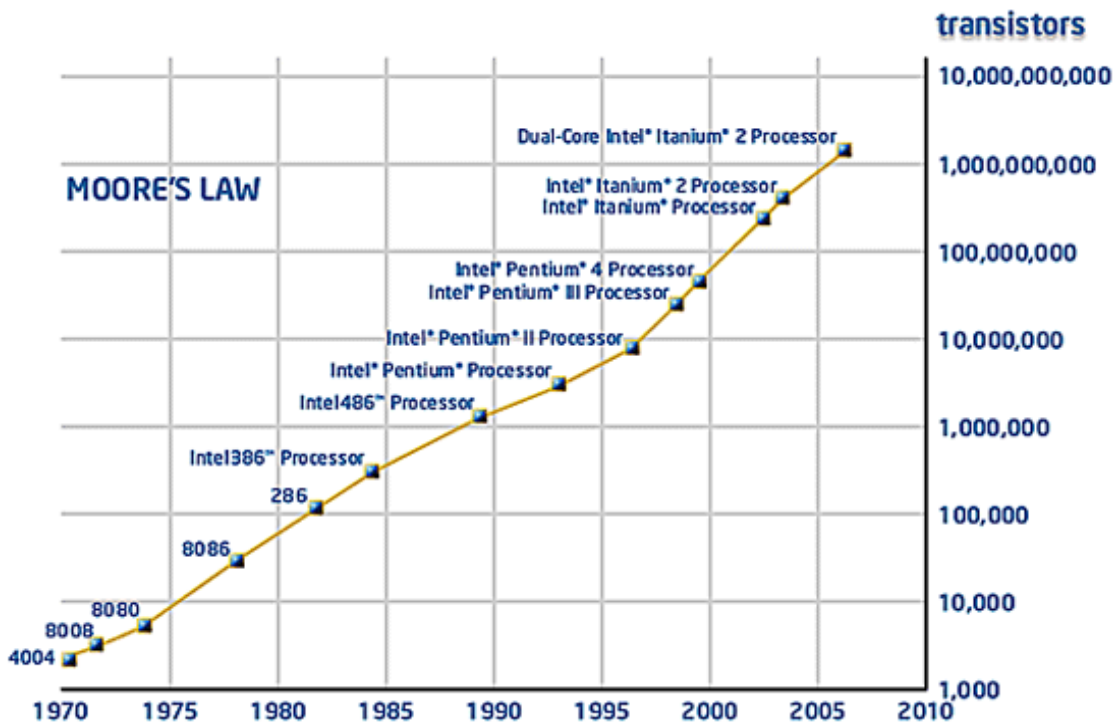
Table 2.1: Critical particle size to retain tetragonal BT	16
Table 2.2: Effect of additives on the ferroelectric transitions in BT- their solubility limits are also provided.	26
Table 2.3: Comparison on the effect of citric acid to ethylene glycol ratio on powder characteristics	36
Table 2.4: List of binders used for non-aqueous processing of BT ceramics	49
Table 2.5: Stages of sintering	57
Table 2.6 : List of glass compositions	67
Table 3.1: The details of the raw materials used for synthesis	85
Table 3.2: Molecular weights of the chemicals used for synthesis	85
Table 3.2: List of ingredients used for wet processing	100
Table 3.3: Properties of the binders	101
Table 3.4: List of Binder composition	101
Table 4.1: Thermal analysis results of the precursors using different barium sources	112
Table 4.2: Phase evolution during nano BT synthesis under conventional, microwave and hybrid heating conditions	122
Table 4.3: The activation energy and pre exponential factor for different microwave power for the t-BT formation in hybrid heating	128
Table 4.4: Lattice parameters of BT, BZT-10, BZT-20 and BZT-30 precursors calcined at 900°C for 5 hours in conventional heating and 700°C for 30 minutes in microwave heating. ( $c/a \pm 0.0004$ )	134
Table 4.5: BET surface area and dielectric properties results of the BZT compositions calcined at 900°C for 5 hours using conventional heating & 700°C for 30 minutes using microwave heating	135
Table 4.6: Lattice parameters of the BSZT-10/10, BSZT-20/10, BSZT 30/10 and BSZT 40/10 calcined at 900°C for 5 h in conventional heating and 700°C for 30 min in microwave heating	138

Table 4.7: BET Surface area and dielectric properties results of the BZT compositions calcined 900°C for 5 hrs using conventional heating & 700°C for 30 min using microwave heating	139
Table 4.8: Powder characteristics of the BT powders used	141
Table 4.9: The effect of PVB:EC ratio on rheological behaviour of the n-S-BT inks	151
Table 4.10: The effect of EC ratio on viscosities at different shear rate and thixotropic behaviour of the n-S-BT ink	154
Table 4.11: Screen printing conditions used for making nano MLCCs	159
Table 4.12: Onset of sintering for n-S-BT and $\mu$ -BT chip at different heating condition	162
Table 4.13: SEM micrograph of the n-S-BT and $\mu$ -BT chip sintered using different heating methods	165
Table 4.14: The representative room temperature electrical properties of the n-S-BT and $\mu$ -BT chips sintered at different conditions measured at 1 kHz & 1 V	166
Table 4.15: Onset of sintering for nano Sakai BT powders with 2.5wt% dopants	169
Table 4.16: Dielectric properties of the n-S-BT and Dopants	170
Table 4.17: Sintered densities of n-S-BT with different amount of dopants	170
Table 4.18: The room temperature electrical performance of the n-S-BT with different dopants concentration sintered at 1120°C for 1 h using microwave heating at 1 kHz and 1 V	173
Table 4.19: The densities of the nano MLCC sintered at different conditions	174
Table 4.20: Room temperature electrical properties of the nano MLCCs with 2.5 wt% dopant sintered using different heating method at 1 kHz & 1 V	176

# Chapter 1

## 1. INTRODUCTION

Electronic ceramics industry is constantly driven by technological challenges and innovation. Electroceramics provide the basic components to support a variety of electronic products including computers, industrial controls, consumer automotive devices, and digital switches. They are used as active components such as semiconductors to control voltage and current, or as passive components such as capacitors, varistors, and resistors<sup>1</sup>.



**Figure 1.1: Trend in number of transistors on a chip following Moore's law**  
(Reproduced from reference 2)

In the late 1960's Gordon Moore, the cofounder of Intel corporation, made a memorable observation that has since become known as Moore's Law. According to Moore's Law, the number of transistors on a chip doubled every 18 months and remarkably, the trend remained true for the past five decades (Figure 1.1)<sup>2</sup>.

Consequently, the individual electronic component size decreased continuously despite the difficulty of fabrication, which makes the materials normally obeying the classical physics, to follow quantum physics<sup>3</sup>. Thus the modern electronics industry is driven by miniaturization. This necessitates the reduction in dimension of all passive components to micrometer scale, without compromising on performance and the reliability. One of the best possible ways to achieve component size reduction is through the use of multiple layers of ceramics (MLC) in a single device. Compared to the bulk electroceramics, the multilayered ceramics offer several advantages in terms of performance, reliability, cost and component space savings. In particular, for applications such as mobile electronic equipment (cellular phones or portable personal computers), use of MLC's dominate at present and will play a major role in future too.

Capacitors are energy storage devices used in most of the modern electronic applications. Multilayer ceramic capacitor (MLCC) is the most widely used capacitor type, made of titanate based materials, constitutes more than half of the entire global capacitor market, worth multibillion U.S dollars.

The capacitance of the MLCC, is given by

$$C = \frac{\epsilon_0 \cdot \epsilon_r \cdot (n-1) \cdot A}{d} \quad \text{in Farad} \quad \text{Equation 1.1}$$

$\epsilon_0 \approx 8.85 \times 10^{-12}$ , in Farad per meter,

$\epsilon_r$  – Relative permittivity of the material, no units

A - Effective electrode area per electrode, in square metres,

n – Number of electrodes (metal layers), no units

d- Electrode spacing, in metres

Therefore the way to increase the capacitance is by either improving the dielectric permittivity of the ceramic material or by reducing the thickness of the dielectric

ceramic layers. This demands the need for developing new high dielectric permittivity materials and processing techniques to achieve thinner ceramic layers without deteriorating the device performance.

Although researchers have developed a number of new high dielectric permittivity materials, translating the powder materials into a product MLCC device is faced with many hurdles such as toxicity, chemical stability, and compatibility of the material with the industrial process choice.

Significant improvements have been made on the processing techniques such as screen printing and tape casting, which enabled the manufacture of MLCCs with 1-10  $\mu\text{m}$  ceramic layers. The development of integrated passive circuits, demand for high performance with miniaturization, steers the electronics industry to search for new processing techniques like inkjet printing. This process is still in its infancy and possesses a significant disadvantage of low green density of the prints.

The titanate ceramics use high temperature and air atmosphere for sintering. Since most metals oxidize at high temperatures, there is a need to use precious metals like Ag-Pd alloys as electrodes. The ever rising cost of Pd is of big concern for electronic industry. Hence there is strong need for moving towards cheaper metal electrodes.

Use of nanocrystalline ceramics can be expected to lower the processing temperature of the dielectric device and hence provides the opportunity for using cheap electrode materials with less Pd. In addition, nanostructured materials are expected to provide better dielectric properties that enable to form thinner ceramic layers. Thus, there is intense research interest on manufacturing of nano MLCCs.

Tetragonal barium titanate (BT) is one of the most widely used capacitor material, mainly because of its superior dielectric properties, environmental friendly nature and ease of manufacture. Electrical properties of these materials can be further tailored for different operating conditions of the device by compositional modifications and controlling nano grain structures.

The challenges related to the use of nanomaterials for capacitor applications are:

- (i) making the single phase tetragonal nano BT powder with less agglomeration
- (ii) to understand the rheological behaviour of nano BT inks and make them suitable for industrial MLCCs manufacturing and
- (iii) fabricating high density capacitors without abnormal grain growth.

The conventional nano BT synthesis methods require high temperature for tetragonal phase formation that leads to particle growth/agglomeration. Although a number of wet chemical synthesis routes emerged such as co-precipitation, precursor methods, hydrothermal synthesis etc., these routes requires a subsequent high temperature calcination stage, leading to formation of hard agglomerates. Microwave heating has been used for the nano ceramic synthesis and has been proven to assist bulk nucleation<sup>4</sup> and produce powders with less agglomeration.

The nanopowders were expected to form high viscous inks compared to micrometer sized powders for the same solids loading due to their high surface to volume ratio. This requires the development of suitable dispersants and binders for achieving high solids content, low viscosity suspensions.

The sintering of MLCCs requires high temperature and long soaking times for obtaining maximum densification, which in turn result in larger and abnormal grains. A rapid and efficient heating method is required to retain the nanostructures without abnormal grain growth. It has been demonstrated that microwave assisted heating enhances densification whilst retaining the grain size due to less demanding processing conditions<sup>5,6</sup>. As Barium titanate is a dielectric material and has inherent electric dipoles, it can also readily couple with the microwave frequencies<sup>1</sup>.

Therefore the present study was aimed at achieving BT based nanostructured multilayered ceramic capacitors (MLCCs) by systemically studying the various processing stages; starting with the powder synthesis, making nano ink formulations suitable for screen printing, sintering of component using microwave assisted heating methods and performance evaluation of the end products.

Thus, the primary objectives of the present work are:

- Synthesis of nano BT and compositionally modified BT formulations
- Preparation of nano BT inks and fabrication of X7R nano BT MLCCs through screen printing
- Sintering of nano BT MLCCs using different heating techniques
- Performance evaluation of the nano BT MLCCs.

The thesis is divided into five chapters; the overall objectives and report structure are outlined in this chapter.

Chapter 2 provides an overview on capacitors – their types and MLCCs, typical dielectric materials used for capacitor applications with a focus on barium titanate (BT) and the influence of compositional modifications on BT structure and performance. The current methods available for producing nanocrystalline BT powders and the associated difficulties in producing large quantities are briefly discussed. The fabrication methods used for MLCCs and challenges involved in processing nanocrystalline powders compared to micron BT powders are also emphasised. Finally, different ways of achieving dense nanostructured BT ceramics – effect of sintering aids/ flux additions used are highlighted. A brief account of the nature of microwave-material interactions is also outlined along with the advantages and disadvantages of the microwave approach over the conventional heating methods.

Chapter 3 summarizes the experimental work performed; the synthesis employed with different heating methodologies; the nano BT ink formulations developed; sintering aids used along with different characterization and measurement techniques employed at various stages of the work are also given in detail.

Chapter 4 discusses the results of the experimental work and discusses the possible mechanism involved during the microwave assisted synthesis of nano BT and BT based formulations. Clear evidence for the existence of a genuine ‘microwave effect’ during nano ceramics synthesis, was elucidated. Attempts on the optimization of

process variables for nano BT ink production and fabrication of nano MLCCs devices are presented here. The use of microwaves and dopant additions during nano BT sintering to achieve maximum densification with minimum grain growth and their effect on the electrical properties are also discussed in detail.

Chapter 5 highlights the important outcomes of the present project and provides the possible directions for future work in this challenging and rewarding field of study.



## Chapter 2

### 2. LITERATURE REVIEW

#### 2.1. Capacitors

A capacitor is an electrical/electronic device that can store charge and, in turn, energy during the application of an electric field between a pair of conductors (called "plates") and release this energy on demand. It consists of two metal conductors isolated by a non-conducting material capable of storing electrical charge for release at a controlled rate and at a specified time. The process of storing energy in the capacitor is known as "charging", and involves electric charges of equal magnitude but opposite polarity, building up on each plate.

The charge storing ability of the capacitor is measured as capacitance and calculated using the following equation

$$\text{Capacitance of the material (C)} = \frac{(\epsilon_0 \epsilon_r A)}{d} \text{ in Farad} \qquad \text{Equation 2.1}$$

Where,  $\epsilon_0$  – permittivity of the free space =  $8.845 \times 10^{-12}$ , in Farad per meter,

$\epsilon_r$  – Relative permittivity of the material, no units

A – Cross sectional area of the material, in square metres,

d – Distance between the metal electrodes, in metres.

Capacitors are often used in electric and electronic circuits as energy-storage devices. They can also be used to differentiate between high frequency and low frequency signals. This property makes them useful in electronic filters. It is also used in electrical circuits for blocking direct current while allowing alternating current to pass, in filter networks for smoothing the output of power supplies, in resonator circuits that tune radios to particular frequencies and for many other purposes.

Capacitors are an indispensable part of many electronic devices from camera flash units to modern computers.

### 2.1.1. Types of Capacitors

There are a wide variety of capacitor types including electrolytic, ceramic, tantalum, plastic, mica, and others. Each capacitor type has its own advantages and disadvantages which dictates its typical application. In some capacitors, the plates may be flat, and normally these capacitors will have rectangular or, more exactly, cuboid shape. Some will be tubular and in these capacitors the plates will be wound around. In some cases, it may be dipped in an insulating coating: in others, it may be contained within a metal can. The most commonly used capacitors are ceramic, plastic film types, electrolytic and tantalum based. These names refer to the type of dielectric that is used within the capacitor.

Depending upon the purpose, capacitors are classified as snubber capacitors, filter capacitors, clamp capacitors, etc and can also be split into two major groups, polarised and unpolarised. Each group has its own circuit symbol<sup>7</sup>.

Polarized capacitors have high dielectric permittivity and hence large capacitance values, measured in microfarads, are achieved with small size. Electrolytic (aluminium) and tantalum capacitors are also polarised but have low voltage ratings (6 V). Tantalum capacitors are expensive and are even smaller in size.

Unpolarised capacitors have low dielectric permittivity and hence results in small capacitance values (microfarads). They are mostly ceramic capacitors and are less expensive. There are other kinds like variable capacitors, with very small capacitances (picofarads). These are represented symbolically in Figure 2.1

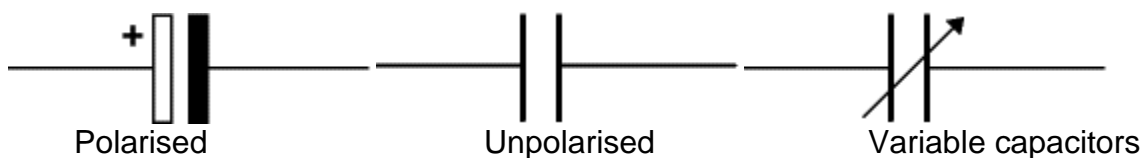


**Figure 2.1: Symbolic representation of different types of capacitors**  
(Reproduced from reference 8)

Ceramic capacitors come in various shapes and styles (Figure 2.2), including:

- disc, resin coated with through-hole leads for mounting
- multilayer rectangular block, surface mount chip
- bare leadless disc, sits in a slot in the PCB and is soldered in place, used for UHF applications
- tube shape, which is less popular now



**Figure 2.2: Different kinds of ceramic capacitors**  
(Reproduced from reference 9)

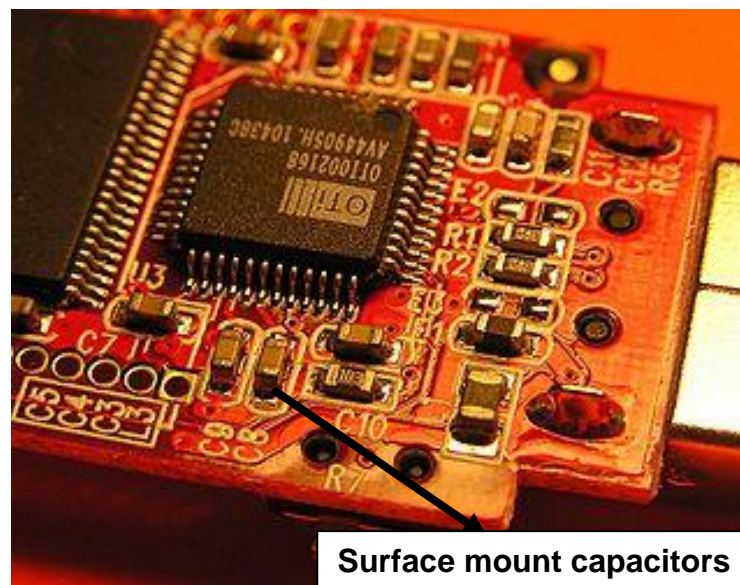


**Figure 2.3: Typical surfaces mount components on a Flash drive circuit board**  
(Reproduced from reference 10)

Due to the demand for complex electronic circuits and printed circuit boards (PCBs) to be miniaturized, the usage of the dip coated and leaded capacitor types has reduced and surface mount capacitors are now widely used.

Surface mount technology (SMT) is a method for constructing electronic circuits in which the components (SMC or Surface Mounted Components) are mounted directly onto the surface of PCBs. An SMT component is usually smaller than its through-hole counterpart because it has either smaller leads or no leads at all. It may have short pins of various styles, flat contacts and a matrix of solder balls or terminations on the body of the component. A typical PCB with SMCs is shown in Figure 2.3.

**2.1.2. Multilayered ceramic capacitors (MLCCs)**

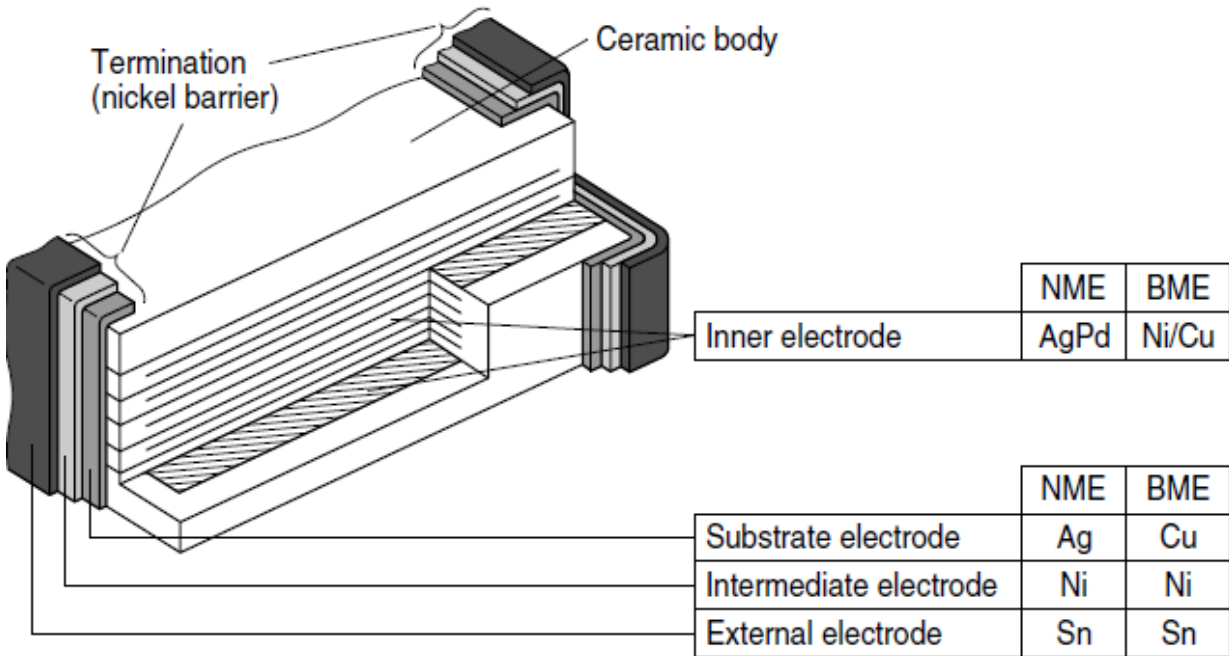


**Figure 2.4: Schematic representation of the MLCC cross sectional view**  
(Reproduced from reference 11)

The surface mount capacitors (SMCs) consist of alternate layers of dielectric and metal electrodes stacked together with an end termination electrode. When ceramic dielectric materials are used, they also are referred to as multilayer ceramic

capacitors (MLCCs). A schematic diagram of the typical cross section is shown in Figure 2.4.

According to equation 2.1, the capacitance is directly proportional to the cross sectional area of the device and inversely proportional to the thickness of the dielectric material. Making the dielectric material into thin (micrometer) sheets and stacking with alternative metal electrodes increases the capacitance of the capacitors.

MLCCs are mainly classified into two categories depending on the chemical composition of the dielectric and the electrical properties, viz. as class 1 and class 2.

**Class 1 capacitors:**

- Consists of a mixture of oxides and titanates with dielectric permittivity,  $\epsilon$ , <200
- Have linear temperature coefficient with reversible temperature dependence
- Have no variation of capacitance with voltage
- Have low losses up to ultra high frequency range.
- Have high insulation resistance

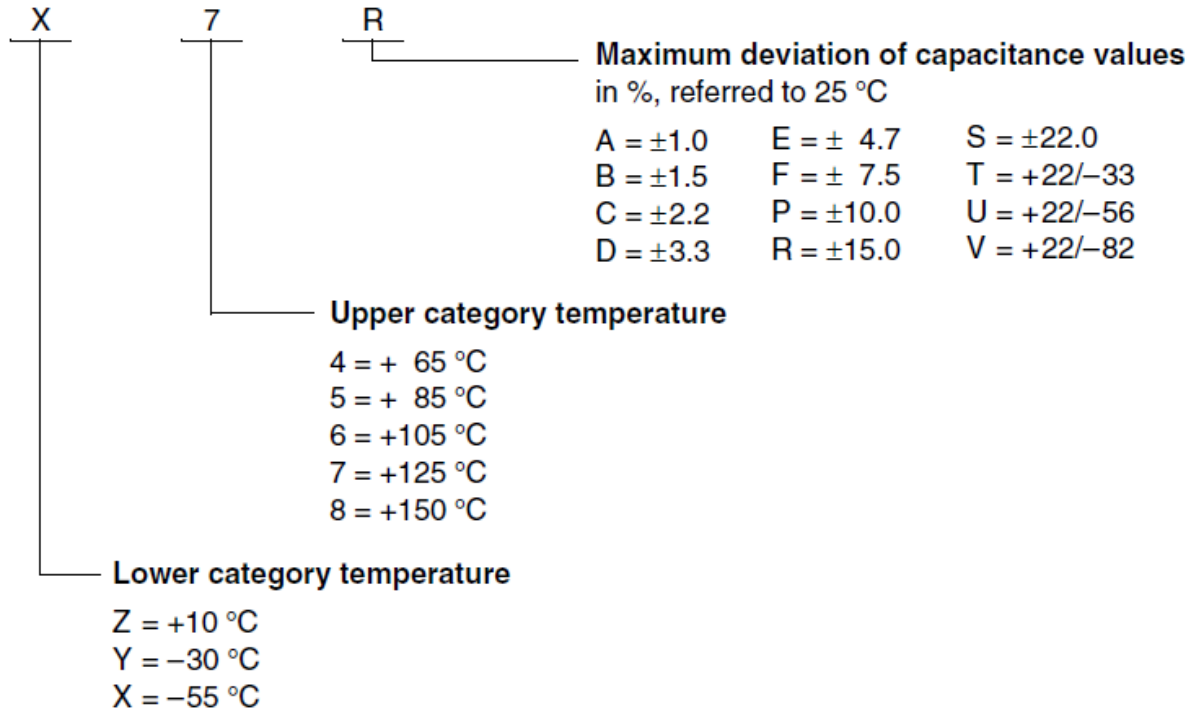
Applications: resonant circuits, filters, timing elements

**Class 2 capacitors:**

- Consists of barium, strontium, calcium titanates and zirconates with dielectric permittivity in the region of  $\epsilon \approx 200$  to 10,000.
- Have non-linear dependence of capacitance on temperature and voltage
- Have higher losses and lower insulation resistance
- Have high capacitance value even with small size

Applications: coupling, blocking, filtering

Temperature characteristics for class 2 capacitors are as follows,



For example, X7R means the temperature stability of the device is between -55°C to 125°C and associated with a capacitance change of ± 15%.

**(i) Effect of thickness of the ceramic layer on the capacitance of the capacitor**

The capacitance of the MLCCs, C [C/ V = F] is given by

$$C = \frac{\epsilon_0 \cdot \epsilon_r \cdot (n-1) \cdot A}{d} \quad \text{in Farad} \quad \text{Equation 2.2}$$

$\epsilon_0 \approx 8.85 \times 10^{-12}$ , in Farad per meter,

$\epsilon_r$  – Relative permittivity of the material, no units

A - Effective electrode area per electrode, in square metres,

n – Number of electrodes (metal layers), no units

d- Electrode spacing, in metres

Hence, by decreasing the thickness of the dielectric layer, capacitance will increase. The difficulty in achieving this is that the dielectric layers have to be sintered without creating any short circuit between the electrode layers. In addition, the differential shrinkage of the ceramic and metal layer has to be monitored, which can cause buckling and/or delamination. The initial particle size of the ceramic and metal electrode materials need to be reduced to enable formation of defect free thin layers.

### **2.1.3. Ceramic capacitor materials**

#### **(i) Titanate based materials**

Most of the ceramic capacitor materials are based on niobates and titanates. The three main types of ceramic capacitors, NPO/C0G, X7R, and Z5U, are mostly made of titanate-based materials, among which, BaTiO<sub>3</sub> (BT) forms the predominant baseline material. Recently a company named EESstor developed a compositionally modified barium titanate super capacitor of 1 MJ/Kg energy density (commercial existing super capacitors have 0.01 MJ/Kg) with higher capacitance<sup>12</sup>. These super or ultra capacitors have key applications in the automotive industry such as regenerative batteries for brakes and hybrid vehicles. These units were made using barium calcium zirconium titanate coated with alumina and glass in order to achieve the high level of capacitance<sup>13</sup>.

### **2.2. Barium titanate (BT)**

Barium titanate is the first and most important piezoelectric ceramic developed and it is still widely used<sup>14</sup>. The reasons being:

- It is chemically more stable than other Pb based materials;
- It has wider temperature range of operation than other piezoelectric ceramics;
- It's easy manufacturing techniques;
- It has very good coupling factors;

2.2.1. Crystal structure and Polymorphs of BT

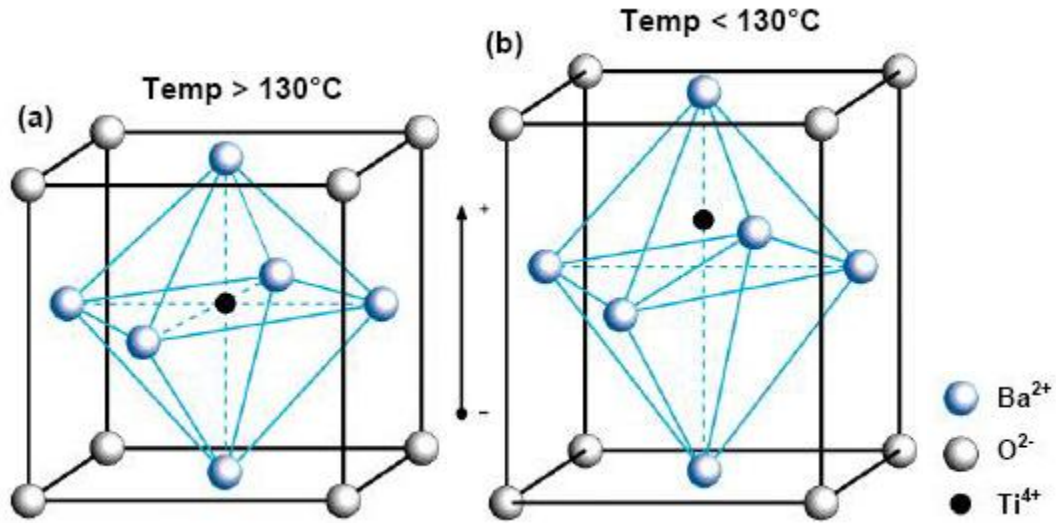


Figure 2.5: The typical BT crystal structure above its Curie temperature (Reproduced from reference 15)

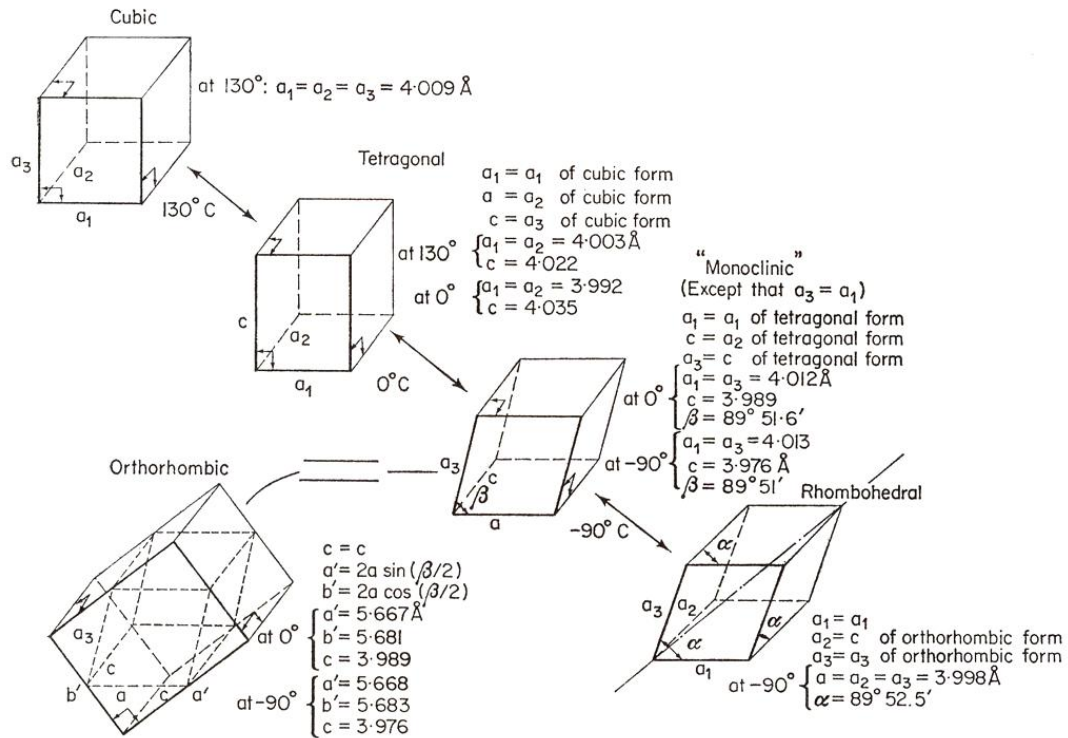


Figure 2.6: The polymorphic transformations of BT at different temperatures (Reproduced from reference 14)



Barium titanate has good ferroelectric properties because of its basic perovskite crystal structure. It has a simple cubic unit cell with large cation ( $\text{Ba}^{2+}$ ) on the corners, a smaller cation ( $\text{Ti}^{4+}$ ) in the body centre and oxygens ( $\text{O}^{2-}$ ) in the face centers (Figure 2.5). The structure is a network of corner-linked oxygen octahedra, with smaller cations filling the octahedral holes and the large cation filling the dodecahedral holes<sup>14</sup>. At room temperature, BT exists in tetragonal symmetry and has an off-centred small  $\text{Ti}^{4+}$  cation in the large oxygen octahedral cage, creating a dipole moment, hence the dielectric permittivity.

BT has two basic structures, a perovskite form that is ferroelectric at certain temperatures and a non-ferroelectric hexagonal form. It undergoes a reconstructive transformation at different temperatures. Figure 2.6 show the polymorphs at different temperature and the change in lattice parameters with increasing temperature. In each temperature range, the direction of the ferroelectric dipole parallels the elongation of the unit cell<sup>14</sup>.

The three ferroelectric polymorphs have a displacement of the central  $\text{Ti}^{4+}$  ion within the oxygen octahedron. It was verified that the  $\text{Ti}^{4+}$  ion in the tetragonal structure moves physically in phase with an applied electric field<sup>14</sup>. In addition, all 3 different transitions of BT are first order transitions. In addition, the phase transition depends on the purity, synthesis/sintering route and particle/grain size of the powder<sup>12</sup>.

### **2.2.2. Effect of particle and grain size on dielectric properties**

Dielectric properties are strongly dependent on purity and particle size. The presence of hydroxyl ( $\text{OH}^-$ ) and carbonate ( $\text{CO}_3^{2-}$ ) groups on the BT particles synthesized through some of the wet chemical routes found to decrease the dielectric permittivity. The dielectric permittivity of the impurity-free BT increases with decreasing particle size in the range of 1  $\mu\text{m}$  to 0.1  $\mu\text{m}$ , but decreases from 0.1  $\mu\text{m}$  to 40 nm, Figure 2.7. It has been reported that BT stabilizes with cubic symmetry with decreasing particle size<sup>16</sup>. The phase change in nano sized BT particles and the critical particle size have been extensively studied by many researchers. However, critical particle size to retain the tetragonality is still inconclusive, Table 2.1, as it

depends on the synthesis route, purity, and quality of the BT powder. Similarly, there are many controversial ideas on critical grain size of BT to retain the tetragonality. In addition, reduction in grain size affects the transition temperature significantly and changes from a traditional sharp transition to a more diffuse transition<sup>17</sup>.

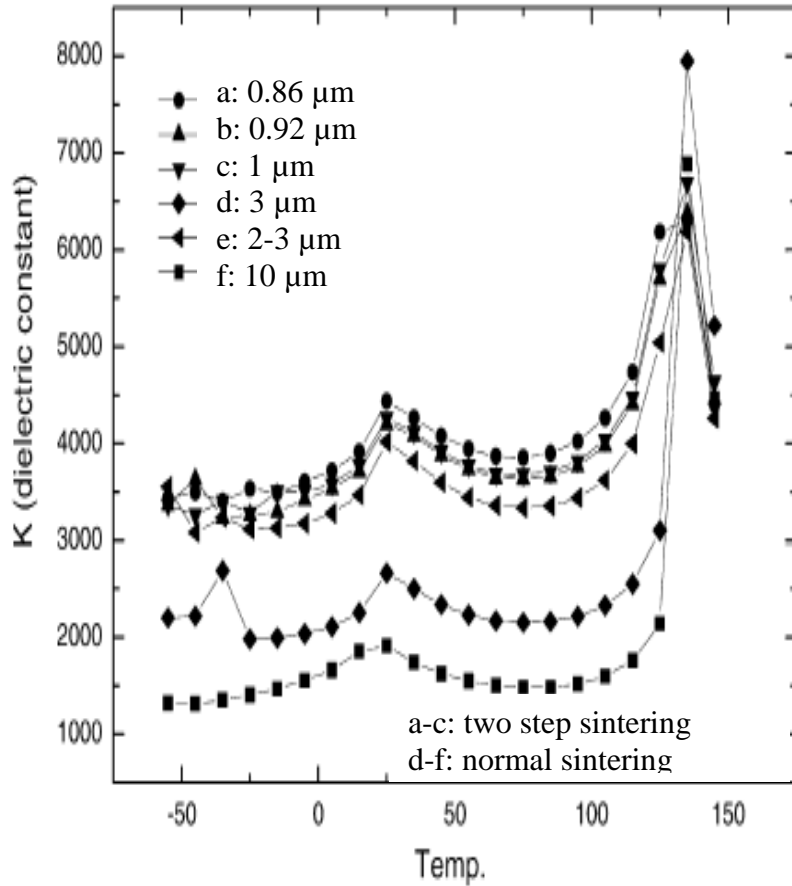


**Figure 2.7: Reported dielectric permittivity of BT as a function of grain size**  
(Reproduced from reference 16)

**Table 2.1: Critical particle size to retain tetragonal BT**

S.No	Synthesis route	Critical particle size, nm	Reference
1	Alkoxide derived	<100	18
2	Sol-gel	30-250	19, 20
3	Hydrothermal	20-150	21, 22
4	Polymeric precursor	20-30	17
5	Micro emulsion precipitation	20-30	23

### 2.2.3. Variation of dielectric properties with temperature and frequency

The relative permittivity increases to a maximum at the transition temperature and then decreases on further increases in temperature. Also, on increasing the applied frequency, the relative permittivity decreases. Figure 2.8 shows the typical temperature variation of the relative permittivity and dielectric loss of unpoled BT ceramic. The Curie Weiss law gives the maximum relative permittivity at the Curie point,

$$\epsilon_{rmax} = \frac{C_w}{(T_c - T_o)} \quad \text{for } T < T_c \quad \text{Equation 2.3}$$

$$\epsilon_r = \frac{C_w}{(T - T_o)} \quad \text{for } T > T_c \quad \text{Equation 2.4}$$

where,  $C_w$  - Curie constant  
 $T_o$  - Curie Weiss Temperature  
 $T_c$  - Curie temperature

For first order phase transition;  $T_c > T_o$

For Second order phase transition;  $T_c = T_o$

So from Equation 2.3,  $\epsilon_{rmax}$  at  $T_c$  will become infinite for a second order transition, which is impossible. Usually, for BT ceramics deviations from the Curie Weiss law are noticed in a narrow temperature region above the Curie point.

Traditionally, BT ceramics show a very sharp maximum peak at the transition temperature. Phase transitions showing broad  $\epsilon_r$  maxima and large deviations from the Curie Weiss Law are called diffuse phase transitions. This cannot be easily described by classical theory of ferroelectric phase transitions<sup>14</sup>. The transition in BaTiO<sub>3</sub> is a typical displacive transition with the softening of the lattice on the <100> axis.

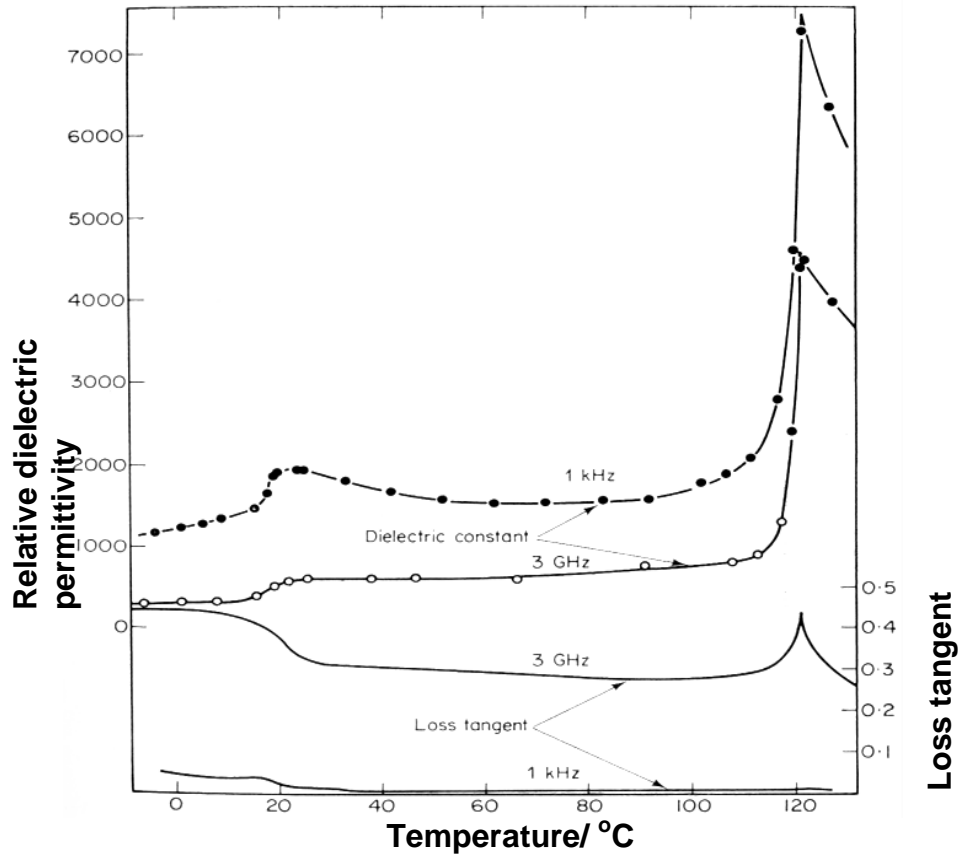


**Figure 2.8: The typical variation of BT dielectric permittivity with temperature and frequency**  
(Reproduced from reference 14)

#### 2.2.4. Effect of density / porosity on dielectric properties

Relative permittivity also decreases rapidly with a decrease in the relative density of BT samples. Figure 2.9 shows relative permittivity decrease with a very small increment in the porosity of the sample, reaching near zero for samples with 0.4% porosity<sup>14</sup>. A low sintered density indicates the presence of porosity in the microstructure. The pore may be filled with air, which has a low dielectric permittivity and hence lowers the overall relative permittivity of the sample. Moisture can be easily absorbed in the pores, creating a conducting medium and hence a weak conductive path for short-circuiting. Thus the presence of porosity reduces the dielectric permittivity, increases the dielectric loss and also lowers the breakdown strength.

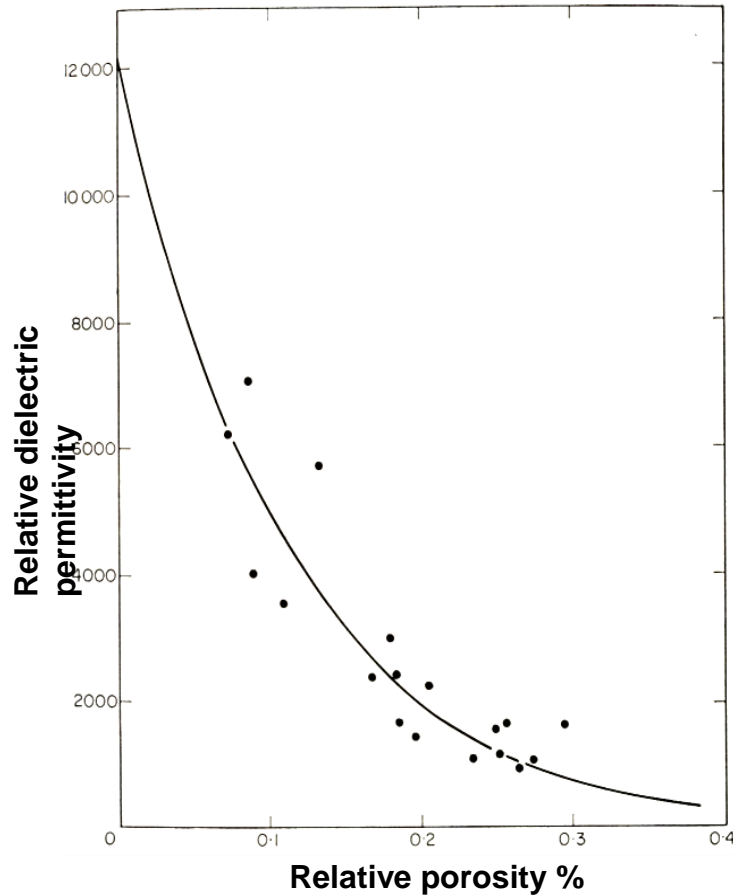


**Figure 2.9: Typical variation of BT dielectric permittivity with sample porosity**  
(Reproduced from reference 14)

### 2.2.5. Effect of compositional modifications on dielectric properties of BT

A wide variety of cations can be substituted into the Ba (A site) and Ti (B site) position of the BT perovskite structure, if they are of similar size and total equivalent oxidation state. During the substitution most of the perovskite structures are distorted. Some of the common distortions are cations displacement within octahedra and tilting of octahedra. The factors that contribute to these distortions are ionic radius of the substitution atoms. The degree of distortion in  $ABO_3$  perovskite can be determined using the following equation and are defined as Tolerance factor,  $t$ ,

$$t = \frac{(R_a + R_o)}{\sqrt{2(R_b + R_o)}} \quad \text{Equation 2.5}$$

Where,  $R_a$ ,  $R_b$ ,  $R_o$  indicate the ionic radii of cations and anion respectively. If  $t$  is close to 1, the structure exhibits ideal cubic symmetry. When the  $t$  value is  $\leq 0.81$ , the A site substituent is less than the ideal and hence the  $BO_6$  octahedra tilt to fill the space. A stable perovskite have  $t$  values of approximately  $0.78 \leq t \leq 1.05$ . For instance pure barium titanate;  $t=1.06$ , ( $t \geq 1$ ) due to the fact that the  $Ti^{4+}$  ion is smaller in its cavity;  $BaZrO_3$  and  $SrTiO_3$  have  $t$  value of 1 and that because the  $Ba^{2+}$  is larger than its cavity. Structures with a tolerance factor of 0.95-1 are cubic; lower values are slightly distorted and non ferroelectric, whilst values over 1 tend to be ferroelectric<sup>24,25</sup>. The tolerance factor is used as an estimate, as the perovskite are not exclusively ionic. However, substitutional chemistry cannot be determined by the tolerance factor alone, for which the tensor nature of the strain, as well as charge and charge distribution effects, have to be considered<sup>26</sup>. The tolerance factor is a very useful tool to compare similar ions on the same site as it gives correct trends<sup>14</sup>. In addition, less reliable comparisons between different sites and different charge states can be made provided correct coordination numbers are considered, namely, 12 and 6 for the A and B sites respectively. For such comparisons, tolerance factors for substitution ions on the A and B sites are referred as  $t_A$  and  $t_B$  respectively, taking into account the correct coordination number.

In  $BaTiO_3$  solid solution, substituent atoms in the lattice affect the structural integrity and hence the lattice soft mode is inevitably affected. Li and Wu attempted to understand the transition character of paraelectric to ferroelectric transition, in relation to the lattice soft mode behaviour for different solid solutions of  $(Ba,Sr)TiO_3$ ,  $(Ba,Ca)TiO_3$ ,  $Ba(Ti,Zr)O_3$ ,  $Ba(Ti,Sn)O_3$  and concluded that Ti site substituents have a diffuse phase transition character whilst Ba site substituents preserve a sharp phase transition. Ti site substituents reduce the strain with temperature but the recovery of the  $\langle 100 \rangle$  axis strain can take place only for low concentrations.

Therefore, BT compositions can be modified by isovalent and aliovalent substitution of different cations in the  $Ba^{2+}$  and  $Ti^{4+}$  positions. The main purpose here is to alter the Curie Point and improve the dielectric properties. The effect of isovalent

substitution on transition temperatures are shown in Figure 2.10<sup>14</sup>. The details of the inferences from the figure are discussed below.

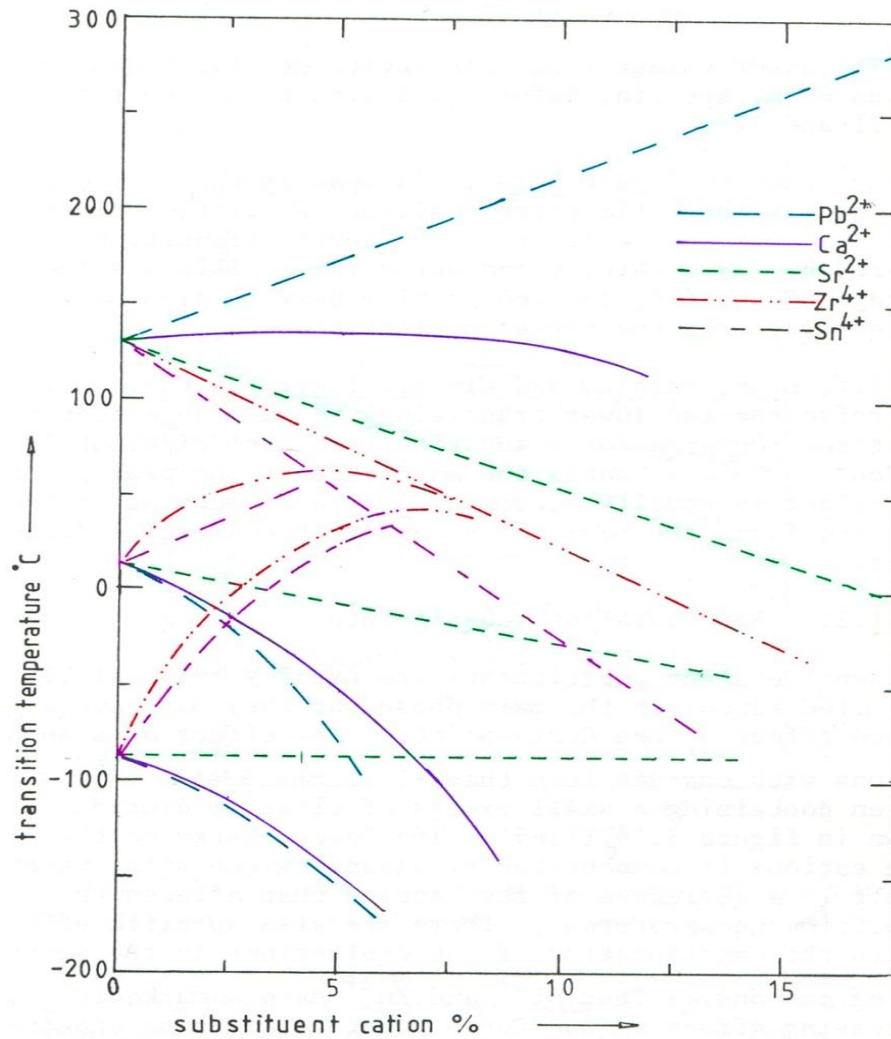


**Figure 2.10: Variation of the transition temperatures for different amount of isovalent substituent**  
(Reproduced from reference 14)

### (i) 'Ba' Site Substituents

#### Strontium ( $\text{Sr}^{2+}$ )

Barium strontium titanate (BST) is a ferroelectric solid solution material that exhibits high relative permittivity coupled with good thermal stability and a Ba/Sr

composition-dependent Curie temperature,  $T_C$ . The ionic radius of  $\text{Sr}^{2+}$  (0.112 nm) is smaller than  $\text{Ba}^{2+}$  (0.135 nm) cation. Partially replacing Sr with Ba decreases the unit cell volume of the material, thus tetragonality decreases. This requires less energy and hence less temperature, for the tetragonal to cubic phase transition and thus reduces the transition temperature. From Figure 2.10 it is noteworthy that the Curie Point decreases linearly with solid solution of  $\text{Sr}^{2+}$  replacing  $\text{Ba}^{2+}$ . It is noted that BST solid solutions have higher peak relative permittivity than pure  $\text{BaTiO}_3$ .

The main purpose of addition of  $\text{Sr}^{2+}$  into BST is to shift the Curie temperature towards room temperature, offering a high relative permittivity, low leakage current and low dielectric dispersion against frequency<sup>14,27</sup>. Previous studies on the dielectric properties of BST ceramic solid solutions have shown that the compositions with  $\text{Sr} \leq 0.2$  has exhibited normal ferroelectric behaviour, while a relaxor characteristic (diffuse phase transition and dielectric dispersion) has been observed in the  $\text{SrTiO}_3$  rich region ( $\text{Sr} > 0.2$ ). The phase transition behaviour changes from sharp to diffuse.

### **Lead ( $\text{Pb}^{2+}$ )**

Although  $\text{Pb}^{2+}$  (0.119 nm) has a smaller ionic radius than  $\text{Ba}^{2+}$ , the Curie Point is increased with Pb substitution and the temperature of the tetragonal to orthorhombic and orthorhombic to rhombohedral transition decreases, Figure 2.10. In addition, at room temperature dielectric permittivity reduces simultaneously. The  $\text{Pb}^{2+}$  ion has a larger electronic polarizability than  $\text{Ba}^{2+}$  or  $\text{Sr}^{2+}$ , which intensifies the interaction between the Ti ions and thus raises the Curie Point<sup>12</sup>. Complete solid solution forms for all Pb concentrations<sup>14,28,29</sup>. Due to the high coercive field of  $\text{PbTiO}_3$  at high  $\text{Pb}^{2+}$  compositions, it is difficult to pole. Poling is the process of aligning the spontaneous polarized regions in the ceramic using sufficiently high voltages. When the coercive field is high, the polarized regions realign partially even after the poling. The major disadvantages of Pb are its greater volatility, making it difficult to maintain the desired composition, and its toxic nature; hence it is not environmentally preferable<sup>14</sup>.



## (ii) 'Ti' Site Substituents

### Zirconium (Zr<sup>4+</sup>)

Partial substitution of Ti<sup>4+</sup>, ionic radius 0.745 nm, with Zr<sup>4+</sup>, ionic radius 0.86 nm, forms the solid solution Ba(Zr<sub>x</sub>Ti<sub>1-x</sub>)O<sub>3</sub>, BZT, with an associated increase in the lattice parameter and consequent changes to the crystal structure, phase transition temperatures and the dielectric properties compared to pure BT

Ba (Zr<sub>x</sub>Ti<sub>1-x</sub>)O<sub>3</sub> (BZT) compositions have a very high relative permittivity and broad maxima around the Curie Temperature. Like Sr, Zr is an effective substituent for decreasing the Curie Temperature towards room temperature<sup>30</sup>. The Ti<sup>4+</sup> ion can reduce its valence state to Ti<sup>3+</sup> when processed under reducing atmospheres, producing a semi conductive BT. However, Zr<sup>4+</sup> is chemically more stable than Ti<sup>4+</sup>, therefore, substitution of Ti<sup>4+</sup> by Zr<sup>4+</sup> suppresses the conduction by electronic hopping between Ti<sup>4+</sup> and Ti<sup>3+</sup> and can decrease the leakage current of the BaTiO<sub>3</sub> system<sup>31</sup>.

In the BZT solid solution, substituting Ti by Zr distorts the oxygen octahedra. As the ionic size is larger than the Ti, the adjacent oxygen will be pushed outward to the centre of the neighbourhood octahedral along the <100> direction. Hence, the open space for Ti displacement at this axis is reduced and retarded, repressing the transition dynamics for polarization. Thus, a sluggish dielectric response and diffuse phase transition behaviour is resulted. The insertion of one oxygen will drive the other oxygen outward and thus widens the open space for movement along the <110> and <111> axes. Consequently, the transition temperature of the other two low temperature phases is raised<sup>14</sup>.

Previous research performed using submicron-sized powders has suggested that BZT remains tetragonal at Zr additions of up to ~0.2 mol%, then changes to pseudo-monoclinic over the range 0.2 – 0.6 mol% before becoming rhombohedral at Zr substitution levels up to ~20 mol%. Above the latter, BZT is cubic at room temperature<sup>32</sup>. Pure BT undergoes a sharp ferroelectric to paraelectric (tetragonal to

cubic) transition at 130°C. With up to 10 mol% of Zr, BZT ceramics exhibit a similar behaviour with a shift in the phase transition temperature from 130 to 110°C. By 30 mol% of Zr addition, they show diffuse phase transition behaviour<sup>33</sup>. Above 30 mol%, the Zr-rich compositions exhibit diffuse phase transitions and dielectric dispersion, showing a relaxor-like behaviour<sup>34</sup>. These phase transition temperatures and phase boundary compositions are dependent on the crystallite size of the primary particles<sup>35</sup>. As BZT is the solid solution of BaTiO<sub>3</sub> and BaZrO<sub>3</sub> and the latter exhibits cubic symmetry at room temperature, the critical size for BZT to retain tetragonality is smaller than that of BT<sup>36</sup>. In addition, the coordination number decreases with increasing Zr content, indicating the compounds are becoming more and more covalent<sup>37</sup>

Thus, BZT has a number of advantages compared to BT, including:

- high relative permittivity and a broad maximum relative permittivity at the Curie Temperature,
- lower ferroelectric Curie Point,
- greater chemical stability
- depression of conduction by electronic hopping,
- decrease in the leakage current, and
- reduction in the average grain size and a decrease in the dielectric permittivity, allowing a low and stable leakage current to be maintained.

### **Tin/Stannate (Sn<sup>4+</sup>)**

Even a small increase in the Sn concentration has been found to bring down the tetragonal to cubic transition temperature and increase the orthorhombic to tetragonal and rhombohedral to orthorhombic transition temperatures. A number of researchers<sup>29,38,39,40</sup> have observed that by increasing the Sn concentration, the temperature of the ferroelectric–paraelectric phase transformation decreases and becomes more diffuse within a wide temperature range<sup>41</sup>. In addition, Kumar et al., found that the three-phase transitions coalesced and formed a single broad maxima peak with 10 mol% Sn content<sup>42</sup>. Tiwari et al., have devoted considerable effort to

explain the diffuse ferroelectric transition in  $\text{Ba}(\text{Sn}_x\text{Ti}_{1-x})\text{O}_3$ <sup>43</sup>. These compositions were found to have no other structural phase transitions in their ferroelectric state.

$\text{Sn}^{4+}$  substitution has also been found to increase the alkali resistance of BT. Hence this material is now important for applications involving humid conditions like boundary layer capacitors and multifunctional temperature humidity control gas sensors<sup>44</sup>.

### (iii) Aliovalent substitution

Substitution of ions of suitable size but unmatched valence, although limited in solubility, can cause profound effects on the dielectric and piezoelectric properties of BT. Acceptor dopants, with 3+ cations, create oxygen vacancies in  $\text{BaTiO}_3$ . Whilst donor dopants, with 5+ cations, have more free charge carriers, creating a lossy hysteresis loop and facilitate domain wall motion. The diffusion of oxygen vacancies is much faster than cation vacancies as the distance between the nearest oxygens (0.28 nm) is smaller than Ti-Ti or Ba-Ba (0.4 nm)<sup>45</sup>. Thus the defect dipoles and oxygen vacancies in the donor doped BT easily realign with spontaneous polarization of the domain walls, thereby lowering the dissipation energy at lower temperatures  $<T_c$ . Even at high temperature, the free charge carrier conductivity increases the dissipation factor<sup>46</sup>.

Table 2.2 shows the effects of additions of isovalent and aliovalent ions with higher and lower valency on the ferroelectric transitions of  $\text{BaTiO}_3$ . Nb has a 14 mol% solubility limit and shows relaxor behaviour above 6 mol%<sup>14</sup>. Substitutions of  $\text{Zr}^{4+}$ ,  $\text{Nb}^{5+}$ ,  $\text{Ta}^{5+}$  and  $\text{La}^{3+}$  result in good high temperature resistivity and suppression of the Curie peak<sup>14</sup>. Whilst very small quantities (0.1%) of  $\text{Co}^{3+}$ ,  $\text{Ni}^{2+}$ ,  $\text{Cr}^{3+}$  improve the transducer properties and  $\text{Fe}^{3+}$ ,  $\text{Co}^{3+}$ , and  $\text{Ni}^{2+}$  promote the formation of the hexagonal phase that  $\text{Ca}^{2+}$  and  $\text{Sr}^{2+}$  addition inhibits<sup>14</sup>. Yttrium substitution has a much lower solid solubility of only 0.122% and shows a single broad diffuse phase transition<sup>33</sup>.  $\text{Y}^{3+}$ ,  $\text{Bi}^{3+}$ ,  $\text{Sb}^{5+}$ ,  $\text{W}^{6+}$ ,  $\text{La}^{3+}$ ,  $\text{Gd}^{3+}$ ,  $\text{Er}^{3+}$  and other rare earths modify the volume resistivity of the  $\text{BaTiO}_3$  ceramic<sup>14</sup>.

**Table 2.2: Effect of additives on the ferroelectric transitions in BT- their solubility limits are also provided.**  
(Reproduced from reference14)

Additive	Solid solution limit, mole%	Change of transition temperatures (°C) per mole % additive:		
		Curie point	O-T	R-O
<b>Isovalent</b>				
Pb (Ba)	100	+3.7	-9.5	-6.0
Sr (Ba)	100	+3.7	-2	0
Ca (Ba)	21	+,-	-6.7	-6
Zr (Ti)	100	-5.3	+7	+18
Sn (Ti)	100	-8	+5	+16
Hf (Ti)	100	-5	+7	+16
<b>Higher valence</b>				
La	>15	-18	+,-	+,-
Nb	14	-26	+12	+25
Ta	14	-29	+12	
Y (Ba)	>2	+2.5	-19	
Bi	0.67	+18	-40	
Mo (Ti)		+	0	-
W (Ti)	0.8	-18	-	0
<b>Lower valence</b>				
Mg (Ti)	1	-2	0	0
Ni (Ti)	3	-8	-	+5
Co (Ti)	30	-40	+	-
Fe (Ti)	>21/2	-75	-	-
Al (Ti)	<5	+	+	-
Cr (Ti)	>6	+	5	+
Ag (Ba)	>0.2	-25	-	-

(O-T is Orthorhombic to Tetragonal; R-O is Rhombohedral to Orthorhombic)

Currently  $(\text{Ba}_{1-x}\text{Sr}_x)(\text{Zr}_y\text{Ti}_{1-y})\text{O}_3$  and  $(\text{Ba}_{1-x}\text{Ca}_x)(\text{Zr}_y\text{Ti}_{1-y})\text{O}_3$  are of significant research interest because of the superior ferroelectric properties they exhibit<sup>47</sup>. Ho et al.,<sup>48</sup> studied the effects of Zr on the structural and dielectric properties on  $(\text{Ba,Sr})\text{TiO}_3$  solid solution and reported that the relative permittivity of 66,000 was measured at the transition temperature for the  $(\text{Ba}_{0.75}\text{Sr}_{0.25})(\text{Zr}_{0.1}\text{Ti}_{0.9})\text{O}_3$  formulation. Recently a maximum dielectric permittivity of 26,600 at room temperature was reported for  $(\text{Ba}_{0.7}\text{Sr}_{0.3})(\text{Zr}_{0.1}\text{Ti}_{0.9})\text{O}_3$  composition, powders synthesized using a co-precipitation route<sup>47</sup>.

### 2.2.6. Effect of microstructure on dielectric properties

As mentioned before in the case of dielectric ceramics, during the application of an electric field domain wall motion takes place causing the dissipation of energy.

Below  $T_c$ , the losses ( $\tan\delta$ ) are high. Above  $T_c$ , the dielectric loss is very low as there are no domains and the loss is mainly due to the conduction loss at high temperatures above  $T_c$ <sup>49</sup>.

When doped BT is sintered at high temperatures, the conduction takes place through electron transfer between titanium ions,  $Ti^{4+} + e^- \rightarrow Ti^{3+}$ . The BT grains remains conducting but the structure and composition of the grain boundary changes during cooling. The oxygen is adsorbed on the surface and diffuses to the grain boundary sites, forming the defect structure along the grain boundaries. The oxygen at the grain boundaries attracts the electrons from nearby  $Ti^{3+}$  ions, creating the insulation barrier<sup>49</sup>. A schematic diagram of the defect perovskite structure formation is shown in Figure 2.11. Thus the electrical resistance of the ceramic is inversely proportional to the grain size, i.e. the smaller the grains, the more insulating the grain boundaries and hence the higher the resistance.

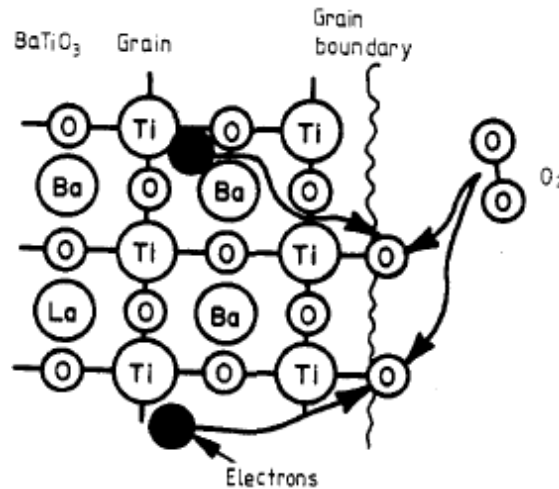


**Figure 2.11: Schematic diagram of defect perovskite formation**  
(Reproduced from reference 49)

BT dielectric ceramics have to form a core-shell structure for optimum performance to improve the insulation resistance and achieve X7R characteristics, i.e. the core of the grains are nearly pure BT, retaining the ferroelectric phase, whilst, the shell like grain boundaries form a paraelectric phase due to partially dissolved dopants in the BT lattice, which reduces the Curie Temperature<sup>42</sup>, Figure 2.12. This provides

temperature stable characteristics of the capacitance and a reliable performance in MLCCs.

The critical things to be considered in achieving the core-shell structures are<sup>50</sup>;

- being thermodynamically unstable,
- selecting proper dopants to react with BT grains,
- Uniformly distributing dopants around the BT particles.

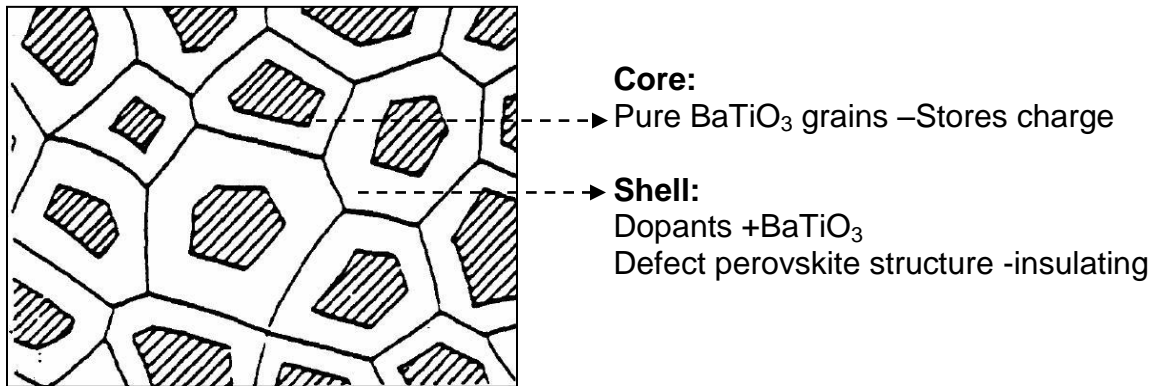


**Figure 2.12: Schematic representation of the core shell structure in a BT ceramic**

(Reproduced from reference 50)

### 2.3. Electrode materials used in MLCCs

As discussed, other than the dielectric, the next important constituent of a capacitor is the metal electrode. The basic criteria for the selection of metal electrodes are<sup>51</sup>:

- Having good electrical conductivity
- Having melting temperature higher than the sintering temperature of the ceramic layer
- Having equilibrium oxygen pressure of metal/metal oxide system
- Low cost
- Adhesion of the metal to the ceramic surface

Some of the candidates for electrode materials are silver, gold, tin, copper, nickel, iron, platinum and palladium, etc. However, the need to fire in air constraints the metals that can be used.

Noble metals like Pt, Au and Pt-Au alloys can be used in the temperature range of 800-1500°C, matching the sintering temperature of BT (~1350°C) but are very expensive. The BT sintering temperature can only be lowered to 1100-1200°C using flux addition or glass composition forming a liquid phase and is discussed in detail in the following section.

Silver is cheap and has a low melting point of 961°C, so can be fired to 600-800°C. The main disadvantages of silver are (i) it has a poor adhesion on ceramic surfaces; normally a small amount of glass frits was added to improve the wetting on the ceramic without reacting with it, (ii) it has a tendency to easily penetrate into the ceramic surfaces and to the grain boundaries especially, at high temperature or in the presence of moisture and in the presence of an electric field, (iii) Sometimes this leads to the possibility for dendrite growth from cathode to anode, creating a low resistance path. Thus, pure silver cannot be used as electrode materials for thin ceramic dielectrics. Alloying with 10-15 wt% Pt / Pd / Au diminishes the above difficulties; hence the alloy has emerged as a promising electrode material. Among Pd, Pt and Au, Pd has a low solubility in BT, even at high temperatures and has good adhesion with no deleterious effects. Hence, Pd and Ag-Pd alloys are widely used in MLCCs.

### **2.3.1. Use of cheaper metal electrodes in MLCCs**

As discussed above, the electrodes are currently made of precious metal/alloys to allow co-sintering in air with the dielectric ceramic layers. The proportion of the electrode cost to overall cost increases with increasing stacking layers (and miniaturization), hence a significant strategy for cost reduction in capacitors is the use of cheaper metal electrodes. After multiple researches on this aspect, methods for reducing cost of the internal electrodes have been classified into the use of:

1. Ag / Ag-Pd alloy with high Ag content ( $\geq 70$  wt%) to achieve low sintering temperature of the dielectrics, and
2. Base metals like Ni and Cu by using a non reducible dielectric that can be fired in a reducing atmosphere. Under the reducing atmosphere firing conditions, conventional BT dielectrics reduce to become semi conductive. However it is important to note that non reducible dielectrics have had to be developed to maintain the high insulation resistance in order to use the base metal electrodes, BMEs. In reducing atmosphere sintering conditions, the partial pressure of the respective metal electrodes and their oxides needs consideration, Figure 2.13.
3. Low melting fluxes and glass components have been added, to the BT dielectrics, which in turn reduces the firing temperature.

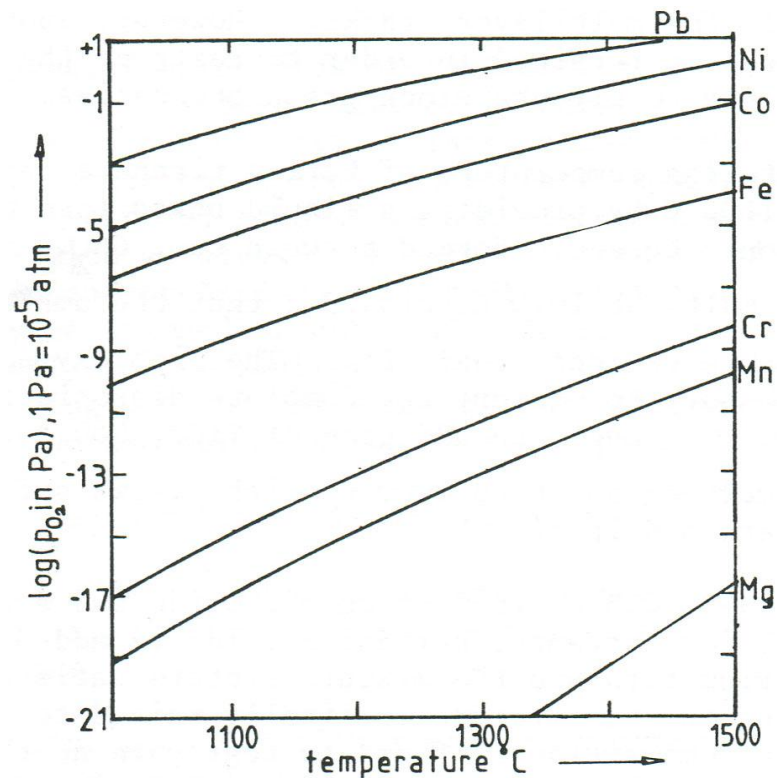


**Figure 2.13: Equilibrium oxygen pressure of metal/metal oxides at higher temperature**  
(Reproduced from reference 51)



Copper has a low melting point, 1080°C, hence to use it with the above mentioned, challenges the ceramic sintering temperature have to be lowered to <900°C. Comparing the equilibrium oxygen pressures of metal/metal oxides for selected elements, calculated from their free energy from Figure 2.13, nickel is a good candidate as it has a higher melting point of (1452°C) and has higher metal/metal oxide equilibrium oxygen vapour pressure compared to iron and cobalt.

### **2.3.2. Processing issues during co-sintering of metals and ceramics**

The first challenge was to develop a chemically stable dielectric. Since the 1970's, this has been achieved using Mn and Cr, as the conduction electrons are trapped by the acceptor dopants without decreasing the insulation resistance. In the 1980's it was found that it could be achieved by dissolving small amounts of excess BaO or CaO in the dielectrics. The cations sit on the Ti sites and act like Mn but results in grain boundary secondary phases. These materials have a short life of insulation resistance at high temperature. In the late 1990,'s the use of rare earth cations were explored and these succeeded in achieving longer life characteristics. However, the cost of the rare earths is high and there are toxicity issues, hence the research is still ongoing. The development of non reducible dielectrics using intermediate sized cations / rare earths that can occupy both Ba and Ti sites by balancing the donor/acceptor ratio have given the opportunity to use Ni electrode MLCCs. In recent years there has been great progress made for Ni electrode MLCCs using novel processing methods<sup>52</sup>.

A major driver in the MLCC industry is the miniaturization of components and a simultaneous increase in the multifunctionality so that electronic devices that use them can shrink in size. Whilst there are issues to be handled, due to the thickness of ceramic and metal layer decrease, including electrode buckling, delamination and short circuiting, the primary goal is to develop and then use fine dielectric and electrode powders. These will allow both thinner layers to be achieved and also significantly increase the chances that they remain intact as the layer thickness decreases. In addition, the lower sintering temperature of the finer dielectric

properties will enhance the potential for co-sintering with base metal electrodes (BME), which are based on low cost silver and nickel. Considerable research is therefore underway on the synthesis of nanostructured materials.

#### **2.4. Nanocrystalline ceramics**

Nanocrystals are referred to regime between the molecular clusters and crystals of micrometre size. The physical and chemical properties of material changes as the particle size decreases below micrometre due to quantum size effects, surface and interface effects and crystallographic changes.

Nanostructures have been developed for high-end technologies through scientific understanding by two main approaches:

- Super lattice and quantum dot devices, and
- Three dimensional ultrafine polycrystalline structures, also called nanostructured materials.

Polycrystalline ceramic materials with grain size of <100 nanometres are defined as nanocrystalline ceramics. The fractions of atoms in the interface regions are large, and even the defects are of nanoscale and this change the bulk nature of the materials. For instance, nanoceramics tend to undergo plastic deformation through increased grain boundaries and grain boundary sliding<sup>53</sup>, prone to have low thermal conductivity, show higher optical transparency, enhanced ionic and electrical conductivity

Although, property enhancement is the key aspect for using nanocrystalline powders, major driving force for using nanopowders is their ability to lower the sintering temperature. The submicron BT sinters at 1250°C, hence the MLCCs should have 30% Ag - 70% Pd. Whereas, using the nano BT, which can sinter at 1150°C, a cheaper 70% Ag - 30% Pd electrode can be used for the fabrication of MLCCs. Thus the cost of devices comes down drastically without compromising the performance. Therefore, multilayered electro ceramic devices greatly benefit by using nanopowders. The first main step to achieve nanostructured materials is to

produce the starting powders at nanoscale i.e., nanopowders. To achieve this, there are number of 'Bottom up' and 'Top down' synthesis methods developed, as outlined below.

#### **2.4.1. Different ways of producing nanopowders of BT**

The classical approach for synthesizing BaTiO<sub>3</sub> is the so-called "Mixed oxide route," which is based on the formation of perovskite phase by diffusion controlled solid-state reaction, starting from equimolar mixtures of barium carbonate (BaCO<sub>3</sub>) and titania (TiO<sub>2</sub>), typically at temperatures between 850°C and 1400°C. This process has resulted in particles of several micron sizes, with some unwanted secondary phases<sup>54</sup>. The main disadvantages of this route are:

- (i) Incomplete chemical reactions due to improper mixing;
- (ii) requires several iterations of mixing to get uniform powders;
- (iii) Possibilities for contamination during mixing;
- (iv) Higher processing temperature;
- (v) Large resultant particle sizes.

Hence, several wet chemical routes have emerged to produce fine BT nanopowders as discussed below. Their advantages and disadvantages are also highlighted.

##### **(i) Alkoxide derived precursors method**

The pioneering process, developed by Mazdiyasi (1969)<sup>55</sup> and his co-workers utilized simultaneous hydrolytic decomposition of titanium ethoxide and barium isopropoxide. Amorphous alkoxide derived gels are converted into crystalline BaTiO<sub>3</sub> by heat treatment at higher temperature (400 – 650°C). A minimum calcination temperature of 500 and 700°C is necessary to remove the residual carbon. As the entire process is carried out under the inert atmosphere, there is no BaCO<sub>3</sub> formation during this process. The exact mechanism of BaTiO<sub>3</sub> formation has not yet

reported<sup>56,57,58,59</sup>. This route results in fine and pure crystalline BaTiO<sub>3</sub> powder. The problems associated with this process are the high cost of alkoxide reagents and the premature hydrolysis of extremely moisture sensitive barium precursor.

### **(ii) Oxalate process**

This is identified as one of the best processes for obtaining BaTiO<sub>3</sub> powders with perfect stoichiometry in large quantities. This process has a good atomic level of mixing. The Barium and Titanium chlorides reacts with water and oxalic acid, to precipitate double oxalate (BaTiO(C<sub>2</sub>O<sub>4</sub>)<sub>2</sub>.4H<sub>2</sub>O)<sup>60</sup> and the oxalates are dried and calcined to form BaTiO<sub>3</sub>. This process typically results in fine cubic BaTiO<sub>3</sub> powders that on additional heat treatment form soft agglomerates of the tetragonal phase<sup>58,61</sup>.

### **(iii) Co-Precipitation process**

The co-precipitation route is one of the promising methods for synthesizing fine nanopowders at low temperatures but control of agglomeration in this process is found to be difficult. Also densifying the powders of this route is quite difficult because of its high purity. Hence additional energy and care is to be taken during sintering or else the product results in poor dielectric properties<sup>58,62</sup>. The co precipitation process is limited to cation solutions with similar solubility. In this process, metal salts are dissolved in an alkaline medium to form intermediate compounds and get precipitated. The precipitates have to be further calcined to form single phase BaTiO<sub>3</sub>.

### **(iv) Hydrothermal synthesis**

The Hydrothermal synthesis is a method of synthesis of fine nanopowders, which depends on the solubility of metal oxides/hydroxides in hot water under high pressure. Although ultra fine powders are obtained using this route, the stoichiometry is affected by the solvent type, the amount of solvent and their difficulty in controlling. The processing parameters such as pH, reaction time, temperature, pressure and concentration of the ionic species in the solution do affect the physical and chemical characteristics of the BaTiO<sub>3</sub> powders formed<sup>58,63</sup>. This

process is scalable but the main disadvantage is the purity, it leaves an adsorbed hydroxyl ion on the surface of the particle that can affect the sintering and dielectric properties of the resultant electro ceramics.

**(v) Sol gel derived process**

This is one of the oldest synthesis routes for making nanopowders and can be scalable. The process relies on the stabilization of titanium complex under alkaline conditions and its neutralization by  $Ba^{2+}$  ion. The metal cations are arrested in the network of gel and inhibit the particle growth. Hence, this process results in fine nanopowders with less agglomeration. Although it results in fine crystalline particles, this method also involves control of several parameters such as pH, temperature, intensity of agitation and rate of addition of the titanium precursor<sup>58,64</sup>. A gelling agent is added to form a gel network of the metal cations and upon calcination, the dried gels results in fine cubic nano  $BaTiO_3$  powder. In addition, many times, powders produced in this route are found not having good dielectric properties because of the adsorbed hydroxyl groups<sup>58</sup>.

**(vi) Polymeric precursor method**

This process utilizes the ability of certain  $\alpha$ -hydroxycarboxylic acid such as citric acid (CA), lactic acid, glycolic acid to form polybasic chelates with titanium, zirconium and niobium<sup>65, 66</sup>. The chelates undergo polyesterification when heated with polyhydroxyl alcohol such as ethylene glycol (EG).

Advantages of Polymeric Precursor method are;

- It is possible to prepare materials in the form of powders, films, fibres.
- Quasi atomic dispersion of constituent components, which facilitates synthesis of the crystallized powder with ultra fine particle size and high purity.
- Low temperature process and the starting materials are cheap and readily available, hence providing cost savings<sup>60-79</sup>.

The three main steps involved in these reactions are;

- Dehydration reaction
- Decomposition/Oxidation reactions of the organic species to form intermediate phases such as  $\text{BaCO}_3$ ,  $\text{TiO}_2$  or  $\text{Ba}_2\text{Ti}_2\text{O}_5 \cdot \text{CO}_3$  and
- Decomposition/Reaction between intermediate phases leading to the formation of  $\text{BaTiO}_3$  as the final reaction product.<sup>67, 68, 69, 70, 71</sup>

Effect of (citric acid to ethylene glycol) CA/EG ratio:

The intermediate polymeric network mainly controls the final particle size. The viscosity of polymeric gel increases with CA/EG ratio. The mobility of metal cations is less in high viscosity gel. Also, the resin structures can be less uniform in terms of spatial distribution of metal ions among the macromolecular chain and the packing of macromolecular chains due to lower polymeric chain. Thus for high CA/EG ratio, the average distance between the metal cations is less and hence this high packing density facilitates the oxide formation at low temperatures. But the particle surface area increases with decreasing CA/EG ratio<sup>72</sup>.

The particle size of calcined powder is also influenced by the nature of decomposition of the gel which in turn depends on the CA/EG ratio. Also CA/EG has a strong influence on stabilizing the phase in the polymeric gel. For instance, tetragonal YSZ was stabilized at room temperature and even reheating up to  $1000^\circ\text{C}$  doesn't result in change of phase.

**Table 2.3: Comparison on the effect of citric acid to ethylene glycol ratio on powder characteristics**

Low CA/EG	High CA/EG
<p><i>Porous structures</i></p> <p><i>Aggregates with pores</i>  <i>Large Agglomerates size</i>  <i>Tendency for partial sintering of the crystallites</i></p>	<p><i>Less porous structures</i>  <i>Decomposes gradually on wide temperature range</i>  <i>Less aggregates with pores</i>  <i>Less agglomerations</i></p>

Effect of molar and pH ratio:

The molar ratio of metal cations to citric acid and pH of the solution can influence the chelation and affect the thermal decomposition of the polymeric precursor. When molar ratio is increased, chelation of cation and citric acid changes from unidentate to bridging complex, which can be easily decomposed at low temperature. The pH value might affect the chelation between cation and citric acid but has no influence on the formation of  $\text{BaTiO}_3$ <sup>73</sup>.

Reaction mechanism:

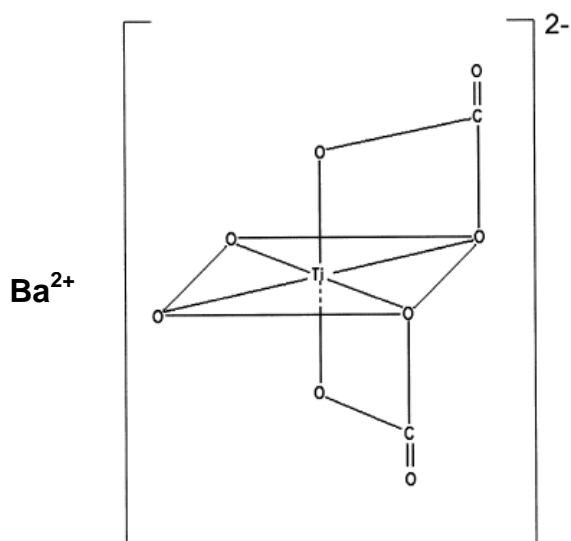


**Figure 2.14: The intermediate structure of the BT chelate**  
(Reproduced from reference 74)

There have been several attempts over the years, to understand the reaction mechanism during thermal decomposition of (Ba, Ti) polymeric precursors for  $\text{BaTiO}_3$  formation. Initially, it has been reported that the existence of oxycarbonate intermediate phase ( $\text{Ba}_2\text{Ti}_2\text{O}_5\cdot\text{CO}_3$ ) is crucial before forming  $\text{BaTiO}_3$  (Figure 2.14).

There have been many contrasting ideas on the thermolysis of precursors to an intermediate product. Gopalakrishnamurty et al. have first pointed about the existence of oxy carbonate intermediate phase when using barium titanyl oxalate<sup>75</sup>. Subsequently, some more authors have identified an intermediate phase

composition as  $\text{Ba}_2\text{Ti}_2\text{O}_5\cdot\text{CO}_3$  using different characterization techniques such as X-Ray diffraction<sup>76</sup>, HREM and EELS combined with quantum-mechanical DFT calculations<sup>69,77</sup>. It has also been suggested that the intermediate phase could be a mixture of fine  $\text{BaCO}_3$  and  $\text{TiO}_2$ <sup>78,79</sup>. Other than the above, the possibility of stabilizing hexagonal  $\text{BaTiO}_3$  as an intermediate with  $\text{Ti}^{3+}$  ions has been proven through X-Ray photoelectron spectroscopy<sup>80</sup>.

#### 2.4.2. Synthesis of compositionally modified BT nanopowders

The BST powders have been prepared using conventional mixed route and it has been found that the stoichiometry influences the dielectric properties significantly<sup>81</sup>. Several other wet chemical routes like acetate based sol-gel method<sup>82</sup>, co precipitation<sup>83</sup>, polymeric precursor method<sup>84, 31, 85</sup> etc. have also been successful in synthesising BST nanopowders.

Similarly BZT nanopowders have been synthesised through co-precipitation<sup>86</sup> and alkoxide precursor route at less demanding synthesis conditions<sup>87</sup>. It has also been qualitatively explained that BZT formation has been mainly controlled by the acid base neutralization reaction<sup>88</sup>. Bernardi et al. have synthesized BZT nanopowders by Pechini method and achieved single phase tetragonal  $\text{BaTiO}_3$  at 900°C and orthorhombic BZT nano powders (30 nm) at 600°C<sup>89</sup>. They have also found that there has been no effect of the particle size with increasing Zr content.

#### 2.4.3. Difficulties in producing nano BT powders

Although there has been lot of synthesis routes emerged for nanocrystalline ceramic synthesis, until now, production of nanoceramic powders in large quantities has always been a major hurdle. Gas phase condensation has gained popularity after Gleiter produced iron particles of 10 nm size<sup>90</sup>. Following that other oxide ceramics like  $\text{ZnO}$ <sup>91</sup>,  $\text{MgO}$ <sup>92</sup>,  $\text{TiO}_2$ <sup>93,94</sup>,  $\text{Al}_2\text{O}_3$ <sup>92</sup> have also been produced. Few techniques like gas condensation, combustion synthesis, thermo chemical synthesis, co-precipitation, hydrothermal synthesis, and sol-gel processing have been available to produce good quality nanopowders but with agglomeration. Hence, to match the



demands of the market, researchers and industries are working collaboratively towards achieving a low cost process, to produce genuine nanopowders in large quantities, without their inherent processing issues. This is being discussed in the following section.

## **2.5. Processing of nanocrystalline powders**

The main challenges in the fabrication of the multilayered capacitor devices using nanopowders are

- controlling the agglomeration,
- achieving homogeneous, defect free, dense green compact,
- attain a well dispersed suspensions with high solid loading with desirable flow characteristics,
- controlling grain growth whilst achieving maximum density during sintering.

Some of these key difficulties of processing nanopowders are discussed here.

### **2.5.1. Control of agglomeration**

Thermodynamically, nanopowders are highly unstable, as they have high surface free energy. The stress ( $\sigma$ ) due to the excess surface energy ( $\gamma$ ) with a radius of curvature (R) is giving by Laplace equation:

$$\sigma = \frac{\gamma}{R} \quad \text{Equation 2.6}$$

Hence, the adjacent nanoparticles tend to bond together and form soft/hard agglomerates based on the strength of the bonding. Sometimes the hard agglomerates are very difficult to be removed (or crushed to their primary constituents) during processing<sup>95</sup>. This prevents uniform mixing of other ingredients like dispersants, binders, sintering aids, dopants etc during processing.

A schematic representation of different kinds of pores in an agglomerated powder is shown in Figure 2.15a. The agglomerated powders are characterised by multimodal

pore size distribution, a typical pore size distribution of nano powder is shown in Figure 2.15b. The peaks at  $<50$  nm represents the inter particle/intra agglomerate pores and are called as the primary pores. The peak at less than  $1 \mu\text{m}$  is referred as the inter-agglomerate pores, i.e. the pores formed between agglomerates.

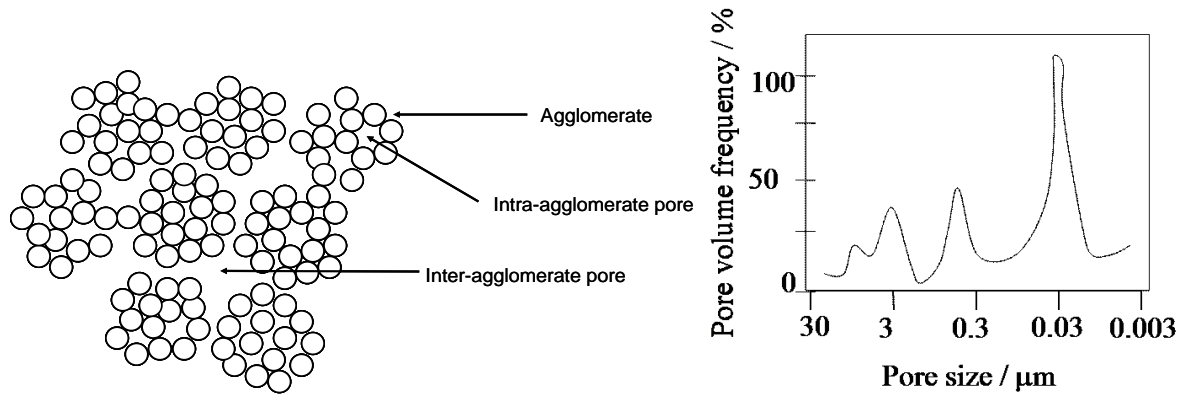


**Figure 2.15: (a) Schematic representation of agglomerates in the nanopowders (b) Typical pore size distribution of the agglomerated nanoceramics powders**  
(Reproduced from reference 96)

These agglomerates can be broken during pressure assisted sintering techniques. However, these are very sensitive for pressure less sintering, because the driving force for densification, shrinkage, and shrinkage rate inside the agglomerates can differ from those in between agglomerates, which can lead to internal stresses, appearance, and stabilisation of large pores or micro cracks. During the sintering of agglomerated nanopowder compacts, the intra agglomerate pores are removed at early stages of sintering, leaving large inter agglomerate pores, which are unsuitable to pin the grain boundaries and requires much higher temperature, resulting in grain growth. This results in deterioration of the anticipated nanostructure. Hence, it is very crucial to eliminate the agglomerates in nanopowders at the early stage of processing.

### 2.5.2. Difficulties in dry processing of nanopowders

The green bodies of nanopowders have large number of initial particle contacts, small pores, and uniform pore size distribution compared to the submicron powders. This favours high sintered density. Although nanopowders lower the time and

temperature for sintering, many sintering defects can be found in the green compacts due to non-uniform density distribution and lack of close packing. Though nanocrystalline powders are prone to less sized defects than micron powders, the difficulty arise in the elimination of pores from the green compact.

During cold compaction, the powder undergoes several stages like sliding and rearrangement of particles, elastic compression of particle contact point and fragmentation of ceramic materials. In nanopowders, sliding and rearrangement of particles are highly restricted due to high frictional forces among the particles<sup>97</sup>. The irregular particle boundaries help to form agglomerates, hence particle rearrangements are hindered, and this leads to lower green density. In addition, the nanopowders can cause high frictional force with the die wall, causing die wear and require hard die materials. Therefore, the major challenges to overcome during dry pressing of the nanopowders include poor flowability, increased die wall – particle interaction, high inter-particle friction, agglomeration and low green density of the final compacts. In addition, more precaution and safety measures are needed while handling the dry nanopowders.

### **2.5.3. Challenges in the wet processing of BT nanopowders**

The three main criteria' to achieve during wet processing of nanopowders are,

1. a well dispersed stable suspension
2. high solid loading with low viscosity
3. good flow characteristics

Thus, the first main step in the wet processing is to achieve a well-dispersed stable suspension in a solvent medium.

#### **(i) Dispersability of nanopowders**

According to the Derjaguin-Landau-Verwey-Overbeek (DLVO) theory, the sum of repulsive electrical double layer interaction and the vanderwaals interaction between

particles gives the stability of the colloidal system. This is represented by the equations

$$V_{\text{total}} = V_{\text{DL}} + V_{\text{vdw}} \quad \text{Equation 2.7}$$

$$\text{and } V_{\text{total}} = V_{\text{vdw}} + V_{\text{elect}} + V_{\text{steric}} + V_{\text{structural}} \quad \text{Equation 2.8}$$

where,  $V_{\text{vdw}}$  is the attractive potential energy due to vanderwaals interactions between particles;

$V_{\text{elect}}$  is the repulsive potential energy resulting from electrostatic interactions between like charged particle surfaces;

$V_{\text{steric}}$  is the repulsive potential energy resulting from steric interactions between particle surfaces coated with adsorbed polymeric species;

$V_{\text{structural}}$  is the potential energy resulting from the presence of non-adsorbed species in solution that may either increase or decrease suspension stability. The various types of stabilisations like electrostatic, steric and structural changes are schematically illustrated in Figure 2.16. In order to overcome the force of attraction between the particles, repulsive forces of either electrostatic, steric, or electrosteric origin must be employed to achieve well-dispersed suspension.

Electrostatic forces between particles can be generated by excess charge on the particle surface. Thus, the charged layers repel each other and are called electrical double layer, represented by Zeta potential. The strength of double layer and repulsive forces depend on dielectric properties of the particle and the dispersing medium. Zeta potential is controlled by pH, concentration of additives, ionic strength etc. This is very important in aqueous dispersions.

Similarly, steric stabilization is achieved by adsorbing polymeric layer on the particle surface. This is very important in a non-aqueous medium.

Electrostatic and steric stabilization together form electrosteric stabilization. These polyelectrolytes/ dispersants contain at least one type of ionisable group (e.g.,

carboxylic, sulphonic acid groups) with molecular structure that ranges from homopolymer such as poly acrylic acid or polyethylene imine to block copolymers with one or more ionisable segments.

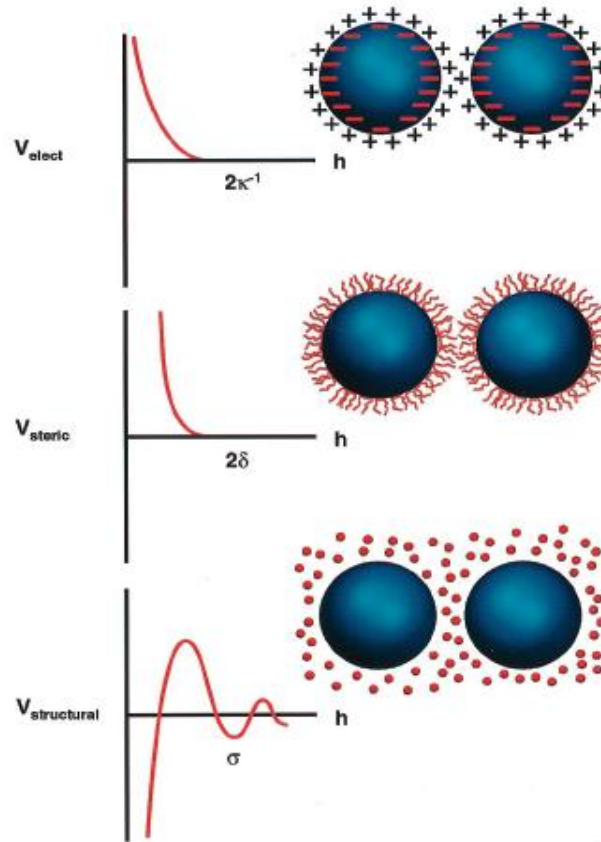


**Figure 2.16: Schematic illustration of the interaction potential energy and relevant length scales for (a) electrostatic, (b) steric, and (c) structural contributions, where  $\kappa^{-1}$  is the effective double-layer thickness,  $\delta$  the adlayer thickness, and  $\sigma$  the characteristic size of species resulting in ordering within the inter particle gap.**

(Reproduced from reference <sup>98</sup>)

Therefore, dispersant has been used to adsorb/coat the particle surface and increase repulsive force between the particles and prevent particles from agglomerating/settling. The strength of repulsive force depends on the dielectric properties of colloidal particle and the medium. Thus, the dispersant has to change the particle surface and create a repulsive force slightly higher than the attractive

van der waals force, to achieve well-dispersed stable suspension with high solid loading.

The main difficulties during the preparation of nanopowder dispersions are,

- Nanopowders have tendency to form aggregates in a dispersing medium because of the high inter particle attraction.
- It restricts the usage of dispersant with smaller molecular size, as it has to cover the particle surface and nanoparticles having high surface area.
- The amount of dispersant required to achieve well dispersed suspension increases with decrease in particle size, which in turn increases the viscosity of the suspension and this limits the maximum solids loading.
- Also limits the medium used for processing, nanopowders behave differently in different processing medium, which needs thorough understanding.

Many previous studies have been carried out on micron BT dispersion and stabilization in aqueous and non aqueous medium using polymers<sup>99</sup> and polyelectrolytes/dispersants<sup>100,101</sup> respectively

### (ii) Aqueous processing

As explained earlier, zeta potential is the key to obtain electrostatic stabilization and hence the isoelectric point (IEP- at which zeta potential is zero) is important. This gives a pH range at which the surface charge density is high, to generate a strong repulsive force forming double layer. The oxide surface ionization is denoted by



where,  $MOH^{2+}$ ,  $MOH$ ,  $MO^{-}$  represent positive, neutral, and negative charge on surface respectively<sup>102</sup>. Below IEP, the oxide surface is positively charged and above IEP its negatively charged, hence anionic and cationic polyelectrolytes adsorb on the oxide particle surface below and above the IEP respectively and change the surface charge as a function of pH.

Thermodynamically BT is unstable in acidic medium, as  $\text{Ba}^{2+}$  leach out from the oxide surface, changing Ba/Ti ratio at the particle surface.<sup>103</sup> (Figure 2.17)

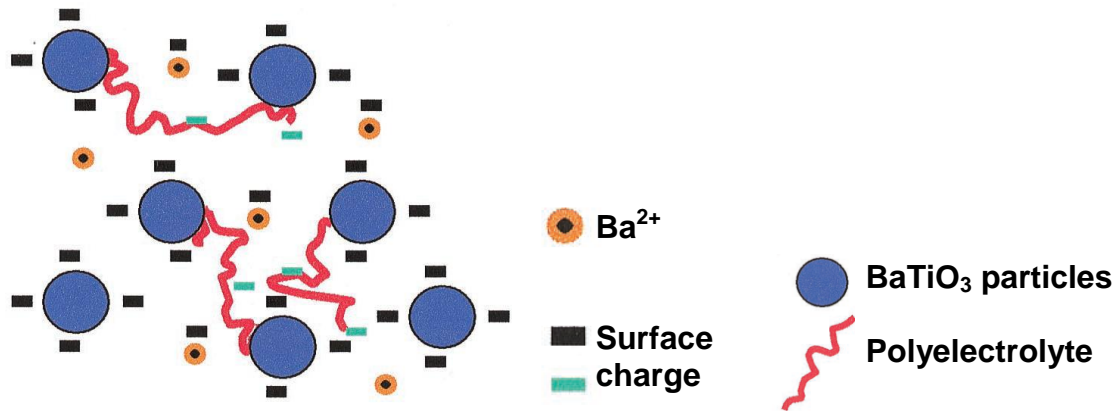
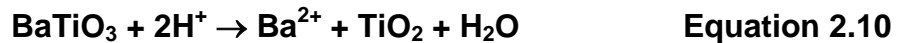
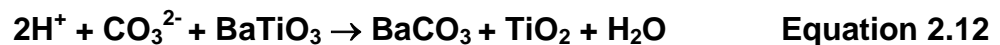
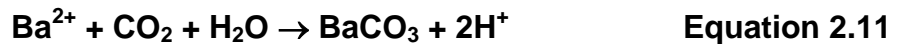


**Figure 2.17: Schematic representation of  $\text{Ba}^{2+}$  dissolution during aqueous processing**



The leached  $\text{Ba}^{2+}$  combines with  $\text{CO}_2$  in the water and forms  $\text{BaCO}_3$  and deposit on the particle surface, preventing further leaching<sup>104</sup> of  $\text{Ba}^{2+}$ .



Due to dissolution of  $\text{Ba}^{2+}$ , a shift in IEP has been observed with increasing solid content.  $\text{BaTiO}_3$  exhibits IEP values varying from 2.2 to 12<sup>101,102, 104, 105,106</sup> based on the solution conditions. Also the Ba leaching will be very vigorous in the nano BT powders because of its high surface area. Hence, there is very less scope for aqueous processing of nano BT. Attempts have been made on using different polyelectrolytes to stabilize aqueous nano BT suspensions<sup>101, 102,103,107,108,109,110,111</sup> but due to the lack of stability of BT in water at nanoparticle sizes, exhibiting different IEP values, showing difficulty in process consistency.

**(iii) Non-aqueous processing:**

To avoid the  $Ba^{2+}$  leaching, which can change the Ba/Ti ratio during aqueous processing<sup>112</sup> non-aqueous processing has been widely used.

Several studies have reported usage of nonaqueous solvent mediums like toluene, methyl ethyl ketone, ethanol, acetone, hexane, butyraldehyde, benzaldehyde, etc. and azeotropic and zeotropic solvent mixtures. In non-aqueous medium, the steric stabilization plays an important role in particle dispersion. Few dispersants mostly used in the non-aqueous medium are triton-X, menhaden fish oil and phosphate ester.

Use of non-aqueous medium has many advantages like

- Good dispersion of powders
- High solid loading
- Low viscosity
- Controlled/ fast drying rate
- Dissolve all the other ingredients

Most of solvents are non-polar (solvents with dielectric permittivity  $<15$ ). Technically, the dielectric permittivity measures the solvent's ability to reduce the field strength of the electric field surrounding a charged particle immersed in it and hence the dispersability of the nanopowders. In addition, because of its low viscosity, good dispersability and the ability to dissolve all other ingredients homogeneously, it is possible to use nanopowders with high solid loading. Above all, fast drying rate is closely tied with the production rate. Hence, non-aqueous processing is the most preferred method for multilayer capacitor manufacturing.

**2.6. Fabrication of multilayered capacitor devices**

Compared to dry processing, wet processing methods like tape casting, screen-printing are mostly used for the fabrication of multilayer devices, as they yield good packing of particles and are suitable for mass production (Figure 2.18).



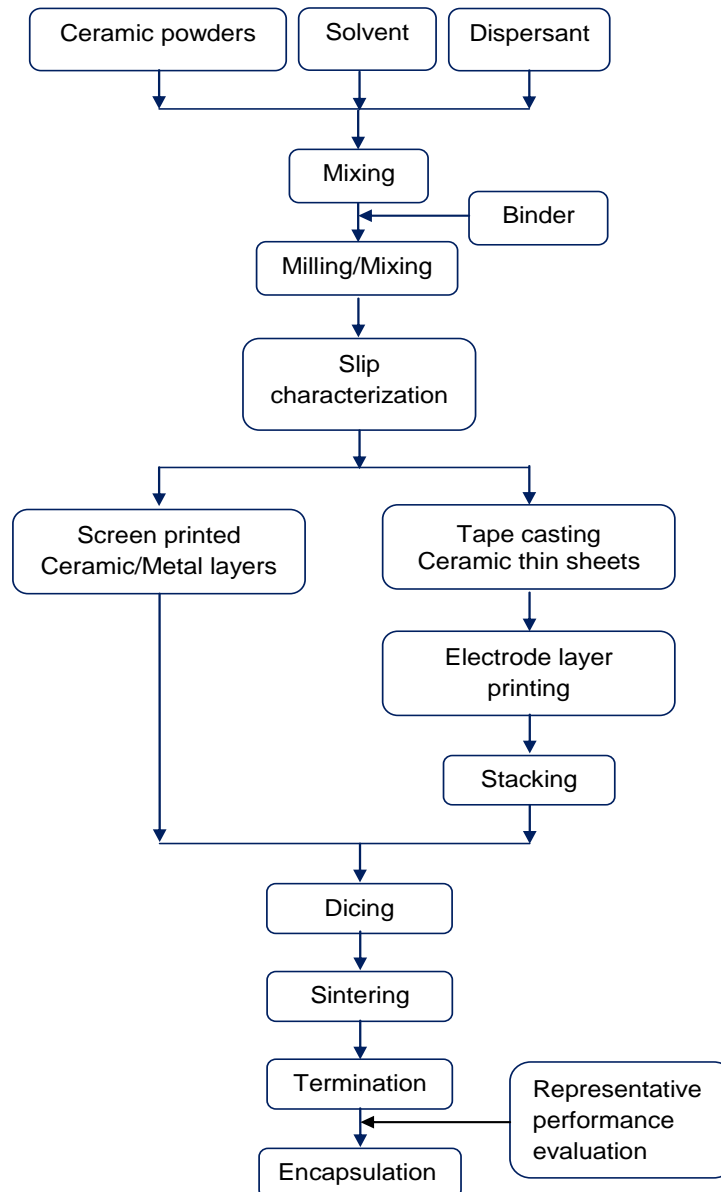


**Figure 2.18: Flow chart showing fabrication steps involved during multilayered device manufacturing**

Thus the main ingredients for preparing the inks/slurry suitable for green processing are ceramic powder, solvent, dispersant/ surfactant and binder.

### 2.6.1. Solvents:

The solvent is the primary liquid medium carrying the ceramic particles and distributing other ingredients uniformly/homogeneously. The solvents are selected based on the ceramic powder, dispersant and binder, as it should disperse all the

ingredients. Low viscous non-polar solvents with high dielectric permittivity are preferred as they lead to good dispersion of ceramic powder and can help to achieve high solids loading with low viscosity. Sometimes zeotropic and azeotropic mixture of solvents are used mainly to increase the ability to dissolve and improve the drying speed, rheological control and safety<sup>113</sup>.

### **2.6.2. Dispersants:**

Dispersants are used for good dispersion of particles, wetting of binders to improve particle packing and stability of the ink. The desired characteristics of the dispersants/deflocculants are:

- To separate the primary particle so that binders can coat them individually
- To increase the solid loading and maintain moderate viscosities after binder addition
- Decrease the amount of solvent in the suspension, for cost and safety
- Decrease the amount of solvent in the slurry/ ink in order to dry the slip fast with less shrinkage
- To burn out completely prior to sintering to avoid contaminating the final product

The most commonly used deflocculants are phosphate ester, menhaden fish oil, polyvinyl butyral, glycerol trioleate, glycerol tristearate, linoleic acid, oleic acid, citric acid, stearic acid, salts of polyacrylic and methacrylic acids, corn oil, safflower oil, linseed oil, synthetic waxing ester etc<sup>113</sup>.

### **2.6.3. Binders:**

Binders are the most important processing additives to the slurry/ink. Binders provide the network that holds the entire system together for further processing. As it is the only continuous phase, the binders have great effect on the green ceramic layer/ tape properties such as printability, strength, smoothness, laminating, durability, flexibility, plasticity etc. The factors to consider for selecting binders are

solubility, viscosity, strength, cost, Tg (glass transition temperature) or ability to modify the Tg, ash residue, burnout temperature and released byproducts<sup>113</sup>.

**Table 2.4: List of binders used for non-aqueous processing of BT ceramics<sup>113</sup>**

Non aqueous binders		
Vinyls	Acrylic	Cellulose
Polyvinyl alcohol, Polyvinyl butyral, Polyvinyl chloride, Vinyl chloride-acetate	Polyacrylate esters, Polymethyl methacrylate, Polyethyl methacrylate	Cellulose acetate- butyrate, Nitrocellulose, Ethyl cellulose, Hydroxyethyl cellulose, Hydroxypropyl methyl cellulose

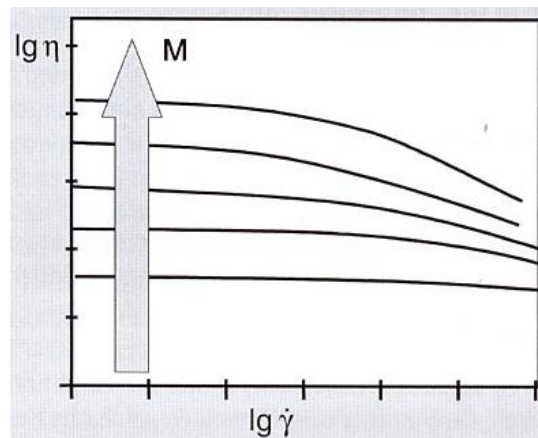


**Figure 2.19: Dependence of shear viscosity on average molar mass (M) of the polymeric binders**

(Reproduced from reference 114)

The two main families; polyvinyls and polyacrylates have been used through years as binders. Essentially binders should be film formers, hence should have long chain polymers, or should become long chain polymers during drying. The polymeric chain length is categorized by their molecular weight. Binders with low molecular weight have small polymeric chain and hence have low viscosity (Figure 2.19) enabling high solid loading. However, this result in ceramic layer with less strength so will require more amounts of binders and leads to high viscosity. Hence, binders with a blend of different molecular weights are widely used to achieve a balance of high solid loading and strength of the ceramic layer/ tape with moderate viscosity. The proportion of lower molecular weight binders increases with decreasing particle size<sup>114</sup>.

#### 2.6.4. Milling operations:

The rule of thumb for filling the mill with slip is about  $\frac{1}{2}$  to  $\frac{2}{3}$ <sup>rd</sup> of the total volume with grinding media in the mill. The grinding media should be completely immersed in the slip. The critical operating speed (in rpm) of the ball mill ( $N_c$ ) is  $76.6/\sqrt{D}$ , where  $D$  is the inner diameter of the mill in foot<sup>115</sup>. For practical purpose, the mill is operated in the range of 35 to 115% of the maximum speed. Operating the mill at high speed just rotates the material at the periphery of the cylinder and no milling take place. In addition, the mill should be used only for an optimum period of time, and over milling can generate heat inside and can cause agglomeration of the powder.

#### 2.6.5. Ink Rheology:

Rheology is the science of deformation and flow of matter. The rheology of ceramic slip/ink is critical for the multilayer processing as it reveals the characteristics and properties including the structure and stability of the ink. The most important parameters of interest are viscosity,  $\eta$ , shear stress,  $\tau$ , the viscoelastic property,  $G^*$  elastic or storage modulus,  $G'$ , viscous or loss modulus,  $G''$ .

The two plate model is used to understand the simple flow behaviour, Figure 2.17a. Consider two parallel plates with a fixed bottom plate and an upper plate, pulled with an applied force,  $F$ . Assuming the sample adheres both plates without any slide and has laminar flow, Figure 2.20b,

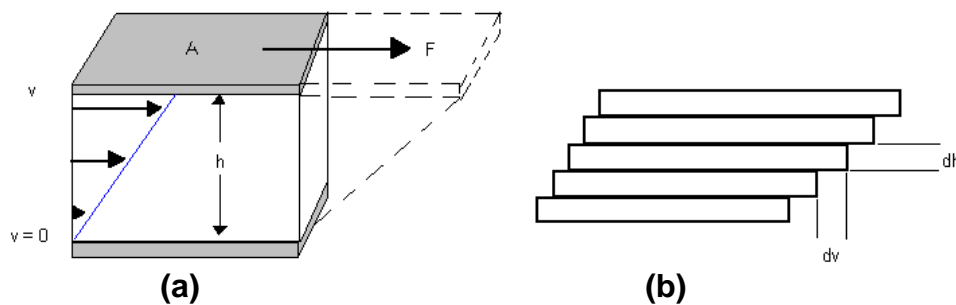


**Figure 2.20: Two plate model**  
(Reproduced from reference 116)

shear stress,  $\tau$ , is given by force ( $F$ , in Newtons) per unit area ( $A$ , in  $m^2$ ):

$$\tau = \frac{F}{A} \quad \text{Equation 2.13}$$

shear rate,  $\gamma$ , can be found by,

$$\gamma = \frac{v}{h} \quad \text{Equation 2.14}$$

where  $v$  is the velocity in  $ms^{-1}$  and  $h$ , the height in m.

Viscosity, the measurement of resistance to flow, is given by

$$\eta = \frac{\tau}{\dot{\gamma}} \quad \text{Equation 2.15}$$

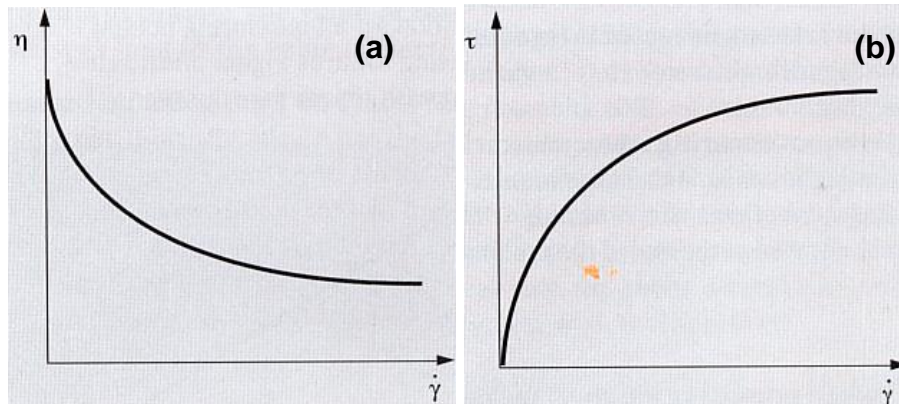


Figure 2.21: Typical (a) viscosity curve and (b) flow curve of shear thinning behaviour (Reproduced from reference 114)

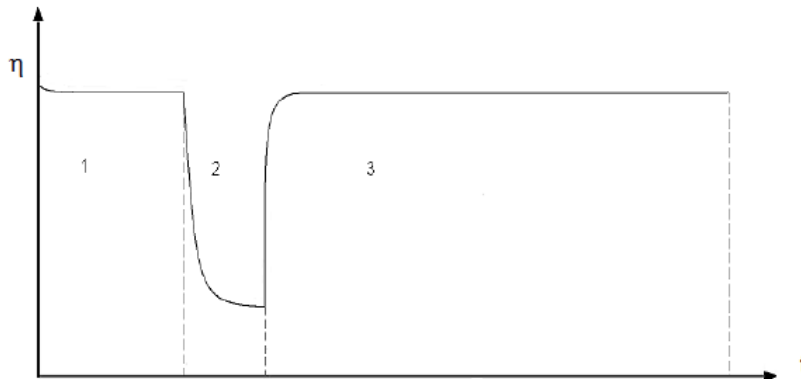
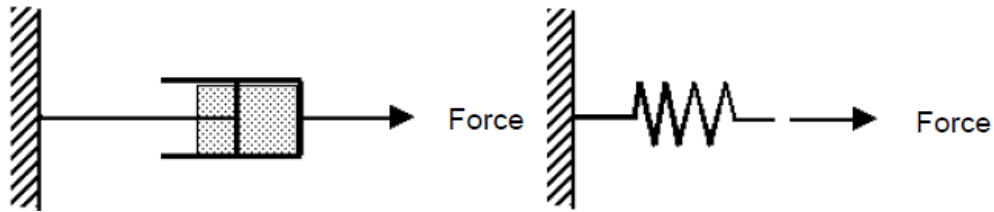


Figure 2.22: Typical thixotropic behaviour in a 3 interval rotational test

Ceramic slip/ inks should have viscoelastic and shear thinning behaviour. The viscosity of the shear thinning ink decrease with increasing the load or shear rate (Figure 2.21).

Thixotropic behaviour is defined as reduction in structural strength during a shear load phase and a nearly complete structural regeneration during the period of rest. It is a reversible cycle of deformation and regeneration. The typical behaviour is shown in Figure 2.22 and comprised of three stages.

1. Reference interval: refers to material at rest
2. High shear interval: infers material under high shear conditions like printing, during which structural deformation of the material occurs, viscosity decreases and ink spreads uniformly
3. Regeneration interval: represents material under low shear conditions, facilitating regeneration of the structure to get ready for the next layer of similar print quality.



**Figure 2.23: (a) Dash pot model; (b) Spring model**

The ideal viscous behaviour is given by the dashpot model (Figure 2.23a), under the constant shear force, the piston moves as long as the force is acting on it, forcing through a narrow annular gap between the piston and the cylinder wall. The force applied is directly proportional to the speed of piston. Once the force is removed, the piston stops at its position, resulting in permanent deformation.

Whereas in the ideal elastic behaviour, given by spring model (Figure 2.23b), under the constant shear force, the spring shows the deformation at a constant value corresponding to the force. Once the force is removed, the spring recoils elastically immediately, completely and there is no permanent deformation.

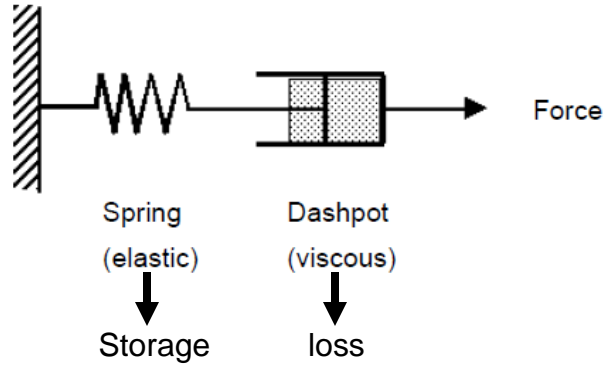


**Figure 2.24: Maxwell model**

The viscoelastic behaviour is given by the combination of both spring and dash pot model in series (Figure 2.24). Viscoelastic materials show both elastic and viscous behaviour within their structure. The viscous part obeys Newton's law and elastic part follow Hooke's law. The ink consists of ceramic materials acting as a solid/elastic part and the solvent with dissolved polymers (binders) providing liquid/viscous part and hence shows the viscoelastic behaviour. For a viscoelastic ink, the degree of deformation remains permanent due to the viscous part of the liquid.

The elastic and viscous parts of the ink are represented by storage and loss moduli respectively. The storage modulus,  $G'$  represents the deformation energy stored by the sample during the shear, after the load removal, this energy acts as a driving force to reform partially or completely providing the elastic behaviour. The loss modulus,  $G''$  represents the deformation energy used by the sample. This energy is utilised to change the materials' structure and lost to the environment as heat, which is irreversible.

The loss factor is given by the ratio of viscous to elastic region, where  $\delta = \pi/4$ .

$$\tan\delta = \frac{G''}{G'} \quad \text{Equation 2.16}$$

### 2.6.6. Tape casting:

Tape casting process, also known as doctor blading or knife coating, is widely used in plastic, paper, paint manufacturing other than electro ceramics industry. The basic principle of tape casting process is illustrated in Figure 2.25, consisting of a slip reservoir, a doctor blade, a carrier and drying zone. The blade is stationary and the carrier moves or vice versa. The blade and carrier gap determines the thickness of the layer and can be controlled. The “doctor” is a scraping blade for the removal of excess substance from a moving surface/ slip reservoir being coated. The “doctor” is a scraping blade for the removal of excess substance from a moving surface/ slip reservoir being coated.

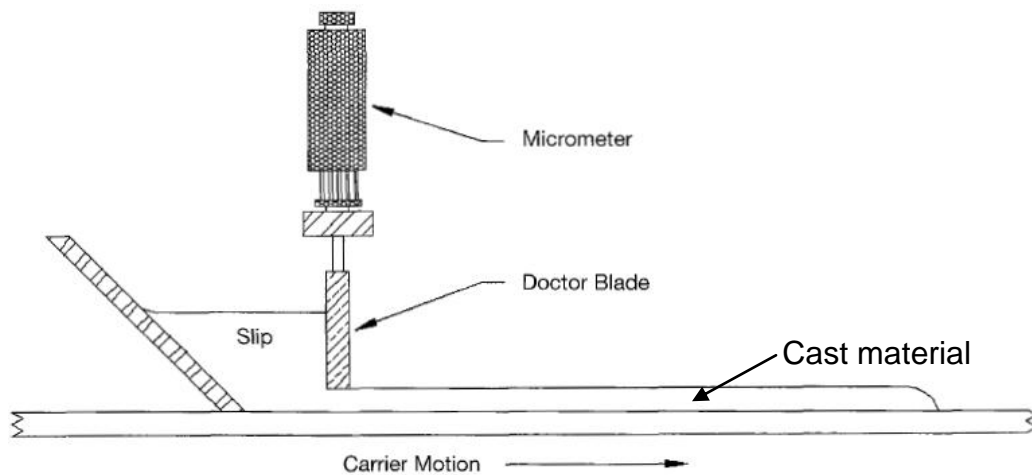


**Figure 2.25: Schematic diagram showing the tape casting procedure**  
(Reproduced from reference 113)

The chief advantage of tape casting process is that it is one of the best ways to form large-area, thin, flat ceramic or metal parts, which are virtually impossible to press or extrude. The green ceramic layer can be punched, stacked, or even cut into various shapes and sizes; hence, multilayer can be easily manufactured using this process.

### 2.6.7. Screen-printing:

Screen printing technique has the advantage of forming thin layers of ceramic and metal inks on a single machine or together. Compared to tape casting, it is a simple process, capital cost is less, requires less space and labour.



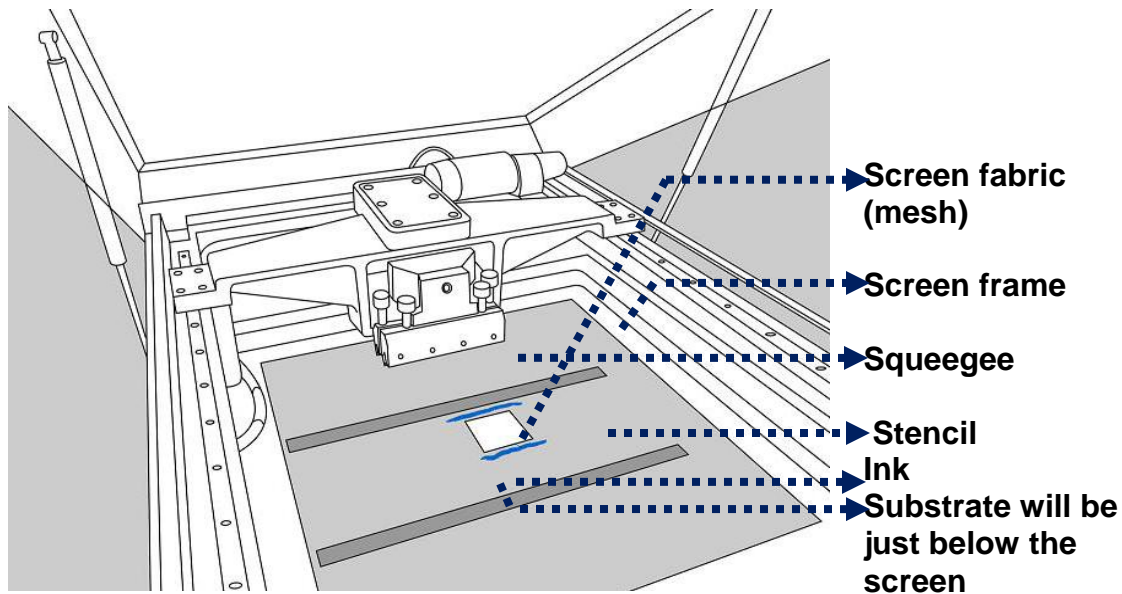


**Figure 2.26: Schematic picture showing the ink deposition during screen printing technique**

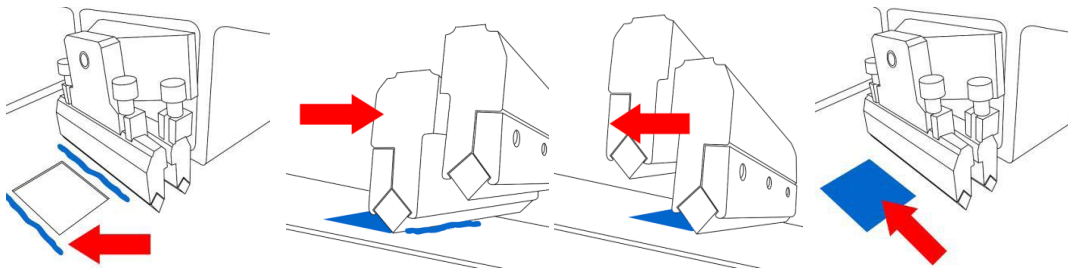


**Figure 2.27: Schematic representation of various steps involved in screen printing process (Reproduced from reference 117 )**

This equipment consists of six basic components as shown in Figure 2.26, a stencil, a screen fabric (mesh), screen frame, squeegee, ink, and substrate<sup>118</sup>. The ceramic ink (viscous paste) of suitable rheology is first spread across the mesh using one squeegee, which is referred as 'flow/ spread'; following this the ink is forced through the open meshes of the screen using another squeegee which is now referred as 'print' (Figure 2.27). The main parameters like squeegee speed, squeegee pressure, print gap between the screen and the substrate, the screen fabric, mesh size etc. have to be optimized to yield a thin, defect free, dense ceramic film<sup>119</sup>. A similar process can be used for printing metal inks also.

The screen/mesh is held in tension on a frame, allowing the particles of given size to flow through the mesh. Controlling thickness of the film, volume and drying also needs consideration. The screen fabric supporting the stencil is also important as it can affect the durability, edge definition of the prints and can affect the off contact distance, print gap and the printing speed. Among the screen fabrics used such as silk, polyester, or metal, stainless steel screens are advantageous as they can maintain high tension over longer periods. They also have good chemical resistance hence can be used with non-aqueous solvents<sup>120</sup>. The fabric fibres are placed at a set distance, allowing the openings in the mesh similar to that of woven textiles<sup>121</sup>. Snap-off is the distance from the top of the substrate to the screen mesh. Zero snap-off is referred as on-contact printing and with any snap-off its' referred as off-contact printing.

The three basic function of the squeegee are<sup>122</sup>,

- Control the amount of ink deposited on the substrate
- Bring the screen in contact with the substrate
- Wipes the screen of the ink.

The five squeegee parameters that can affect the downward force of the squeegee which in turn affect the amount of ink deposited are blade hardness, blade angle, squeegee speed, squeegee angle and blade profile. A hard squeegee with less vertical blade angle and a fast speed reduces the amount of ink deposited. Increasing the squeegee pressure increases the ink deposit; low pressure is normally preferred as excessive pressure can damage the mesh and print quality. As aforementioned, the ink viscosity and its rheological behaviour are critical to achieve good quality ceramic layers through screen printing process.

## **2.7. Sintering of BT ceramics:**

Sintering is a method for making components from powder by heating the material (below its melting point) until the particles adhere to each other. Sintering is traditionally used for manufacturing ceramic and powder metallurgy objects.

Technically densification of a particulate compact is referred as sintering. The adjacent particles bond strongly and the particle or grain size grows, removing the pores<sup>123,124,125</sup>. The minimum criteria for sintering are, there must be

- a mechanism for material transport and
- an energy source to activate and sustain the material transport.

The primary mechanism of material transport is diffusion and viscous flow. Heat is the primary source of energy along with particle contact, gradients and surface tension playing their part. Sintering occurs in different stages based on the sequence of physical changes to the particle bonding and disappearance of porosity<sup>124</sup>.

**Table 2.5: Stages of sintering**

<b>1<sup>st</sup> stage: (initial)</b>	Rearrangement of particles Initial neck formation	Bonding occurs at the point of contact where surface energy is highest and material transport can occur.
<b>2<sup>nd</sup> stage: (intermediate)</b>	Size of the neck grow Grain growth High shrinkage Pore phase continuous	Grain boundaries move
<b>3<sup>rd</sup> stage: (Final)</b>	More grain growth Grain boundary pores eliminated	Porosity is removed by vacancy diffusion. Pore removal and vacancy diffusion are aided by movement of grain boundaries and controlled grain growth.

The nano powder sintering onset temperature (0.2-0.4  $T_m$ ) is generally lower than conventional submicron powder compacts (0.5-0.8  $T_m$ ). Three processes compete during sintering viz., particle coarsening, densification, and grain growth, each with slightly different activation energy (E). However, it is essential to identify whether the 'nanosintering mechanism' is different from the submicron powders<sup>126</sup>. Coarsening is by surface diffusion processes, densification is by grain boundary diffusion, and the grain growth is by lattice diffusion as the impurity or limits the pore movement.

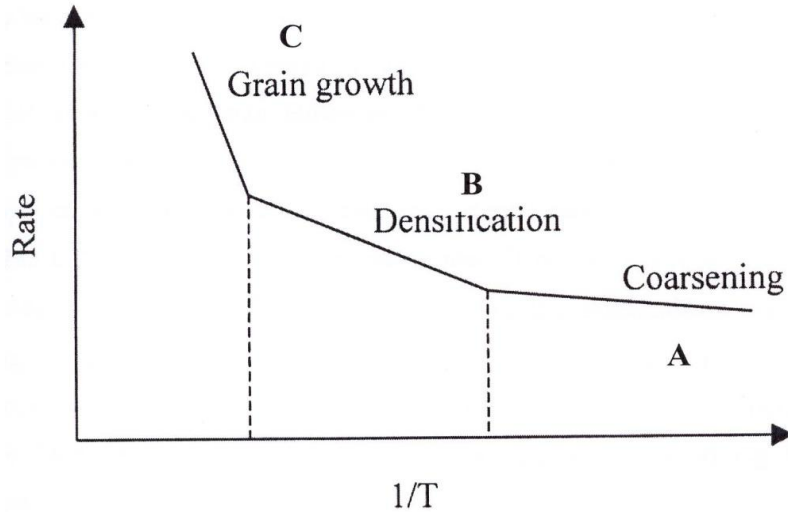


**Figure 2.28: Rate versus Temperature.**  
(Reproduced from reference 127)

The slope of the straight line in the plot of inverse temperature versus rate of a kinetic process is proportional to the activation energy<sup>127</sup>. The schematic representation is shown in Figure 2.28.

$$E_c < E_d < E_g \quad \text{Equation 2.17}$$

Where, the subscripts refer to coarsening, densification and grain growth.

The plot is divided into three regions A, B and C. Coarsening occurs in regime A that is at low temperatures. This can be avoided by rapid heating through this temperature regime. Grain growth occurs in region C at higher temperature and can be avoided by limited period of exposure at this temperature regime. Although densification occurs at intermediate regime B but is not desirable as the pores limit grain growth until small residual pores are achieved. Normally, the pores act as driving force for sintering and it is similar to the capillary force; smaller the pore size higher is the driving force. Hence, maximum densification can be achieved with finer pore size. Usually a narrow window within C regime can be used to achieve maximum densification and fine nanostructures<sup>123</sup>.

In nanopowders, number of atoms in the surface is almost equal to the atoms bound inside the particles; hence, the surface diffusion is rapid in the initial stage of sintering. The grain coarsening occurs due to surface diffusion, resulting in neck formation. There are contradictory ideas on the neck formation and densification in nanopowders. It has been reported that minimum grain boundary energy is achieved by the adjacent nano particle rotations and densification occurs through grain boundary slip, dislocation, grain rotation, viscous flow, and even grain boundary melting<sup>126</sup>.

Another problem in nanopowders sintering is the elimination of large pores from the green sample. Mayo developed a modified sintering law for nanosintering with the pore size effect on densification<sup>128</sup>

$$\frac{1}{\rho(1-\rho)} \times \frac{d\rho}{dt} \propto \frac{1}{d^n} \times \frac{1}{r} \times \exp\left(\frac{-Q}{RT}\right) \quad \text{Equation 2.18}$$

Where,  $\rho$  - Density,  $d$  - Particle size,  $n$  - a constant dependent on the sintering mechanism,  $r$  - Pore radius,  $Q$  - Activation energy,  $R$  - Gas constant and  $T$  - Temperature.

Accordingly, maximum densification occurs for the finest pore size. Also based on the pore pinning effect, smaller pore size is critical to achieve final nanograin size. Hence, the small and uniform pore size distribution in green sample is desirable. Often, pore distribution and final density after sintering have been dictated by the pore size and distribution in the green sample and starting density. The weakly agglomerated powders or powders with crushable agglomerates can result in high green density with small and uniform pore size distribution and hence can lead to high sintered density; however controlling grain growth is very critical.

Figure 2.29 shows the Arrhenius plot of the rates of densification and grain growth. Thus, the theory of rapid sintering predicts that a finer and uniform grain structure will result by rapid heating to the high temperature region<sup>125</sup>.

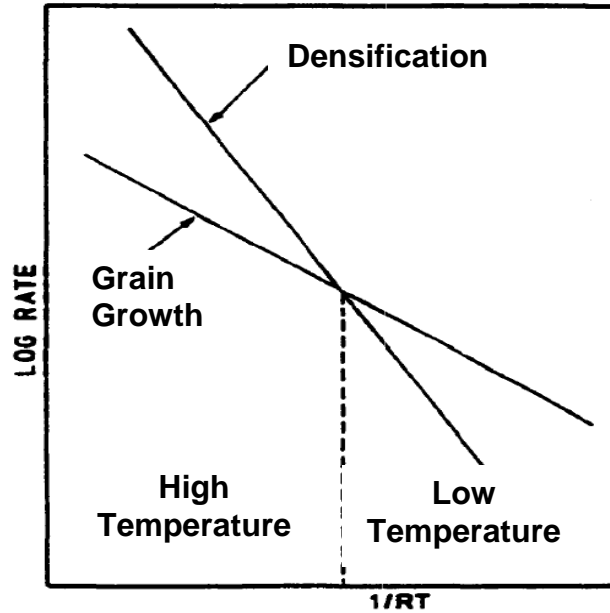


**Figure 2.29: Arrhenius plot of rates of densification and grain growth**  
(Reproduced from reference 125)

### 2.7.1. Types of sintering:

There are variety of mechanisms through which sintering can occur. They are described below;

#### (i) Solid state sintering

Solid state sintering takes place when the ceramic green body is completely sintered in a solid state at a sintering temperature. Solid-state sintering takes place through diffusion; that is movement of atoms or vacancies along the surface / grain boundaries or through the lattice dislocations / volume of the materials. The driving force for solid state sintering is the difference in free energy or chemical potential between the free particle surface and the points of contacts between adjacent particles.

Sintering studies on solid state sintering of BT ceramics still has some controversy. The main problems associated with understanding BT solid state sintering are<sup>129</sup>

- The activation energy/ enthalpy of diffusing ions are scattered and not conclusive because of various sintering techniques, powders used by different researchers and multiple mechanisms that occur concurrently during sintering.
- Dopants addition to achieve the desirable electrical performance, reacts with BT and many times lead to liquid phase sintering
- Low liquid eutectic temperature of  $\text{BaTiO}_3\text{-Ba}_6\text{Ti}_{17}\text{O}_{40}$  at  $\sim 1312^\circ\text{C}$  in the  $\text{BaO-TiO}_2$  system above which liquid phase sintering takes place.
- Even slight excess  $\text{TiO}_2$  forms  $\text{Ba}_6\text{Ti}_{17}\text{O}_{40}$  by solid state sintering itself.
- The trace impurities in the BT powder can lower the liquid phase formation temperature to  $1250^\circ\text{C}$ .
- Fast firing to high sintering temperature is also not possible, as BT can undergo cubic  $\rightarrow$  hexagonal phase transformation at  $1430^\circ\text{C}$ .
- The possible temperature range for solid state sintering is  $<1250^\circ\text{C}$ , however this often leads to formation of plate like grains with facet along  $\{111\}$ .

Hence, it is difficult to achieve pure solid state sintering in the BT ceramics.

### **(ii) Liquid phase/Reactive liquid sintering**

When a liquid phase is present or formed during the sintering process, it's referred as liquid phase sintering. If large enough liquid is formed, the viscous flow of the liquid binds the particle to a density where there is no grain growth, and this is referred as viscous flow sintering. In some systems during the early stages of sintering a reactive liquid is formed which acts as a catalyst for densification and evaporates at the final stages leaving the sintered body, often referred as reactive/transient liquid sintering.

As mentioned the previous section 2.7.1 (i), BT ceramics are prone to undergo liquid phase sintering due to the formation of low temperature eutectic in the undoped ceramics, excess  $\text{TiO}_2$ , traces of impurities etc.

As aforementioned, MLCCs are fabricated using wet processing route. Phosphate ester is the most frequently used dispersant in these cases. During the sample

binder burnout, the phosphate ester leaves the residue of Phosphorus on the BT particle surface. The residual phosphorus can react with BT to form liquid phase. In addition, it is very common to use dopants to improve insulation resistance and attain the desirable temperature characteristics, which also enhance the liquid phase sintering. The effects of liquid phase formation on the BT grain growth are very important for the performance of the MLCC.

### **2.7.2. Grain growth in BT ceramics**

During sintering, with increasing temperature, individual particles in the green bodies get heated and react to form a grain to reduce their free energy. The atoms at the grain boundaries have more broken chemical bonds and hence high energy compared to the bulk of the grains, which is the driving force for grain growth.

Grain growth can take place in two ways: (i) Normal grain growth and (ii) exaggerated grain growth.

#### **(i) Normal grain growth**

Normal grain growth occurs with rough grain boundaries while the faceted boundaries lead to abnormal grain growth due to the non-linear mobility of the facet under the driving force. Choi and Kang studied the effect of grain boundary structure on grain growth and densification of BT ceramics, and concluded that the facet boundaries do require a critical driving force to overcome the vacancies energy barrier and provide a perfect source/ sink for atoms<sup>130</sup>.

#### **(ii) Abnormal grain growth (AGG)**

The Gladman (1966) model<sup>131</sup> of abnormal grain growth is one in which one grain grows at the expense of the other neighbouring grains (referred as abnormal grain growth). AGG can happen when the normal grain growth is inhibited.

The AGG can occur with even slight excess of TiO<sub>2</sub> in BT and can happen in two ways. BT forms a eutectic liquid with Ba<sub>6</sub>Ti<sub>17</sub>O<sub>40</sub> at 1312°C, where even a small % excess TiO<sub>2</sub> reacts with BaTiO<sub>3</sub> to form a eutectic melt along with BT. The eutectic



liquid phase promotes densification but gives rise to discontinuous grain growth of the BT. The abnormal grains are found to be faceted but equiaxed (Figure 2.30). Even below the eutectic temperature, abnormal grain growth has been observed via solid state diffusion, resulting in growth of double twined crystallites and elongated twin lamellae. The grains with faceted solid/ liquid interface can grow by two dimensional nucleation.

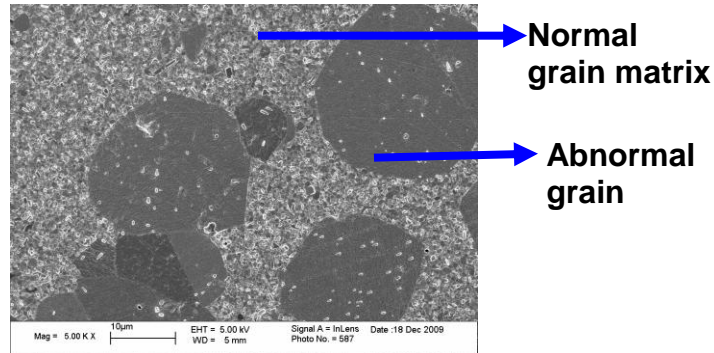


**Figure 2.30: Abnormal grain growth in BT ceramics sintered at 1300°C**

Lee et al., have demonstrated that the grain boundary faceting is necessary for abnormal grain growth and the presence of  $\{111\}$  twins is not a necessary condition but will be beneficial for abnormal grain growth<sup>132</sup>. Kingery et al. have reported that abnormal growth rate to be independent of time, as long as the grain size of the matrix remains unchanged<sup>123</sup>. The number of nuclei,  $N$  increases exponentially with time,  $t$ :

$$\frac{dN}{dt} = a \exp(bt) \quad \text{Equation 2.19}$$

$N$  is the number of discontinuously growing grains (nuclei) per  $\text{cm}^3$ ,  $a$  and  $b$  are the empirical constants. Most of the nuclei in the BT exhibit straight boundaries like faceted crystal planes. The Radius of nuclei ( $R_g$ ) increases proportionally with time.

$$R_g = G(t - c) \quad \text{Equation 2.20}$$

$G$  is the growth rate of the grain, and  $c$  is the incubation time.

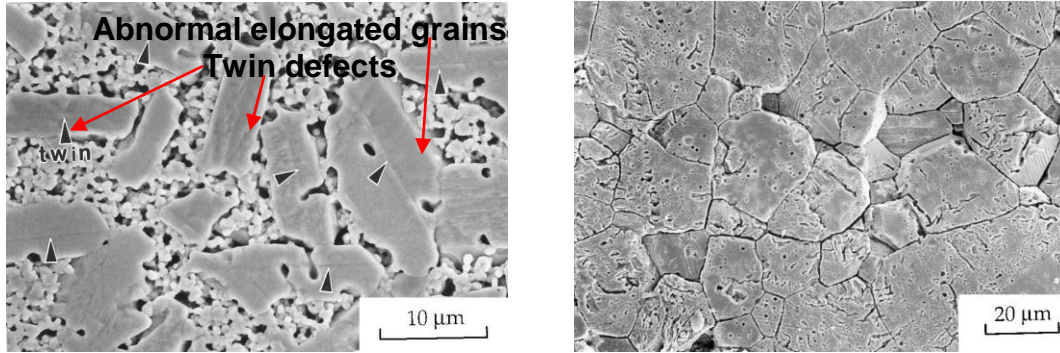


**Figure 2.31: Microstructure of BT sintered with (a)  $\text{TiO}_2$  excess-showing abnormal elongated grains and twin defects at  $1215^\circ\text{C}$ <sup>133</sup>, (b) BaO excess-showing intergranular cracks at  $1250^\circ\text{C}$  (Reproduced from reference 133)**

The number of abnormal grains per unit of volume ( $N_{AV}$ ) is calculated by the expression<sup>134</sup>,

$$N_{AV} = (\rho N^2 A) / (2NL) \quad \text{Equation 2.21}$$

Where,  $\rho$  is the density of the material,  $N$  is the number of normal grains,  $A$  is the area of the sample and  $L$  is the thickness or length of the sample.

Rios et al., have worked on the effect of temperature, time and excess  $\text{TiO}_2$  on the sintering kinetics of BT and have demonstrated that the number of abnormal grains per unit volume is independent of temperature but depends on excess  $\text{TiO}_2$ <sup>135</sup>. Though, the number of abnormal grains per unit volume doesn't change with temperature they grow in size with temperature.

The solubility of  $\text{TiO}_2$  in  $\text{BaTiO}_3$  is very less, hence the excess  $\text{TiO}_2$  form fine precipitate dispersion within the matrix suppress the normal grain growth, acting as the pinning force at the grain boundaries.

The pinning force,  $Z$  is given by 135,

$$Z \propto \frac{\text{mol\% excess TiO}_2}{S_v} \quad \text{Equation 2.22}$$

where  $S_v$ , is the grain boundary area per unit volume.

The excess BaO forms Ba<sub>2</sub>TiO<sub>4</sub> which is a highly hygroscopic phase. This precipitates at the grain boundaries of the BT grain. Ba<sub>2</sub>TiO<sub>4</sub> absorbs moisture and reacts to form Ba(OH)<sub>2</sub>, leaching out Ba<sup>2+</sup>, deteriorating the electrical properties of BT ceramics. This also results in more intergranular cracking and the ceramic sample becomes very fragile<sup>133</sup>.

The phosphorus residue of the phosphate ester dispersant remains segregated at the grain boundaries and this inhibits the grain growth up to 1300°C. Sintering above 1300°C, leads to the formation of barium phosphate, Ba<sub>3</sub>(PO<sub>4</sub>)<sub>2</sub>, as secondary phase with abnormal grain growth<sup>136</sup>. It is expected that P<sup>5+</sup> incorporate into the BaTiO<sub>3</sub> lattice and for charge compensation Ti<sup>4+</sup> converts to Ti<sup>3+</sup>. This increases the dielectric loss due to grain boundary conductivity. In order to achieve better performance of nano MLCCs and to develop a clear understanding on the limitations and challenges involved, a methodical approach is required for nano BT (n-S-BT) sintering.

## 2.8. Approaches for nano BT sintering

Since 1990's, there have been lots of advancements in the theory and practice of sintering of nanocrystalline powders. The grain growth/ microstructure of BT ceramics during sintering can be controlled by 3 distinct approaches.

1. Use of the dopants/additives to inhibit the grain growth: Utilize segregation of dopants to grain boundaries and suppression of grain boundary mobility
2. Use of controlled/ reduced atmosphere: Due to reduced atmosphere, Ti<sup>3+</sup> ions increase, which suppress the grain boundary mobility and change the grain structure from faceted to rough. There is some evidence that reducing atmospheres can affect grain growth in barium titanate<sup>137,138</sup>.
3. Novel sintering techniques: To minimize the grain growth and achieve maximum densification like use of high pressure, spark plasma sintering, non-isothermal rapid rate sintering<sup>139</sup>, rate controlled sintering<sup>16</sup>, two step sintering<sup>140</sup>, laser and microwave assisted sintering.

### 2.8.1. Sintering aid/ Flux additions during BT sintering

There are many patented works on flux sintering of BT to lower the sintering temperatures for cost savings. The important area of interest/research is the correlation between the flux composition, microstructure and dielectric properties of the flux sintered BT. The flux material must satisfy a set of requirements; it should lower sintering temperature without deteriorating the desirable dielectric properties like high dielectric permittivity, low dissipation factor, temperature characteristics of the capacitance change (TCC) etc.

Objectives of the flux are,

- to achieve a high sintered density;
- should be free from low-k impurity;
- should not give rise to any secondary phases;
- dilution of dielectric permittivity should be maintained to a minimum;
- minimum interaction with the parent material.

Various types of fluxes for BT have been discovered and investigated including glass frits, low melting oxides, fluorides, borates, silicates etc.

#### (i) Flux additions:

Lithium fluoride (LiF): Walker et al. have first reported that addition of 0.5-3 wt% LiF enhances BT densification and lowers the sintering temperature<sup>141</sup>. Subsequently, researchers have attempted to sinter BT at 900°C for long period and showed improved dielectric properties<sup>142,143</sup>. However, it has been found that during long duration heating, Li and F has been lost, increasing dielectric loss<sup>144</sup>. Hence, BaLiF<sub>3</sub> has been used as a sintering aid<sup>145</sup>. This has showed liquid phase formation at 740°C, leaving Li<sub>2</sub>TiO<sub>3</sub> at the grain boundaries<sup>146</sup>.

Bismuth oxides: This results in liquid phase sintering at 1120°C and has good temperature characteristics, low dielectric loss but the addition dilutes the dielectric permittivity and lowers the insulation resistance<sup>147</sup>. It has been found that the Bi ion

diffuses into the BaTiO<sub>3</sub> lattice and forms a complex perovskite phase resulting in grain-core/grain-shell structure<sup>148</sup>. However, on long duration heating, complete dissolution of Bi into solid solution has been noticed. This has been avoided by using Bi<sub>2</sub>O<sub>3</sub>-B<sub>2</sub>O<sub>3</sub> flux as a sintering aid<sup>149</sup>.

Boron oxide: B<sub>2</sub>O<sub>3</sub> has been first used as a flux material for BT in 1969<sup>150</sup>. Since then, lot of research work has been carried out using B<sub>2</sub>O<sub>3</sub> due to its low melting point. B<sub>2</sub>O<sub>3</sub> with CdO densifies BT at 1100°C with grain growth<sup>151</sup>. Increasing Cd/B ratio results in excess Cd precipitation along the grain boundary and this suppresses the grain growth. It has been observed that addition of Bi<sub>2</sub>O<sub>3</sub> with B<sub>2</sub>O<sub>3</sub> and CdO, densifies BT with a lower amount of flux. Lots of other flux compositions have also been attempted like ZnO-B<sub>2</sub>O<sub>3</sub>, PbB<sub>2</sub>O<sub>4</sub><sup>152</sup>, CdO.B<sub>2</sub>O<sub>3</sub>, 2CaO.Al<sub>2</sub>O<sub>3</sub>.2B<sub>2</sub>O<sub>3</sub><sup>153</sup> etc.

Copper oxide (CuO): CuO based fluxes results in grain growth and flattens the curie peak<sup>154</sup>. The CuO-BaO mixture has been found to improve densification, yielding high dielectric permittivity, low loss tangent and flattens the dielectric curve<sup>155</sup>.

**(ii) Glass compositions:**

Glass compositions contain a combination of glass forming oxides (Table 2.6). B<sub>2</sub>O<sub>3</sub> is a good glass former because of its low temperature melting compounds. Glass former cations are normally insoluble in perovskite titanate due to the incompatible cation size and charge. Type I modifiers are very insoluble and Type II are partially soluble (≤5 mol%).

**Table 2.6 : List of glass compositions**

Glass former	Modifier (type)		
	I	II(A)	II(B)
B <sub>2</sub> O <sub>3</sub>	PbO	CdO	Bi <sub>2</sub> O <sub>3</sub>
SiO <sub>2</sub>	BaO	ZnO	Y <sub>2</sub> O <sub>3</sub>
GeO <sub>2</sub>	SrO	Li <sub>2</sub> O	Sb <sub>2</sub> O <sub>3</sub>
	CaO	CuO	WO <sub>3</sub>
			Nb <sub>2</sub> O <sub>5</sub>

Number of glass compositions have been developed and used as a sintering aid to enhance the BT densification through liquid phase sintering. There are number of patents<sup>156, 157, 158, 159</sup> based on the combination  $\text{Al}_2\text{O}_3$ ,  $\text{SiO}_2$ ,  $\text{TiO}_2$ ,  $\text{B}_2\text{O}_3$  etc. and these borosilicate glasses lower the sintering temperature to  $1100^\circ\text{C}$  but dilutes the dielectric permittivity. Lead germinates compositions ( $\text{PbO} \cdot \text{GeO}_2 \cdot \text{SiO}_2$ ) are found to reduce the sintering temperature to even  $750^\circ\text{C}$ <sup>160</sup>.

$\text{BaTiO}_3$  sintered with glass additives may not yield desired dielectric properties due to presence of low dielectric permittivity grain boundary phase. The glass composition has to be tailored to achieve densification with minimal grain growth, secondary phase and porosity. Another key factor is to control the diffusion into the parent BT lattice, if not glass will act as a flux and/or modifier<sup>161</sup>. For hydrothermal synthesized BT,  $\text{PbO} \cdot \text{B}_2\text{O}_3$  gives extensive grain growth with  $0.7 \mu\text{m}$ ,  $\text{PbO} \cdot \text{SiO}_2$  gives  $0.5 \mu\text{m}$  grain size and  $\text{Bi}_2\text{O}_3 \cdot \text{B}_2\text{O}_3$  yields good densification and minimal grain growth<sup>162</sup>. Use of calcium borosilicate glass with LiF is found to accelerate the densification at a lower sintering temperature and also yields high dielectric permittivity  $>1700$ <sup>163</sup>.

### **2.8.2. Reduced atmosphere**

It has been proven in many systems as well as BT that reducing the partial pressure of the sintering atmosphere can control the grain size. Because of low partial pressure in the pores compared to the grains, it enhances the densification and pins grain boundary mobility. But the difficulty in using this route for oxides is, it can create oxygen deficient structure. Especially for electro ceramics like BT, due to reduced atmosphere,  $\text{Ti}^{4+}$  reduces to  $\text{Ti}^{3+}$  ions, which suppress the grain boundary mobility and changes the grain structure from faceted to rough but has higher conductivity, creating a semiconducting BT. Hence it has to be reheated and annealed in oxygen atmosphere again during which grain growth takes place again. In addition, controlled atmosphere kilns are very expensive and involve additional steps; it is difficult for the industries to adapt this technique.

### 2.8.3. Novel sintering techniques

#### (i) Rapid rate sintering

During pressure assisted sintering, along with the thermal energy, external pressure is applied to achieve uniform and maximum density for the hard ceramic materials. This method is commonly used for production of high cost ceramics and prototype ceramics, for which high density must be guaranteed. For ceramics, commonly used pressure sintering methods are hot pressing and hot isostatic pressing.

In rapid sintering, the heating schedule is optimized to enhance the densification rate than the coarsening rate. Thus, the surface diffusion regime can be avoided and the sample is moved to temperatures needed for densification. The rapid heating suppresses the early grain growth and enhances the densification kinetics. The rapid heating technique will be useful to systems where activation energy for densification is much higher than that of coarsening.

Mostaghaci and Brook have sintered submicron BaTiO<sub>3</sub> at 1450°C for 5 min with minimal grain growth<sup>164</sup>. Polotai et al have used rapid rate two stage sintering with atmospheric control and achieved fully dense nanocrystalline ceramics of ~ 110 nm grain size, with the 3.5 X grain growth factor<sup>165</sup>. Also dense BT ceramics (~98% relative density) with <100 nm grain size have been obtained in recent years by using ultra high pressure sintering in a multianvil press<sup>166</sup>.

#### (ii) Spark plasma sintering

Spark Plasma Sintering (SPS) is a novel sintering technique, which is also known as Field Assisted Sintering Technique (FAST) or Pulsed Electric Current Sintering (PECS). The main characteristic of the SPS is that the pulsed DC current directly passes through the graphite die, as well as the powder compact, in case of conductive samples. Therefore, the heat is generated internally, in contrast to the conventional hot pressing, where the heat is provided by external heating elements. This facilitates a very high heating or cooling rates (up to 600 K/min), hence the sintering process is generally very fast (within a few minutes). The speed of the

process ensures that it has the potential for densifying powders with nanosize or nanostructures whilst avoiding coarsening which accompanies standard densification rates. Whether plasma is generated inside has not yet been confirmed;. Especially when using non-conductive ceramic powder compacts. However, it has been experimentally verified that densification has been enhanced by the use of a pulsed DC current or field.

Dense BT ceramics with <50 nm grain size and ~97% relative density are produced by spark plasma sintering<sup>167</sup> but their dielectric permittivity are less compared to the coarse grains. However adapting these techniques for large-scale production of MLCCs is very difficult.

### **(iii) Laser sintering**

Selective laser sintering (SLS) is an additive/rapid manufacturing technique that uses a high power laser (for example, a carbon dioxide laser) to fuse small particles of plastic, metal, or ceramic powders into a mass representing a desired 3-dimensional object. SLS can be used to process almost any material, provided it is available as powder and that the powder particles tend to fuse or sinter when laser heating is applied. This is the case for most materials. Powders that depict low fusion or sintering properties can be laser sintered.

Compared to other rapid manufacturing methods, SLS can produce parts from a relatively wide range of commercially available powder materials, including polymers (nylon, also glass-filled or with other fillers, and polystyrene), metals (steel, titanium, alloy mixtures, and composites) and green sand. The physical process can be full melting, partial melting, or liquid-phase sintering. Moreover, depending on the material, up to 100% density can be achieved with material properties comparable to those from conventional manufacturing methods. In many cases, large numbers of parts can be packed within the powder bed, allowing very high productivity. Still Laser sintering requires lots of further probing and not many success stories are available on ceramics.



#### **(iv) Microwave sintering**

In microwave heating, as microwave couples with the dipoles of the material directly, it has been found to lower the processing time and temperature required. The properties of the nanocrystalline powders are mainly controlled by the grain boundaries. As the grain boundaries are the primary sites of the electric dipoles, microwave sintering in particular is attractive for the densification of nanocrystalline powders. In addition, the grain growth at lower temperatures can be avoided by the rapid heating associated with the microwave sintering.

### **2.9. Microwave assisted heating**

#### **2.9.1. Microwave vs. Conventional heating**

Conventional heating is commonly achieved with electrical furnaces that allow temperatures as high as 2500°C to be reached. The main process variables are the firing schedule used (temperature as a function of time) and the atmosphere<sup>123,124,125</sup>.

The most commonly used type of furnace is the electrical resistance furnace, in which, the current carrying resistor called as furnace heating element, provides the heat. The maximum temperature of the furnace and the atmosphere is limited by the heating elements<sup>123,124,125</sup> used.

In conventional heating, the heating occurs due to the thermal radiation and depends on the thermal conductivity of the materials being processed. Hence, as metals have high conductivity the heating is easier and uniform with conventional heating. Whereas, the ceramics because of their lower thermal conductivity takes a longer time to achieve uniform heating<sup>175</sup>. This necessitates the need to go for microwave heating where the heating is independent of the conductivity of the material.

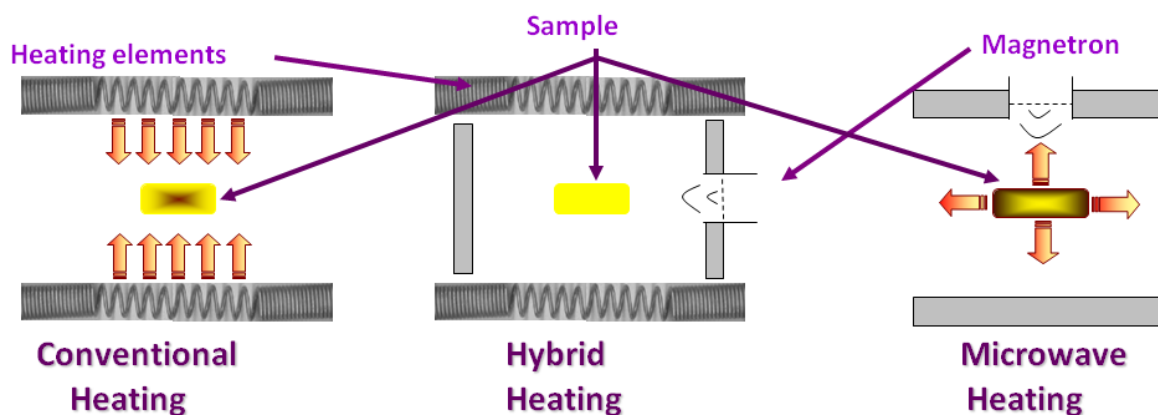


**Figure 2.32: The typical heating mechanism of conventional, hybrid and microwave heating**

The first papers on the use of microwaves for synthesis reactions appeared in the open, peer-reviewed literature in 1980's. Since then, several thousand articles have been published, numerous conferences have focused on the advancement of microwave techniques for material processing, and the use of microwave processing is also now the hot topic for combinatorial and parallel strategies<sup>168</sup>.

Studies have shown significant process enhancements by microwave heating including very fast heating rates, much lower sintering temperature, enhanced and accelerated diffusion rates, high production yields and selective activation or suppression of reaction pathways. Fundamentally, microwave heating is different to conventional means<sup>169</sup>. In microwave technique, heat is generated internally by the interaction of microwaves with the material. However, the control of microwave heating is more complicated than conventional heating. The heating depends not only on the operational parameters of the microwave source but also on the electrical and thermal properties of the material. An additional complication is that some of these electrical and thermal parameters change with the temperature.

### 2.9.2. Characteristics of microwaves

Microwaves are electromagnetic waves with a frequency in the range of 0.3-300 GHz (1 mm-1 m wavelength) (see Figure 2.33). The wavelength is of the same order as the linear dimensions of most practical ceramics. Milestone

microwave lab stations (Institute working on digestive studies in U.S.A) use a specific, fixed frequency of 2,450 MHz (2.45 GHz).

Microwaves, like all electromagnetic radiation, have an electrical component as well as a magnetic component. Microwaves travel similar to the light and depends on the medium it changes its path. Microwaves are reflected by metals and absorbed by the dielectric materials. Microwaves travel in the free space at the speed of light.

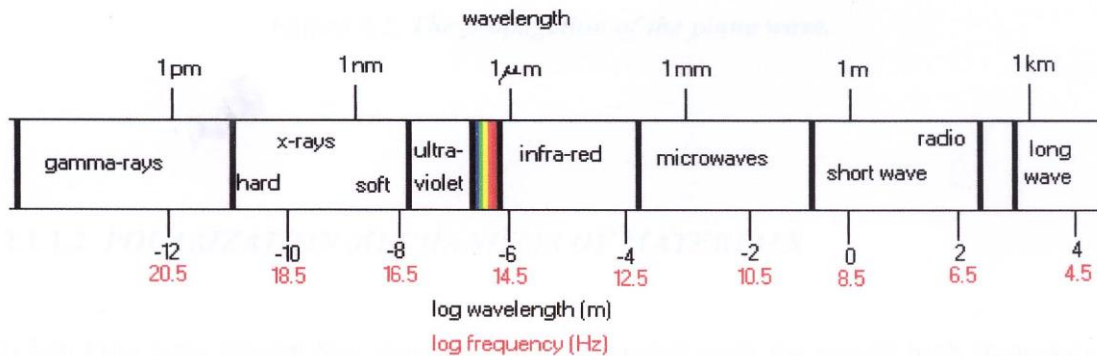


**Figure 2.33: The electromagnetic spectrum**  
(Reproduced from reference 170)

### 2.9.3. Interaction of microwaves with materials

Microwaves obey the laws of optics and can be transmitted, absorbed or reflected depending upon the material type as shown in Figure 2.34. When materials are heated using high frequency electromagnetic waves, usually the heating is produced by the interaction of components of the wave and the charged particles in the material. Therefore, the conduction and polarization mechanisms are responsible for the heating. The interaction of microwaves with materials and the ability to produce heat in some materials is mainly governed by electric and magnetic field of components, amplitude, phase angle and the ability of the wave to propagate.

Microwaves penetrate metals only in a thin skin of the order of 1  $\mu\text{m}$ ; continuous metals can therefore be considered to be opaque to microwaves or to be good reflectors of microwaves. Most electrically insulating (or dielectric) ceramics such as  $\text{Al}_2\text{O}_3$ ,  $\text{MgO}$ ,  $\text{SiO}_2$  and glasses are transparent to microwaves at room temperature. However, when heated above a certain critical temperature  $T_c$ , they begin to absorb

and couple more effectively with microwave radiation. Other ceramics such as  $\text{Fe}_2\text{O}_3$ ,  $\text{Cr}_2\text{O}_3$  and SiC absorb microwave radiation more effectively at room temperature<sup>171</sup>.

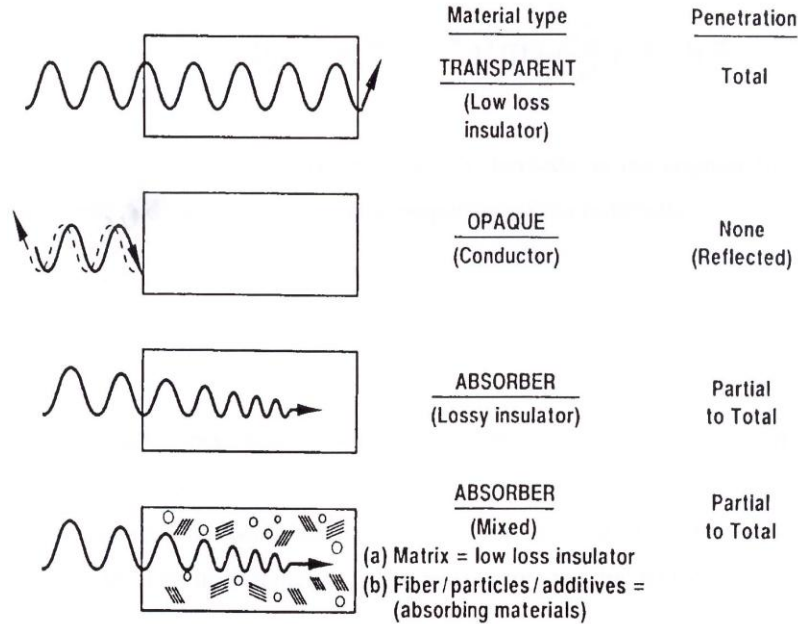


**Figure 2.34: Interaction of microwaves with material.**  
(Reproduced from reference 172)

Important properties of a material for the interaction are the permittivity,  $\epsilon$  (for a dielectric material), and the permeability,  $\mu$  (for the magnetic material). Commonly, relative permittivity  $\epsilon_r$  (also called as relative permittivity)  $=\epsilon/\epsilon_0$ , and the relative permeability  $\mu_r = \mu/\mu_0$ , are used<sup>173</sup>.

In alternating fields, the behaviour is best described with the help of complex quantities,  $\epsilon_r^*$  and  $\mu_r^*$ , defined by the equations

$$\epsilon_r^* = (\epsilon' - j\epsilon'') = \epsilon_0(\epsilon' - j\epsilon''_{ff}) \quad \text{and} \quad \mu_r^* = \mu'_r - j\mu''_r \quad \text{Equation 2.23}$$

Where  $j = \sqrt{-1}$ ,  $\epsilon_0$  - permittivity of the free space and  $= 8.86 * 10^{-12}$  F/m,

$\epsilon'_r$  – Relative dielectric permittivity and  $\epsilon''_{eff}$  – effective dielectric loss factor

When microwaves penetrate into the material, the electromagnetic field induces translational motion in the free and bound charges (e.g., electrons and ions) and in dipoles. The induced motion is resisted because it causes departure from the natural equilibrium of the system. This resistance, due to frictional, elastic, and inertial forces, lead to the dissipation of energy<sup>173,174</sup>. As a result, the electric field associated with the microwave radiation is attenuated and heating of the material occurs. The loss tangent ( $\tan\delta$ ) is used to represent the losses arising from these mechanisms.

$$\tan\delta = \frac{\epsilon_r''}{\epsilon_r'} = \frac{\sigma_{ac}}{\omega\epsilon_0\epsilon_r'} \quad \text{Equation 2.24}$$

$\sigma_{ac}$  - alternating current conductivity

$\omega$  - microwave angular frequency

The average power dissipated per unit volume of the material is given by

$$W = \frac{E_0^2 \sigma_{ac}}{2} = \frac{E_0^2 \omega \epsilon_0 \epsilon_r''}{2} = \frac{E_0^2 \omega \epsilon_0 \epsilon_r' \tan\delta}{2} \quad \text{Equation 2.25}$$

Where  $E_0$  - amplitude of the electric field ( $E = E_0 e^{j\omega t}$ )

According to equation 2.25, the power absorbed by the material depends on

- the frequency and square of the amplitude of the electric field, and
- the dielectric permittivity and loss tangent of the material,
- E is dependent on the size, geometry and location of the material within the microwave cavity and design and volume of the cavity.

By analogy to the dielectric case outlined here, corresponding equations can be derived for the interaction of the microwave field with a magnetic material.

As the electric field is attenuated, the depth of the penetration (D) of microwaves is an important and useful parameter, which is the penetration depth at which the incident power is reduced by one-half

$$D = \frac{3\lambda_0}{8.686 \pi \tan\delta \left( \frac{\epsilon_r'}{\epsilon_0} \right)} \quad \text{Equation 2.26}$$

Where,  $\lambda_0$  is the incident or free space wavelength. Although at longer wavelengths and lower frequencies, the penetration depth is high, the heating depends on the material since the internal E field could be low.

Finally, the relative dielectric permittivity ( $\epsilon_r'$ ), and loss tangent ( $\tan\delta$ ) are the most important and measurable parameters as both affect the power absorbed, and half power absorbed at penetration depth and thus influence the volumetric heating behaviour of a given material. The  $\epsilon_r'$ , is a measure of polarizability of the materials in the electric field and  $\tan\delta$  is a measure of the absorption of the microwave energy within the material<sup>175,171</sup>. As the absorbed power and depth of penetration depends on the dielectric property information, this is very important for microwave assisted materials processing.

In magnetic materials, magnetic dipoles may be able to couple with the magnetic component of electromagnetic field and provide an additional heating mechanism. Similar to the dielectric properties, the magnetic permeability,  $\mu'$ , and loss,  $\mu''$ , must be considered. There is relatively less information in the open literature on the microwave processing of magnetic materials.

#### 2.9.4. Mechanism of microwave heating

Many experimental results have suggested that a non-thermal influence of microwave field exists on mass transport. It has first been observed with oxygen diffusion enhancement in sapphire crystals in a 28 GHz millimetre-wave furnace<sup>176</sup>. A 40% decrease in activation energy for bulk diffusion has been observed under millimetre-wave heating as compared to conventional heating. Many researchers have observed an enhancement of densification during microwave solid-phase sintering of ceramics<sup>177</sup>. Microwave sintering of zirconia ceramics has revealed a non-thermal nature of this enhancement and it has been found that the variation of

density with temperature is 'S' shaped<sup>178</sup>. In addition, the densification shifts towards lower temperatures using microwave power in some microwave sintering trials<sup>5</sup>. A study of microwave assisted oxidation of melt-processed bulk YBCO ceramics has revealed significant enhancement of diffusion-controlled absorption of oxygen<sup>179</sup>. Another study on spinodal decomposition of ionic solutions has showed microwave effects on diffusion controlled process. A significant difference in evolution of titanium oxide –tin oxide solid solution samples are observed under microwave and conventional heating<sup>180</sup>. This effect, supposedly, has originated from the interaction of the microwave electric field with the space charge structure of compositional fluctuations. Reports on microwave processing of nanostructured porous alumina membranes have concluded that the porosity decreases consistently with increasing time of microwave exposure whereas it does not change in conventional heating for the same time/temperature profiles<sup>181</sup>. This suggests that microwave field enhances the rate of mass transport along the membrane surface by about two orders of magnitude.

Theoretical models have been developed to understand the microwave non-thermal enhancement of transport phenomena and have been justified with experimental findings. The primary difference between microwave and conventional processes is in the nature of their energy supply routes. In conventional process, energy is delivered to the materials mostly by means of equilibrium thermal radiation, which has continuous spectrum. The process of thermal radiation absorption by the material is usually viewed as the excitation of lattice oscillations, which have an equilibrium spectrum<sup>182</sup>. In contrast to the thermal radiation, the prevailing mechanism of microwave absorption in dielectric materials is the excitation of electron/ion oscillation at the frequency of the microwave source.

As aforementioned, microwaves interact with dielectric materials causing dielectric heating. Electric dipoles in the dielectric materials respond to the electric field component of the microwave. When the dipole reorientation is unable to respond to the frequency of the alternating electric field of the microwaves, it results in a phase lag in the reorientation and a polarization current arises in phase with the applied

field<sup>178</sup>. The component in phase current is given as  $I \sin\delta$ , where,  $\delta$ , refers to the phase lag,  $E$  and  $I$  refers to the field strength and current respectively. Measure of the heating effect is given by  $\sin\delta \approx \tan\delta = \epsilon''/\epsilon'$ -dissipation factor or loss tangent.

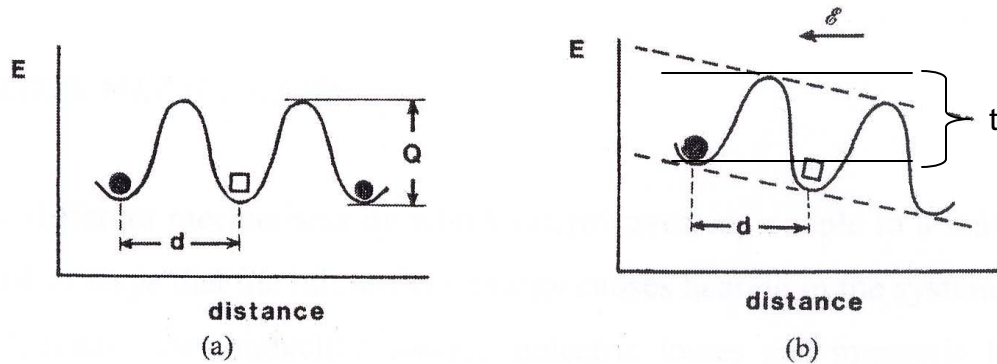


**Figure 2.35: Schematic representation of a potential barrier for an atom (●) to exchange its lattice site with a vacancy (□) (a) without an external electric field; (b) With an external electric field (Reproduced from reference 183)**  
 d-distance between two adjacent lattice sites; Q-activation energy

The simple ways for short range motion of atoms in solid is through vacancy or interstitial ion movement. When ions move in the crystalline solid, they must have sufficient energy to pass over an energy barrier. In addition, there must be a vacancy next to given atom<sup>184</sup>. Hence, the vacancy concentration is very important and when an external electric field is applied, shrinks the distance for the atom to overcome (t) thus the activation barrier reduces (Figure 2.35)

The ion mobility is given from Fick's first and second laws,

$$\mu = \frac{D.e}{K_b.T} \quad \text{Equation 2.27}$$

Where,  $D$  –diffusion coefficient,  $e$ - charge of the electron,  $K_b$ - Boltzmann's constant and  $T$ - temperature.  $D$  can be obtained from Arrhenius equation,

$$D = D_o \left[ \frac{-Q}{K_b.T} \right] \quad \text{Equation 2.28}$$



$D_0$  - pre-exponential factor which depends on the vibrational frequency of the atoms and some structure parameters,  $Q$  – activation energy for diffusion of ion in a solid and,

$$Q = E_v + E_m \quad \text{Equation 2.29}$$

$E_v$  - Activation energy that needs to form a vacancy and

$E_m$  - Energy for an atom to overcome the energy barrier.

Therefore, it is clear that the conductivity of the solid greatly depends on the absolute temperature, the number of defects and ions and their activation energies in the solid. As the grain boundaries provide vacant lattice sites, it is used as preferred paths for migration<sup>185</sup>.

Thus, there are many interesting but controversial results and suggestions have been reported on the mechanism of microwave heating the materials. Theories put forward include;

- Enhanced diffusion to increased vibrational frequency of the ions caused by the electric field of the microwave radiation<sup>186</sup> and hence the activation energy for a reaction decreases.
- The Arrhenius pre exponential factor is increased, as it depends on the vibrational frequency of the atoms at the reaction<sup>187,188</sup>
- The electric dipoles in the material couple with the electric field of the microwaves.
- Ponderomotive (time averaged, non-zero) action of high frequency electric field on charged vacancies in the ionic crystal lattice acts as a driving force and enhance the atomic mobility<sup>189,190</sup>

### 2.9.5. Limitations of microwave heating

As mentioned earlier controlling the temperatures in microwave heating is more complicated than in conventional heating. Because of the rapid heating, a common

problem occurred is “thermal runaway” and it can lead to melting of the sample or to the local hot spots formation. Non-uniformity in the microwave field leads to variation in energy absorption of the material and hence leads to different temperature at different parts of the sample.

Another problem is the difficulties associated with the accurate temperature measurement during microwave heating. The traditional thermocouples cannot be used, due to the interference with the microwave field<sup>191</sup>. In addition, the inverse temperature profile leads to the underestimation of the central temperature of the sample.

These can be avoided by using hybrid heating i.e., providing additional heating from the heating elements to provide uniform heating. This flattens out the inverse temperature profile. The use of optical fibre thermometry (OFT) also enables the measurement of the temperature precisely.

#### **2.9.6. Microwave/ conventional hybrid heating**

As aforementioned, temperature profile or temperature distribution is dependent on microwave power level, electric field distribution and materials properties. Microwaves get deposited directly with the material, interact and heat it up volumetrically. In addition, as the surroundings are cooler, it can result in inverse temperature profile, i.e. a hot interior than the surface. In conventional heating as it relies on the thermal conduction and radiation, the heat is transmitted from surface to the center. Figure 2.34 shows the schematic representation of the temperature distribution in the sample during conventional, microwave and hybrid heating.

Thus, hybrid heating combines both conventional and microwave heating, provides uniform heating and temperature distribution and hence reduces the processing temperature and yields finer microstructure providing better properties for the final ceramic. It takes the advantages of both the heating techniques, which greatly contributes in ceramic processing.<sup>192</sup>.

## 2.10. Microwave assisted processing of nanocrystalline BT ceramics

Several reviews have been published on the mechanisms and fundamental aspects of microwave sintering of ceramics such as  $\text{Al}_2\text{O}_3$ ,  $\text{ZrO}_2$ ,  $\text{Y}_2\text{O}_3$ ,  $\text{BaTiO}_3$  etc. However, relatively very few reported work is available on the microwave processing of nanocrystalline ceramics. Since the present work is primarily focussed on the microwave synthesis and sintering of barium titanate based capacitive materials, only reported publications pertaining to these types of materials are discussed below in detail.

Few researchers have attempted to synthesize  $\text{BaTiO}_3$  using microwaves. Felgner et al. have investigated on the mechanism of  $\text{BaTiO}_3$  formation in microwave and conventional heating using  $\text{BaCO}_3$  and  $\text{TiO}_2$  as starting materials<sup>193</sup>. Fewer attempts on using microwave heating in wet chemical synthesis like sol-gel, hydrothermal synthesis have been made so far. Ma et al. have first compared conventional and microwave heating during hydrothermal synthesis of  $\text{BaTiO}_3$  and have calcined it at  $850^\circ\text{C}/4\text{ hr}$ <sup>194</sup>. The results have suggested that the metastable cubic phase crystallises much faster in microwave heating without altering the transition temperature. As there has been significant lack of accuracy on temperature measurements, these may not be considered reliable. Malgne et al., have attempted microwave heating of barium titanyl oxalate and obtained cubic  $\text{BaTiO}_3$  at  $500^\circ\text{C}$  and tetragonal above  $700^\circ\text{C}$ <sup>195</sup>. Amalnerkar et al. have investigated the microwave heating effect during a Solvothermal technique<sup>196</sup>. Guo et al. have succeeded in synthesizing tetragonal  $\text{BaTiO}_3$  at  $240^\circ\text{C}/12\text{ hr}$  in Microwave-Hydrothermal system and produced 240 nm particle size powders<sup>197</sup>.

Thakur et al. have also synthesized  $\text{BaTiO}_3$  using  $\text{BaCO}_3$  and  $\text{TiO}_2$  as starting materials, sintered it using a 3 kW, 2.45 GHz microwaves at  $1450^\circ\text{C}/25\text{ min}$  and have achieved 97% T.D compared to the conventional 94% T.D at  $1450^\circ\text{C}/4\text{ hrs}$ . The result infers that microwave-sintered samples have larger lattice parameter and the  $T_c$  is shifted to higher temperature side<sup>198</sup>. Masaki et al. have achieved sintered BT at lower sintering temperature when using microwaves at 800 W/ 30 min and at

960W/ 10min<sup>199</sup> using barium borate as additive for achieving liquid phase sintering. However, they have not mentioned the sintering temperature used. Recently Sadhana et al. have reported that BaTiO<sub>3</sub> nanopowders (<80 nm) can be synthesized at 160°C/ 45 min using a Microwave –Hydrothermal system and even attempted to sinter it at 1050°C/ 30 min using microwaves and have achieved 93% T.D. However, the sintered sample resulted in cubic phase<sup>200</sup>.

There have been some reports on formation of compositionally modified BaTiO<sub>3</sub> and the results provide inference that microwave heating can not only produce single phase nanocrystalline ceramics and also helps to lower the synthesis and sintering conditions and resulting in excellent properties<sup>201,202,203,204,205,206,207,208,209,210</sup> for the ceramics produced.

From the literature, it is promising that finer microstructure associated with lowering sintering temperature and improved properties can be achieved through microwave processing. However, the clarity on temperature measurement and the specific role of microwaves in reaction/sintering enhancement is still lacking. None of the researches published so far has attempted to verify the genuine microwave effect during synthesis in a hybrid environment. It can be anticipated that proper utilization of microwave heating will result in much better properties. Therefore, in order to achieve better properties for nano BaTiO<sub>3</sub> at less demanding processing conditions, it is important to study the effect of microwaves during different stages of ceramic processing and this is where the current project work commences.

### **2.11. Scope of the present project**

Although, there are many researches attempted to make nanostructured ceramics and there are successful methodologies for producing nanopowders or achieving dense nanostructures after sintering, a holistic approach of converting a nanopowder into a nanostructured MLCC device has not been attempted in detail.

This project aims at converting a nano BT powder into a MLCC device. This has been achieved by looking at holistic view on all stages of powder preparation, green

processing, sintering and performance evaluation. This also helps to translate the developments made in one stage to other. Microwave assisted heating has been utilised in this research to achieve nanostructured BT ceramics.

Thus, the objectives of the present work are:

- Synthesis of nano BT and compositionally modified BT formulations using microwave assisted heating approaches.
- Elucidate the role played by microwaves during nano BT synthesis
- Preparation of nano BT ink suitable for green processing and fabrication of nano BT MLCCs through screen printing
- Fabrication of X7R nano BT MLCCs through dopants optimization
- Sintering of nano BT MLCCs using conventional, microwave and hybrid processing conditions
- Performance evaluation of the nano BT MLCCs against benchmark micron based MLCCs.

## Chapter 3

### 3. EXPERIMENTAL WORK

#### 3.1. Overall Methodology

This chapter explains the experimental procedure involved in this project. Figure 3.1 explains the overall work flow and the different characterisation techniques involved.

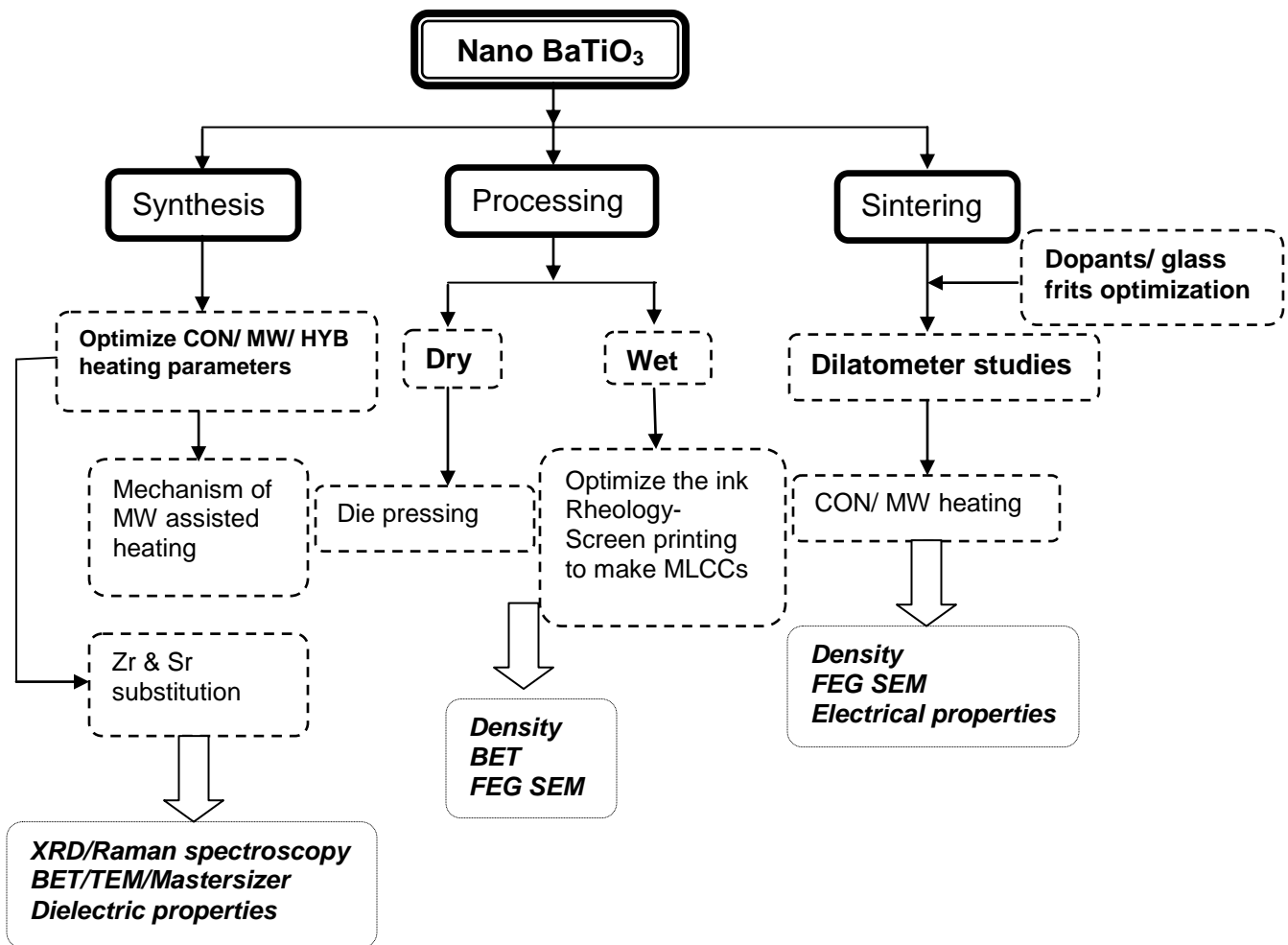


Figure 3.1: Flow chart of overall experimental work

### 3.2. Synthesis of nano BT based formulations

#### 3.2.1. Raw materials used

The chemicals used for synthesis of BT and compositionally modified BT powders syntheses using the polymeric precursor method are listed in the Table 3.1.

**Table 3.1: The details of the raw materials used for synthesis**

Name of the Chemical	Chemical formula	Supplier	Purity
Barium Carbonate	BaCO <sub>3</sub>	Fluka	>99%
Barium acetate	Ba(C <sub>2</sub> H <sub>3</sub> O <sub>2</sub> ) <sub>2</sub>	Sigma Aldrich	>98%
Barium hydroxide	BaOH.9H <sub>2</sub> O	Sigma Aldrich	>98%
Titanium tetra isopropoxide	Ti[OCH(CH <sub>3</sub> ) <sub>2</sub> ] <sub>4</sub>	Sigma Aldrich	>97%
Citric acid	C <sub>6</sub> H <sub>8</sub> O <sub>7</sub>	Fluka	>98%
Ethylene glycol	C <sub>2</sub> H <sub>6</sub> O <sub>2</sub>	Fluka	>98%
Zirconium nitrate	Zr(NO <sub>3</sub> ) <sub>2</sub>	MEL Chemicals	>99%
Strontium carbonate	Sr(CO <sub>3</sub> ) <sub>2</sub>	Fluka	>99%

#### 3.2.2. Synthesis procedure (wet chemical procedure used)

Synthesis of nano barium titanate was carried out by a citrate polymeric precursor method. Figure 3.2 gives the detailed process flow chart for the synthesis of BaTiO<sub>3</sub>.

The molecular weight of the chemicals used such as citric acid, ethylene glycol, barium carbonate and titanium tetraisopropoxide used for BT synthesis was given below.

**Table 3.2: Molecular weights of the chemicals used for synthesis**

Chemicals	Molecular weight, g/mol
BaTiO <sub>3</sub>	233.24
BaCO <sub>3</sub>	197.35
Ti[OCH(CH <sub>3</sub> ) <sub>2</sub> ] <sub>4</sub>	284.24
Citric acid (CA)	210.14
Ethylene glycol (EG)	62.07

The ratio of metal cations (Ba: Ti) was maintained as 1:1 and the ratio of citric acid to ethylene glycol was maintained as 1:4 (as explained in section 2.4.1). The overall molar ratio of Ba: Ti: CA: EG was taken as 1:1:10: 40.

First, one molar citric acid solution was prepared by mixing the one mole weight of citric acid to 1 litre of distilled water at room temperature. 0.1 mole of titanium tetraisopropoxide was mixed separately with 4 moles of ethylene glycol at 80°C.

For Zr substitution,  $Zr(NO_3)_2$  was mixed along with the above, maintaining the required Ti:Zr ratio. After the complete dissolution of titanium isopropoxide in ethylene glycol forming a transparent liquid, the prepared citric acid solution was added to it and mixed at 80°C with constant stirring using a magnetic stirrer for 2 hrs. After 2 hrs, it forms a transparent solution, to which 0.1 mole of  $BaCO_3$  powder was weighed, added, dissolved and mixed until it became pale yellow transparent solution. For Sr substitution,  $Sr(CO_3)_2$  was added along with  $BaCO_3$ , keeping (Ba±Sr):(Ti±Zr) as 1:1. The continuously mixed solution was then heated at 200°C for 5 hrs in an oven to promote polymerization and removal of organic solvents. Heating at this temperature resulted in a viscous dark brown glassy resin. The glassy resin was charred at 400°C for 2 hrs in air atmosphere that resulted in a fluffy black solid mass, which was lightly ground into a powder using an agate mortar and pestle. Powder obtained in this way is referred as a "Precursor". These precursors were then calcined at different temperatures (600 to 900°C) for varying time durations using microwave and conventional heating methods.



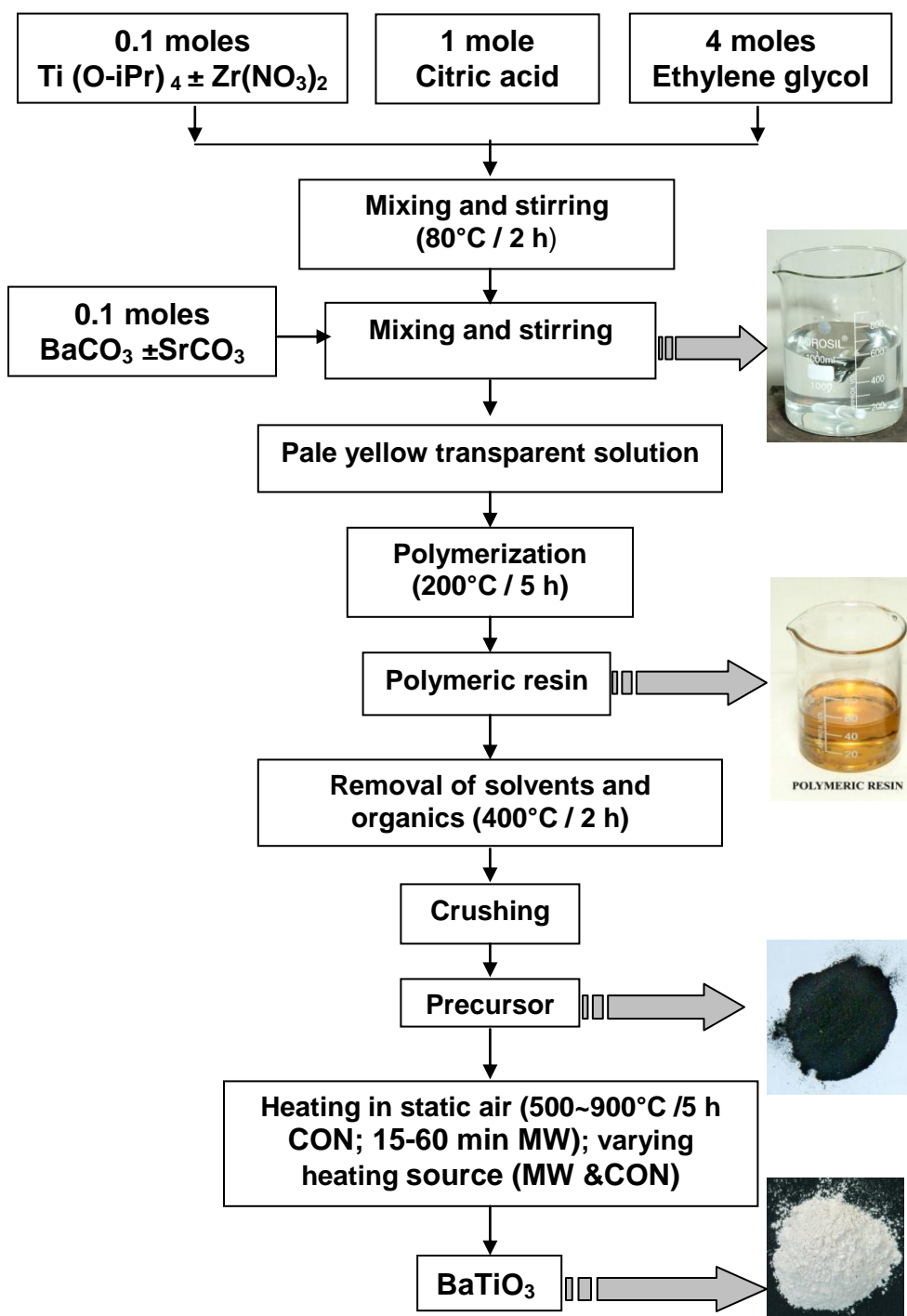


Figure 3.2: Flow chart for synthesis of BT and compositionally modified BT using citrate polymeric precursor method

### 3.2.3. Heating methodologies employed (Conventional vs. Microwave vs. Hybrid)

#### (i) Conventional heating

The muffle furnace (Carbolite U.K Ltd.,) was used for conventional synthesis of BT based materials. The calcination temperatures were varied from 600 to 900°C for 5 hr at 5°C heating and cooling rates.

#### (ii) Microwave heating

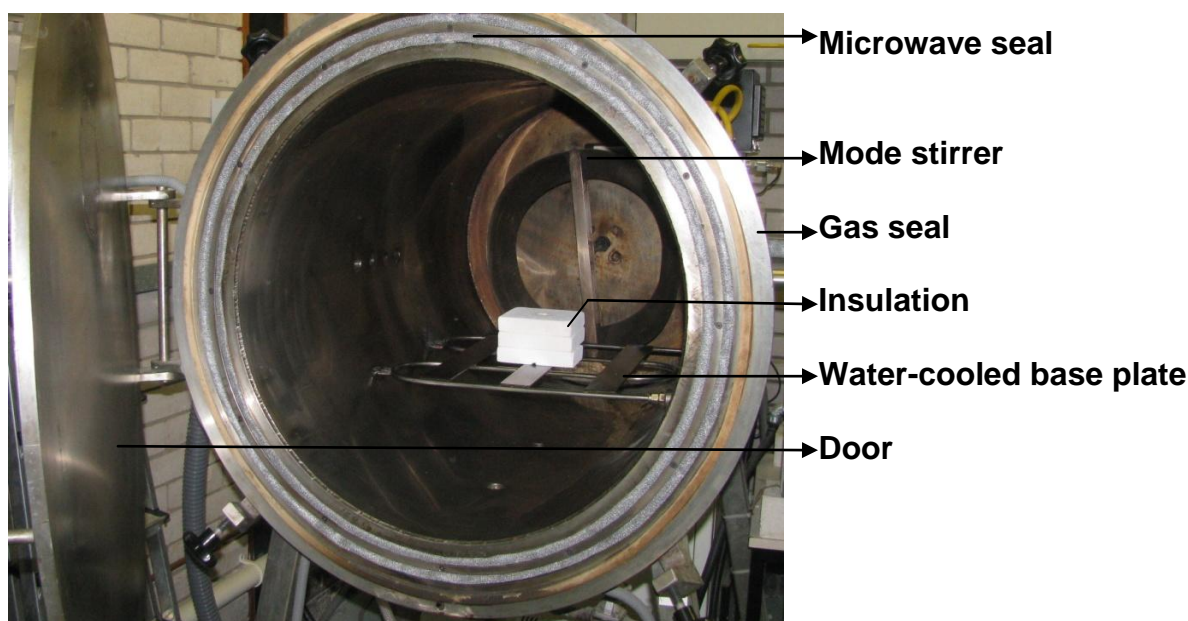


**Figure 3.3: Microwave cavity at Loughborough used for BT powder synthesis and sintering**

The microwave calcination was performed in a multimode cavity operating at a frequency of 2.45 GHz and capable of providing an adjustable output power up to a maximum of 6000 W. The microwaves from the magnetron were transmitted through a wave-guide system and launched into the cavity after reflecting onto a mode stirrer rotating at 70 rpm. The microwave applicator was capable of handling a controlled atmosphere during processing. The cavity was provided with a water-cooled base plate to hold the samples and outer cooling jacket for safety. A number of ports for thermocouple entry and a view port for pyrometer were also available. A reflected

power-monitoring unit and a three-stub tuner helped to tune the microwave system with minimum reflected power. The precursor was the primary susceptor and SiC rods were used as secondary susceptors to ensure thermal homogeneity. Figure 3.3 shows the microwave cavity used for the present work and Figure 3.4 shows the sample arrangement inside the microwave cavity. The precursor powders were weighed and taken in a fused silica crucible. An insulation box (casket) made using high purity alumina fibre with a top view port was used to prevent the heat loss during the microwave heating<sup>211</sup>. The sample was aligned properly for viewing and temperature measurements.

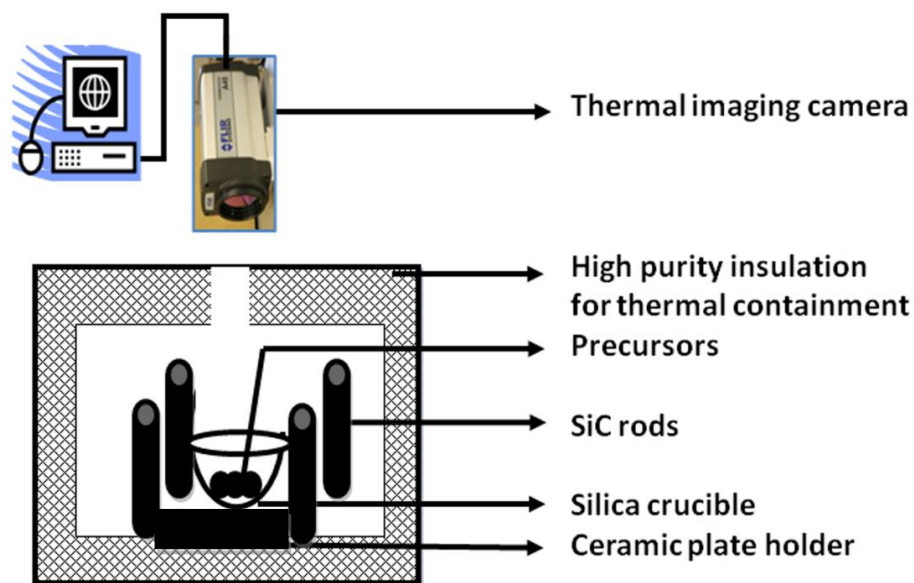


**Figure 3.4: Sample arrangements in the microwave cavity.**

A thermal imaging camera (ThermoVSION™ A40, Boston, U.S.A) was used which covers a temperature range of  $-40^{\circ}\text{C}$  to  $2000^{\circ}\text{C}$  with  $\pm 0.1^{\circ}\text{C}$ , 320 x 240 pixels. Temperature measurements were made in five modes like spot, line, area, isotherm, and difference. It measures and takes images of the emitted infrared radiation from the material, for which the emissivity of the material and the distance between of the material and camera lens were important parameters. Thus, it would give the overall temperature distribution of the material accurately. In addition, an optical pyrometer (Minolta/Land Cyclops 152 pyrometer) was used to measure the temperature of the

material during microwave heating. It could measure the temperature range from 600 to 2000°C at 1/3° measurement angle. In the pyrometer, the optical systems were used to focus the energy emitted by the material on to the detector, which was radiation sensitive. The detector output is proportional to the difference of radiation energy from the material, the optical system, and the specific radiation wavelengths. The emissivity of the material was an important variable to convert the detector output to the accurate temperature.

### (iii) Hybrid heating

The hybrid microwave furnace used was supplied by C-Tech Innovation Ltd and it consisted of magnetron, wave-guide, cooling system, circulator, microwave tuner, and hybrid microwave cavity (an applicator). Figure 3.5 shows the picture of the sample arrangements in the hybrid microwave furnace inside a rectangular metallic box, a stirrer, alumina fibre insulation and six MoSi<sub>2</sub> heating elements. The microwave power was supplied by the magnetron, present behind the cavity. The magnetron was set to supply up to 1.2 kW of 2.45 GHz microwave power. The Eurotherm controllers besides the cavity control the conventional heating. The furnace was designed specially with both conventional and microwave heating sources to operate separately and simultaneously<sup>191</sup>.

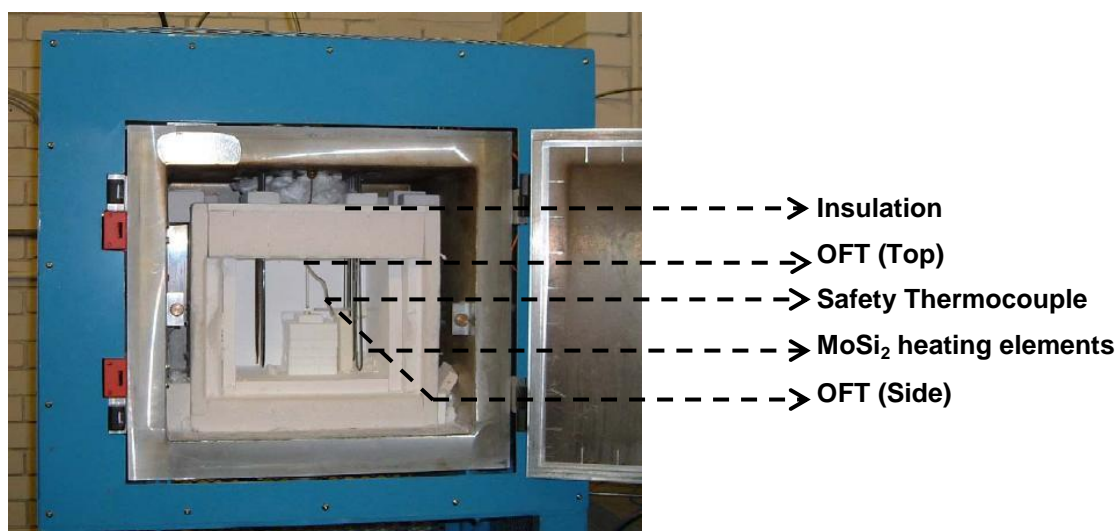


**Figure 3.5: Sample arrangements in the hybrid microwave furnace at Loughborough used for BT powder synthesis and sintering**

To further understand the mechanism of microwave heating during nano BT synthesis, another set of experiments were conducted under identical thermal history in the hybrid furnace. Same amount of the precursor (5 g) was taken in a fused silica crucible for all the experiments. For all the calcinations, the samples were held at 500°C for 30 min at the beginning to attain thermal equilibrium before the start of the calcination. This step can minimize the possible temperature gradient across the sample. The calcination temperature of 700°C was chosen to attain BT formation. Maintaining identical thermal mass and identical time-temperature profiles (700°C for 30 min) at 15°C/min heating rate for each synthesis trials, the microwave power level was fixed between 0 and 1000 W, in 200 W increments, and the conventional power was varied to provide the same calcination schedule. Changes in input conventional power, forward microwave power and reflected microwave power were all monitored continuously. This allowed direct comparison of the effect of phase formation or reaction enhancement caused by use of microwaves. Throughout the work, temperature was measured and controlled using Optical fibre thermometry (OFT) (M10 and M100, Luxtron, U.S.A) at the center of the sample. The temperature at the sample end was also measured using another OFT<sup>212</sup>. This allowed the temperature gradient across the each sample to be determined. The OFTs were shielded using a very low dielectric loss ceramic tube to minimise radiation influence from heating elements. The accuracy of temperature measurement was calibrated using melting point of vanadium pentoxide through a separate set of measurements and it was found to be  $\pm 3^\circ\text{C}$ <sup>191</sup>. In addition a thermal imaging camera (ThermoVSION™ A40, Boston, U.S.A) was also used to evaluate the overall temperature distribution of the material. For activation energy calculations, more calcination experiments were conducted at different soaking temperatures (600, 700 and 800°C) with varying soaking times (5-120 min) using different microwave power levels (0, 600, 1000 W).

### **3.2.4. Characterization related to the synthesis of BT**

#### **(i) Thermal analysis**

Thermal analysis of the crushed precursor powder was carried out up to 1000°C. This helped to analyse crystallization and the phase evolution of BaTiO<sub>3</sub>. This equipment recorded the Differential Thermal Analysis (DTA) and Thermo gravimetric Analysis (TGA) simultaneously (SDT 2960 Simultaneous TGA/DSC, TA instruments, U.K Ltd.). TGA was also used for compositional analysis and determination of thermal stability. The DTA was used to determine the heat change associated with the decomposition and phase transformation of the material. In general a sharp exothermic peak is an indicative of crystallization or fusion process, where as broad endothermic peaks in conjunction with weight loss signify dehydration or decomposition reactions.

The enthalpy of formation of intermediate compounds and BT was calculated using TA instruments built in software, Universal Analysis. The calculated area under the peaks corresponding to the formation of intermediate and BT of weight corrected/normalised DTA curves, resulted in enthalpy value of J/mol.K.

Modulated Differential Scanning Calorimetry (MDSC; Q2000, TA instruments, U.K Ltd.) operating between -180°C to 725°C with liquid nitrogen cooling was used to measure the enthalpy of phase transition of synthesized BT compositions.

#### **(ii) XRD**

The phase formation and crystallinity was analyzed by X-Ray diffractometer (D8 model, Bruker AXS GmbH, Karlsruhe, Germany) using Cu K $\alpha$  (1.5408 Å) radiation with 0.02° step in the range of 20-60°. The powder samples were spread on the glass slide, pressed flat and exposed to the X-ray radiation. The angle of incidence was varied between 20-80°, the corresponding diffraction intensities were collected. The results were recorded to the computer system connected. The approximate crystallite size was calculated using X-Ray line broadening using Sherrer formula.

$$t = \frac{0.9\lambda}{\beta \cos \theta} \quad \text{Equation 3.1}$$

where,  $\lambda$ - wavelength of the X-ray radiation

$\theta$ - Maximum peak angle

$\beta = (\theta_1 - \theta_2)$  is the full width at half maximum, with  $\theta_1$  and  $\theta_2$  are the start and end angle of the half maximum peak

The lattice parameters were calculated using the following formula.

For cubic,

$$a^2 = \frac{d^2}{(h^2 + k^2 + l^2)}; \text{ where } d = \frac{\lambda}{2 \sin \theta} \Rightarrow \sin^2 \theta = \frac{\lambda^2}{4a^2} \left[ \frac{4}{3} (h^2 + k^2 + l^2) \right] \quad \text{Equation 3.2}$$

For tetragonal,

$$\frac{1}{d^2} = \frac{(h^2 + k^2)}{a^2} + \frac{l^2}{c^2} \quad \text{Equation 3.3}$$

$$\Rightarrow \sin^2 \theta = \frac{\lambda^2}{4a^2} \left[ \frac{4}{3} (h^2 + k^2) + \frac{l^2}{(c/a^2)} \right] \Rightarrow \sin^2 \theta = \frac{\lambda^2}{4a^2} (h^2 + k^2) + \frac{\lambda^2}{4c^2} l^2 \quad \text{Equation 3.4}$$

For  $l=0$  planes i.e., (HK0) planes;  $\sin^2 \theta = \frac{\lambda^2}{4a^2} (h^2 + k^2) \therefore a^2 = \frac{\lambda^2}{4 \sin^2 \theta} (h^2 + k^2)$

Substituting the 'a' valued from these planes, 'c' values were calculated from the other planes where  $l \neq 0$ .

### (iii) Micro-Raman spectroscopy

Micro-Raman spectroscopy (Raman LabramHR spectrometer, Horiba Jobin Yvon SAS, Villeneuve d'Ascq, France) was used for BT phase confirmation. The equipment consisted of a liquid nitrogen cooled CCD detector, two objective lenses of X10 and X50 magnification, Ar ( $\lambda$  -514 nm) and He-Ne ( $\lambda$  -632.8 nm) lasers, a video monitor and a computer (Figure 3.6). The powder samples were pressed flat on the glass slide; focus using the optical microscope and then exposed to the laser



radiation. The incident radiation wave number and the corresponding the intensities were collected through the computing systems connected to the instrument.

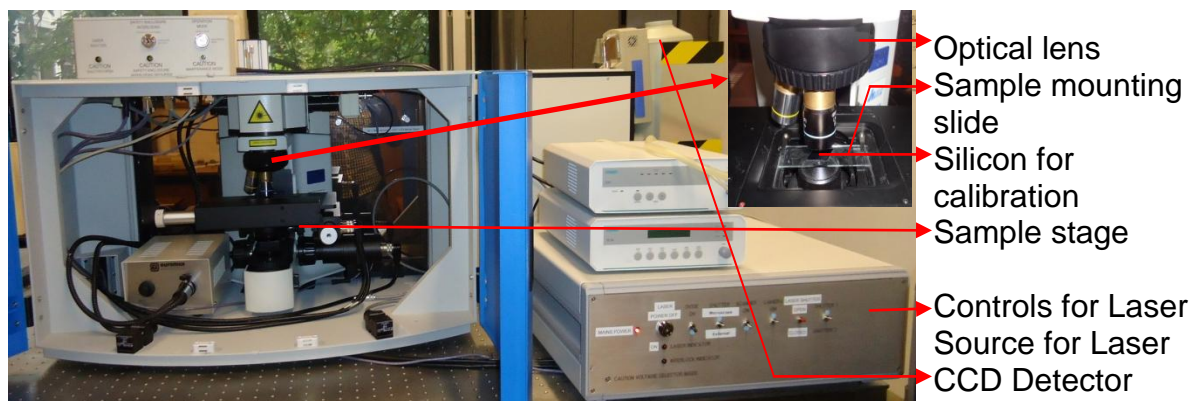


**Figure 3.6: Sample arrangements for micro Raman spectroscopy technique**

Firstly, the BT nanopowders were spread flat on a glass slide and a specific area was focused using the optical microscope connected to the video monitor. The sample stage was controlled using the computer. The micro-Raman spectra of the samples were recorded using He-Ne laser (20 mW) in the range of 100 to 1100  $\text{cm}^{-1}$  for 10 sec. The spot size of data collection was around 1  $\mu\text{m}$ . Five representative readings were taken for each measurement.

#### **(iv) Transmission electron microscopy**

The accurate particle/crystallite size was determined using Transmission electron microscopy (TEM) JEOL JEM 2000FX (JEOL Ltd. Tokyo, Japan). The TEM also gave an idea about the shape of the particles and the nature of any agglomerates and their size. The selected area electron diffraction (SAED) was performed using TEM. The samples were subjected to a parallel beam of high energy electrons. In that case, electrons were treated as wave-like, rather than particle-like. Because the wavelength of high-energy electrons was a fraction of a nanometer, and the spacing's between atoms in a solid was only slightly larger, the atoms acted as a diffraction grating to the electrons, which were diffracted. Some fraction of them were scattered to particular angles, determined by the crystal structure of the sample, while others continued to pass through the sample without deflection. It



resulted in ordered spots corresponding to the planes of that crystal structure. Hence this technique was used to confirm the crystallinity of the powders.

The powder samples were well dispersed in methanol solution using ultrasonication for 5 min. The thin carbon coated copper grids were used as a holder and few drops of the dispersion were sprinkled on it and mounted on the TEM sample holder. Further the sample holder was inserted into the chamber, evacuated, exposed to the electron beams and analysed.

#### (v) BET surface area analysis

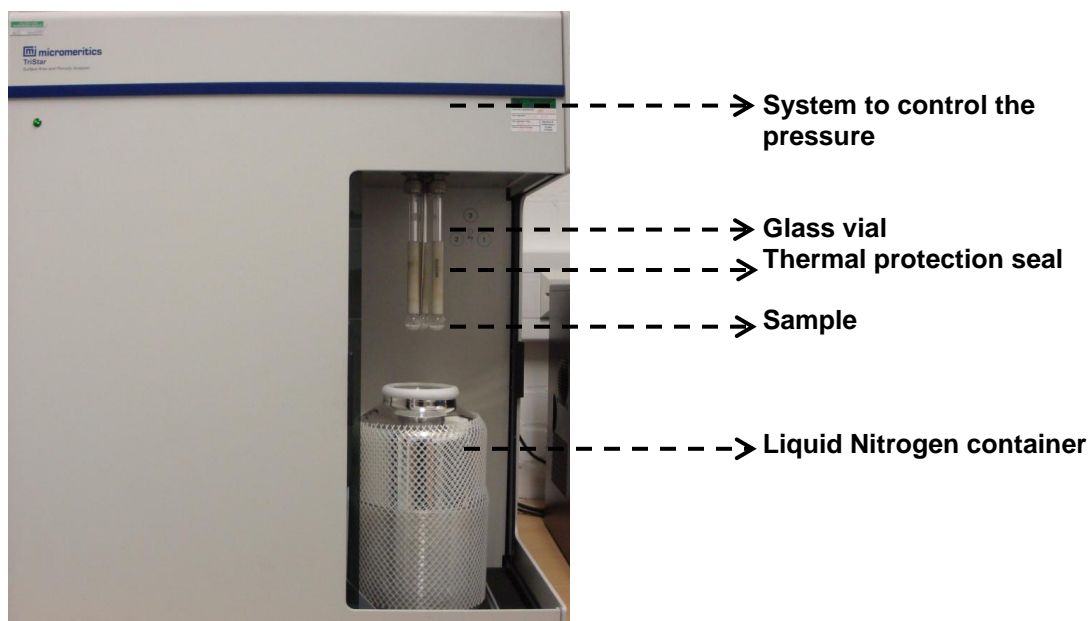


**Figure 3.7: Sample arrangements for BET surface area analysis**

The BET surface area, pore size and pore size distribution of the powders and green samples were measured using an automated BET gas adsorption analyser (Tristar™ 3000, Micromeritics Instrument Corporation, Norcross, USA) as shown in Figure 3.7. Before testing, all the samples were degassed in a nitrogen atmosphere for 60 minutes at 150°C. During the testing, the sample was evacuated to less than 20  $\mu\text{m}$ , Hg vacuum, cooled down to 77 K and then high purity nitrogen (>99.99% pure) was dosed in a predefined manner. The use of relative pressure,  $p$ , with respect to the saturation vapour pressure,  $p_0$ , at a constant temperature of

adsorption was utilized during the measurements. 40 adsorption and desorption points were collected with  $p/p_0$  values in the range 0.05 to 0.99. The Tristar™ 3000 had a resolution within 0.05 mmHg and accuracy 0.5% of full scale<sup>213</sup>.

The powder samples were weighed and taken on the round bottom long neck tube. The moisture content in the samples were removed by passing N<sub>2</sub> gas at 150°C for 1-2 hours before loading in the instrument. The Tristar software was used to set up and the results were collected using the computing systems. Using the surface area results, the powder particle size was calculated using the following formula.

$$D = \frac{6 \times 10^3}{\rho \times S_{BET}} \quad \text{Equation 3.5}$$

Where, D –Particle diameter,  $\rho$  - Density of the material,  $S_{BET}$  – BET Surface area

#### **(vi) Malvern Mastersizer**

The particle size distribution was measured using a particle size analyser (Mastersizer 2000, Malvern Instruments, Worcestershire, U.K) capable of measuring 20 nm to 2000  $\mu\text{m}$ . This works on the principle of laser diffraction technique, “The particle passing through the laser beam will scatter light at an angle that is directly related to their size: Large particle scatter at low angle and small particle scatter at higher angle”. The powders were dispersed in a ethanol solvent medium, ultrasonicated for five minutes to break the soft agglomerates, and circulated into the cell. Five measurements were taken for each sample.

#### **(vii) High frequency dielectric property measurements**

The dielectric property measurement at high frequency was carried out using the cavity resonator facility at Nottingham University. Resonator was referred to a device or system that exhibited resonance or resonant behaviour that was oscillated at some frequency (resonant frequency) with greater amplitude than at the other frequencies. The oscillations in the resonator were electromagnetic or mechanical (acoustic), when using electromagnetic waves, it was referred as a cavity resonator.

Generally, resonators are used to generate waves of specific frequencies or select specific frequency from the signal. The perturbation cavity resonator was used to measure the dielectric property of the materials at microwave frequency, the materials fills the cavity partially and held in suspension within the sample holder allowing a rapid movement.

The experimental set up consisted of (i) a cylindrical copper resonant cavity of 373.0 mm internal diameter and 37.3 mm of internal height with a water cooling system (ii) a carbolite conventional tube furnace, which operate up to 1800°C with Eurotherm controller, (iii) a computer controlled stepper motion controller (unidex®1) with a motor capable of operating at 6500 rpm, (iv) A Hewlett Packard 8753C vector network analyser, which operate between 300 kHz -6 GHz, operated in two-port transmission mode, connected to the computer for automatic determination of frequency shift and quality factor. In addition, it consisted of sample insertion holes in the cavity wall, a quartz tube of 3 mm diameter was used to hold the samples with microwave transparent pure silica glass wool.

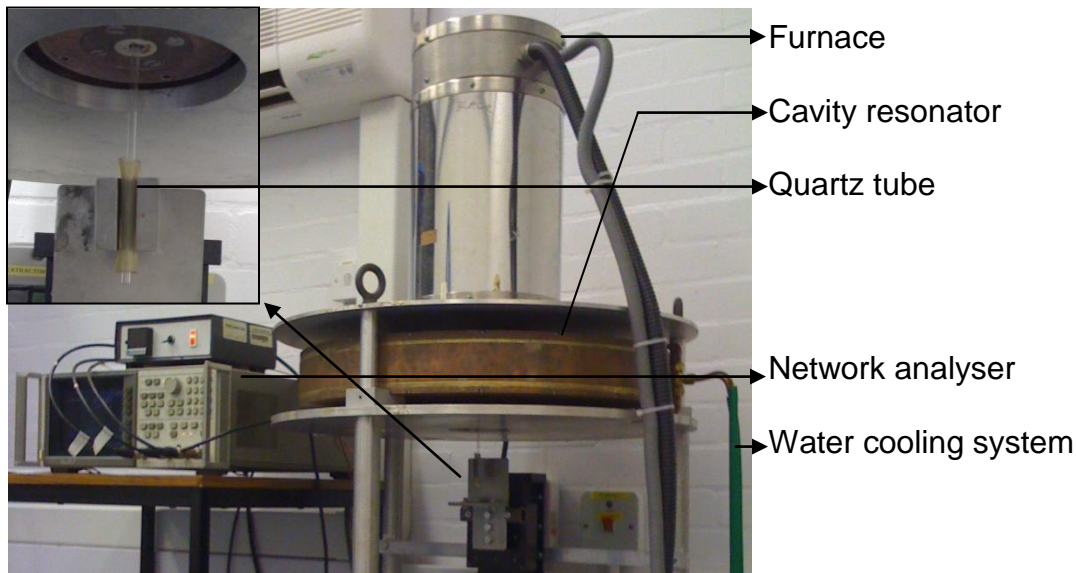


**Figure 3.8: High frequency dielectric measurements facility used courtesy: Nottingham University**

The solved Maxwell's electromagnetic equations for the cavity, with insertion holes set up, including the approximation for sample shape and holders, were given by,

$$\epsilon' = 1 + 2J^2 \frac{\Delta f V_c}{f V_s} \quad \text{Equation 3.6}$$

$$\epsilon'' = 2J^2 \left( \frac{1}{Q_{loaded}} - \frac{1}{Q_{empty}} \right) \frac{V_c}{V_s} \quad \text{Equation 3.7}$$

where,

$\epsilon'$ ,  $\epsilon''$  are real and imaginary part of the complex permittivity respectively;

$Q_{loaded}$ ,  $Q_{empty}$  are the quality factor of the loaded and unloaded cavity respectively;

$V_c$ ,  $V_s$  are the volume of the cavity and sample respectively;

$\frac{\Delta f}{f} = \frac{f_{loaded} - f_{empty}}{f_{empty}}$ ;  $f_{loaded}$ ,  $f_{empty}$  are the frequency shift of the loaded and unloaded cavity respectively;

J is the Bessel function of the first kind.

Firstly, a clean quartz tube of known inner diameter (~3 mm) was taken. The tube was fixed inside the chamber. The region of the quartz tube fitting in the cavity along the length from the bottom fixture was marked using a pen marker. The microwave transparent silica wool was stuffed inside the quartz tube to the height matching the bottom rim of the cavity. The quartz tube was fixed inside the cavity and the resonance frequency ( $f_{unloaded}$ ), quality factor ( $Q_{unloaded}$ ) was measured and recorded. After taking the measurements of frequency and quality factor for the empty tube, powder samples were filled in the tube keeping the aspect ratio of  $\geq 10$ , and the length of the sample was noted. The powder samples were aligned in the centre of the sample and measured using the computer controlled software and the network analyser. The resonance frequency ( $f_{loaded}$ ), quality factor ( $Q_{unloaded}$ ) for the required frequency was measured & recorded. The calculations were made using the above formula in equation 3.5 and 3.6.

For the high temperature measurements, the samples were arranged similarly and the program for temperature control was used to set up the temperature range and

step for increments. The samples moved up in to the furnace, after reaching the required temperature, held for 10 min and automatically dropped down into the chamber for measurement and records.

### **3.3. Processing of the nano BT powders to make green bodies**

The synthesized nano BT and a procured nano BT powder from Sakai chemicals Ltd., Japan (>99% purity) were processed through dry and wet routes as described below. For comparison, sub-micron BT powder from Fisher scientific Ltd., U.K (98% purity) was also processed using similar procedures.

#### **3.3.1. Dry processing**

##### **(i) Compaction of the nano BT powders to form pellets**

The compressibility of the nanopowders were studied using Lloyds mechanical testing machine (L10000 Tensometer, Lloyds Instruments, Fareham, UK) in a hardened steel die of 10 mm diameter. About 5 g of powder was used for each test. Before filling the powder, the die and the plungers were thoroughly cleaned using ethanol. The load was applied using Lloyds mechanical testing machine with a computer interface, which recorded the load versus cross head position continuously. The ramp speed used was 1 mm/min and held at the maximum pressure (380 MPa) for a minute. The density of the compact at any given pressure was calculated from the elastic compliance of the testing system and cross head position. The compact was ejected from the die and then further characterized.

The die pressed compacts were made using 10 mm die with 0.3 g of BT powders at 250 MPa pressure.

#### **3.3.2. Wet processing**

The list of ingredients used for wet processing of BT nanopowders and their properties are given in Table 3.2.

**Table 3.3: List of ingredients used for wet processing**

<b>Name of the Chemical</b>	<b>Product name</b>	<b>Supplier</b>	<b>Purity</b>
Pine oil	Dertol 90 I	D.R.T, France	98%
Phosphate ester	Lubrophos LK-500	Rhone-Poulenc, U.S.A	99%
Polyvinyl butyral	Butvar®B-98	Solutia UK Ltd.,	>97.5%
Ethyl cellulose	Aqualon®	Hercules, Netherlands	>97.5%

**(i) Nano BT ink/slip formulation**

The order of addition of the ingredients was identified to be very critical. First the required amount of dispersant was weighed, to which the calculated amount of solvent was added and then the BT powders were added, stirred in small quantities slowly to avoid any lump formation. A 55 wt% nano BT suspension with varying amount of dispersants (0, 0.25, 0.5, 0.75, 1 wt% the BT powder) were prepared using ball mill for 12 hours with Zirconia media of  $\pm 3$  mm diameter (Jyoti ceramics Ltd., Germany) (equivalent to the weight of the solids). The viscosity of the prepared suspensions was measured using Anton Paar MCR101 Rheometer (Anton Paar Ltd, Hertford, U.K). The Rheology measurements were carried out using 25 mm diameter plate in a parallel plate set up with a measurement gap of 0.5 mm at 20°C. Controlling shear rate test condition (CSR mode) was used, which has been explained in the following section. The dispersant concentration that produces lower viscosity would be more stable and have less amount of agglomeration, hence was considered as the optimum concentration.

Using the optimum amount of dispersant, different batches of BT suspension were prepared with increasing solid content up to 64 wt% ( $\geq 20$  vol%) and the viscosities were measured. The maximum solid content with lower viscosity was chosen as the optimum solid content for the system.

One of the major constituents of the ink is the binder. Hence, binder optimization is very important during the ink preparation. Table 3.3 show the properties of the two different types of binders that were used; polyvinyl butyral (PVB) and ethyl cellulose (EC) of 3 different molecular weight (N4, N10, N24). PVB having short polymeric chain and low viscosity would enable to increase the solid content. EC having low

polymeric chain and high viscosity would provide green strength. Different proportion of PVB: EC and within EC internally, different proportion of different molecular weight EC was varied as shown in Table 3.4. In addition, the total binder concentration was varied between 2-3 wt% optimized proposition of binders, and concentration was chosen based on the ink rheological behaviour. BM1-3 represents the effect of PVB: EC ratio and BM4-7 represents the effect of change in EC ratio locally.

Table 3.4: Properties of the binders

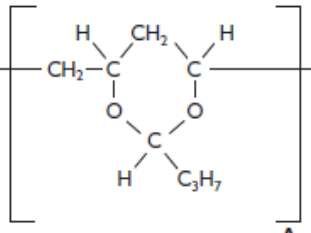
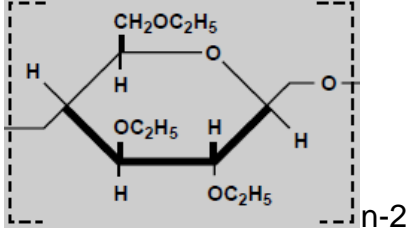
Properties	PVB	Ethyl cellulose (N4-N22)
Chemical formula		
Molar mass	123.7	552.3-1837.3
Density, g/cc	1.1	1.14
Polymeric chain length	5.72 Å	9.3-13.9 Å
Viscosity, cPs		8-24
Yield strength	6.3-7.3 psi	6800-8100 psi
Elongation	8%	10-28%
Tg	72-78	152-162
Solid loading	High	Low
Dispersant interaction	Better	good
Tacky	No	Yes

Table 3.5: List of Binder composition

Binder mix	PVB:EC	Total binder-3wt%		EC Ratio	Ethyl cellulose		
		PVB	EC		N4	N10	N24
BM1	2:3	1.2%	1.8%	1:1:1	0.6%	0.6%	0.6%
BM2	1:1	1.5%	1.5%	1:1:1	0.5%	0.5%	0.5%
BM3	3:2	1.8%	1.2%	1:1:1	0.4%	0.4%	0.4%
BM4	2:3	1.2%	1.8%	6:4.5:3.5	0.8%	0.6%	0.4%
BM5	2:3	1.2%	1.8%	7:4:3	0.9%	0.5%	0.4%
BM6	2:3	1.2%	1.8%	8:3.5:2.5	1%	0.5%	0.3%
BM7	2:3	1.2%	1.8%	9:3:2	1.1%	0.4%	0.3%

**(ii) Nano ink rheology optimization**

The different test conditions were used to understand the ink behaviour. Rotational test was used to understand more complex flow behaviour of liquids, dispersion or gels.

a. Tests with controlled shear rate (CSR):

Shear rate or speed was set to constant. This test method was used for liquids showing self-levelling behaviour (having no yield point) and measurement of viscosity at a defined flow velocity or shear rate, used for practical process condition. As a rule of thumb, the measuring point duration was set minimum to the reciprocal of shear rate to avoid getting a transient viscosity peak. Hence, a preset of 0.01-1000 s<sup>-1</sup> with 50 measuring points and shear rate increased in logarithmic steps with variable measuring duration from 100 to 5 s. Thus, viscosity was plotted against shear rate. The return curve was also obtained, for analysing any thixotropic behaviour of the ink.

b. Tests with time dependant flow behaviour

In this test, shear/ flow behaviour was investigated as a function of time. With the preset of constant shear rate/stress, the measurement consisted of different intervals,

- (i) Rest/ Reference interval – At the start of the test, preset constantly  $\dot{\gamma} = 0.1 \text{ s}^{-1}$ , to enable sample relaxation, fairly a constant viscosity value for the whole sample
- (ii) High-shear interval – presetting at high shear rate,  $\dot{\gamma} = 40 \text{ s}^{-1}$  for 30 sec with 5 points between  $t_1$  and  $t_2$ , during which the internal structure of the ink breaks. Thus it simulates the application process.
- (iii) Low-shear/ Regeneration interval – again this is presetting at low shear or rest condition,  $\dot{\gamma} = 0.1 \text{ s}^{-1}$  for 30 sec with 5 points in the period of  $t_2$  and  $t_3$ , facilitating the regeneration of the ink structure.



The structure regeneration was very critical to achieve consistent prints.

c. Tests with temperature dependant flow behaviour

Viscosity changes with temperature and high viscous materials are prone to have greater temperature dependency. Hence, with the preset shear rate  $\dot{\gamma} = 40 \text{ s}^{-1}$  equivalent to the process, viscosity was measured as a function of temperature. In addition, this test also resulted in softening temperature of the material, which would be useful for processing the ink.

The Arrhenius relation in the form of a  $\eta/T$  fitting function describes the change in  $\eta$  for both increasing and decreasing temperatures.

$$\eta(T) = c_1 \cdot \exp(-c_2/T) = c_1 \cdot \exp[(E_a/R_g)/T] \quad \text{Equation 3.8}$$

Where, T is temperature [K],  $c_1$  [Pa.s] and  $c_2$  [K] are materials constant,  $E_a$  is flow activation energy [kJ/mol] and  $R_g$  is the gas constant =  $8.314 \text{ JK}^{-1}\text{mol}^{-1}$ .

The energy needed for the molecules to exceed the liquid specific energy/ potential barrier is described as flow activation energy. A semi logarithmic curve was plotted with temperature on x axis in linear scale and viscosity on y axis, in logarithmic scale, this is Arrhenius curve.

Viscosity/Temperature shift factor,  $a_T = \eta(T)/\eta(T_{ref})$

According to Arrhenius equation, the shift factor  $a_T = \exp\left[\frac{E_a}{R_g}\left(\frac{1}{T} - \frac{1}{T_{ref}}\right)\right]$

**(iii) FOG Tests**

As a preliminary verification of the printability of the ink, FOG test (Fineness of grains) was conducted on the prepared nano BT inks. This consisted of a fine polished stainless steel bar with a central groove of varying depth marked (25-0  $\mu\text{m}$ ) and a smooth moving blade. The small scoop of ink was spread across on one end of the bar (>25  $\mu\text{m}$ ) and scrapped across the bar. Any hard agglomerates or lumps

retaining in the ink leave a continuous steak of its respective size and discontinuous lines represents the entrapped air bubbles.

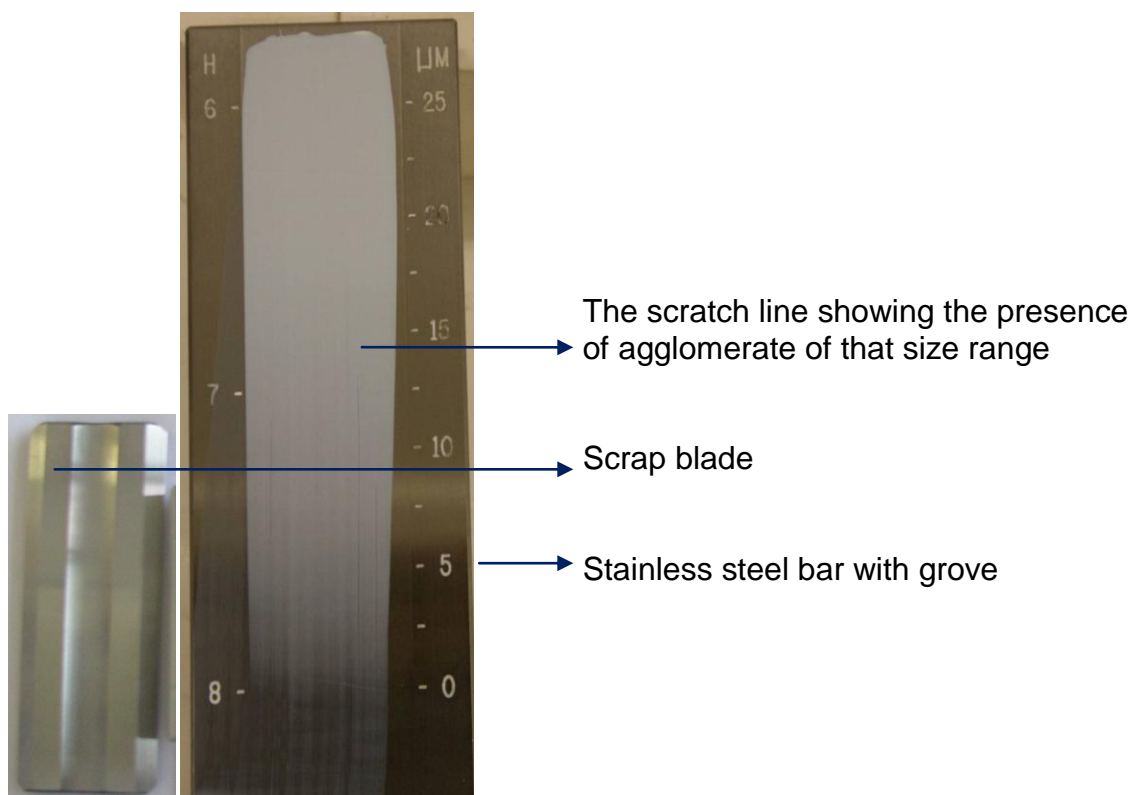


**Figure 3.9: FOG testing kit used for the present work**

#### **(iv) Screen printing of the nano ink**

The nano BT inks prepared using the optimized condition with desirable rheological properties were screen printed using SM Tech Benchmark (Speedline Technologies, Franklin, USA) screen printing machine for the initial trials. The ink was poured on both the sides of the mesh made of steel (#325) and the squeegee was mounted at 45 ° angle. Initial print gap was set to 0.5 mm and then subsequently increased based on the print thickness using 6 Kg squeegee pressure at the constant speed of 25 mm/s.

Large batches of the optimised nano BT ink were tested for processing in commercial production environment at Syfer Technology Ltd. To save the cost, for initial ceramic sintering condition optimization only blank MLCCs (i.e., multilayered

ceramic layers without any electrodes) were printed. The multilayers were cut to the required dimensions up to the substrate surface using diamond wafer of 0.5  $\mu\text{m}$  thickness and debris was removed by water jet. After storing the print at  $-15^{\circ}\text{C}$ , the samples were removed by applying ultrasound at back surface of the substrate. Each ceramic layer consisted of 3 prints with  $90^{\circ}$  rotation for uniformity and then a metal layer was printed.

For initial sintering condition optimization, the ceramic multilayers were screen printed without any electrodes and are referred as chip. The multilayered ceramic capacitor device, screen printed using nano BT ink with optimised amount of dopants and 14 layers of 30:70-Ag:Pd alloy ink (50% Metal and 5%  $\text{BaTiO}_3$ ) was referred as nano MLCCs. The screen printed chip and MLCCs were carried at Syfer Technology Ltd., The thickness of the ceramic layers were 10  $\mu\text{m}$ .

For the initial dopant and glass frit optimization, the nano BT ink was prepared and oven dried at  $120^{\circ}\text{C}$ . This oven dried powders were further ground and compacted at 250 MPa, which is referred as ink derived compact.

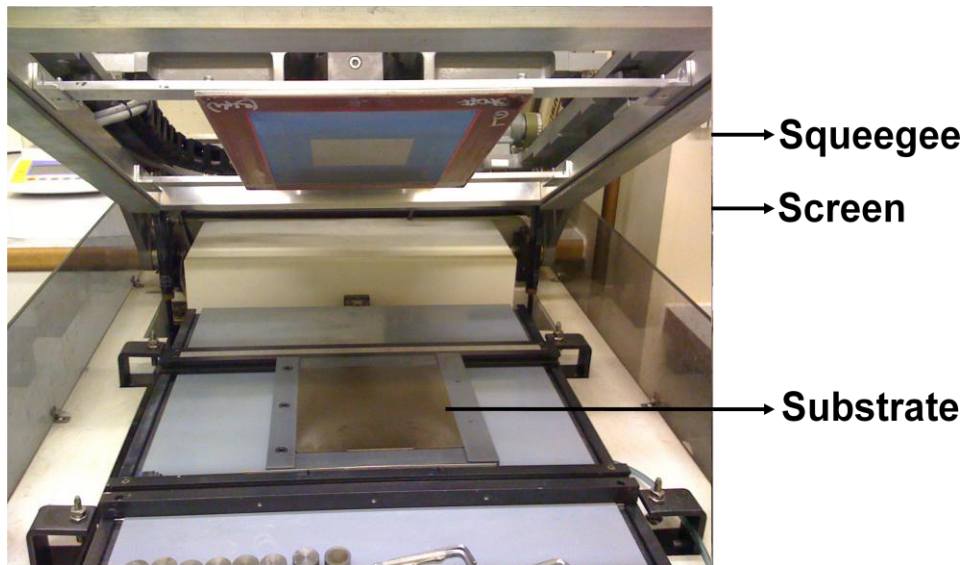


**Figure 3.10: Screen printing facility at Loughborough University**

### **3.3.3. Characterization of the green bodies**

#### **(i) Density measurements**

The green density was determined from the weight (Balance: CP2244, Sartorius, U.K) and dimensions of the sample (measured to  $\pm 0.001$  g and  $\pm 0.01$  mm accuracy). Percentage theoretical density was calculated by taking 6.01 g/cc as T.D for nano BT, wherever appropriate.

#### **(ii) Optical microscopy**

The print surface was analysed using an optical microscope (Reichert Jung MeF3, Wein, Austria). The mesh marks, agglomerates and the layer intactness were analysed using 20 – 50 X magnification.

#### **(iii) Field Emission Gun -Scanning Electron Microscopy**

Field Emission Gun Scanning Electron Microscope (FEGSEM) (Leo 1530VP FEGSEM, LEO Elektronenmikroskopie GmbH, Oberkochen, Germany) was used for further analysis of the green samples at higher magnification. The fractured surface of the green samples was used to verify the presence/absence of agglomerates. The samples were glued on conducting carbon tape and mounted on an aluminium stub; gold coated by sputtering making the sample conductive, also helping to avoid charging of the particles before analysis under the electron gun. The images were recorded using in lens detector with 30  $\mu$ m aperture size at a working distance of 5 mm using 5 kV accelerated electron voltage. In addition, FEGSEM consisted of an Energy-dispersive spectroscopy (EDX) facility that was used for chemical composition and elemental analysis in spot, line, and mapping modes.

### **3.4. Sintering of the green bodies to make components**

Three different types of furnaces conventional, microwave, and hybrid were used for the sintering of the nano BT samples (1050-1250°C for 1-8 h soaking).

The conventional box type furnace (Carbolite Ltd., U.K) consisting of SiC heating elements with a Eurotherm 902 temperature controller (Eurotherm Ltd., U.K) and a K-type thermocouple. The microwave and hybrid furnace described earlier and used for BT synthesis were used for sintering also.

### 3.4.1. Dilatometer studies

A specially designed dilatometer with minimum microwave field interference in the hybrid furnace was used to measure the onset of sintering and shrinkage kinetics with different microwave power levels during the sintering. Figure 3.8 shows the dilatometer in the hybrid furnace and schematic diagram of the instrument.

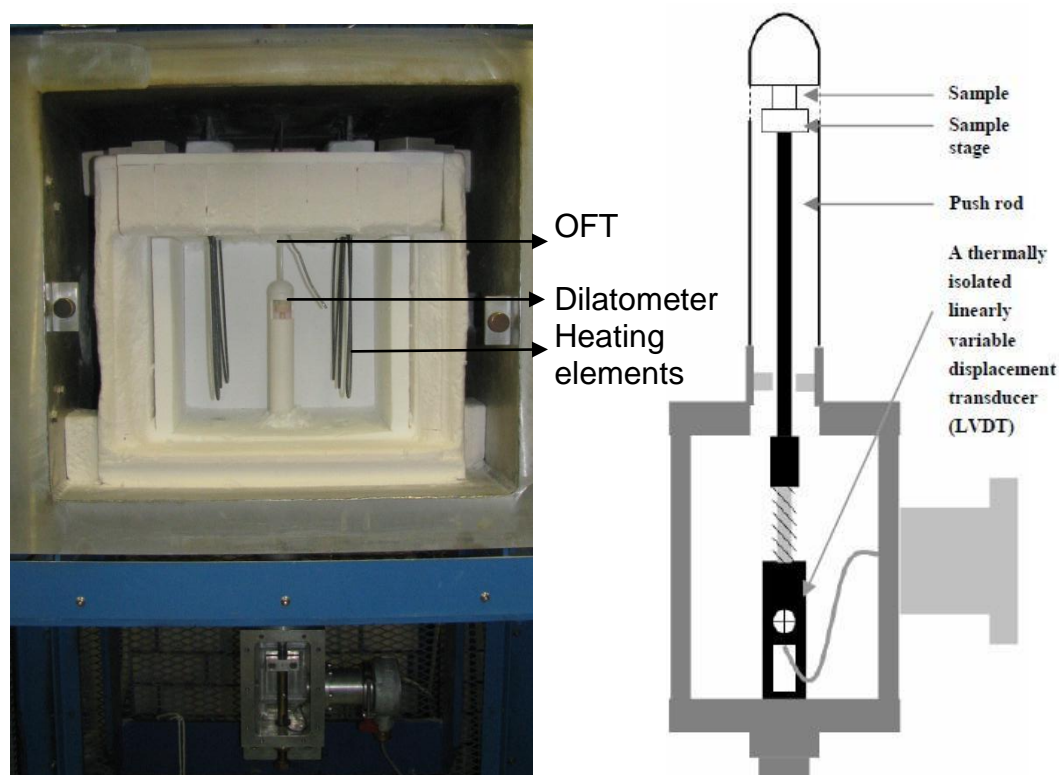


**Figure 3.11: The dilatometer in the hybrid furnace and schematic diagram of the dilatometer.**

The dilatometer consisted of a long alumina closed end tube with a slot opening for sample mounting, an inner alumina push rod to hold the sample and a flat sample stage. The outer alumina tube was glued on an aluminium-resting base, which was screwed to the bottom rod in the furnace for stability. The central push rod was

connected to a spring, which in turn was connected to a sensing device calibrated to  $\pm 2.5$  mm for  $\pm 3500$  readings on the sensing device.

Distance moved in mm = Readings on the sensing device \* 1/1400

Positive data indicates thermal expansion and negative results indicate the shrinkage of the material

To minimise the error involved due to thermal expansion of the dilatometer system, quartz disc of 5 mm thickness was used for calibration, as it has zero or negligible thermal expansion coefficient. The samples results were normalised using the calibrated data. The following equation shows the conversion from dilatometer readings to linear shrinkage:

$$L = \frac{t}{\frac{1}{1400} \times (D - D_0 - D_c) + t} \times 100 \quad \text{Equation 3.9}$$

where L is the linear shrinkage, %; t is the initial thickness of the pellets, mm; D is the dilatometer reading;  $D_0$  is the initial reading of dilatometer;  $D_c$  is the calibration data.

### 3.4.2. Characterization of the sintered bodies

#### (i) Density measurements:

The apparent density of the sintered samples was measured using geometric measurements. The bulk density was measured using Archimedes principle with distilled water as the displacing medium utilizing the proper density correction for the temperature of the medium.

$$\text{Density of sample, } \rho = \frac{M_s \cdot \rho_l}{M_s - M_l} \quad \text{Equation 3.10}$$

Where,  $M_s$ , mass of sample in air,  $M_l$ , mass of sample in water, and  $\rho_l$  is the density of the liquid at measuring temperature. The error involved in density measurements was  $\pm 0.01$  g/cc. Three different measurements were taken for each sample. The

difference between bulk and geometric densities were not noticed. So the geometric densities were mentioned throughout the report.

**(ii) Microstructure and Grain size measurements:**

Similar to the green sample, FEGSEM with EDX was used to analyse the microstructure and elemental analysis of the sintered sample. The unpolished as sintered sample surface was used for grain size analysis. Linear intercept method was used to estimate the grain size of the sample. A line was drawn across the micrograph covering most of the grains. The average grain size was calculated as the number of grains intercepted by the line divided by the line length, based on the mendelson equation.

$$D = \frac{L \times A1}{M \times N} \quad \text{Equation 3.11}$$

Where, D is the mean grain diameter, L is the length of the line, A1- shape correction factor (1.5), M is the magnification (dimensionless) and N is the number of intercepts.

**(iii) Electrical property measurements**

The electrical properties measurements, which were highly significant to this project, were performed at Syfer Technology Limited, Norwich, UK.

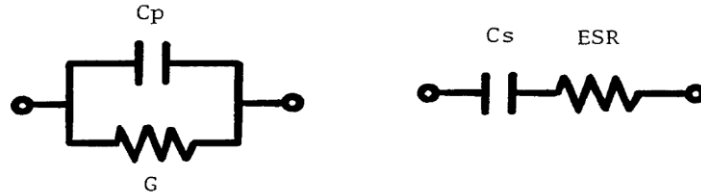
The capacitance was measured using capacitance/LCR meter (HP4278A /U.K) at 1 kHz, 1 V. It had the capability to measure parallel capacitance, Cp or series capacitance, Cs and dissipation factor D, Quality factor Q, Conductance G in parallel with Cp and equivalent series resistance Rs (ESR) in series with Cs. D and Q would be the same in both parallel and series model. Figure 3.12 shows the equivalent circuit for measuring capacitance in parallel and series. The relationships among the parameters are,

$$Cs = (D^2 + 1) Cp \quad \text{Equation 3.12}$$

$$1/ESR = ((1/D^2) + 1) G \quad \text{Equation 3.13}$$

For ideal capacitors,  $D=0$ ,  $C_p=C_s$  and If  $D>1$ ,  $C_s>C_p$

A constant test signal voltage from 0.1 to 1 V was applied in 0.1 V steps using 1 kHz sine signal, output impedance was measured and calculated accordingly.



$$Y = G + j\omega C_p$$

$$D = G/(\omega C_p)$$

$$Q = 1/D$$

$$Z = ESR + j(1/(\omega C_s))$$

$$D = ESR\omega C_s$$

$$Q = 1/D$$

$$YZ = 1$$

**Figure 3.12: Equivalent circuit diagram for parallel and series capacitance measurements**

Insulation resistance (IR) measurement was measured using Megohmmeter IM6 at 100V. Temperature characteristics of the capacitance between  $-55^{\circ}\text{C}$  to  $125^{\circ}\text{C}$  were measured using S&A Inc. 4220 test chamber, and HP4278A LCR meter. Capacitance at RT ( $25^{\circ}\text{C}$ ) was taken as reference value.

$$\% \text{ capacitance change} = (C_T - C_{\text{ref}}) / C_{\text{ref}}$$

The electrical properties were used as a pointer for further optimization of capacitor compositions, formulations.

All the results obtained are discussed in the following chapter.



## Chapter 4

### 4. RESULTS AND DISCUSSION

#### 4.1. BT nanopowder synthesis

##### 4.1.1. Characterization of the starting precursor

The starting BT precursors produced using different barium sources (barium carbonate, acetate and hydroxide) through citrate polymeric precursor method were characterized using differential thermal analysis and high frequency dielectric measurements.

##### (i) Thermal analysis of the precursor

The thermo gravimetric / differential thermal analysis (TGA/DTA) curves of the precursors heated from room temperature to 900°C at 10°C/min heating rate in static air atmosphere are given in Figure 4.1. The (Ba, Ti) precursor undergoes thermal decomposition through a multi step exothermic reaction process, which is completed at 650°C and above which there was no further weight loss. The BaCO<sub>3</sub> and BaOH sources show similar weight loss of ~40%, with an exothermic peak at 440-460°C corresponding to the formation of the intermediate phase from the precursor. The barium acetate source shows a weight loss of ~15%, the intermediate phase forms at lower temperature ~385°C compared to the barium carbonate and hydroxide sources. All the precursors show a second exothermic peak at 580°C referring to the formation of BT and a very small endothermic peak at 660°C confirming the phase transformation of BT from cubic to tetragonal. The enthalpies of formation for BT were calculated as explained earlier in section 3.2.4 and are given in Table 4.1

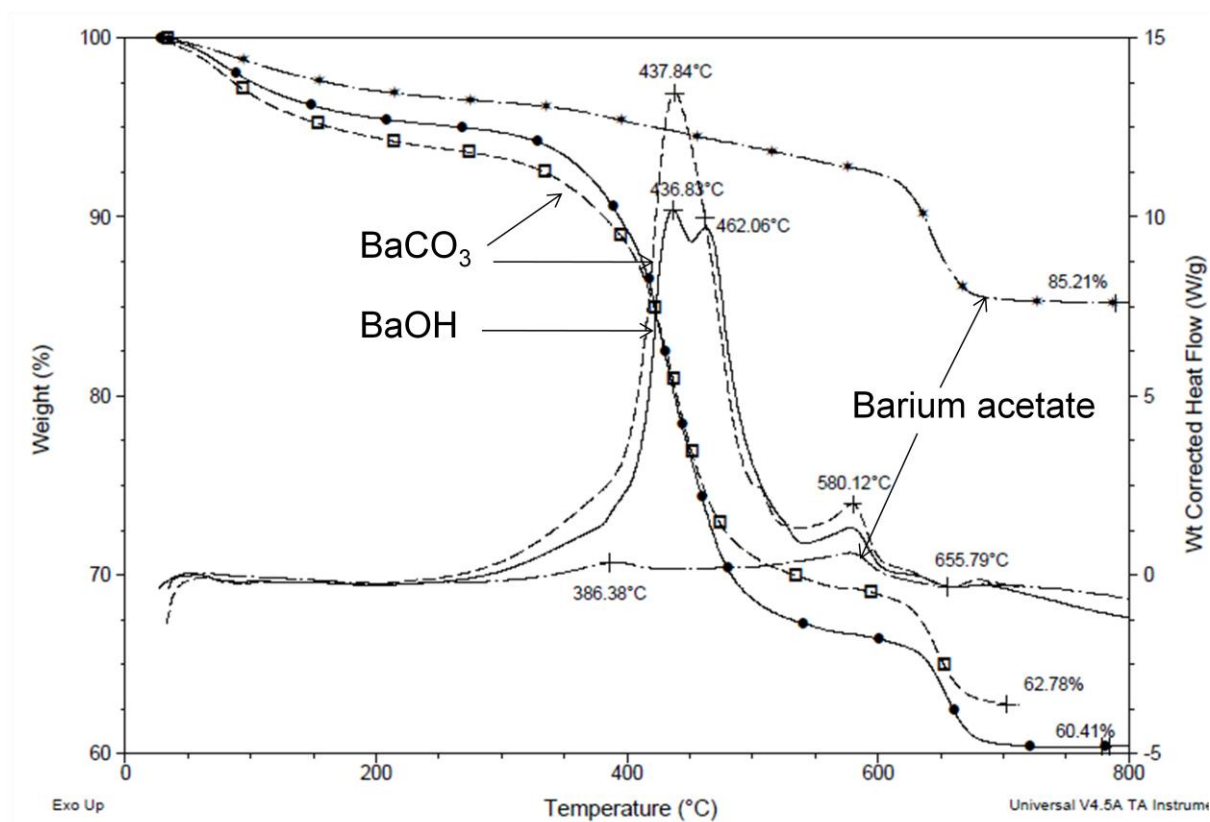


Figure 4.1: Thermal analysis of BT precursor

Table 4.1: Thermal analysis results of the precursors using different barium sources

Barium Source	% Total weight loss	Total BT formation $\Delta H_f$	Intermediate phase formation		BaTiO <sub>3</sub> formation		Tetragonal phase conversion	
			T	$\Delta H_f$	T	$\Delta H_f$	T	$\Delta H_f$
Barium carbonate	40%	113 ± 5	437	83 ± 5	580	25 ± 3	655	5 ± 2
Barium hydroxide	40%	115 ± 5	438	81 ± 5	580	30 ± 3	655	4 ± 2
Barium acetate	15%	102 ± 10	386	20 ± 10	580	73 ± 5	655	9 ± 2

Note:  $\Delta H$  in  $\text{J/mol}^{-1}$  and T in  $^{\circ}\text{C}$

The precursors prepared using barium acetate requires lower temperature to form the intermediate phases that are very stable<sup>214</sup>. This requires more energy to form tetragonal BaTiO<sub>3</sub> (t-BT) phase. However the precursors produced using barium

carbonate and hydroxide require higher temperature for the formation of intermediate phases. It is interesting to note that the final t-BT formation temperature ( $\sim 660^\circ\text{C}$ ) and the total enthalpy of formation ( $\sim 115 \pm 5 \text{ Jmol}^{-1}$ ) remain the same for all the starting precursors. Therefore, for further synthesis experiments, the  $\text{BaCO}_3$  based precursors were used and calcined between 550 to  $900^\circ\text{C}$  for 5 hrs in conventional heating and 30 to 60 min in microwave heating.

## (ii) Dielectric properties of the BT precursors

The dielectric loss and loss tangent of all the starting precursors ( $\epsilon'' = 0.05$ ;  $\tan\delta = 0.02$ ) show that the precursors have reasonably high values of dielectric loss and loss tangent (comparative  $\tan\delta$  value for microwave transparent quartz is: 0.0001 and  $\epsilon'' = 0.0004$ )<sup>215</sup>. Hence, all the BT precursors have similar microwave absorbing behaviour.

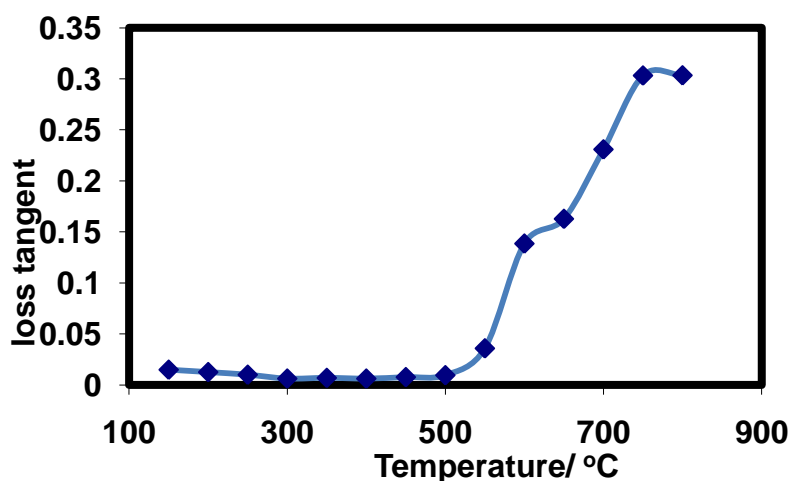


**Figure 4.2: Loss tangent Vs Temperature for BT precursor produced using barium carbonate source at 2.45 GHz using cavity perturbation method**

Figure 4.2 shows the dielectric property variation with temperature for BT precursor produced using barium carbonate. There is not much change in die loss tangent with temperature up to  $500^\circ\text{C}$ . As discussed in the previous sub section, t-BT forms at  $\geq 660^\circ\text{C}$  and hence it is evident that the tetragonal BT phase has better dielectric properties and is a better microwave absorbing material. Hence with increasing

temperature  $>660^{\circ}\text{C}$ , more tetragonal phase nucleates and the obtained product is found to be more microwave active.

*The loss tangent of the BT precursor increases with temperature due to the tetragonal BT (t-BT) formation. Both the BT precursor & the product phase formed are found to be microwave-absorbing.*

#### 4.1.2. Characterization of the calcined powders

The BT precursors produced using barium carbonate source were calcined at  $600\text{-}900^{\circ}\text{C}$  for 1-5 hrs in conventional heating and  $550\text{-}700^{\circ}\text{C}$  for 30-60 min in microwave heating and were characterized for phase formation (XRD, Raman spectra) and particle size (TEM, BET and Mastersizer). The results are discussed in this section.

##### (i) Phase analysis

The XRD results of the precursor powders calcined in conventional and microwave heating are shown in Figures 4.3 and 4.4 respectively. The precursor was found to be amorphous. At low temperatures,  $\text{BaTiO}_3$  occurs with some unreacted secondary phases like  $\text{BaCO}_3$  and  $\text{TiO}_2$ . Complete transformation of tetragonal  $\text{BaTiO}_3$  forms at  $900^{\circ}\text{C}$  for 5 hrs in conventional heating. Though similar trend is observed in microwave heating, single-phase tetragonal  $\text{BaTiO}_3$  (t-BT) was found to form at  $700^{\circ}\text{C}/30$  min itself in this case, Figure 4.4. The maximum peak of cubic phase should be at  $31.530^{\circ}(2\theta)$  (JCPDS 89-2475) and for tetragonal phase it should be at  $31.505^{\circ}(2\theta)$  and  $31.602^{\circ}(2\theta)$  (JCPDS 081-2196). Therefore, it's quite difficult to exactly ensure the phases formed. The width of the peak from (200) and (002) at about  $45^{\circ}(2\theta)$  can be used to resolve this to some extent, inset in Figures 4.3 and 4.4.

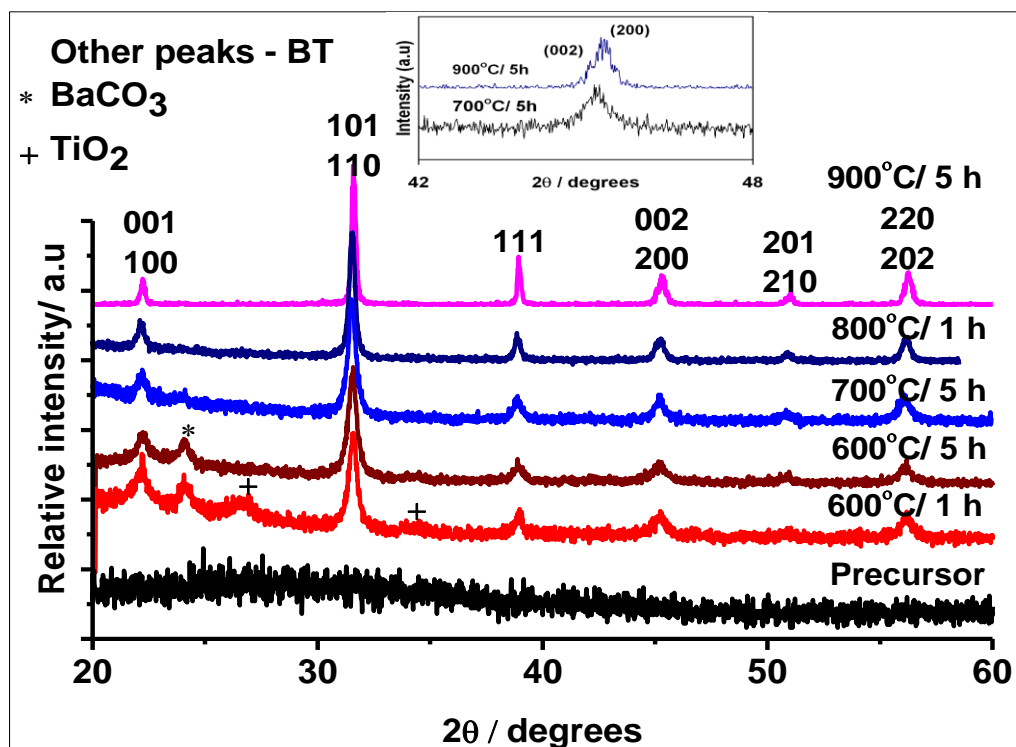


Figure 4.3: The room temperature X-Ray diffraction patterns of the precursor calcined in Conventional heating

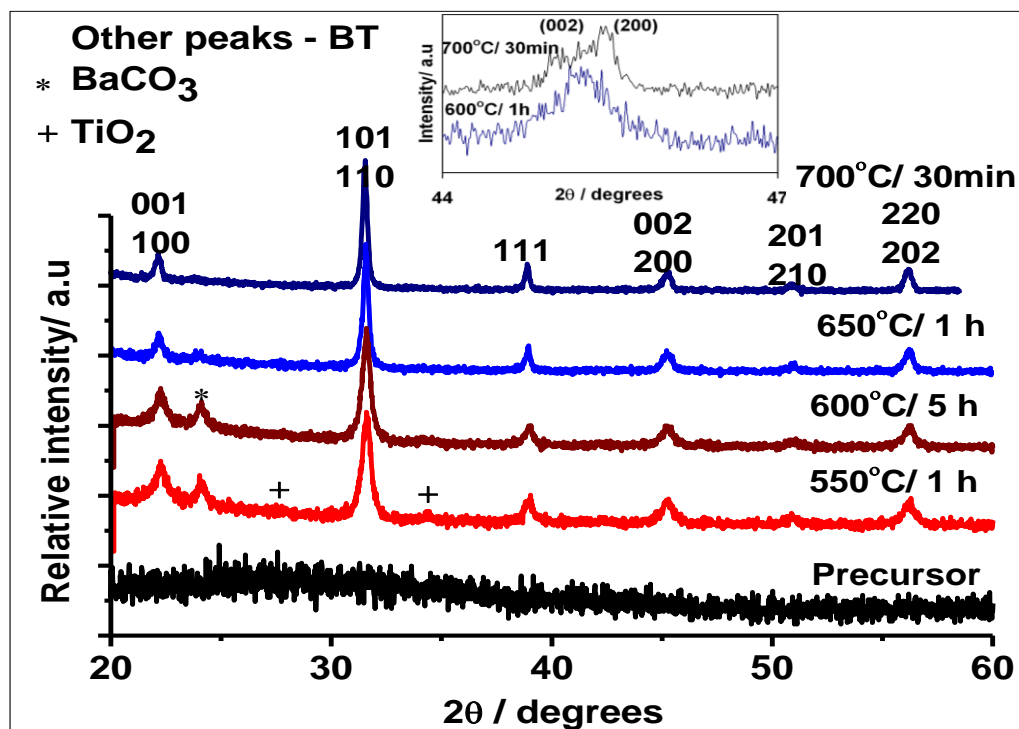


Figure 4.4: The room temperature X-Ray diffraction patterns of the precursor calcined in microwave heating

However, presence of the tetragonal phase is not possible to ascertain completely due to the line broadening of the XRD peaks, due to the combined effects of time crystallite size, non-uniform strain, and instrumental broadening. As the cubic and tetragonal phase peaks are very near, two distinct peaks for tetragonal phases are not always visible. Therefore, to verify the phase formation with different calcination conditions, Raman spectroscopy is used. Raman spectroscopy in general has a better resolution for tetragonal phase identification than X-Ray powder diffraction and is also sensitive to the bond length and angle between the anion and cation, i.e., the local symmetry. Figures 4.5 and 4.6 show the Raman spectra of the powders calcined at different conditions in conventional and microwave heating respectively.

Raman active phonons of the tetragonal  $P4mm$  crystal symmetry are represented by  $3A_1+B_1+4E^{216}$ . Long-range electrostatic forces induce the splitting of transverse and longitudinal phonons, which results in split Raman active phonons represented by  $3[A_1(TO) + A_1(LO)] + B_1 + 4[E(TO) + E(LO)]$ . LO represents longitudinal mode and TO represents transverse mode. It also includes normal mode of Ti atoms. It is well known that the  $BaTiO_3$  tetragonal phase reveals Raman scattering bands at around 250, 520 and 720  $cm^{-1}$  and a sharp peak at around 306  $cm^{-1}$ <sup>216</sup>. On the other hand, all phonons of the cubic  $Pm3m$  symmetry are represented by  $3F_1u + F_2u$ , which include no Raman active normal modes. Although the cubic phase theoretically does not reveal any Raman active modes, this polymorph generally shows broad bands at around 250 and 520  $cm^{-1}$ , which may be caused by local disorder associated with the position of Ti atoms. The characteristic tetragonal peaks at 306 and 720  $cm^{-1}$  starts appearing from 700°C/ 5 h in conventional heating and the intensity of the peaks increases with increasing calcination temperature. The small peak at 640  $cm^{-1}$  in the Raman spectra of the sample calcined at 700°C/ 5 h in conventional heating represents the high temperature hexagonal phase but such phase formation was not observed in microwave-calcined powders, Figure 4.6, for any of the conditions. This disappears with increasing the calcination temperature. The sharper peak noticed at 1064  $cm^{-1}$  represents  $CO_3^{2-}$  asymmetric stretching mode corresponding to the carbonate species.

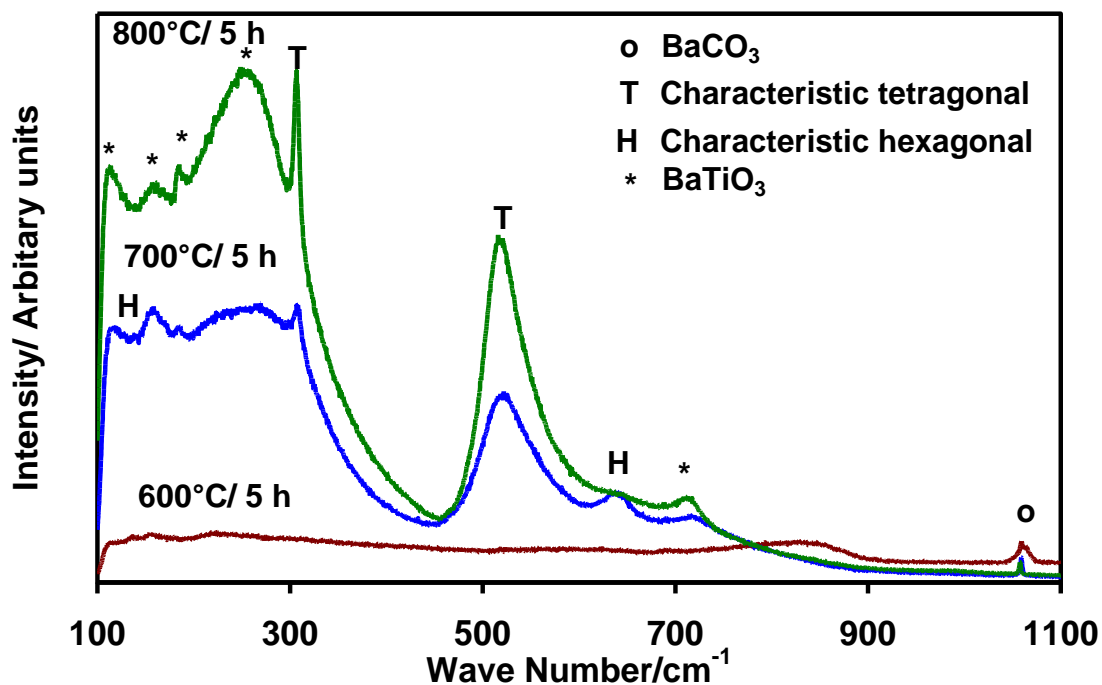


Figure 4.5: The room temperature Raman spectra of the precursor calcined between 600 and 900°C for 5 hrs in conventional heating

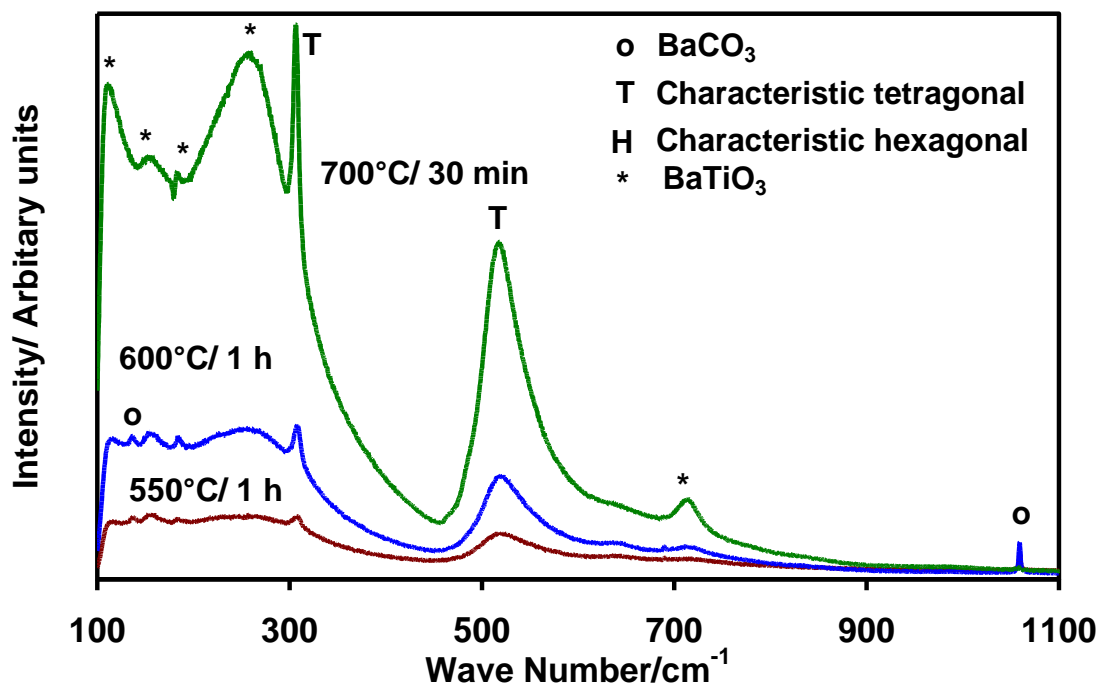
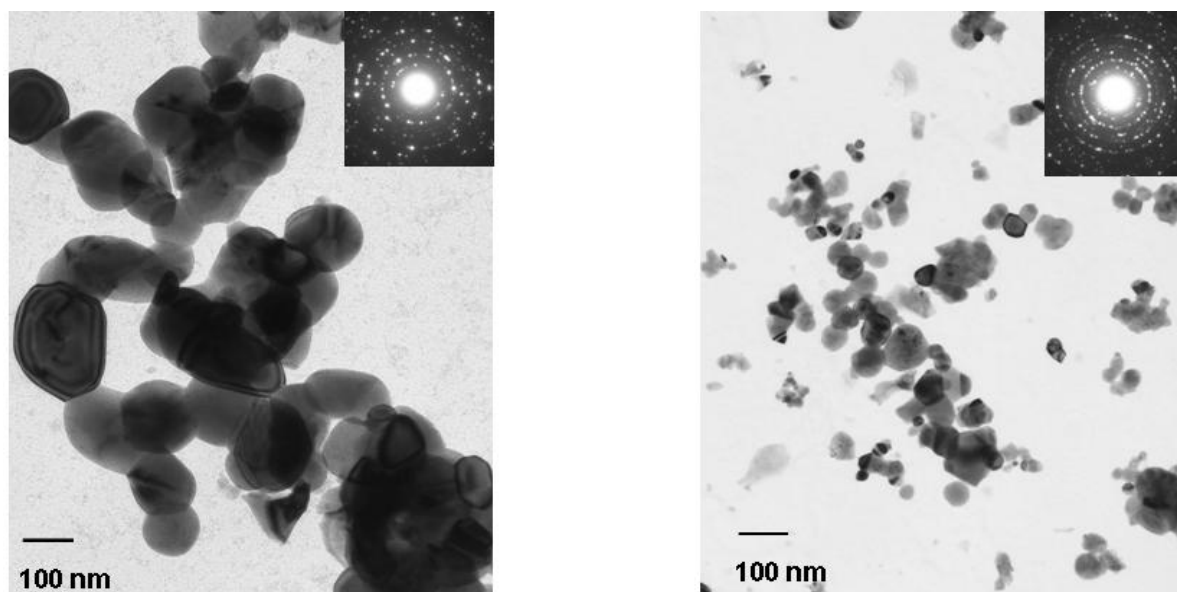


Figure 4.6: The room temperature Raman spectra of the precursor calcined between 550 and 700°C for 1 h in microwave heating

All the powders calcined by microwave heating exhibit distinct bands at 250, 306, 520 and 720  $\text{cm}^{-1}$ . In microwave heating the tetragonal phases start nucleating from 550°C itself. In addition, there is no hexagonal phase coexistence noticed. The powder at 700°C/ 30 min shows well crystalline tetragonal  $\text{BaTiO}_3$  without any traces of carbonate. Also the characteristic dip at 180  $\text{cm}^{-1}$  confirms the long-range symmetry in the powder<sup>29,216</sup>.

*Thus, the single-phase tetragonal  $\text{BaTiO}_3$  forms at 700 °C/ 30 min itself when using microwave heating where as it requires 900 °C /5 hr in conventional heating.*

## (ii) Particle size analysis



**Figure 4.7: The TEM microstructure and SAED pattern of the powders calcined at (a) 900°C /5 h in conventional heating and (b) 700°C/ 30 min in microwave heating**

Figure 4.7 shows the TEM microstructure and SAED pattern of the BT powders calcined at 900°C /5 hr in conventional and 700°C/ 30 min in microwave heating respectively. The BT powders calcined using microwave heating shows more uniform and finer primary particle size of 20 nm and the SAED pattern confirms that



the powders are crystalline. The BT powders calcined using conventional heating shows a broad particle size distribution of about 50-100 nm probably because of the high calcination temperatures used. Microwave methods leads to bulk nucleation in the material<sup>4</sup> and provide less time for particle growth to occur due to the shorter processing times employed. From the particle size analysis results, Figure 4.8, it is clearly seen that the BT nanopowders synthesized using microwave heating has less agglomeration compared to the conventionally produced nanopowders.

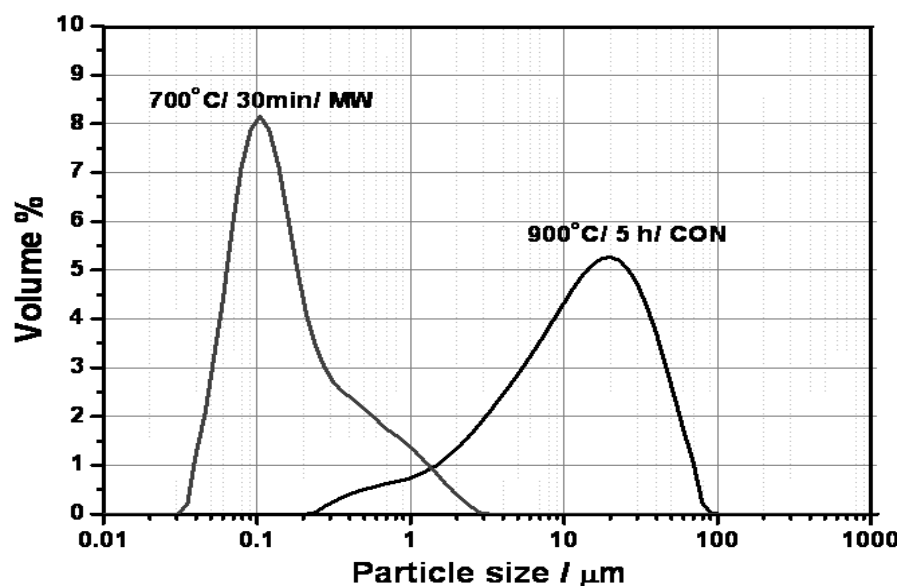


Figure 4.8: Particle size distribution of the BT powders synthesized using conventional (900°C/ 5 h) and microwave heating (700°C/ 30 min)

*Microwave heating results in fine, uniform nanocrystalline powders, with less agglomeration*

#### 4.1.3. Effect of microwaves on hexagonal phase suppression

The small peak at  $640\text{ cm}^{-1}$  in the Raman spectra of the sample calcined at 700°C/ 5 h in conventional heating indicated existence of a high temperature hexagonal phase but such phase formation is not observed in microwave-calcined powders in any experimental conditions, refer Figures 4.4 and 4.5. The reason could be that the

particles may have planar defects in the stacking sequence similar to hexagonal phase of BT, generating similar peaks. The present synthesis route involves thermal decomposition of the organic substances, which induce localized reducing conditions, resulting in the generation of metal ions with a lower oxidation state<sup>216</sup>. It leads to the question of “Why such a lower oxidation state of the ion /defect /hexagonal phase does not occur for microwave heat treated powders?” The possible reasons could be that the defects are generally found to be introduced during the particle growth. The microwave heating probably enhances bulk phase nucleation and provides less time for the particle growth whereas the conventional heating method leads the provision of significant time for particle growth to occur, as seen from TEM results.

#### **4.1.4. Effect of microwaves on nano t-BT phase evolution**

To understand the genuine microwave effects during nano t-BT synthesis a methodical set of experiments were conducted using a hybrid furnace under identical thermal histories. Using identical time-temperature profiles (700°C/ 30 min), the input energy was altered by varying the microwave power between 200-1000 W in the step of 200 W. Initial soak at 500°C/ 15 min helps to achieve the thermal uniformity in all the samples. The conventional power controller maintains the constant temperature during the isothermal holding. The microwave energy supplied provides additional heat and accordingly the conventional power input was reduced to maintain the temperature. Figure 4.9 shows the conventional power input throughout the heating cycle at different microwave power.

As expected the conventional power input slightly reduces for up to 400 W microwave power and above 400 W microwave power, there is significant conventional input power reduction. During the isothermal hold at 700°C, about 50% conventional input power is reduced when 1000 W microwave power was used.

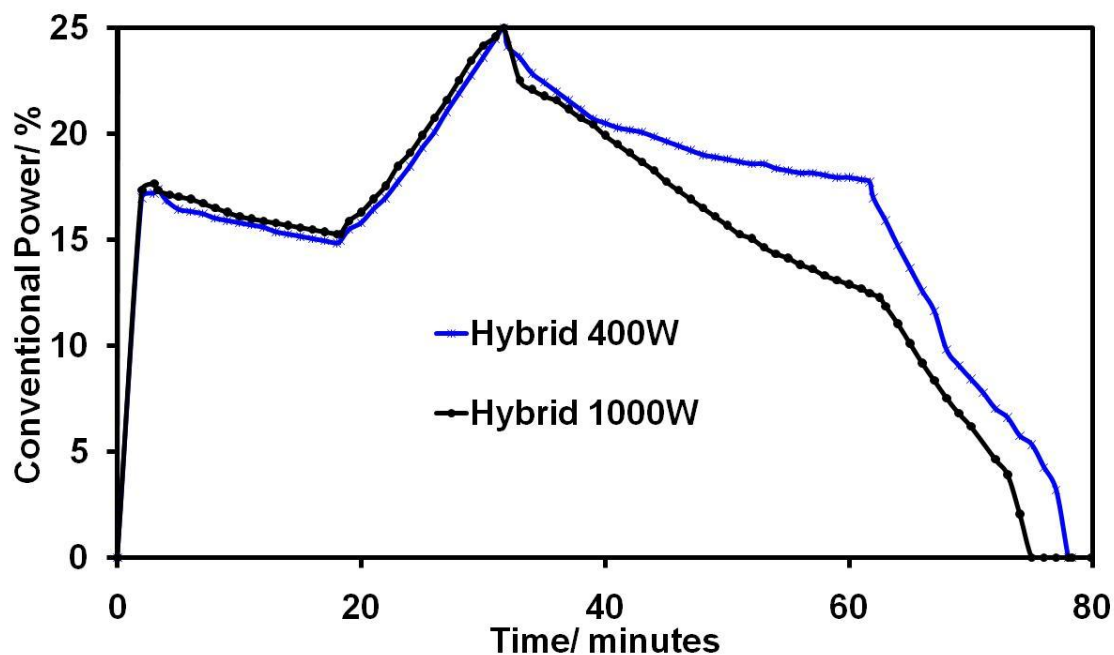


Figure 4.9: Representative Conventional power Vs Time Profiles during hybrid heating with different microwave power levels used.

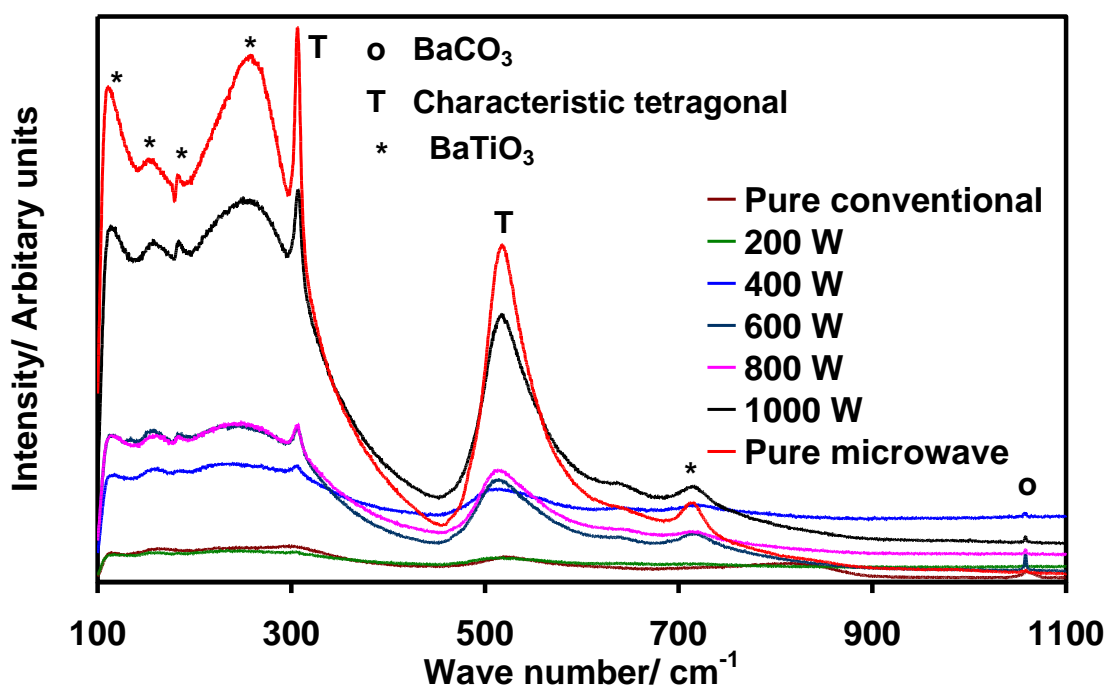
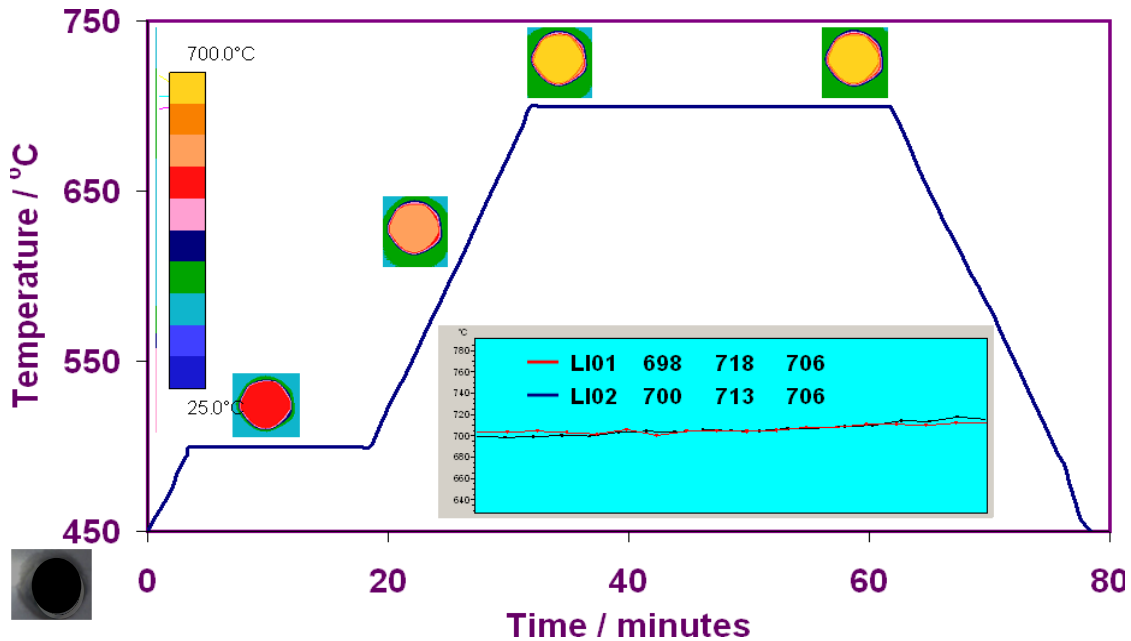


Figure 4.10: The room temperature Raman spectra of the precursor calcined at 700°C /30 min in hybrid heating with different microwave power levels.

Raman spectra of the powders are taken to verify the local symmetry and atomic bonding configurations in nano BT powders. Figure 4.10 shows the Raman spectra of the nano powders calcined at different microwave power levels. Raman spectra provided better understanding on the phase formation of BaTiO<sub>3</sub>. The pure conventional 700°C/30 min sample showed no characteristic tetragonal peaks at 306 and 720 cm<sup>-1</sup> but these peaks appeared for all samples with microwave power input. This is clear evidence that the tetragonal phase start nucleating at 700°C/ 30 min with just 200 W microwave power. In addition, no hexagonal phase coexistence noticed for any of the samples. The tetragonality was found to increase with the increasing of microwave power. The dip at 180 cm<sup>-1</sup> also confirmed the long-range symmetry in the nano BT powder. Table 4.2 shows the consolidated results for the conventional and microwave synthesized nano BT powders.

**Table 4.2: Phase evolution during nano BT synthesis under conventional, microwave and hybrid heating conditions**

	<b>Pure conventional</b>	<b>Hybrid heating</b>	<b>Pure microwave</b>
<b>Hexagonal phase coexistence</b>	700°C/ 5 h	≥200 W at 700°C, 30 min	
<b>Tetragonal phase nucleation</b>	800°C/ 5 h	>200 W at 700°C, 30 min	550°C, 1 h with maximum 900 W
<b>Single phase tetragonal formation</b>	900°C/ 5 h	1300 W at 700°C, 30 min	700°C, 30 min with maximum 1300 W



**Figure 4.11: Temperature distribution across the sample during nano BT synthesis under identical thermal history using hybrid furnace**

It is interesting to note that the tetragonal phase nucleation can be advanced/accelerated by the use of  $\geq 200$  W microwave power under identical time/temperature conditions. Single phase tetragonal BT nanopowders are synthesised using 1300 W of microwave power at 700°C/ 30 min itself compared to the 900°C/ 5 h in conventional radiant heating. In spite of retaining nanoparticle size, there is no hexagonal coexistence noticed at  $\geq 200$  W of microwave power. Figure 4.11 shows the thermal image showing the temperature distribution across the samples and it is quite uniform at various stages of the calcinations suggesting that the enhancement in t-BT phase nucleation seen in hybrid heating is not mainly due to temperature gradients developed. Thus, there is a clear evidence that microwave induced effect noticed is genuine.

*Under identical thermal history, microwaves were found to enhance tetragonal phase formation in BT powders. Thus microwave power is identified as a new tool to alter/control phase evolution during nano t-BT synthesis under isothermal, isobaric conditions*

Comparing the time-temperature profile of the optimized condition for single-phase tetragonal BaTiO<sub>3</sub> synthesis in conventional and microwave heating, Figure 4.12, it is evident that the microwave synthesis requires 1/10th energy of conventional cycle. However, it is difficult to directly compare the conventional and microwave heating cycles as both are operated at different power ratings and conditions.

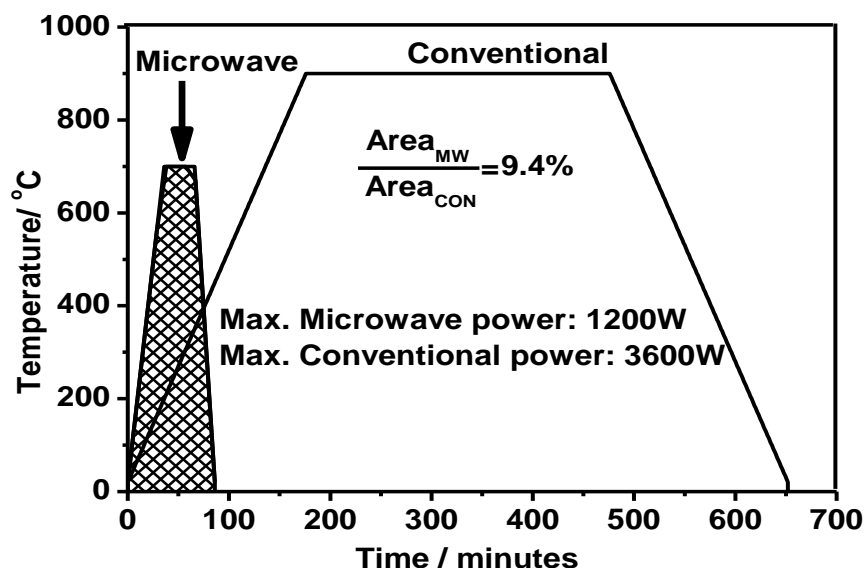


**Figure 4.12: Optimised Time-Temperature profiles for conventional and microwave heating experiments**

#### 4.1.5. Possible mechanism of microwave heating during nano BT synthesis

To further understand the mechanism of the tetragonal phase nucleation and formation at a much lower temperature and time, the BT precursors were calcined at three different temperatures of 600, 700 and 800°C for different durations (5-200 min) at different microwave power levels (0-1000 W) using the hybrid furnace. The % tetragonality of the calcined BT powders were calculated using Raman spectra peak area analysis as explained in Appendix-1.

Most of the chemical reactions are diffusion controlled and the diffusion/reaction rate depends on the processing temperature. Hence, the first step is to calculate the reaction or diffusion rate constant of t-BT formation at a particular temperature with different microwave power levels. The slope of the percentage t-BT formation versus

reaction time plot for powders calcined using different microwave power levels provide gives the reaction/diffusion rate constant, Figure 4.13. The percentage t-BT formation using a pure microwave heating is also given for comparison.

The variation of the percentage t-BT formed as a function of temperature at different levels of microwave power (Figure 4.14) showed very clearly, the t-BT phase conversion is enhanced drastically using microwave power especially at lower temperatures. To observe similar difference in the t-BT formation seen with microwave power variation, it requires more than 150°C temperature measurements, which can be clearly noticeable, suggesting again that the enhancement in reaction kinetics observed here cannot be ascribed to temperature gradient only.

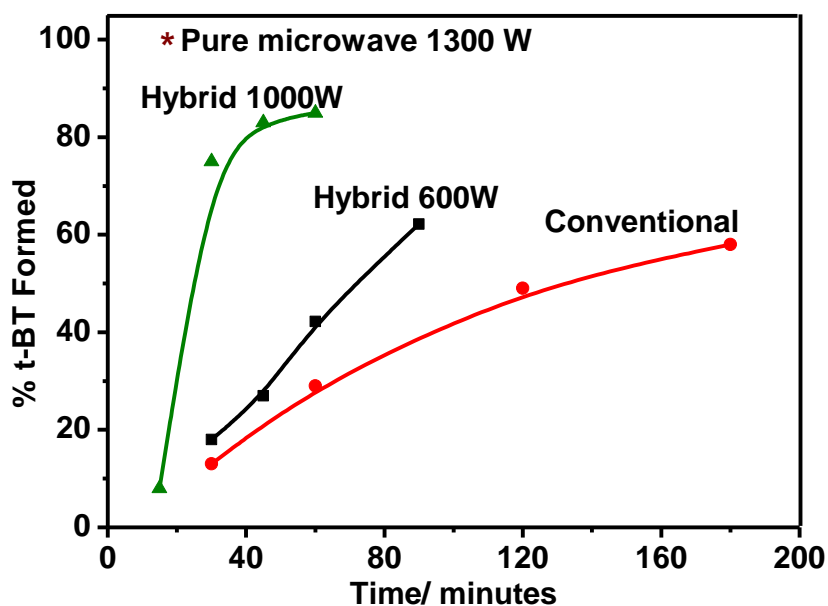
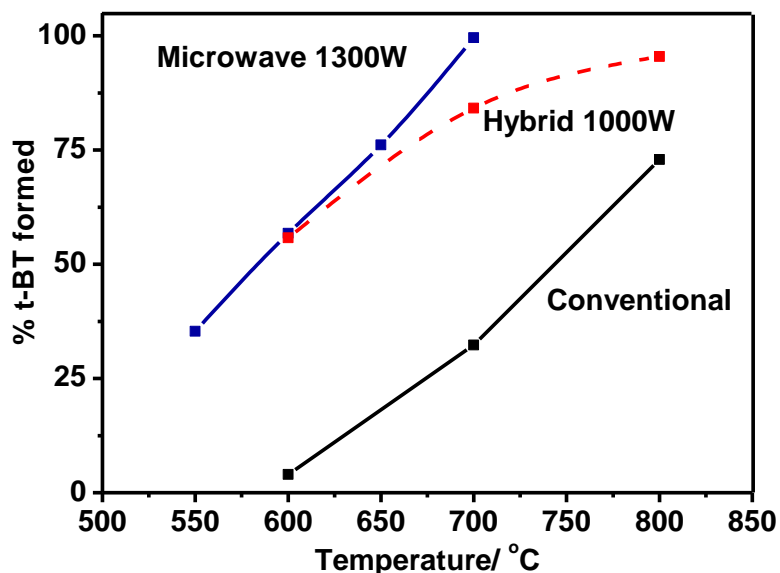


Figure 4.13: Percentage tetragonal BT (t-BT) formation with soaking time in conventional, microwave and hybrid heating for same temperature at 700°C



**Figure 4.14: Percentage tetragonal BT (t- BT) formation with temperature in conventional, microwave and hybrid heating at a constant soaking time, 30 min**

All the data satisfy the classic parabolic model indicating that the diffusion of  $Ba^{2+}$  and  $Ti^{4+}$  ions during the reaction/ formation of t-BT is the rate-controlling step and are list given by,

$$\text{Degree of reaction} = (\% \text{ tetragonal}) = (t_{\text{react}})^{1/2} \quad \text{Equation 4.1}$$

Considering the Arrhenius equation as the description of the reaction kinetics,

$$k = A \exp\left(\frac{-Q}{RT}\right) \quad \text{Equation 4.2}$$

Where,

$k$  - diffusion rate constant;  $Q$  - Activation energy;  $T$  - Absolute temperature;  $R$  - Universal gas constant ( $8.314 \text{ JK}^{-1}\text{mol}^{-1}$ ), and  $A$  - Pre exponential factor

Taking log on both sides of the equation,

$$\ln k = A - \frac{Q}{RT} \quad \text{Equation 4.3}$$



Equation 4.3 is similar to the equation of the straight line  $y = mx + c$ , where the line intersects the y axis at point or distance  $c$ ,  $m$  is the slope of the line and  $(x,y)$  are the co-ordinates of the line. Hence, taking  $\ln k$  on y axis and  $(1/T)$  on x-axis on the plot; the slope of the line is equivalent to  $-Q/R$  and the ordinate gives the pre exponential factor.

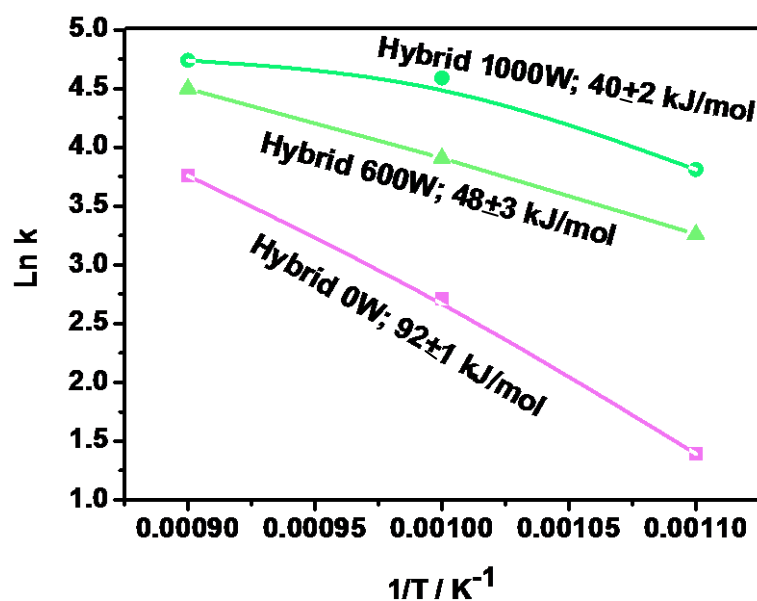


Figure 4.15: Arrhenius plot of the tetragonal BT (t-BT) formation as a function of reciprocal of temperature at various microwave power levels

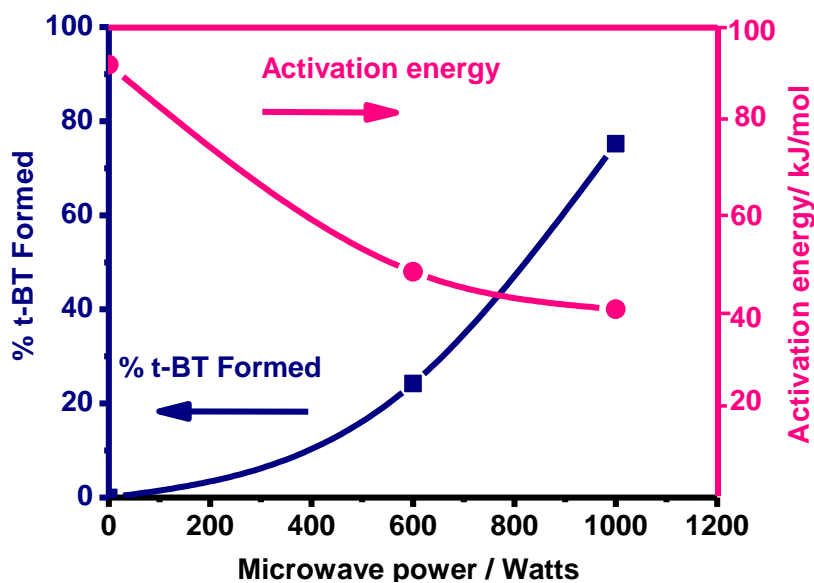


Figure 4.16: The percentage of t-BT formation and change in activation energy with different microwave powers in hybrid heating at 700°C/ 30 min

Thus, from the plot of  $\ln k$  versus  $1000/T$  in Figure 4.15, the activation energy,  $Q$  for the different microwave power level experiments was calculated. The intercept gives the  $\ln A$  from which the pre exponential factor was calculated. Table 4.3 shows comparison of activation energy and pre exponential factor for different microwave power experiments in hybrid heating.

**Table 4.3: The activation energy and pre exponential factor for different microwave power for the t-BT formation in hybrid heating**

<b>Input Microwave Power</b>	<b>0 W</b>	<b>600 W</b>	<b>1000 W</b>
Activation energy, kJ/mol	$92 \pm 1$	$48 \pm 3$	$40 \pm 2$
Pre exponential factor	$13 \pm 1$	$10 \pm 3$	$9 \pm 2$

Thus the activation energy was found to be  $40 \pm 2$  kJ/mol for microwave assisted synthesis with 1000 W of microwave power compared to the conventional experiments whose activation energy was calculated as  $92 \pm 1$  kJ/mol. Thus, the activation energy has been reduced by more than half when 1000 W of microwave power was used during nano BT synthesis. These results match with the literature values<sup>217, 218, 219</sup>.

*Activation energy for tetragonal nano BT formation was found to decrease with increasing microwave power.*

The plausible reasons for the reduction in activation energy could be:

1. As the reactants (precursors) are amorphous, carbonaceous-based compounds which can readily couple with microwaves, this can cause rapid decomposition of the precursors to form the intermediate phases, which can reduce the processing time and temperature. To evaluate this hypothesis, the polymeric resin was heat treated at a different pre treatment temperature, 500°C to vary the initial organics/ carbon content and was latter calcined using identical thermal profiles (700°C/ 30 min/ 1 kW) as before in hybrid furnace. The calcined powders from both the precursors show single-phase t-BT with similar % of tetragonality, Figure 4.17. This indicates that though

microwaves cause a rapid decomposition of the reactants but that alone cannot contribute to the reduction in activation energy by half. At 500°C, some of the decomposition would have taken place already. This changes the nature of the precursors. However, this does not affect the end result significantly.

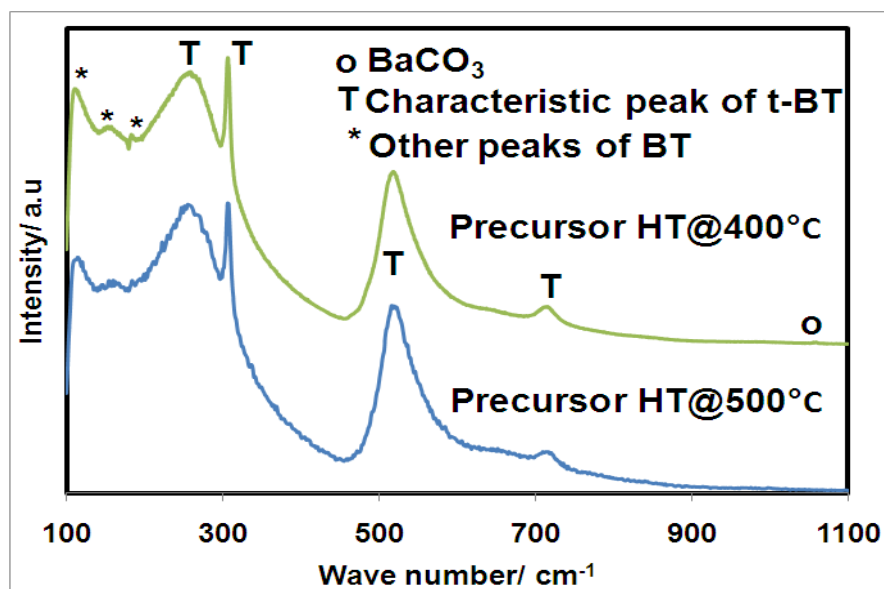


Figure 4.17: The room temperature Raman spectra of BT precursors prepared at 400°C & 500°C and then calcined at 700°C/ 30 min/ 1 kW

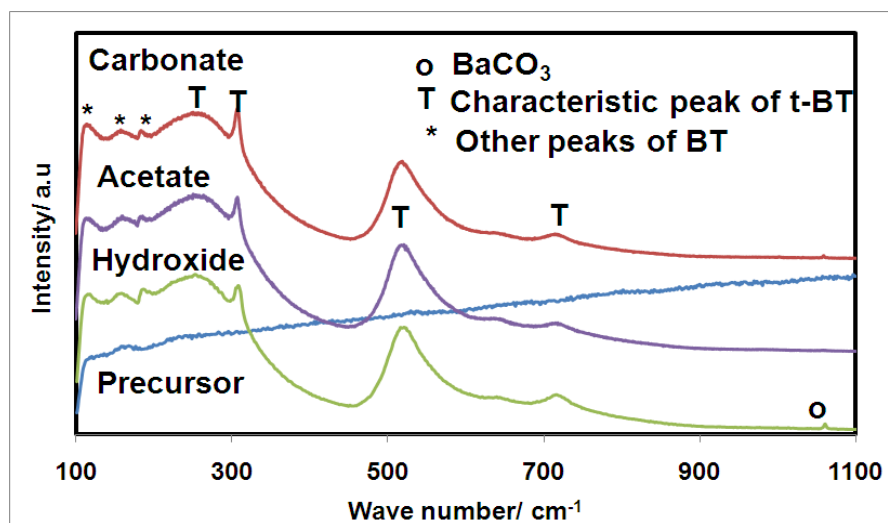
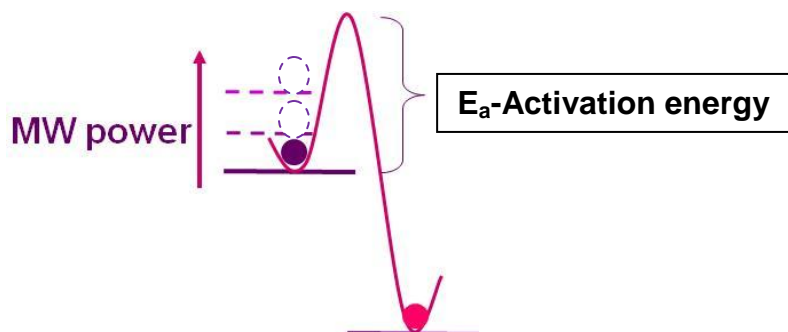


Figure 4.18: The room temperature Raman spectra of the BT precursors produced using different barium sources and calcined at 700°C/ 30 min/ 1 kW in hybrid heating



**Figure 4.19: Schematic diagram on effect of microwaves on diffusion enhancement**

2. However, it is evident that microwaves can possibly lift the energy level of the reactants and reduces the activation energy significantly thus forming the single phase t-BT at the thermodynamic formation temperature, Figure 4.1 in a shorter duration (Figure 4.19). Effective use of the reaction enthalpies during microwave heating can also aid the reaction completion<sup>208</sup> due to bulk nucleation<sup>4</sup>.

Although with the present evidence, we can assume or suggest some plausible reasons for the reduction in the activation energy using microwave power during nano BT ceramic synthesis these may not be the only reasons to account for the observed effect. Hence a detailed investigation on understanding the microwave effect during nano BT ceramic synthesis needs to be carried out, which can form an interesting challenging future research project.

*Thus in microwave assisted heating, reduction in activation energy was noticed as a function of microwave power, which in turn lowers the processing temperature, reduces processing time, and resulted in the enhancement of bulk nucleation of t-BT that resulted in fine, uniform nanocrystalline t-BT powders.*

#### 4.1.6. Synthesis of Zr substituted BT nanopowders

The zirconium content was varied from 0-30 mol% to form BaTiO<sub>3</sub> (BT), Ba(Zr<sub>0.1</sub>Ti<sub>0.9</sub>)O<sub>3</sub> (BZT-10), Ba(Zr<sub>0.2</sub>Ti<sub>0.8</sub>)O<sub>3</sub> (BZT-20) and Ba(Zr<sub>0.3</sub>Ti<sub>0.7</sub>)O<sub>3</sub> (BZT-30) respectively. The dielectric properties of the starting precursors ( $\epsilon'' = 0.05$ ;  $\tan\delta = 0.02$ ) show that the precursors have reasonably high values of dielectric loss and loss tangent. The precursors were calcined at the optimised synthesis condition of BT, 900°C/ 5 h in conventional and 700°C/ 30 min in pure microwave heating.

All the BZT compositions formed are single phase and Figure 4.20 and 4.21 shows clearly how the diffraction peaks shifted to lower angles with increasing Zr content, suggesting an increase in unit cell volume. The Raman spectra for the BZT compositions calcined at 900°C for 5 hours using conventional heating, Figure 4.22, also show that the sample retained the tetragonal crystal structure up to 20 mol% of Zr substitution and on further Zr addition it started losing tetragonality and changed to cubic symmetry. The intensity of the main tetragonal peak at 307 cm<sup>-1</sup> was found to decrease with increasing Zr addition. However, there was no indication of the pseudo-monoclinic or rhombohedral phases observed by other researchers. With increasing Zr, an additional peak at 123 cm<sup>-1</sup> was observed as expected; this mode corresponded to the vibration of Zr atoms in the lattice, which was in agreement with previous results. Similarly, the vibration of Ti atoms in the oxygen octahedra caused the peak at 180 cm<sup>-1</sup>, which decreased in intensity as the ratio of Zr/Ti increased.

Figure 4.23 shows the XRD pattern of the BZT precursors calcined at 700°C for 30 minutes using microwave heating. All the peaks were found to be characteristic of the tetragonal structure. The Raman spectra for the microwave calcined BZT powders, Figure 4.24, confirmed the high tetragonality (exhibiting the signature peak at 307 cm<sup>-1</sup>) of the powders produced. Similar peaks were obtained as found for conventional calcined powders were obtained. The calculated lattice parameters for the conventional and microwave calcined nano powders are shown in Table 4.4

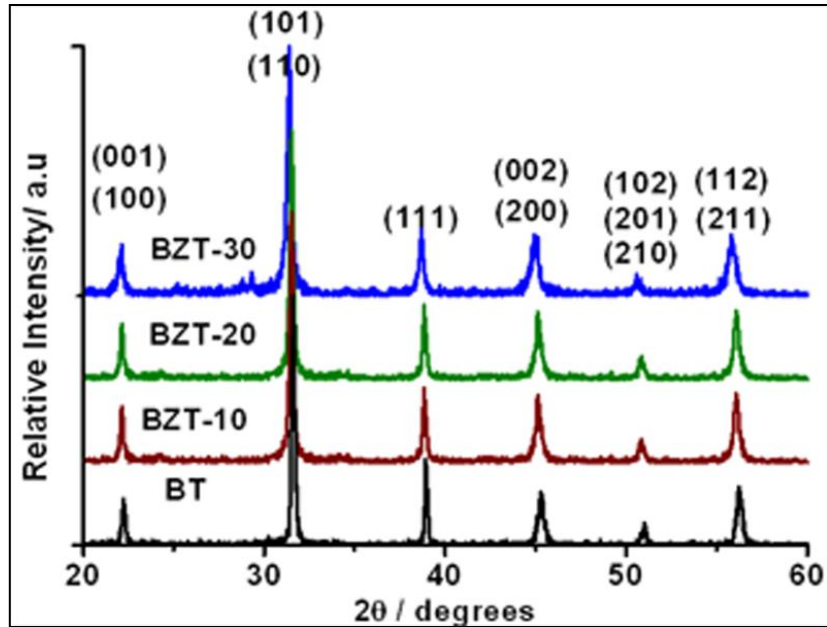


Figure 4.20: Room temperature XRD patterns of the BT, BZT-10 and BZT-20 precursors calcined at 900°C for 5 hours using conventional heating

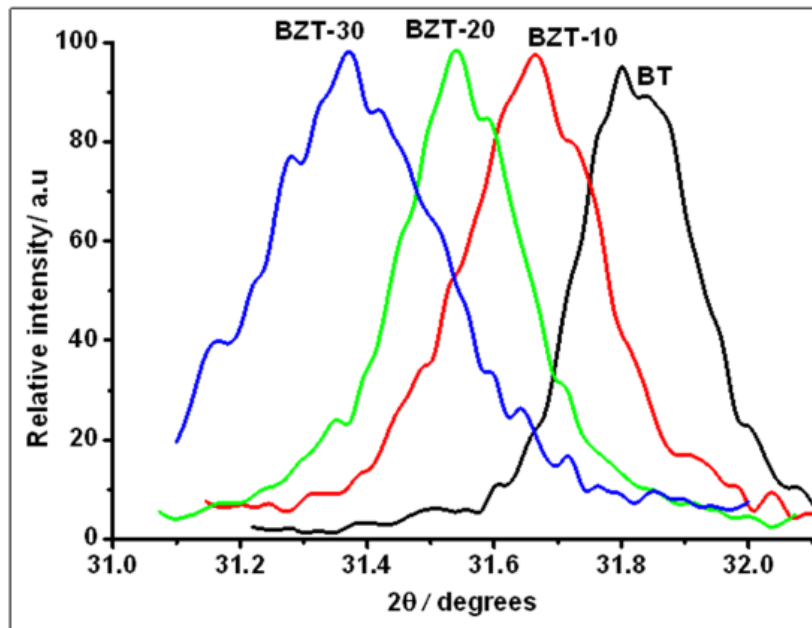


Figure 4.21: Room temperature magnified view of (110) peak shift of the BT, BZT-10 and BZT-20 precursors calcined at 900°C for 5 hours using conventional heating.

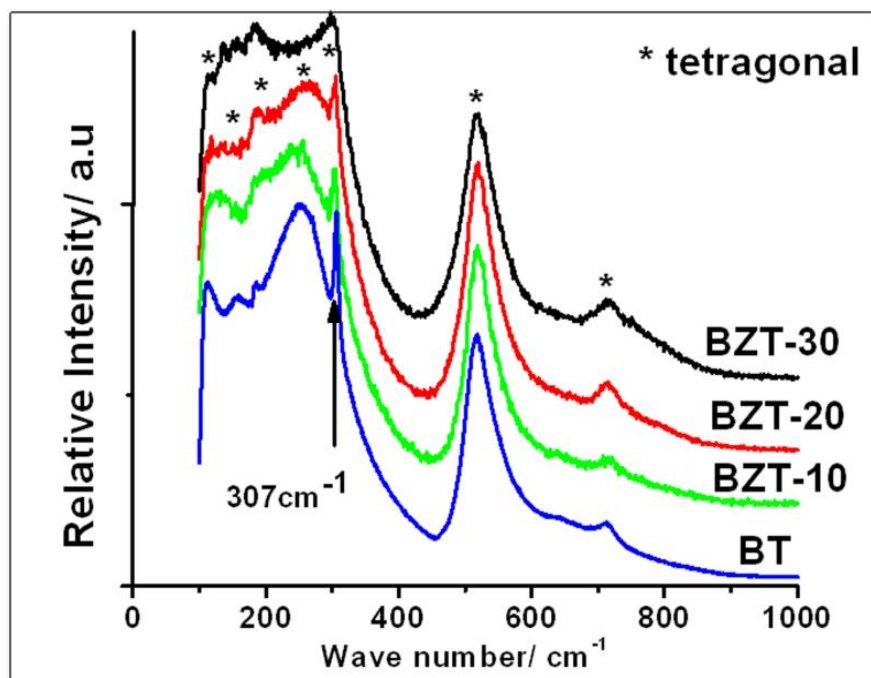


Figure 4.22: Room temperature Raman spectra of BT, BZT-10, BZT-20 and BZT-30 precursors calcined at 900°C for 5 hours in conventional heating.

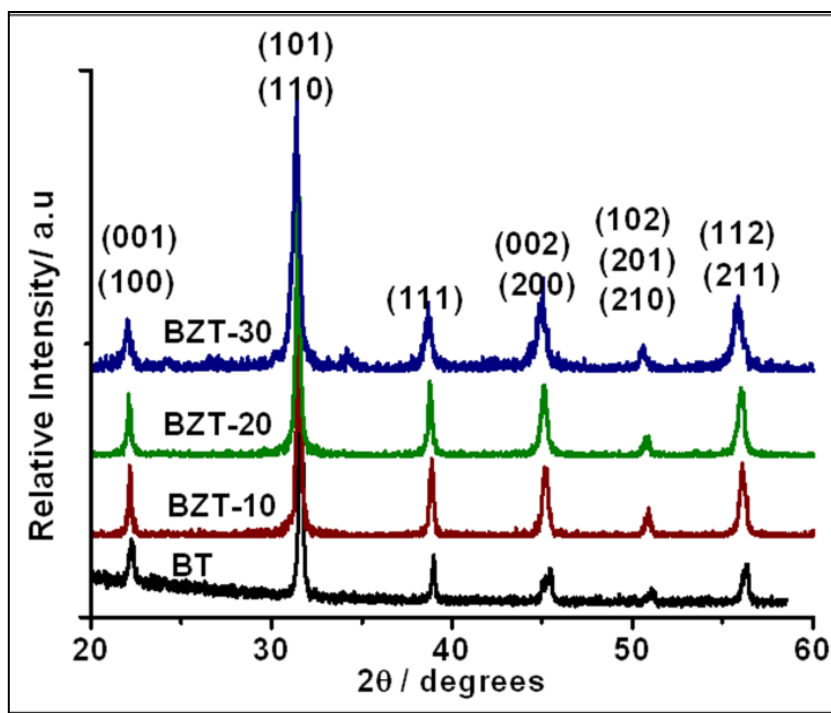


Figure 4.23: Room temperature XRD patterns of BT, BZT-10, BZT-20 and BZT-30 precursors calcined at 700°C for 30 minutes in microwave heating

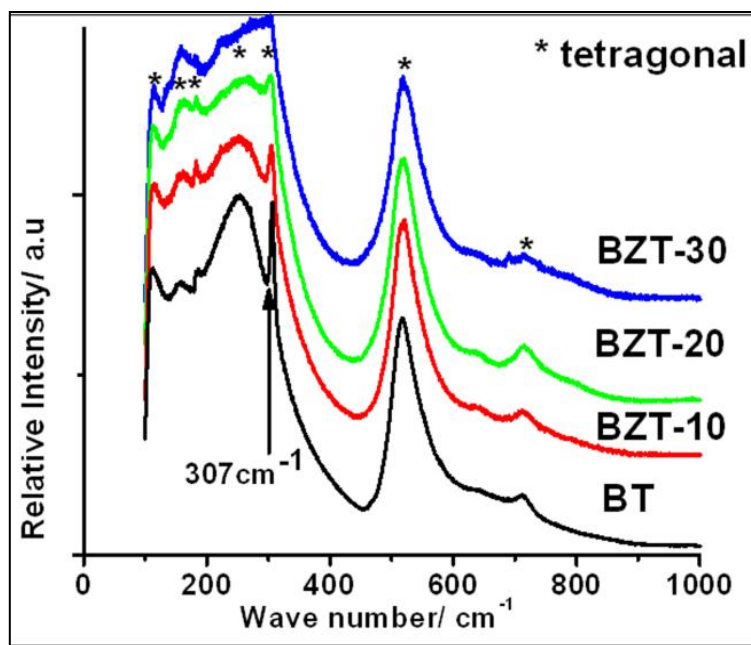


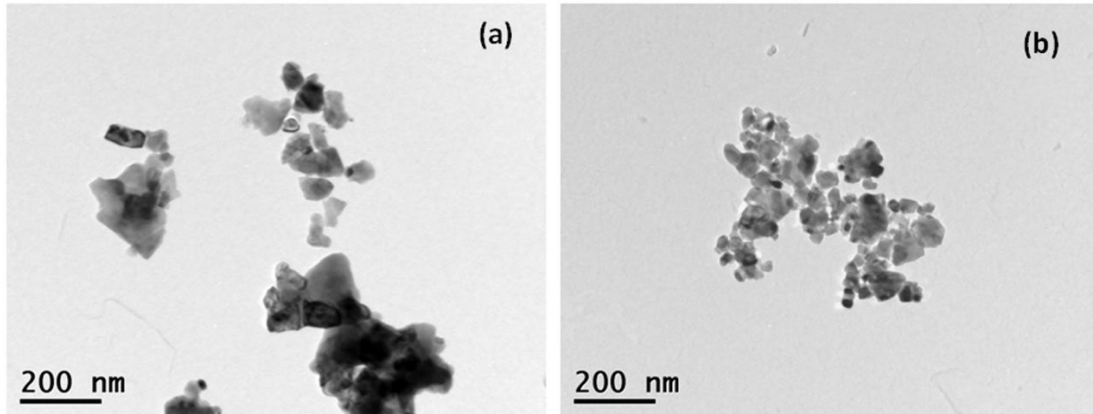
Figure 4.24: Room temperature Raman spectra of BT, BZT-10, BZT-20 and BZT-30 precursors calcined at 700°C for 30 minutes in microwave heating

Table 4.4: Lattice parameters of BT, BZT-10, BZT-20 and BZT-30 precursors calcined at 900°C for 5 hours in conventional heating and 700°C for 30 minutes in microwave heating. ( $c/a \pm 0.0004$ )

CON	a /nm	c /nm	c/a	Lattice volume /nm <sup>3</sup>	MW	a /nm	c /nm	c/a	Lattice volume /nm <sup>3</sup>
BT	4.000	4.017	1.004	64.27	BT	4.008	4.026	1.005	64.67
BZT-10	4.006	4.025	1.004	64.59	BZT-10	4.009	4.027	1.005	64.72
BZT-20	4.013	4.023	1.003	64.79	BZT-20	4.013	4.026	1.003	64.84
BZT-30	4.03	4.03	1.000	65.40	BZT-30	4.026	4.041	1.003	65.48

With the increase in Zr substitution, the cell parameters increase as the ionic radii of Zr is larger than that for Ti, hence the cell volume increases. Microwave calcined powders exhibit slightly larger cell volumes whilst maintaining high tetragonality. Similar observations were made during the microwave assisted sintering of Sr substituted BaTiO<sub>3</sub><sup>214</sup>. The lattice strain associated with the higher cooling rates in the microwave process could also be a contributing factor. Microwave assisted improvement on tetragonality of the nano BT powders was also reported<sup>220</sup>





**Figure 4.25: TEM images of the BZT-20 powders calcined at a) 900°C for 5 hours using conventional heating and b) 700°C for 30 minutes using microwave heating**

The particle sizes of the powders synthesised using the conventional and microwave heating are shown in Figure 4.25. The microwave-calcined powders had a uniform and finer particle size of ~30 nm with less evidence of agglomeration compared to the conventionally calcined powders, which had mean particle sizes in the range of 50 – 100 nm. It is believed that this result is due to the rapid heating and cooling associated with microwave heating that provides less time for particle growth and agglomeration. Table 4.5 provides the surface areas of the microwave and conventionally heated powders and the smaller particle size and lower extent of agglomeration of the microwave powders were probably instrumental in explaining the higher surface areas observed. The lower temperature employed in the microwave process was also probably responsible for the finer crystallite size and larger surface area of the microwave prepared powders obtained.

**Table 4.5: BET surface area and dielectric properties results of the BZT compositions calcined at 900°C for 5 hours using conventional heating & 700°C for 30 minutes using microwave heating**

Compositions	Conventional heating			Microwave heating		
	BET surface area, m <sup>2</sup> /g	$\epsilon'$	$\epsilon''$	BET surface area, m <sup>2</sup> /g	$\epsilon'$	$\epsilon''$
BT	2.7	3.5	0.1	6.1	4.95	0.1
BZT-10	5.5	7.18	0.2	6.7	13.57	0.2
BZT-20	12.2	6.11	0.2	14.0	12.11	0.3
BZT-30	5.7	4.79	0.08	7.8	6.73	0.05

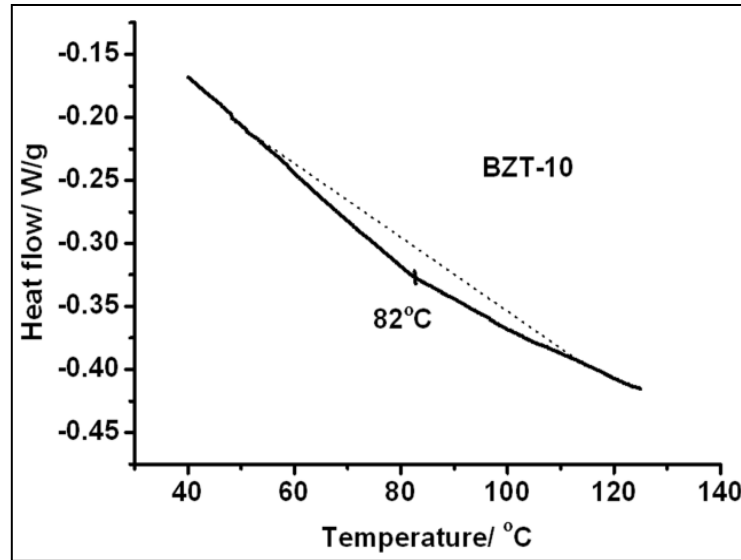


**Figure 4.26: Typical DSC of the BZT10 composition**

The finer particles sizes, higher surface area and the associated better tetragonality of the microwave prepared nanopowders also had an influence on the high frequency dielectric properties observed, Table 4.5. All the compositions of the microwave calcined powders were found to have higher relative permittivity values. The BZT10 showed a tetragonal to cubic phase transition at 82°C, Figure 4.26, which compares well with the literature<sup>35</sup>. It has been reported that in BT, the enthalpy of phase transition decreases with decreasing particle size. For the materials synthesised here, the  $\Delta H$  of the microwave calcined BT powder (0.1 J/mol.K) is found to be lower than that of the conventionally calcined BT powder (0.35 J/mol.K); this could be because of the finer particle size and reduced degree of agglomeration noticed in the microwave calcined BT powders.

*Single phase zirconium substituted BT nanopowders can be produced at 700 °C for 30 min using microwave heating. The BZT nanopowders synthesized through microwave heating has better dielectric properties and the enthalpy of phase transition decreases with decreasing particle size.*

#### 4.1.7. Synthesis of Sr substituted BZT nanopowders

Sr substituted BZT10 was prepared by varying Sr content as 10-40 mol% forming  $(\text{Ba}_{0.9}\text{Sr}_{0.1})(\text{Zr}_{0.1}\text{Ti}_{0.9})\text{O}_3$  (BSZT-10/10),  $(\text{Ba}_{0.8}\text{Sr}_{0.2})(\text{Zr}_{0.1}\text{Ti}_{0.9})\text{O}_3$  (BSZT-20/10),  $(\text{Ba}_{0.7}\text{Sr}_{0.3})(\text{Zr}_{0.1}\text{Ti}_{0.9})\text{O}_3$  (BSZT-30/10) and  $(\text{Ba}_{0.6}\text{Sr}_{0.4})(\text{Zr}_{0.1}\text{Ti}_{0.9})\text{O}_3$  (BSZT-40/10). All the compositions were found to form a single phase tetragonal phase at 900°C for 5 h in conventional heating and 700°C for 30 min microwave heating. The XRD pattern of the BSZT compositions calcined using microwave heating are shown in Figure 4.27. The left shift in peaks to lower angle with increasing Sr content was observed representing the decrease in cell volume. As ionic radii of  $\text{Sr}^{2+} < \text{Ba}^{2+}$ , with increasing Sr content, the unit cell volume tend to decrease which in turn decreases the tetragonality of the powders.

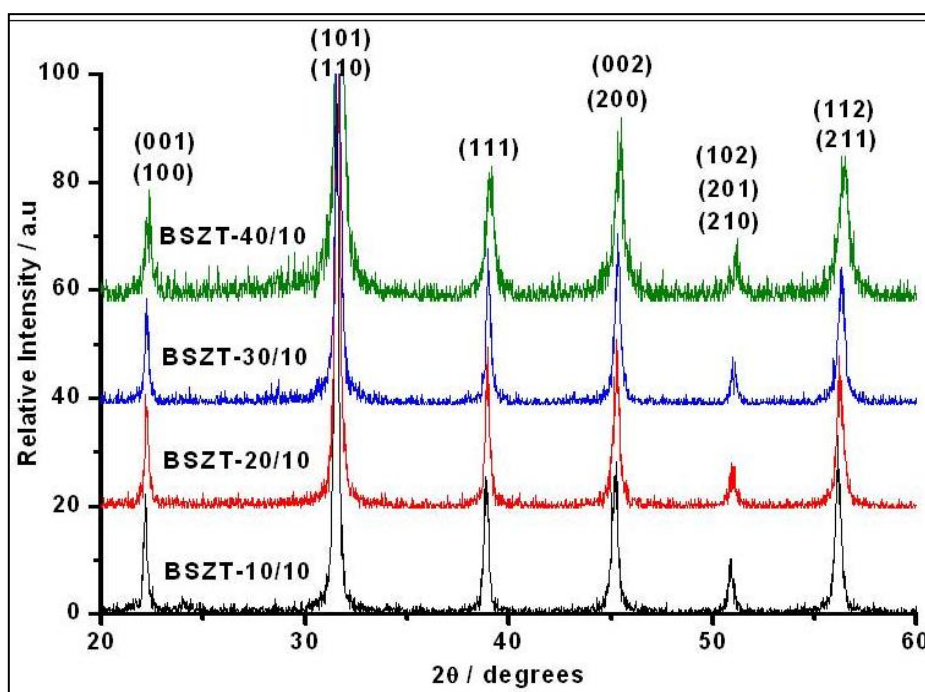


**Figure 4.27: Room temperature XRD patterns of BSZT-10/10, BSZT-20/10, BSZT-30/10 and BSZT-40/10 calcined at 700°C for 30 min in microwave heating**

Further, the tetragonality of the calcined BSZT compositions was confirmed using Raman spectroscopy. The Raman spectra of BSZT composition calcined using microwave heating is shown in Figure 4.28. As explained before, with increasing Sr

content the tetragonality decreases. Table 4.6 gives the lattice parameters of the BSZT powders calcined using conventional and microwave heating. Similar to BZT compositions, in BSZT compositions, it was observed that the microwave-calcined powders had higher cell volume compared to the conventional calcination. As explained before (section 4.1.6) it could be due to the higher cooling rate involved during microwave calcination.

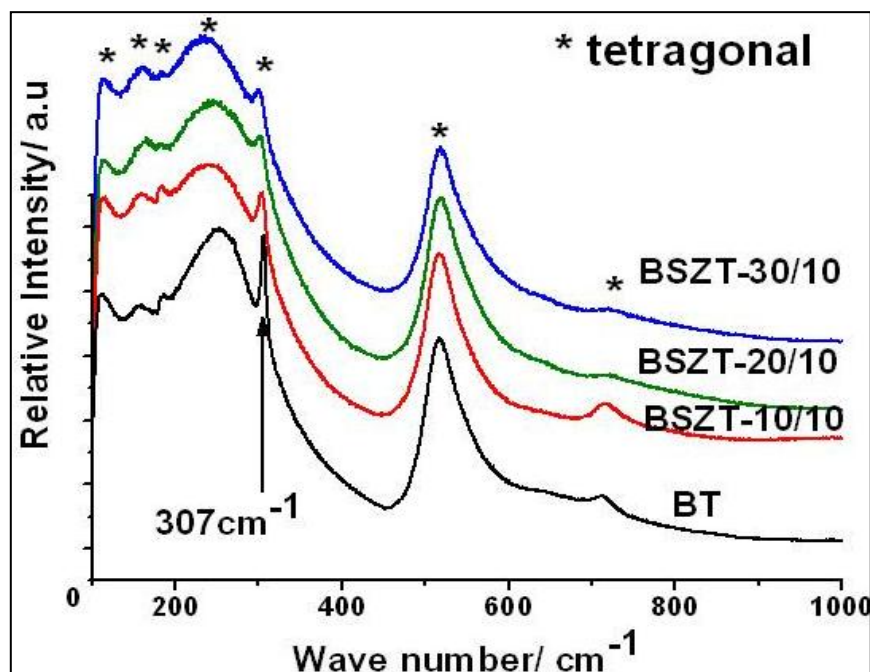


Figure 4.28: Room temperature Raman spectra of BSZT-10/10, BSZT-20/10, BSZT 30/10 and BSZT 40/10 calcined at 700°C for 30 min in microwave heating

Table 4.6: Lattice parameters of the BSZT-10/10, BSZT-20/10, BSZT 30/10 and BSZT 40/10 calcined at 900°C for 5 h in conventional heating and 700°C for 30 min in microwave heating

Composition	Conventional				Microwave			
	a /nm	c /nm	c/a	Volume <sup>3</sup> /nm <sup>3</sup>	a /nm	c /nm	c/a	Volume <sup>3</sup> /nm <sup>3</sup>
BZT-10	4.006	4.025	1.004	64.59	4.009	4.027	1.005	64.72
BSZT-10/10	4.000	4.017	1.004	64.343	4.000	4.017	1.005	64.508
BSZT-20/10	3.999	4.018	1.004	64.247	3.997	4.011	1.004	64.080
BSZT-30/10	3.988	4.006	1.004	63.604	3.995	4.011	1.004	64.036
BSZT-40/10	3.979	3.989	1.002	63.165	3.977	3.979	1.002	62.955

From Figure 4.29 and Table 4.7, it is evident that similar to BT & BZT compositions, the microwave calcinations resulted in finer particle size with less agglomeration and hence good dielectric properties compared to conventionally prepared powders.

**Table 4.7: BET Surface area and dielectric properties results of the BZT compositions calcined 900°C for 5 hrs using conventional heating & 700°C for 30 min using microwave heating**

Compositions	Conventional heating			Microwave heating		
	BET surface area, m <sup>2</sup> /g	$\epsilon'$	$\epsilon''$	BET surface area, m <sup>2</sup> /g	$\epsilon'$	$\epsilon''$
BT	2.7	3.5	0.1	6.1	4.9	0.1
BZT-10	5.5	7.2	0.2	6.7	13.6	0.2
BSZT-10/10	6.7	10.7	0.3	8.8	12.0	0.3
BSZT-20/10	8.3	10.5	0.3	8.9	11.6	0.4
BSZT-30/10	9.2	12.4	0.3	9.2	19.5	0.3
BSZT-40/10	9.2	8.6	0.1	9.2	11.2	0.1

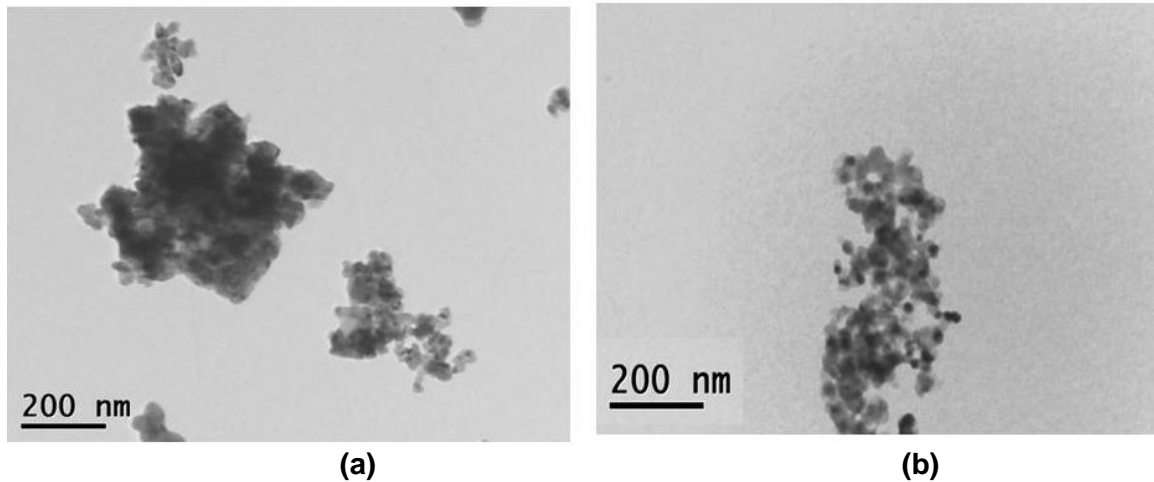


**Figure 4.29: TEM images of the BSZT-30/10 powders calcined at a) 900°C for 5 hrs using conventional heating and b) 700°C for 30 min using microwave heating**

*Single phase strontium substituted barium zirconium titanate (BSZT) nanopowders was synthesized using pure microwave heating. Thus, the synthesis method is generically applicable for other electro ceramic materials.*

## 4.2. Nano BT Processing

### 4.2.1. Powder characteristics

For green body making, the Loughborough synthesized nano BT powders (n-LU-BT), commercially available nano BT powders (n-S-BT) from Sakai chemicals Ltd., Japan and micron BT powders from Fischer scientific Ltd., U.K ( $\mu$ -BT) were used. Initially the procured and synthesized BT powders were characterized for the crystallinity, phase, particle size, and dielectric performance.

From the XRD pattern of the n-LU-BT, n-S-BT and  $\mu$ -BT powders, Figure 4.30, it is evident that all the powders have tetragonal symmetry. The tetragonality is dominantly noticed by peak splitting ( $45^\circ$  peak) in the n-LU-BT and  $\mu$ -BT than the n-S-BT. The n-S-BT powders have a primary particle size of 80-100 nm (Figure 4.31) and agglomerates size of  $\sim$ 100-300 nm (Figure 4.32) with BET surface area-  $12.3 \text{ m}^2/\text{g}$ .

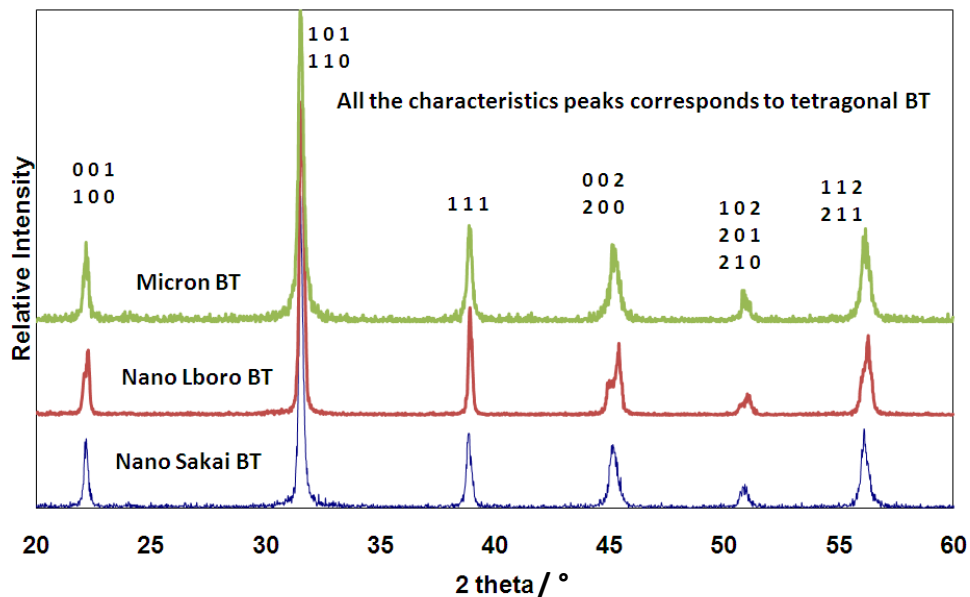


Figure 4.30: XRD pattern of the nano Lboro, Sakai BT and micron BT powders

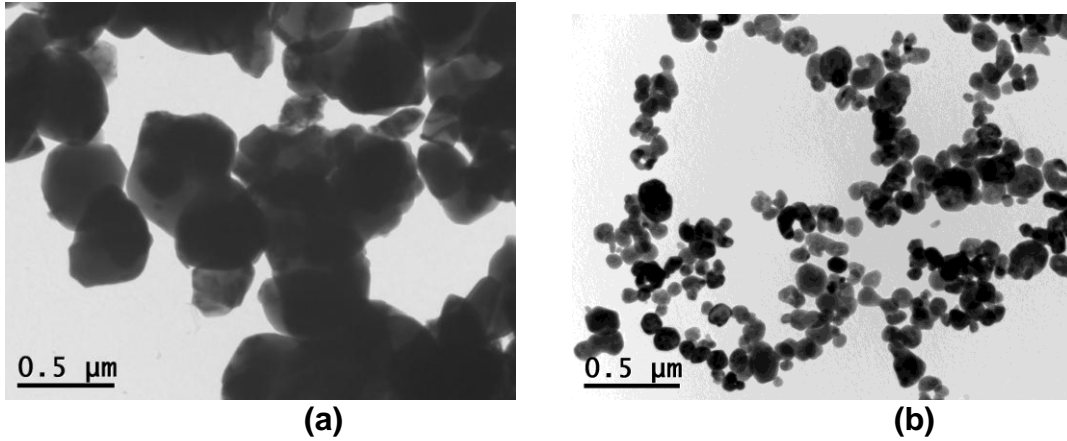


Figure 4.31: TEM image of the (a) micron-Fischer, (b) nano-Sakai BT powders and refer Figure 4.7 for TEM of nano- Lboro synthesized BT powders

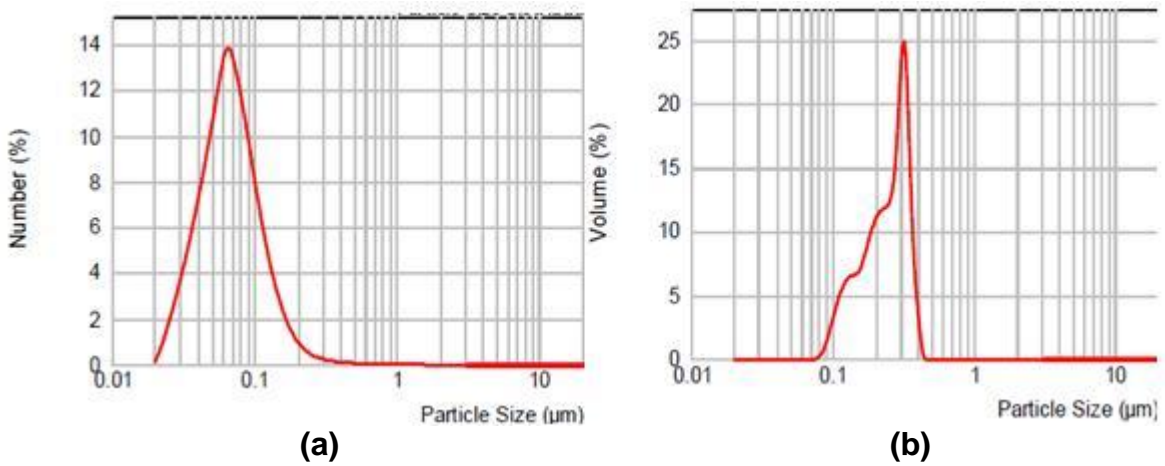


Figure 4.32: Particle size distribution of the nano Sakai BT powders

Table 4.8: Powder characteristics of the BT powders used

Powder	Primary Particle Size	Agglomeration
Nano Sakai	~100 nm	~300 nm
Nano Lboro	~20 nm	~100 nm
Micron	~0.5 μm	~1.3 μm

#### **4.2.2. Nano BT ink formulation**

Since the standard industry preferred method for MLCC manufacture is the screen printing process, printing inks were made using the BT powders. The nano BT ink/slip was prepared using pine oil solvent medium with phosphate ester dispersant and poly vinyl butyral (PVB) and ethyl cellulose (EC) with different molecular weight N4, N10 & N22 as binders.

##### **(i) Effect of dispersant concentration**

First step is to achieve a well-dispersed nano BT powders in pine oil using phosphate ester. Hence, suspensions were prepared with 55 wt% n-S-BT and n-LU-BT powders, with varying dispersant content as 0, 0.25, 0.5, 0.75, 1 wt% with respect to the total suspension. The viscosities of the suspensions were measured using Rheometer with controlled shear stress varying the shear rate. Figure 4.33 and 4.34 shows the viscosity of the n-S-BT and n-LU-BT powders suspension with varying phosphate ester dispersant content respectively.

Figure 4.33 shows that the n-S-BT suspension without dispersant was not stable. As the nanoparticles tend to coagulate, it shows high viscosity at low shear rate or at rest and it breaks with increasing shear rate showing thixotropic behaviour. With addition of dispersant, the nano BT powder were dispersed well and hence lowers the viscosity. In addition, the viscosity decreases with increasing shear rate showing shear thinning behaviour. The viscosity of the nano n-S-BT suspension reaches a minimum with 0.75 wt% dispersant and beyond which it saturates. Further increase in dispersant content lead to the excess dispersant to remain in the solvent without adhering on the powder particle; this can be detrimental for further processing. Figure 4.34 shows that the n-LU-BT powder without dispersant not stable similar to n-S-BT powders. With the addition of dispersant, although viscosity at rest/ low shear rate was lowered. The viscosity of the suspensions increases with increasing shear rate showing shear thickening behaviour. In addition, n-LU-BT powders requires 1 wt% dispersant to achieve minimum viscosity compared to n-S-BT powders.



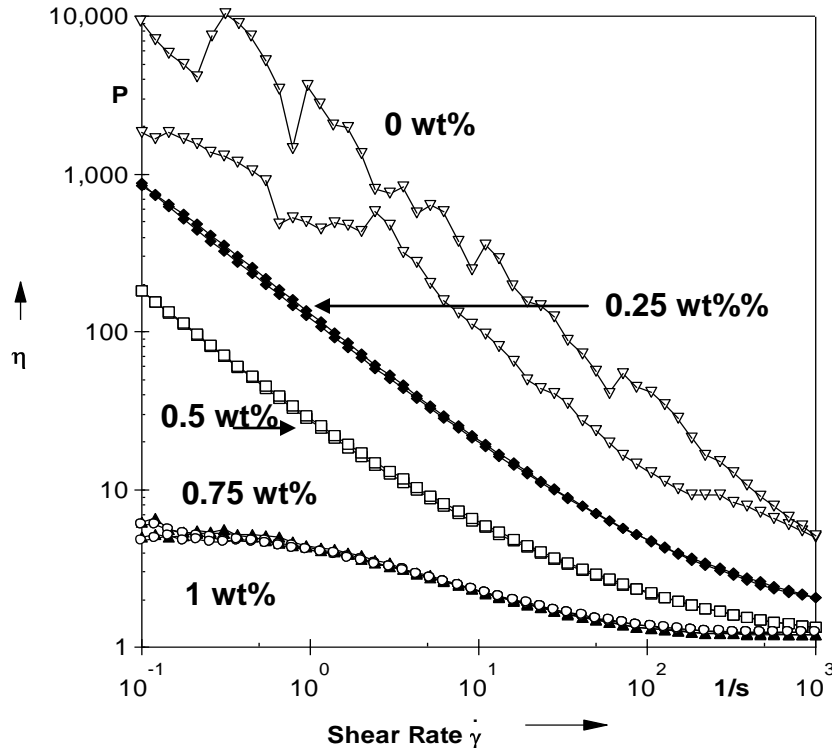


Figure 4.33: Viscosity curves of n-S-BT (55 wt%) suspension with varying amount of dispersants

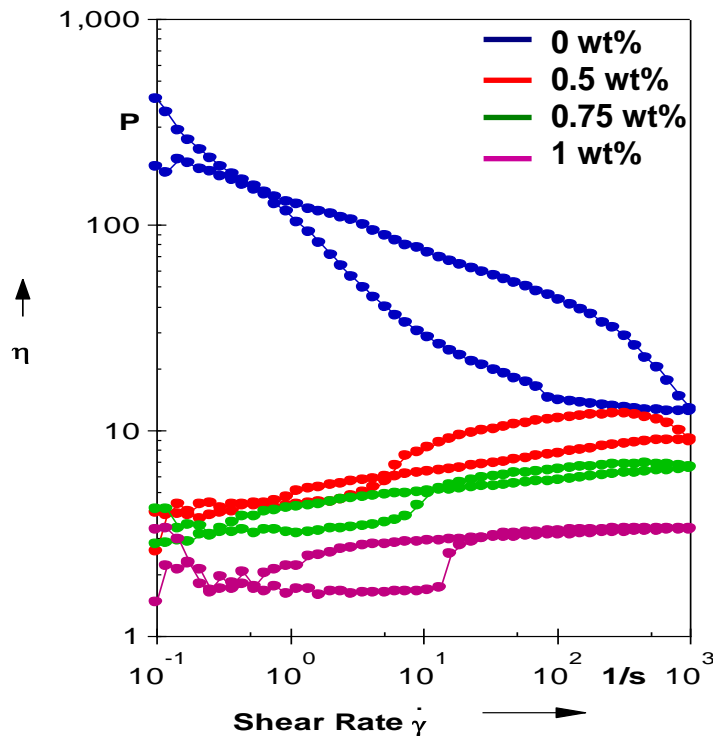


Figure 4.34: Viscosity curves of n-LU-BT (55 wt%) suspension with varying amount of dispersants

The primary particle size of the n-LU-BT (20 nm) is finer than the n-S-BT (100 nm). n-LU-BT has higher surface area and higher volume compared to n-S-BT and hence requires more dispersant to coat the nanoparticles to achieve good dispersion. Above all, the processing characteristics of the nanopowders depend very much on their synthesis route. n-LU-BT powders were produced through carbothermal reduction and microwave-assisted calcination process and hence the particles have faceted morphology with some carbonate ions adhering on the particle surface. Whereas the n-S-BT powders were produced through hydrothermal route, has spherical particle morphology with hydroxyl ions adhesion on their surface. Hence, n-S-BT is more suitable for wet processing than the n-LU-BT powders. n-LU-BT may work well with dry processing methods. However, this is not the preferred method for MLCC production by the industrial sponsor. Screen printing of BT inks is the preferred processing method. Hence the present project was mainly focused on the understanding of nano BT powder processing, sintering, and their electrical performance. Further wet processing with n-LU-BT powders was terminated. Thus from here on for further process optimization and understanding of nano BT powder processing and sintering, only n-S-BT powders were used.

n-LU-BT powders were found not suitable for wet processing. It is very difficult to achieve > 55 wt% solid content using n-LU-BT powders. The viscosity of the n-LU-BT powder suspension was higher than n-S-BT nanopowder suspension for same solids loading. In addition, the n-LU-BT nanopowders were found to be immiscible and exhibiting non-wetting behaviour.

*Thus n-S-BT powders were used for further process optimization and sintering studies. The optimum amount of dispersant required for n-S-BT powders was found to be ~0.75 wt%*

For comparison, the  $\mu$ -BT powders were also dispersed in the pine oil medium with different dispersant concentration. From the viscosity curve in Figure 4.35, it is evident that 0.35 wt% dispersant was sufficient to achieve minimum viscosity at a

solids loading of 64 wt%. With further increasing the dispersant content, the viscosity of the  $\mu$ -BT suspension at low shear rate increases as the excess dispersant remains in solvent. As the dispersant content is proportional to the surface area of the powder particles, with micron BT having less particle surface area, it required less dispersant content for stabilization.

The standard ink was provided by the industrial sponsor for comparison purpose. This will be referred as benchmark ink.

To have the direct comparison of the behaviour of  $\mu$ -BT with n-S-BT, 0.75 wt% of the dispersant was used for  $\mu$ -BT inks also.

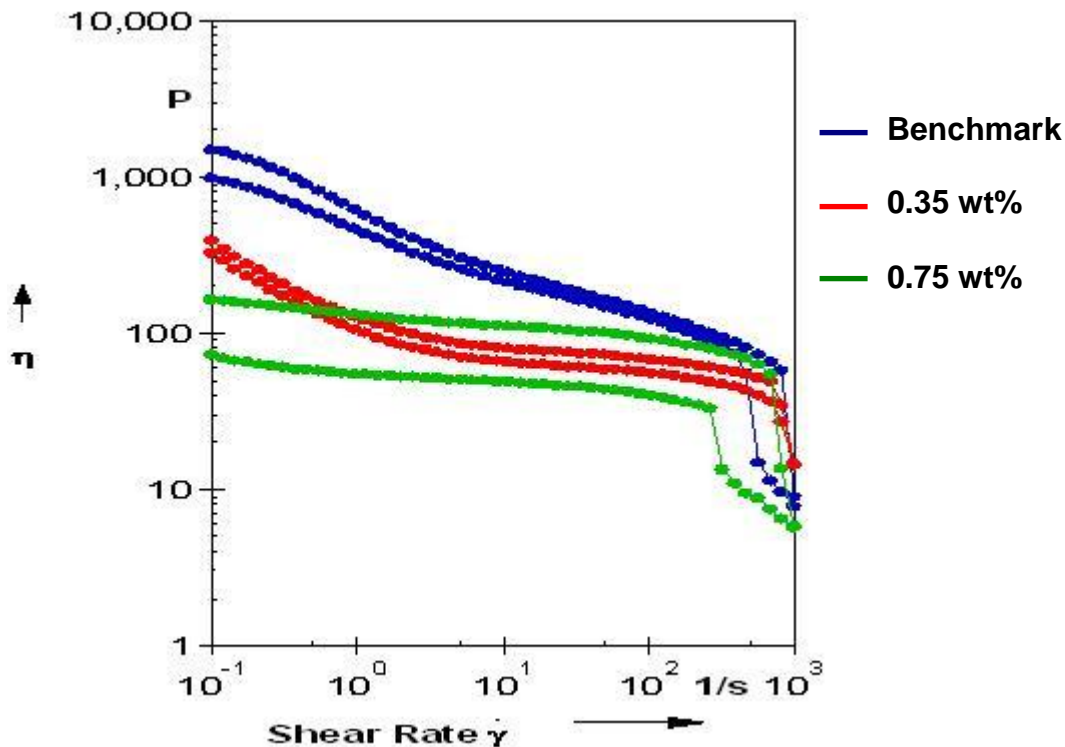


**Figure 4.35: Viscosity curves for  $\mu$ -BT (64 wt%) suspension with 0.35 wt% and 0.75 wt% dispersant**

*Compared to  $\mu$ -BT powders, amount of dispersant required to achieve stable dispersion with n-S-BT powders was found to be almost doubled.*

**(ii) Maximum solid loading**

The characteristics of nano ink will be altered to match with that of the standard ink was provided by the industrial sponsor referred as benchmark. This will allow the changes to the screen printing conditions to a minimum for MLCC fabrication.

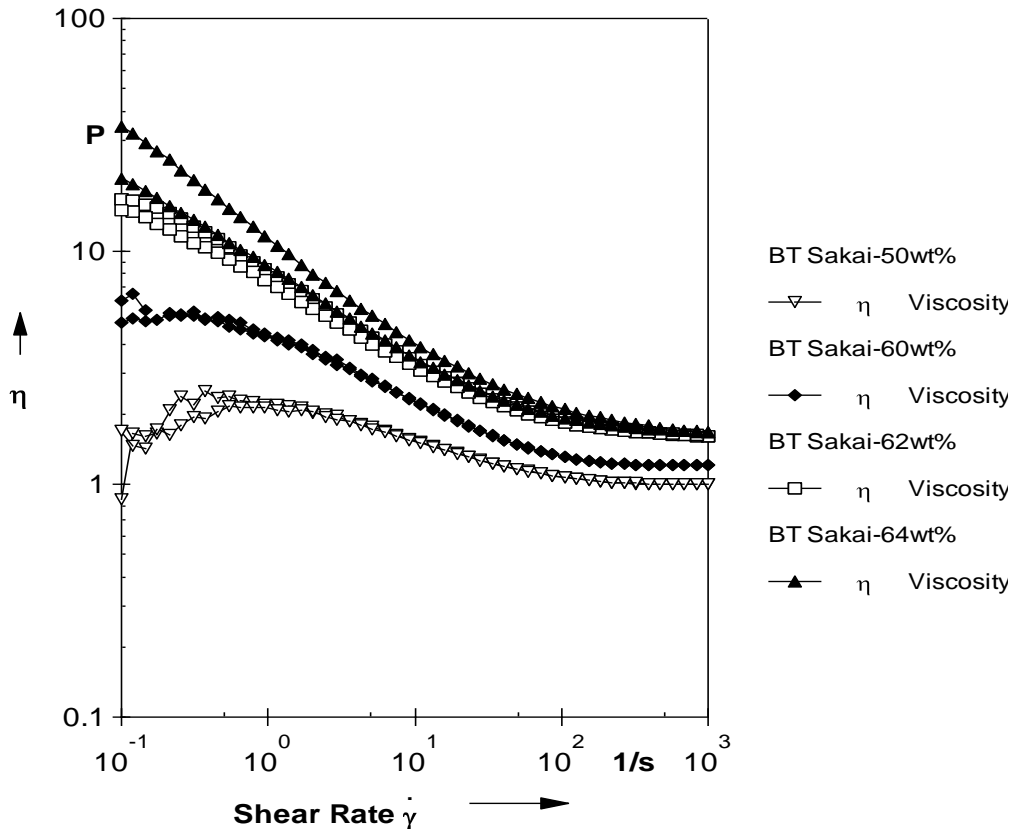


**Figure 4.36: Viscosity curves of the n-S-BT powder suspensions with 0.75 wt% dispersant and increasing solid content**

High solids content of the ink is very important to attain high green density and less shrinkage during densification. As aforementioned, 0.75 wt% dispersant was used and solid content was increased from 55 to 64 wt%. From Figure 4.36 it is evident that the viscosity of the n-S-BT suspension increases with increasing solid content. The n-S-BT suspension with 64 wt% shows the thixotropic behaviour, hence a maximum of 62 wt% ( $\geq 20$  vol%) solid content can be incorporated using n-S-BT powders with 0.75 wt% dispersant in pine oil medium.

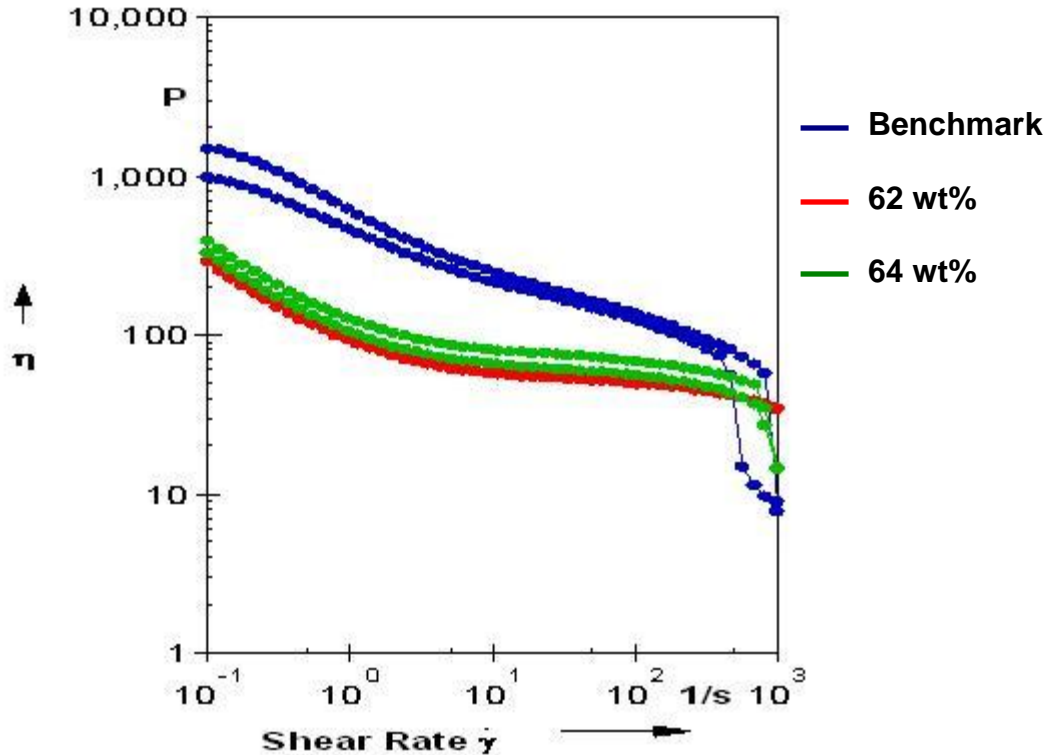


**Figure 4.37: Viscosity curves of the  $\mu$ -BT nanopowder suspensions with 0.75 wt% dispersant and increasing solid content**

In the  $\mu$ -BT powders with 0.75 wt% of dispersant concentration, it is possible to achieve >64 wt% solid loading whilst retaining the low viscosity, Figure 4.37. As the surface to volume ratio of  $\mu$ -BT powders are low compared to n-S-BT powders, a maximum solid content by wt% can be achieved using these  $\mu$ -BT powders. For the equivalent weight, n-S-BT powders occupy more volume compared to the  $\mu$ -BT powders and the viscosity increases significantly at high solids loading. In addition, it is challenging to attain homogeneous mixing of all the ingredients with n-S-BT powders at high viscosity.

*Maximum solid loading of ~62 wt% (~20 vol%) was achieved using n-BT powders with 0.75 wt% dispersant.*

### (iii) Optimizaion of PVB:EC ratio

Polyvinylbutyral (PVB) and ethyl cellulose (EC) were chosen as binders based on sponsors recommendations. In the EC, three different molecular weights, N4, N10 and N22, were used, where 4, 10 & 22 represents their polymeric chain length. From the viscosity curves (Figure 4.38) of the binders, it is evident that, PVB and N4 have lower viscosity compared to N10 and N22. The shear rate thixotropy curve represents the printability or the flow of the ink during printing condition. From Figure 4.39, it is observed that after removing the high shear rate applied, the PVB and N4 required more time to get back to its original viscosity, for which it can be inferred that PVB and N4 has a poor structure recovery compared to N10 & N22.

For manufacturing MLCCs, the nano BT ink should have less viscosity to achieve thin ceramic layers and the structure recovery should be fast for facilitating the next print, in order to achieve each ceramic layer of similar thickness. Hence, it is crucial to have balance amounts of PVB, N4 and N10, N22.

Therefore, it is important to optimise the ratio of PVB: EC and within EC the ratio of N4:N10:N22 to achieve ink rheology for suitable screen-printing of MLCCs. This is addressed below.

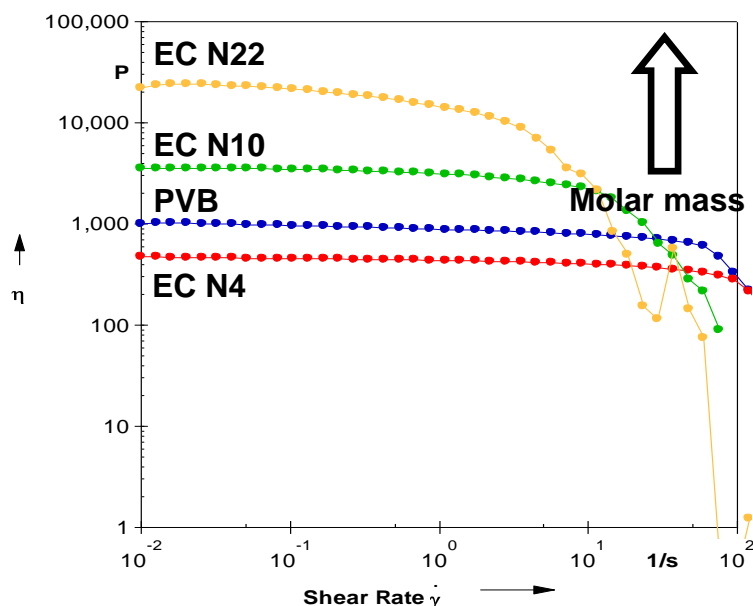


Figure 4.38: Viscosity curves for the different binders used

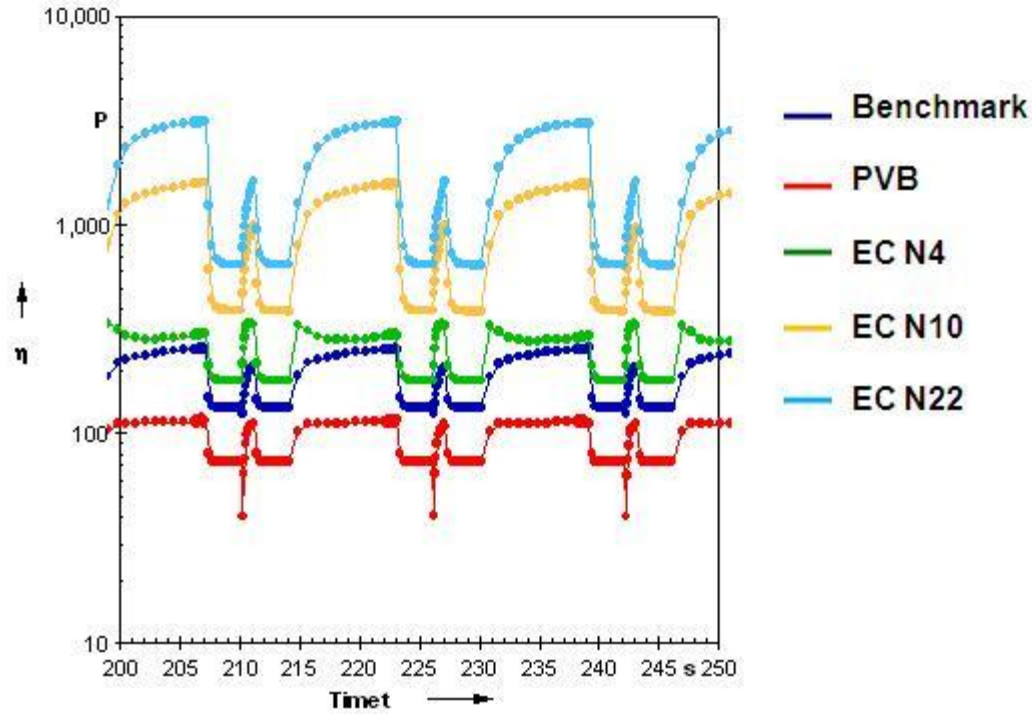


Figure 4.39: Shear rate thixotropy of the different binders used

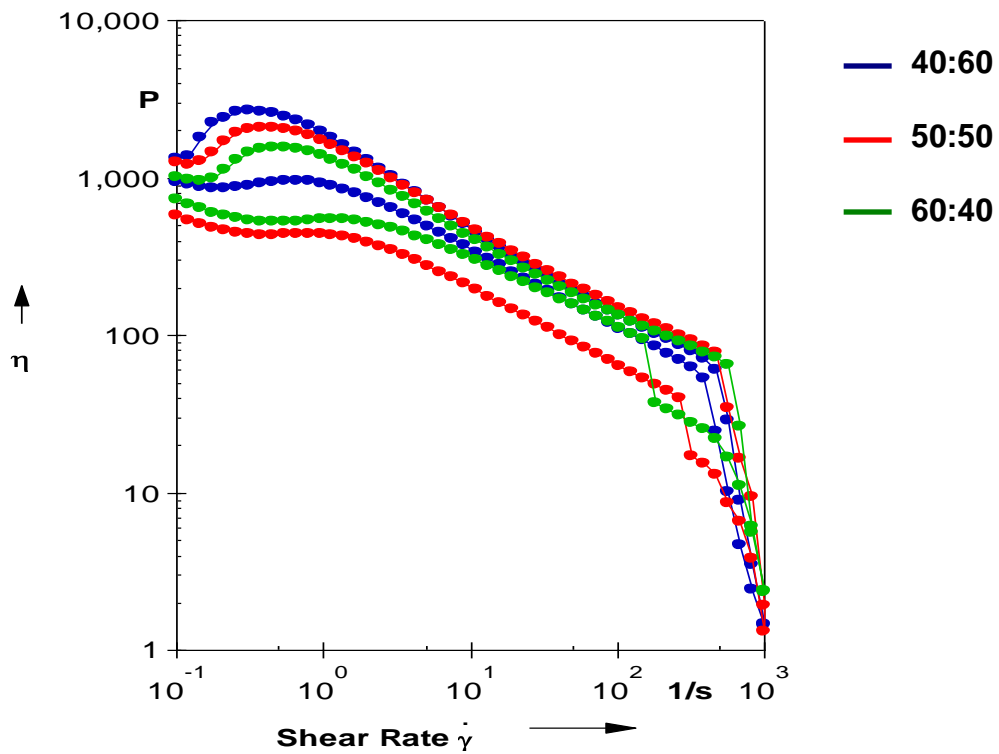
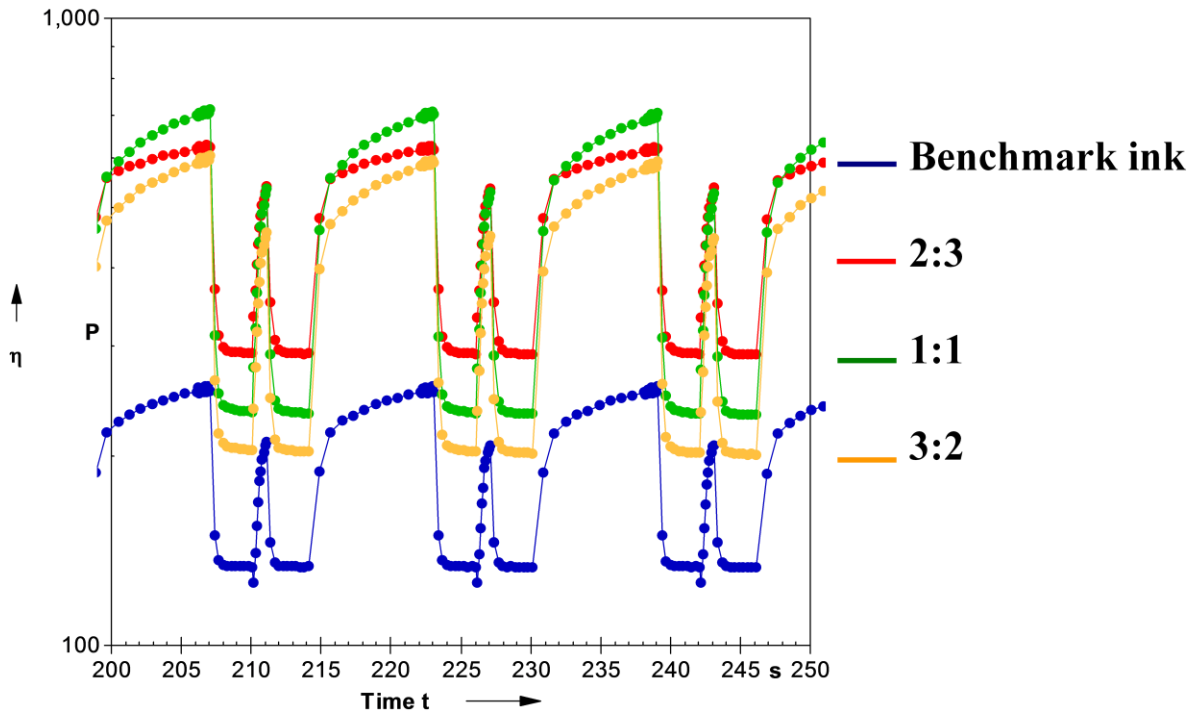


Figure 4.40: Viscosity curve of 62 wt% n-S-BT ink with 3 wt% total binder content - at different PVB: EC ratio



**Figure 4.41: Shear rate thixotropy loop of 62 wt% n-S-BT ink with 3 wt% total binder content – at different PVB: EC ratio**

A 62 wt% n-S-BT ink was prepared with varying PVB: EC ratios of 2:3, 1:1 and 3:2 (i.e., with increasing PVB). Figure 4.40 shows the viscosity curves of the 62 wt% n-S-BT ink with 3 wt% total binder concentration, within which the ratio of EC-N4:N10:N22 as 1:1:1 and PVB:EC ratio was varied as indicated. The gap or difference between the forward and the return loop of the viscosity curve as a function of shear rate is defined as thixotropy. If the gap is very less it is referred as small or good thixotropy, for a reasonable gap with trend remaining same it is referred as medium thixotropy and if both the gap is very wide and not following similar trend it is referred as high or poor thixotropy. Although the viscosity at low shear rate or at rest decreases with increasing PVB because of its smaller polymeric chain structure, the inks was found to have poor thixotropy. Also from Figure 4.41 of shear rate thixotropy loop showed that the viscosity of the print decrease with time especially for inks with high PVB:EC ratio. Thus, the consistency of the ceramic layers prints decreases with increasing PVB.



**Table 4.9: The effect of PVB:EC ratio on rheological behaviour of the n-S-BT inks**

S.No.	PVB:EC	0.1 s <sup>-1</sup>		40 s <sup>-1</sup>	Thixotropy
		Forward	Return		
1	30:70	6395	732	308	Large
2	<b>40:60</b>	<b>1311</b>	<b>946</b>	<b>210</b>	<b>Small</b>
3	50:50	1242	580	231	Medium
4	60:40	1015	732	201	Medium

Table 4.9 shows the comparison of the n-S-BT ink with 3 wt% binder and different PVB: EC ratios. The 2:3 ratio has low viscosity with less thixotropy and has quick structure recovery, consistent over a printing period. Hence PVB: EC ratio of 2:3 was chosen for further processing.

*PVB:EC ratio of 2:3 was found to give low viscosity with small & stable thixotropic behaviour and consistent printability.*

#### (iv) Influence of molar mass of EC

After selecting a PVB:EC ratio of 2:3, within EC, the ratio's of different molecular weight polymers, N4, N10 and N22 were varied as 50:50:50, 60:45:35, 70:40:30, 80:35:25 and 90: 30:20 (i.e., with increasing N4). Initially started with equal amount of N4, N10 & N22 molecular weight and then the lower molecular weight N4 was increased. Nano particles weight can be held together by a small chain polymeric binder. However, long chain polymeric binders have high yield strength and recovery, hence the balance of both are required for multilayer printing.

A 62 wt% n-S-BT ink was prepared with 3 wt% total binder addition PVB: EC ratio was maintained at 2:3 and within EC, N4:N10:N22 ratio was varied as indicated. Figure 4.42 shows the viscosity curves. With increasing of the lower molecular weight N4, the viscosity of the ink at rest (zero shear rate) was found to reduce but the ink exhibited poor thixotropic behaviour. That is in the viscosity curves of the forward and return behaviours do not match or there is more gap between the two curves.

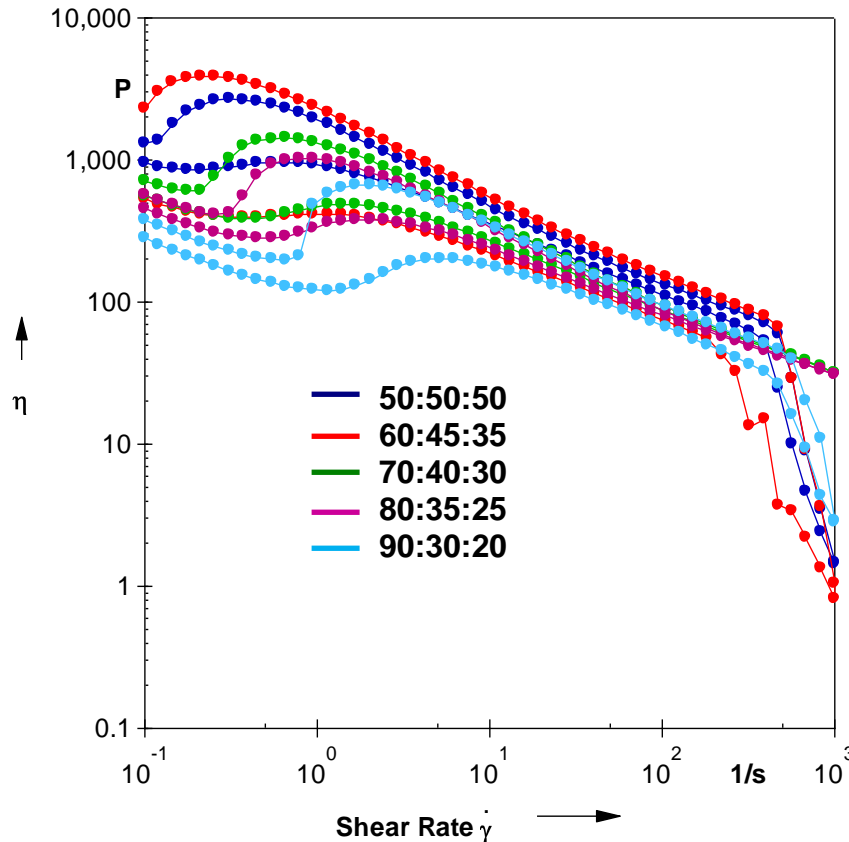


**Figure 4.42: Viscosity curves of 62 wt% n-S-BT ink with 3 wt% total binder content and PVB:EC-2:3-effect of EC-N4:N10:N22 ratio on viscosity**

When the inks are at rest (zero shear rate), the polymeric chains are coiled and entangled. During printing or measurements, with increasing the shear rate/force, the polymeric chains deform in the direction of force and disentangle or temporarily break (Figure 4.43). Hence the viscosity of the ink decreases with increasing shear rate. During the return measurements, the shear rate is decreased from high to low and the polymeric chains are relaxed. Hence, there is more chance for the polymeric chains to return to their original structure/network.

If there is more difference between the forward and return curves i.e., poor thixotropy is seen, it infers that the structure does not recovery quickly, the ink is not ready for printing the next layer with the same thickness and strength.

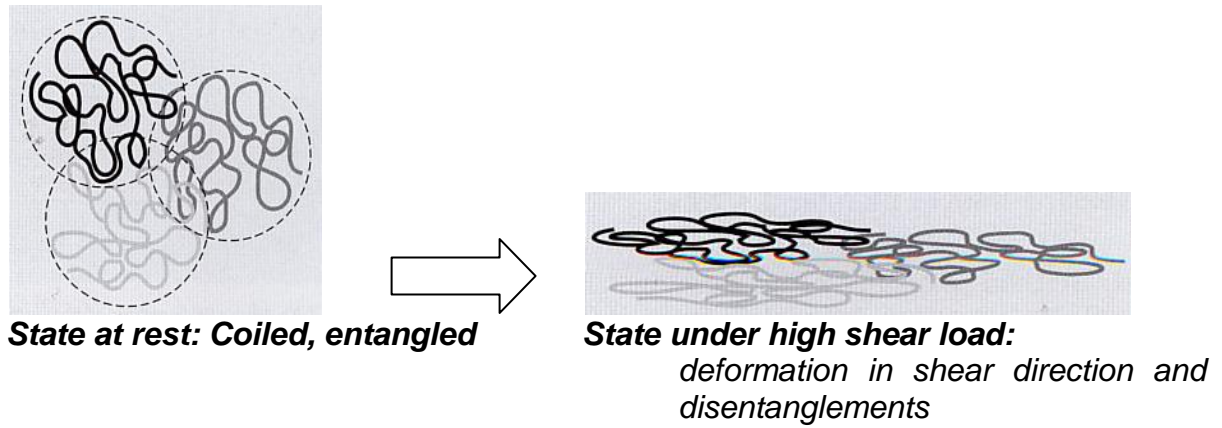


**Figure 4.43: Schematic diagram of polymer molecules behaviour under shear force**

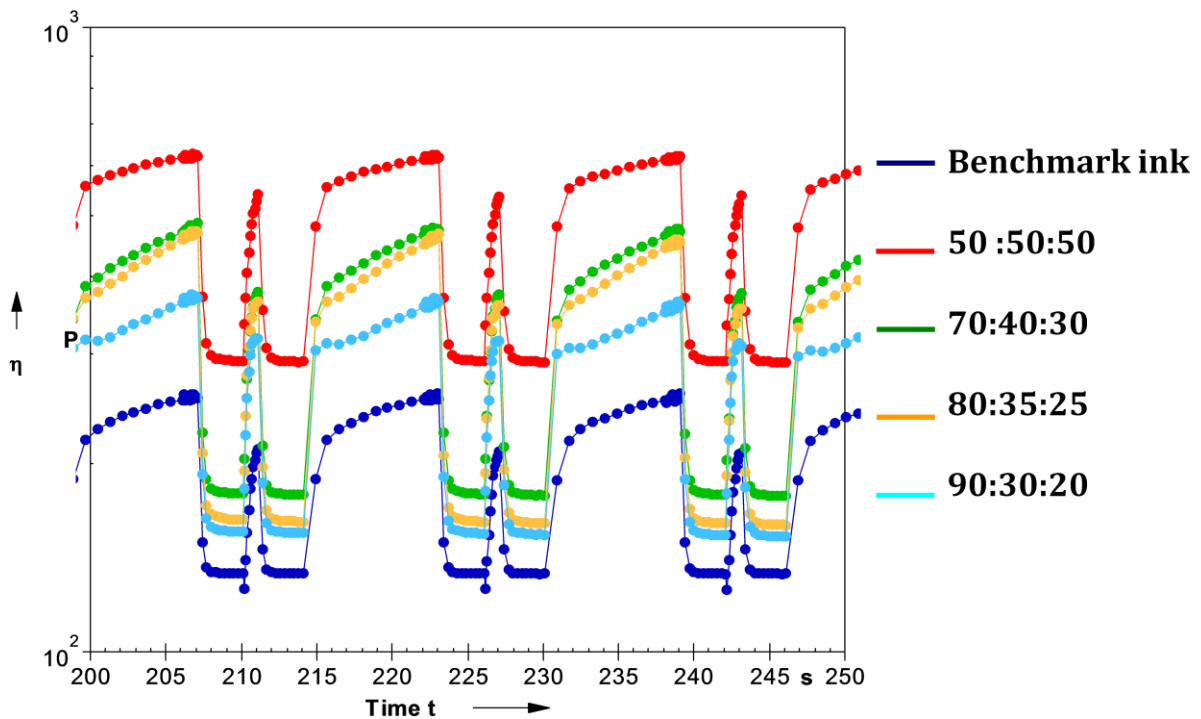


**Figure 4.44: Shear rate thixotropy loop of 62 wt% n-S-BT ink with 3 wt% total binder content and PVB: EC-2:3-at different EC-N4:N10:N22 ratios**

The shear rate thixotropy loop test represents the behaviour of the ink during multiple printing of MLCCs. As explained above during printing, the polymeric chains tend to break due to high shear rate applied but the ink has to recover quickly to its initial state to have similar multiple prints (Figure 4.43).

**Table 4.10: The effect of EC ratio on viscosities at different shear rate and thixotropic behaviour of the n-S-BT ink**

S.No.	EC ratio N4:N10:N22	0.1 s <sup>-1</sup>		40 s <sup>-1</sup>	Thixotropy	Printability
		Forward	Return			
1	50:50:50	1311	946	210	Small	Consistent
2	60:45:35				Large	Poor
3	70:40:30	550	400	153	Poor	Poor
4	80:35:25				Poor	Poor
5	90:30:20				Poor	Poor

From Figure 4.44, it is evident that with increasing of N4, the viscosity of the ink decreases with printing time due to the fact that the small polymeric chains require more time for recovery. Hence, the printability of the ink was found to be poor. Table 4.10 shows the comparison of the n-S-BT ink with different N4:N10:N22 ratio and it is evident that the ratio of 50:50:50 or 1:1:1 has lower viscosity with small thixotropy and consistent printability, satisfying the required characteristics for making MLCCs.

*The EC (N4:N10:N22) ratio of 1:1:1 has been found to show low viscosity with less thixotropy, quicker recovery and hence better printability.*

#### (v) Effect of total binder concentration

After the selection of PVB: EC ratio as 2:3 and N4:N10:N22 ratio as 1:1:1, the total binder concentration was varied as 3, 2.5, and 2 wt%. From Figure 4.45 and 4.46, it can be understood that with decreasing binder content, the viscosity decreases but the ink showed poor thixotropic behaviour. Figure 4.47 shows the stress sweep of the n-S-BT ink with different binder content. As explained in section, G' represents the storage modulus and G'' represents the loss modulus. The 3 wt% ink has higher storage modulus and the green strength compared to 2.5 and 2 wt%. Hence, 3 wt% binder was chosen to prepare desirable MLCCs.

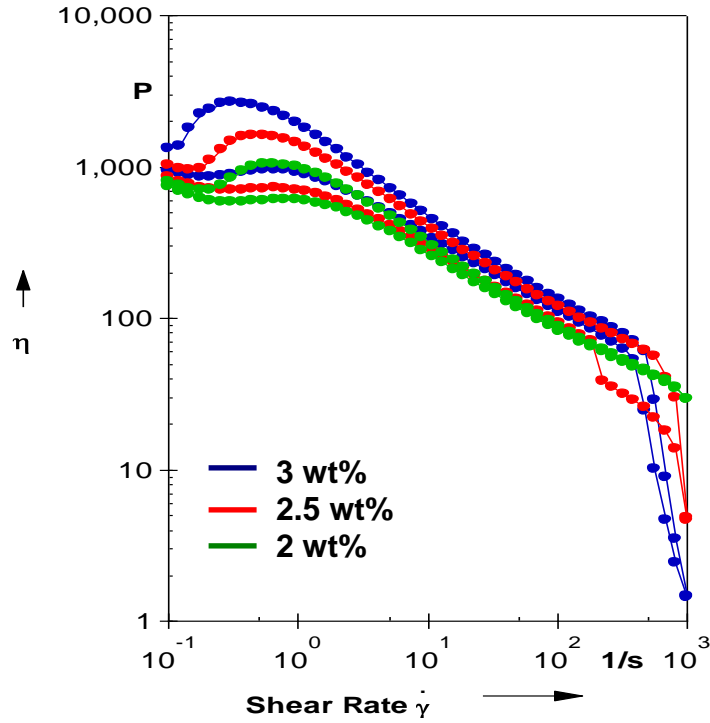


Figure 4.45: Viscosity curves of 62 wt% nano n-S-BT ink with PVB: EC-2:3, EC-N4:N10:N22-1:1:1 –varying the total binder content

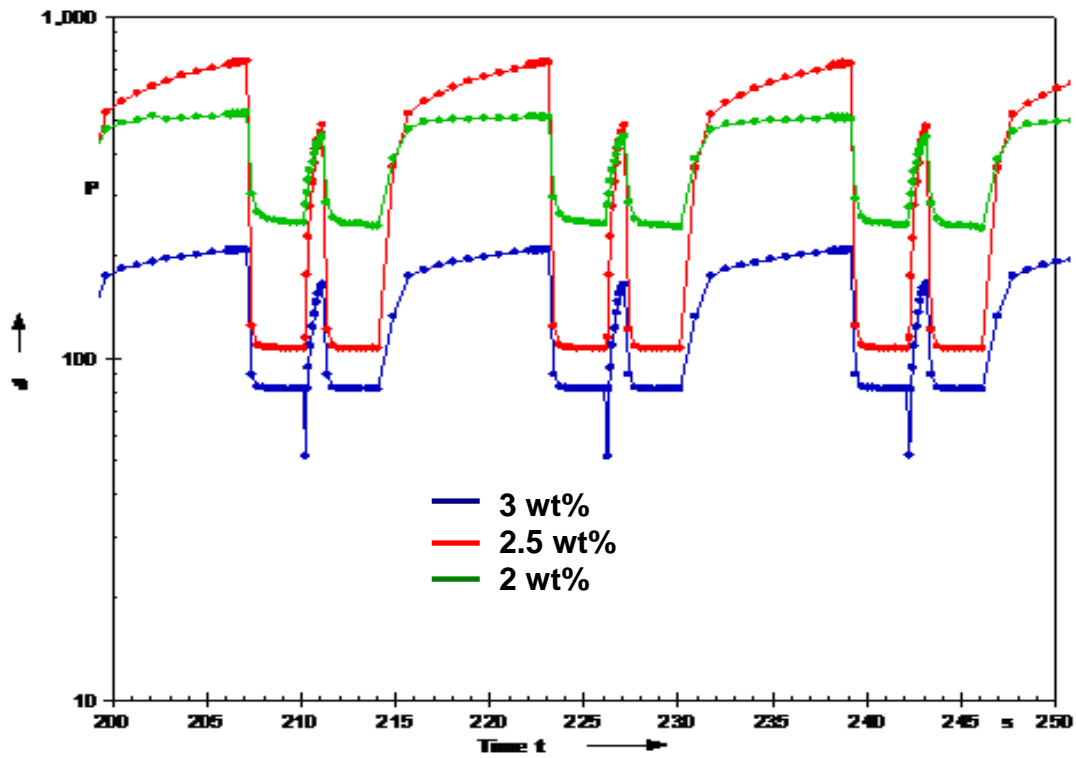


Figure 4.46: Shear rate thixotropy loop of 62 wt% nano n-S-BT ink with PVB: EC-2:3, N4:N10:N22-1:1:1 –effect of variation in total binder content

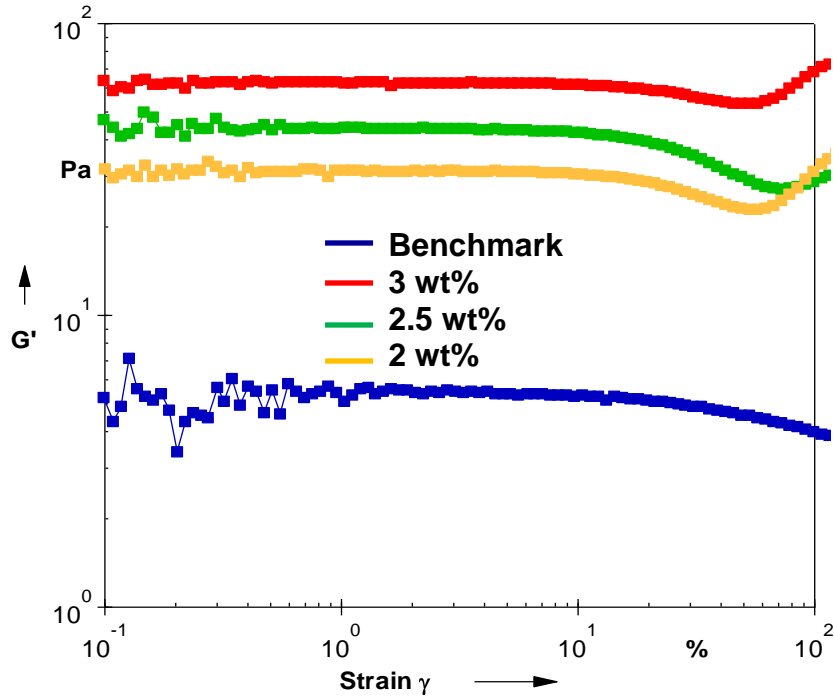


Figure 4.47: The stress sweep of the nano BT ink with varying binder content

*3 wt% total binder concentration with PVB: EC ratio of 2:3 and within EC a N4:N10:N22 ratio of 1:1:1 were used for further nano BT ink formulations.*

**(vi) Temperature characteristics of the optimized nano BT ink**

Based on the discussions above the optimized nano BT ink composition is identified as;

n-S-BT-	62 wt%	
Phosphate ester -	0.75 wt%	
Pine oil –	36.25 wt%	
Binder -	3 wt%-	{
	<b>2:3</b>	
	PVB-1.2 wt%	
	EC-1.8 wt%	
	<b>1:1:1</b>	
		{
		N4-0.6 wt%
		N10-0.6 wt%
		N22-0.6 wt%
Total-	100 wt%	

The temperature characteristics of the nano BT ink is very important during MLCCs manufacturing. As the multilayers of ceramic and electrodes (these inks are

proprietary to the sponsor) were printed simultaneously, the inks have to dry before printing the next layer. The viscosity of the inks were measured with increasing temperature (Figure 4.48) and from the slope of the curve, the flow resistance, or the energy required for the nano BT ink to flow against the fluid viscous force was calculated as described in section 3.3.2.

The minimum energy required for the powder particles to move/flow against the viscosity and strength of the binder/solvent system is referred as flow energy. This is important for the ceramic ink to flow and print during the screen printing process. The optimized n-S-BT ink softens at 80°C and requires more flow energy ( $39 \pm 2$  kJ/mol.K) compared to the  $\mu$ -BT ( $28 \pm 1$  kJ/mol.K) inks. As the particle size decreases, it requires more energy to flow against the high viscosity of the liquid.

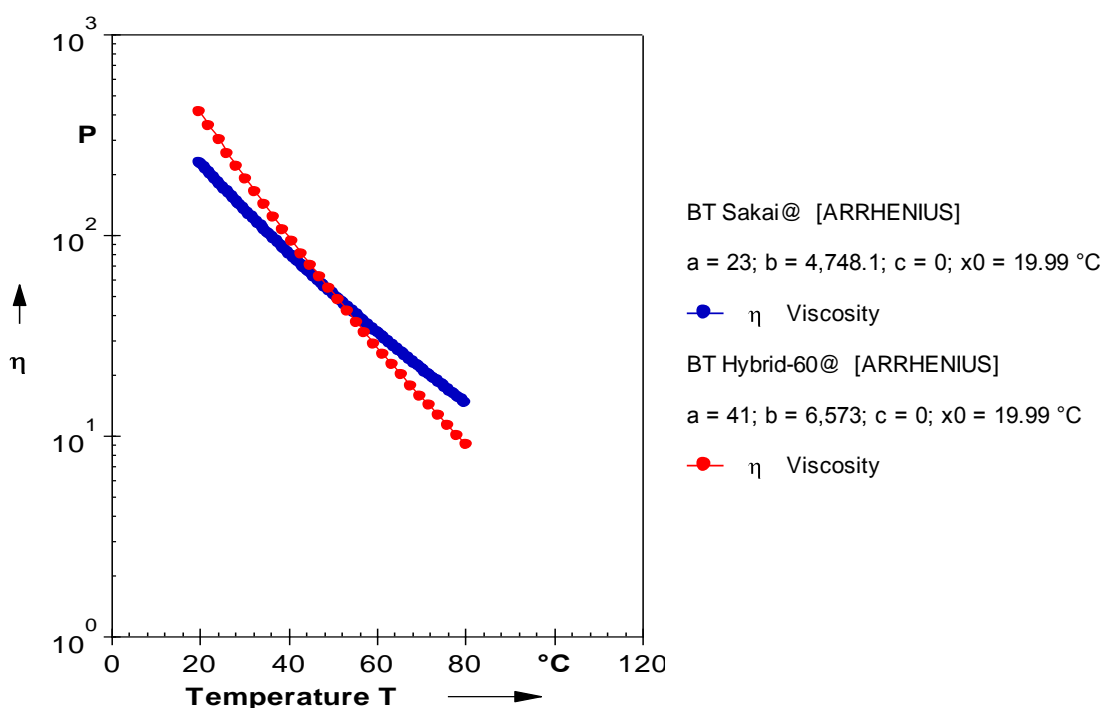


**Figure 4.48: Temperature characteristics of the nano BT inks**

**(vii) Printability of the nano BT ink**

*Lab trials:* Some of the preliminary studies on the printing conditions suitable for nano BT ink were carried out at Loughborough University. The squeegee pressure was varied as 6, 8 & 10 Kg for the constant snap off distance on 1.5 mm. It was found that the nano ink flowability was poor at 6 & 8 Kg force, a 10 Kg load was identified to be a desirable. The snap of distance was then varied from 0.5 to 2.5 mm in steps of 0.5 mm. It was found that at lower snap off distance (<1.5 mm) the print stick to the screen and this leads more pinholes. At higher snap off distance (>1.5 mm) the print does not flow uniformly. Hence 1.5 mm snap off distance was chosen as a suitable snap off distance. Attempts were also made to vary the substrate temperature and blow air temperature to mimic the industrial production conditions, however the restrictions of the small lab scale screen printer design does not provide accurate results. In addition the maximum squeegee speed achievable was 20 mm/sec for the printing trials at Loughborough University compared to 200 mm/sec squeegee speed used for production at Syfer Technology Ltd.

*Industrial trials:* The optimised n-S-BT ink developed at Loughborough University was screen printed to form multilayered ceramic capacitors with and without internal electrodes at Syfer Technology Ltd using the printing conditions given below in Table 4.11. The n-S-BT ink was found to print thinner layers (10  $\mu\text{m}$ ) compared to the  $\mu$ -BT ink (20  $\mu\text{m}$ ) and the ceramic layer thickness was consistent. The printability of the nano n-S-BT ink was good; it has good adhesion on the substrate but with some mesh marks. However, it has few lumps on the layer surface, had lots of porosity. Also, the n-S-BT ink exhibits slightly poor initial flow behaviour as shown in Figure 4.49. Moisture can get adsorbed in the pores and this can lead to lower dielectric permittivity & capacitance. The non-conformal ceramic layers can lower the breakdown voltage of the capacitors. This could be because of the high viscosity and high flow resistance of the fine particles compared to micron BT. Hence, a high-energy shear mixing is required to achieve homogeneous n-S-BT ink.



Table 4.11: Screen printing conditions used for making nano MLCCs

Parameters	Printing conditions
Substrate temperature	40°C
Blow air temperature	90°C
Squeegee pressure	10 ± 0.5 Kg
Squeegee speed	192 ± 30 mm/sec
Snap off gap	1.5 mm

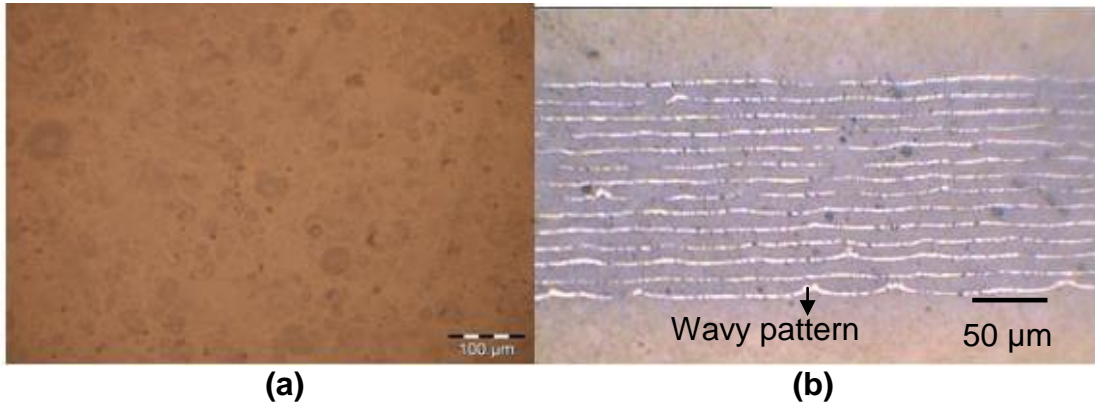


Figure 4.49: Optical picture of the n-S-BT ink prints (a) Top surface of the MLCC, (b) cross section of MLCC with electrodes

*Nano BT ink has poor flow behaviour compared to the micron BT ink*

#### 4.2.3. Characterization of green samples

The screen printed n-S-BT ceramic multilayers of 9.02 x 5.97 x 0.94 mm dimension and 3.2 g/cc ~53.2 ± 0.8% T.D (6.01 g/cc) green density was referred as n-S-BT chip and the micron BT as µ-BT chip. The weight loss during binder removal was about 8.5 ± 0.2%.

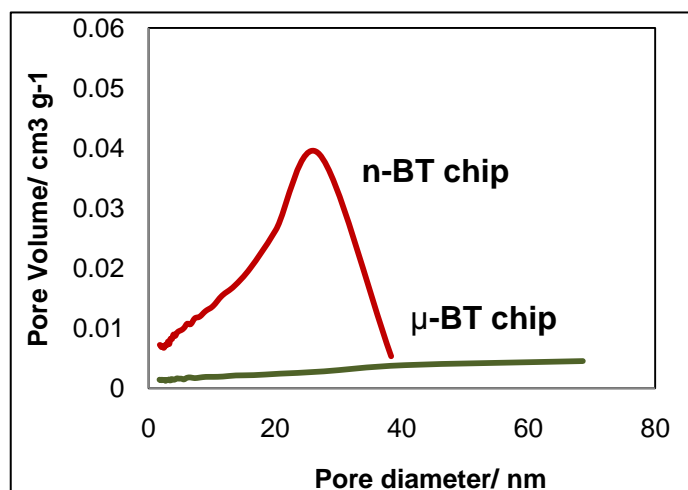


Figure 4.50: BET surface area analysis of the n-S-BT and  $\mu$ -BT chip

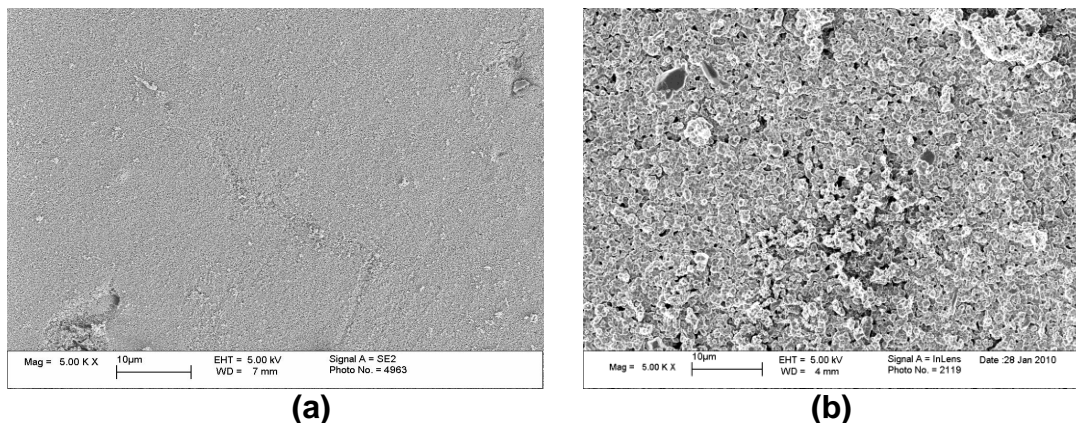


Figure 4.51: SEM micrograph on top surface of the (a) n-S-BT, (b)  $\mu$ -BT chip

The BET surface area analysis of the n-S-BT and  $\mu$ -BT chips (Figure 4.50) clearly showed that n-S-BT powder has small pore size and pore volume associated. The pore size of  $\mu$ -BT chip was beyond the capabilities of measurements of the current BET technique used which is  $<100$  nm. It is possible that the pores present in the  $\mu$ -BT samples could be larger than this and hence require techniques such as Mercury porosimetry. From the SEM micrograph of the n-S-BT chip, Figure 4.51, presence of small lumps were observed on the top surface of the n-S-BT chip. It is evident from Figure 4.51, the surface of  $\mu$ -BT chip was porous and shows some particle pull out.

### 4.3. Nano BT sintering and electrical performance optimization

#### 4.3.1. Dilatometer studies of Nano BT chip

To measure the linear shrinkage of n-S-BT and  $\mu$ -BT samples, dilatometric measurements were conducted with and without the presence of microwaves in a custom built hybrid cavity (refer section 3.41) and the results are plotted in Figure 4.52. During conventional heating, n-S-BT showed an onset sintering temperature of 1205°C whereas the corresponding temperature for  $\mu$ -BT was identified as 1275°C. As nanopowders usually have high surface free energy and highly reactive particle surface, reduction in sintering temperature ensued. Apart from the 70°C reduction in sintering temperature the n-S-BT also showed larger linear shrinkage (13.5%), Table 4.12.

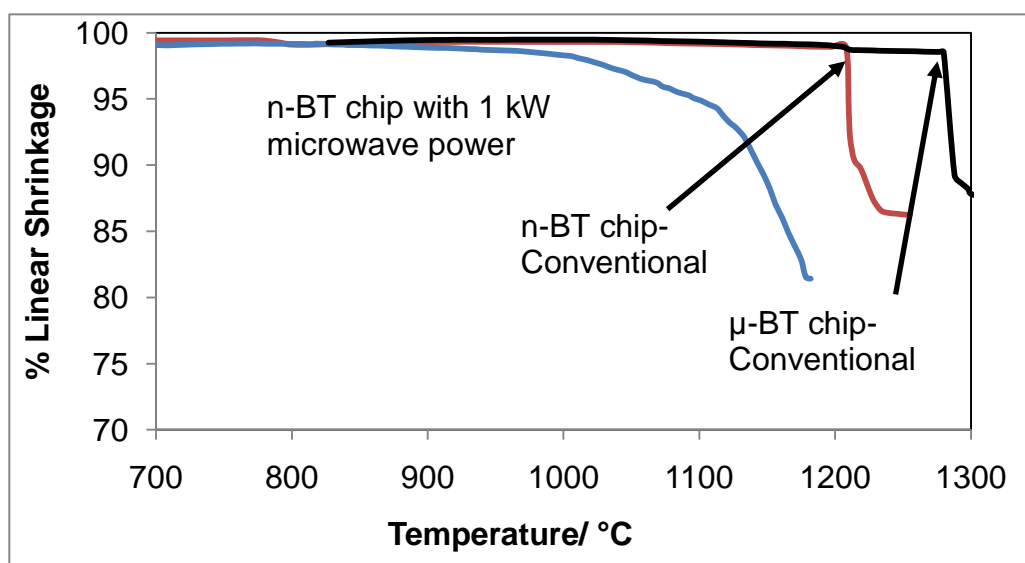


**Figure 4.52: Linear shrinkage Vs Temperature of n-S-BT and  $\mu$ -BT chip**

The sharp fall observed in the shrinkage curve is indicative of liquid phase formation- as explained in section 2.7.2, the presence of phosphorus residues from the phosphate ester in the green sample could result in liquid phase formation<sup>221</sup>. Since dilatometer studies were constrained to measure shrinkage in one dimension only, it may not adequately represent the volume shrinkage of the samples, for which bulk density measurements were performed, Table 4.12.

**Table 4.12: Onset of sintering for n-S-BT and  $\mu$ -BT chip at different heating condition**

Sample	Onset/ $^{\circ}$ C	Max. shrinkage Temperature/ $^{\circ}$ C	% Max. linear shrinkage	% T.D
$\mu$ -BT- 0 kW	1275	1310	12.5%	73%
n-S-BT -0 kW	1205	1200-1230	13.5%	80%
n-S-BT -1 kW	1060	1120-1170	19%	91%

Interestingly, by using 1 kW of microwave power, the sintering onset was found to be further lowered by 100 $^{\circ}$ C with maximum shrinkage/densification occurring between 1120-1170 $^{\circ}$ C. Since t-BT has inherent dipoles, it may readily couple with microwaves above 600 $^{\circ}$ C which could enhance the early stages of densification<sup>189</sup>.

*Thus, it is evident that the use of n-BT together with microwave power can lower the sintering temperature by 150 $^{\circ}$ C, which will play a vital role in further device cost reduction.*

#### 4.3.2. Sintering of n-S-BT chips

Prior to the sintering trials, a heating rate suitable for achieving high density and fine grain size was chosen. The samples were heated to the maximum temperature of 1200 $^{\circ}$ C at 5, 10 and 15 $^{\circ}$ C/min heating rates and the density, grain sizes were measured and the results were plotted in (Figure 4.53). From the graph, it was inferred that high density was obtained at a slower heating rate (5 $^{\circ}$ C/min) but resulted in larger grain size. At 10 $^{\circ}$ C/min heating rate, density was slightly low and the grain size was small. Both density and grain size saturated beyond 10 $^{\circ}$ C/min, hence 10 $^{\circ}$ C/min heating rate was chosen for further sintering studies.

A number of sintering trials were carried out on the n-S-BT chips at various temperatures (1000-1300 $^{\circ}$ C) and timings (1-20 h) using conventional heating at 10 $^{\circ}$ C/min.

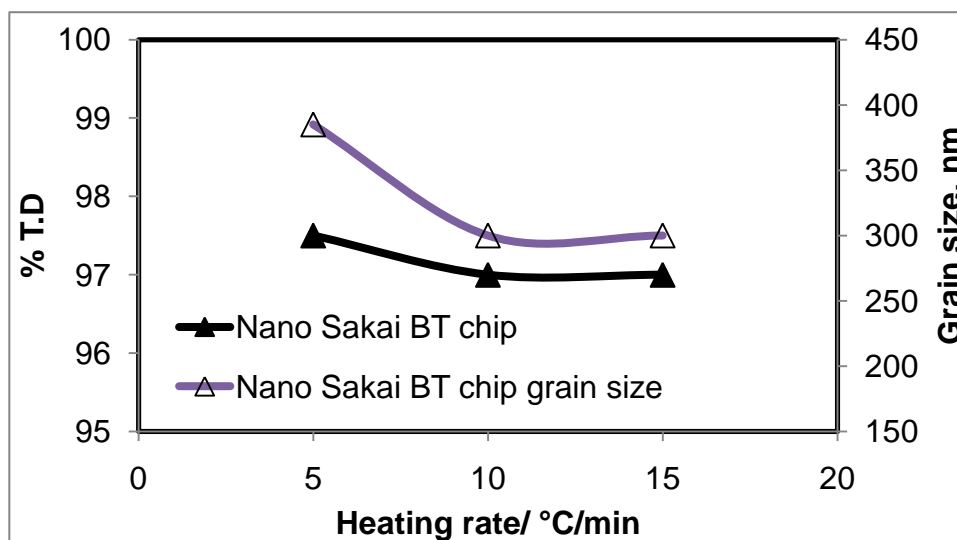


**Figure 4.53: Variation of density and grain size of the n-S-BT chips at various heating rate**

For a constant soaking period of 4 h and 2 h for 0 and 1 kW of microwave power levels respectively, sintering results were plotted in Figure 4.54. The n-S-BT chip showed a sharp increase in densification above 1100°C with maximum density of 95% T.D achieved at 1200°C, with further increase in temperature not showing any significant improvement in density. The results are corroborated with the dilatometry data. In conventional heating; <1200°C the grain growth was found to be less as the samples do not sinter well, at higher temperatures  $\geq 1200^\circ\text{C}$ , densification was found to have improved but resulted in abnormal needle shaped grains. The residual phosphorus segregates to the grain boundaries inhibiting grain growth until 1200°C and above which it reacted with BT forming a secondary phase, Barium phosphate  $[\text{Ba}_3(\text{PO}_4)_2]^{146}$  as reported. The presence of secondary phase would further degrade the electrical performance of the device.

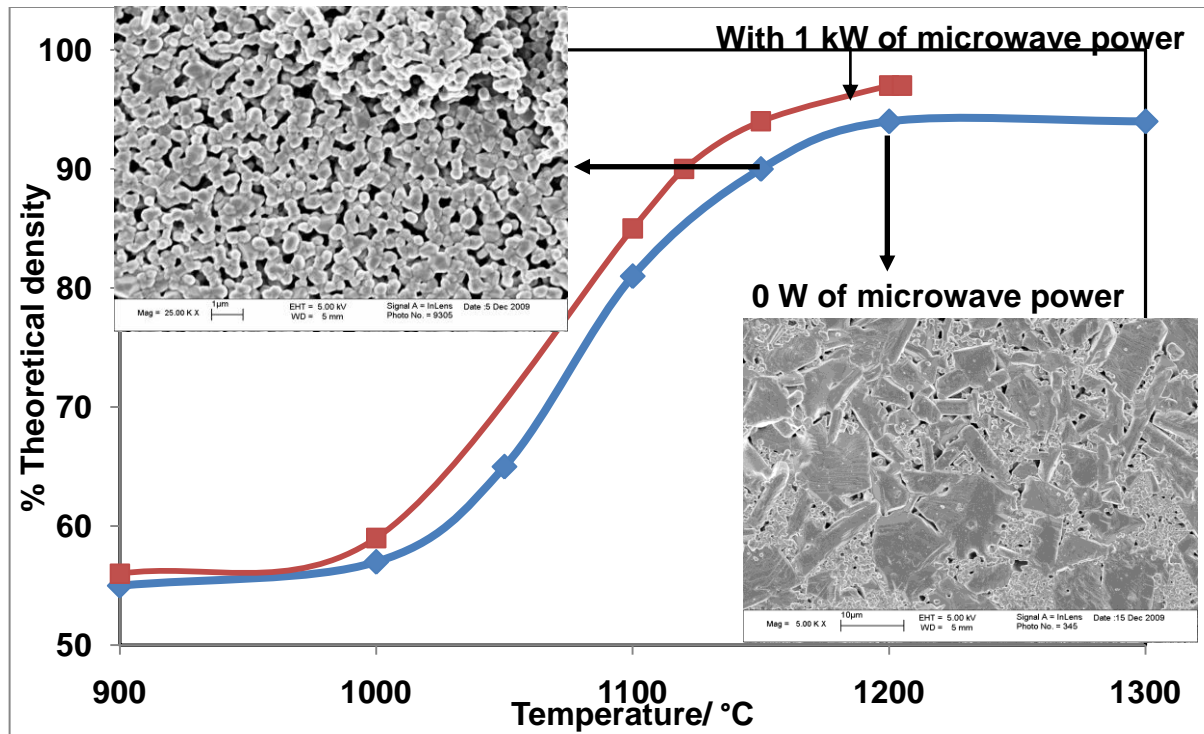


**Figure 4.54: Density of the sintered n-S-BT chip at various temperatures for 4 h and 2 h using 0 and 1kW of microwave power levels in hybrid heating. The insets indicate SEM micrographs of conventionally sintered samples at 1150, 1205°C respectively**

Since phosphorous added BT formulations involve liquid phase sintering, the shrinkage curve is quite sharp (small processing window) involving abnormal grain growth, it is highly unlikely to obtain maximum densification and minimum grain growth by employing standard conventional sintering procedures. Even a two stage sintering procedure often found to work well with nanocrystalline pure BT formulations<sup>222</sup> was no up to the task in this case, as described in Appendix-2. Hence microwave assisted sintering procedures were employed for the sintering of n-S-BT chips.

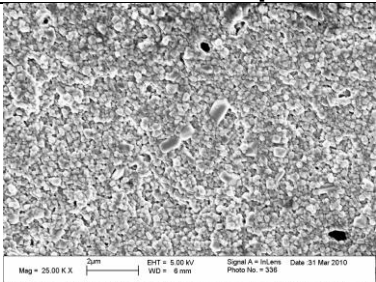
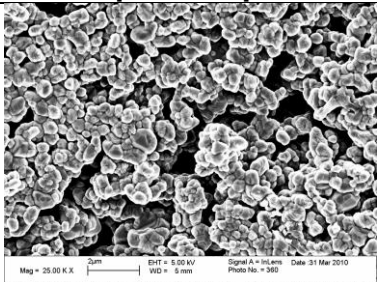
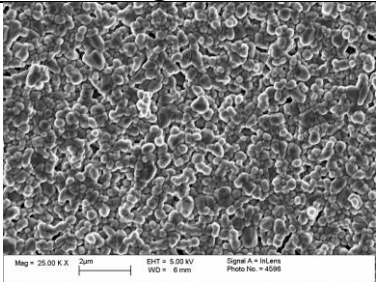
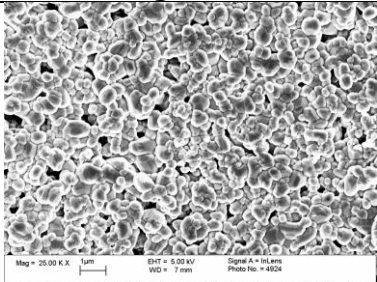
The n-S-BT chips were further sintered using pure microwave and hybrid heating at various temperatures (1120 - 1200°C), soaking times (30 min - 3 h) and at various microwave power levels. In pure microwave heating, the n-S-BT chip was found to be sintered between 1120 - 1150°C with minimal grain growth and without secondary phase formation. In hybrid heating conditions, 1205°C for 1 h with 1 kW



of microwave power resulted in a maximum density of >98% T.D with 300-400 nm average grain size. At higher temperature >1205°C abnormal grain growth was noticed. Thus though the densification behaviour of n-S-BT chip was found to be similar in both conventional and microwave heating, the fact that the higher densification was achieved in microwave assisted heating at any given temperature, Figure 4.54.

The SEM micrographs of the n-S-BT &  $\mu$ -BT chip sintered using conventional and hybrid heating at 1205°C were shown in Table 4.13. The densification of both n-S-BT and  $\mu$ -BT chip was found to be enhanced (on set of sintering lowered by -100°C) when using microwaves.

**Table 4.13: SEM micrograph of the n-S-BT and  $\mu$ -BT chip sintered using different heating methods**

Sample	n-S-BT chip	$\mu$ -BT chip
1205°C- 8h- CON	 <p style="text-align: center;"><b>~4.9 g/cc~83%</b></p>	 <p style="text-align: center;"><b>~4.0 g/cc~67%</b></p>
1205°C- 2 h- 1 kW	 <p style="text-align: center;"><b>&gt; 5.8 g/cc ~ 98%</b></p>	 <p style="text-align: center;"><b>5.3 g/cc ~88%</b></p>

### 4.3.3. Electrical properties of the n-S-BT powder

The measured relevant electrical properties (as mentioned in section 3.4.2) of the n-S-BT and  $\mu$ -BT chips sintered using different heating methods were given in Table

4.14. The n-S-BT has high capacitance compared to the  $\mu$ -BT chip. The dielectric permittivity of the n-S-BT chip at 1150°C for 1 h using microwave heating was comparable to the  $\mu$ -BT chip sintered at 1250°C for 4 h using conventional heating, leading to a 100°C reduction in processing temperature. As the dielectric permittivity depends on densification and grain size, microwave sintered n-S-BT resulted in better dielectric permittivity.

**Table 4.14: The representative room temperature electrical properties of the n-S-BT and  $\mu$ -BT chips sintered at different conditions measured at 1 kHz & 1 V**

Sample	Sintering condition	Density, % T.D	Cap, pF	$\epsilon_r$	IR, ohms	Dissipation factor, %
<b>Expected range</b>			$\geq 600$	$\geq 3500$	$\geq 1000$	0.5-1
<b>n-S-BT</b>	1250°C-4 h-CON	93%	751	4668	150	0.8
	1150°C-1 h-MW	76%	673	5247	200	1.1
	1205°C-1 h-1 kW	99%	708	4768	600	0.7
<b><math>\mu</math>-BT</b>	1250°C-4 h-CON	87%	691	5369	50	3.1
	1150°C-1 h-MW	72%	134	1163	40	7

The n-S-BT has shown a lower dissipation factor compared to the  $\mu$ -BT chips as these values are inversely proportional to the sintered density. Dissipation factor represent the dielectric loss ( $\tan\delta$ ) of the capacitance. The lower dissipation factor is very important for capacitor applications, since a high loss value will lead to heat generation during device operation, the heating can damage the components and circuits.

The n-S-BT sintered chips have shown better insulation resistance than  $\mu$ -BT chips. However, the overall values are lower than expected. As explained in section 2.2.6, the insulation resistance is inversely proportional to the grain size. Therefore, the n-S-BT chip that had a finer grain structure was found to have higher insulation resistance compared to  $\mu$ -BT.

Thus with overall comparison of the key electrical properties like capacitance, dielectric permittivity, dissipation factor except insulation resistance, the n-S-BT sintered at 1150°C performs better than the  $\mu$ -BT sintered at 1250°C. The grain boundary structure is responsible for insulation resistance (IR) and in pure BT since



core shell structure is not well developed (dopants and additives are crucial for its evaluation) as compared to doped commercial capacitors, the observed IR was lower. To improve IR, doping studies were performed as described in section 3.3.2

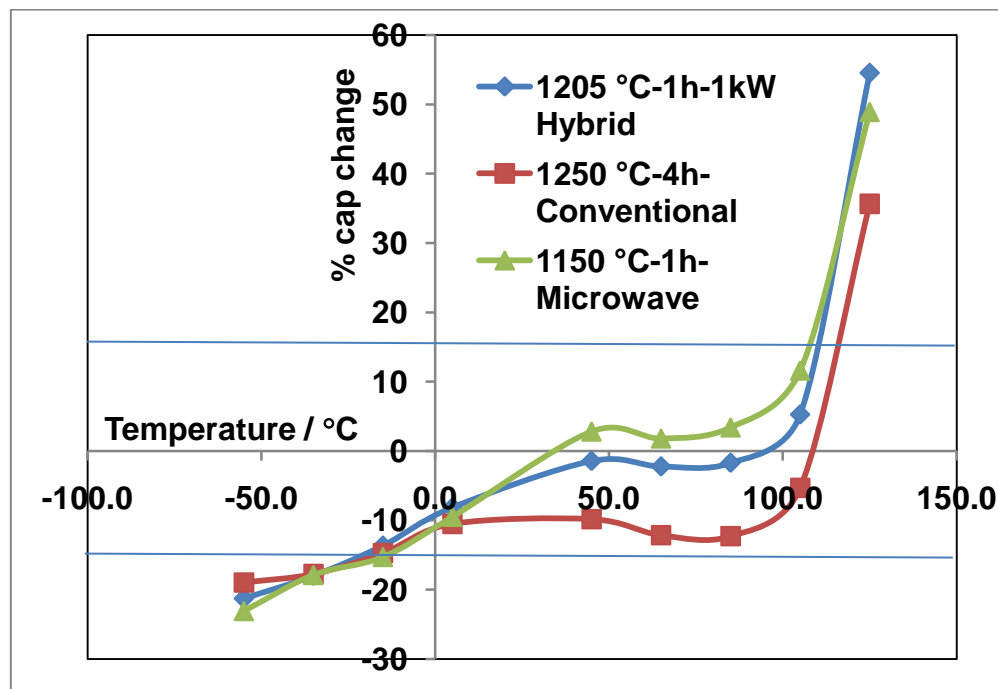


**Figure 4.55: Temperature change of capacitance (with reference to room temperature) of n-S-BT chip sintered using conventional, microwave and hybrid conditions**

The temperature change of capacitance (TCC) characteristics of the n-S-BT chip sintered using different heating methods is shown in Figure 4.55. TCC is another crucial property for the capacitors. It gives the relation between the capacitance and operating/working temperature, thus indicates the reliability of the device. As all the samples are made of pure BT, it does not have a proper core-shell structure as described above and hence it undergoes the phase transition temperature ( $\sim 125^{\circ}\text{C}$ ). Hence, to improve the insulation resistance, the dissipation factor, and the temperature change of capacitance for X7R characteristics, the BT has to be doped to create an insulating grain boundary phase which helps to form the desirable core shell structure<sup>223</sup>.

#### 4.4. Effect of dopants on sintering and electrical performance

##### 4.4.1. Characteristics of the dopants

The proprietary dopants containing some of the oxides of Er, Yb, Co, Sm, Dy, Ce, Nd, Nb, Y, La, Si, etc. were obtained from Syfer Technology Ltd. to achieve the core shell structure suitable for providing X7R characteristics. The as-received dopants has a primary particle size of  $\sim 0.2 \mu\text{m}$  and agglomerate size of  $0.65 \mu\text{m}$  &  $2 \mu\text{m}$  with a surface area of  $7.85 \text{ m}^2/\text{g}$ . Since the as-received dopants had big agglomerates, Figure 4.56, a micronizer was used (to break the agglomerates; different milling times of 5-10 min were employed). A 5 minutes micronization helped to crush the bigger agglomerates of  $\sim 2 \mu\text{m}$ , Figure 4.57, but there was no effect noticed on the smaller agglomerates ( $\sim 0.65 \mu\text{m}$ ). With increase in micronising time no further improvement noticed.

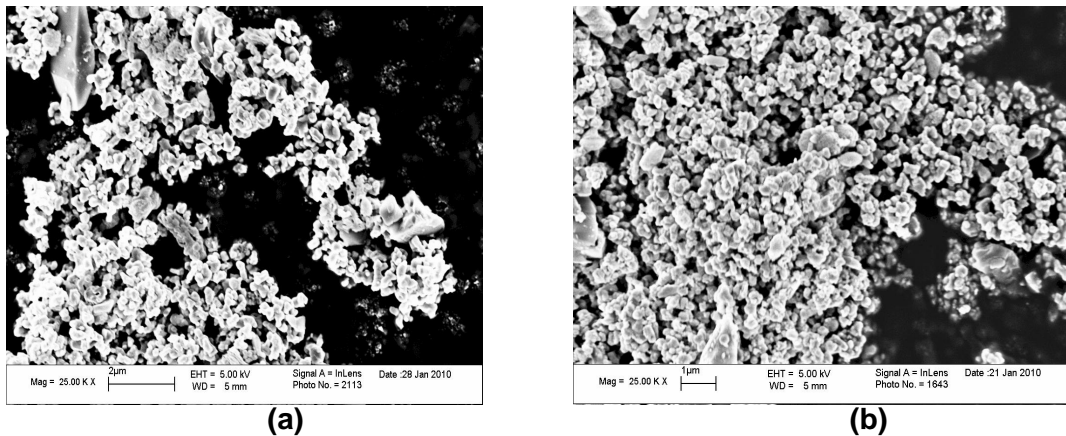


Figure 4.56: SEM micrograph of the dopants (a) as received and (b) after 5 min of micronization

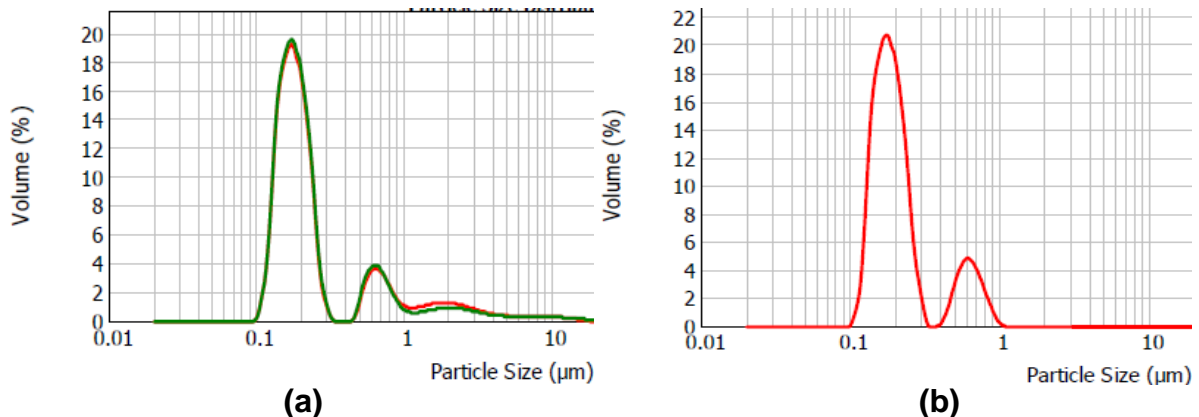


Figure 4.57: Agglomerate size distribution of the (a) as received & (b) after 5 min of micronization

#### 4.4.2. Effect of dopants on the sintering kinetics

The dilatometer curves of n-S-BT with 2.5 wt% of dopant ink derived compacts are shown in Figure 4.58. The onset sintering temperature of n-S-BT was found to be lowered by  $\sim 100^\circ\text{C}$  (curves 1 and 3) when using 2.5 wt% of dopants with the maximum shrinkage noticed between  $1100\text{--}1150^\circ\text{C}$ . The addition of dopants was known to form various reactive liquid phases<sup>224,225</sup>. The formation of these phases can help to enhance the densification and reduce the sintering temperature.

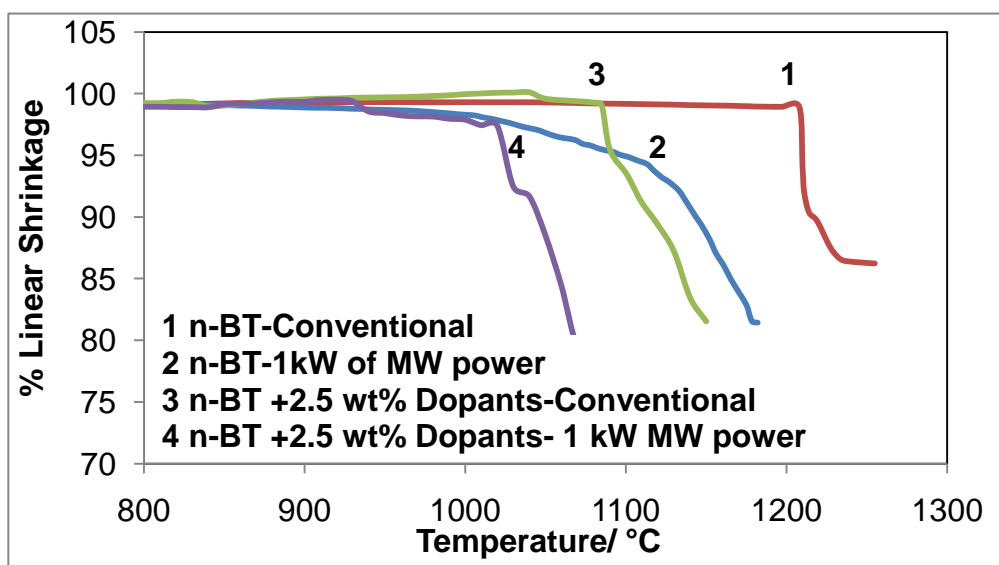


Figure 4.58: Shrinkage Vs Temperature of the n-S-BT with 2.5 wt% of dopants (MW-Microwave power)

Table 4.15: Onset of sintering for nano Sakai BT powders with 2.5wt% dopants

Sample	Onset/ $^\circ\text{C}$	Max. Shrinkage/ $^\circ\text{C}$	% Max. 1D Shrinkage	% T.D
n-S-BT -0 kW	1205	1230	13.5%	80%
n-S-BT -1 kW	1060	1230	19%	91%
n-S-BT -2.5 wt% dopants	1080	1100-1150	19%	80%
n-S-BT -2.5 wt% dopants-1 kW	1020	1080-1120	20%	85%

Using 1 kW of microwave power, the onset sintering was further reduced by another  $50^\circ\text{C}$  when compared to conventional heating. This could be due to the better microwave coupling characteristics of the dopants added as noticed in their dielectric properties, Table 4.16.

Table 4.16: Dielectric properties of the n-S-BT and Dopants

Materials (measured at R.T)	$\epsilon'$	$\epsilon''$
n-S-BT powder	6.34	0.17
Dopants powder	3.8	0.04
n-S-BT+2.5 wt% dopants	6.64	0.14
n-S-BT+2.5 wt% dopants Heat treated powder at 1000°C – re-measured at RT	22.2	0.5

*Addition of dopants with microwave heating was found to reduce the sintering temperature by ~150°C.*

#### 4.4.3. Optimising the amount of dopants

For the initial optimization, the n-S-BT ink derived compacts (prepared as per section 3.3.2) were sintered using conventional and microwaves heating. The sintered densities of the n-S-BT ink derived compacts with varying amount of dopants such as 0, 0.5, 1, 1.5, 2, 2.5 and 3 wt% is tabulated in Table 4.17. The sintered density was found to increase with increasing amount of dopants. A maximum density of 94% T.D was achieved with 2.5 wt% of dopants at 1205°C for 2 h in conventional heating. Similar density of 94% T.D could be achieved at 1120°C itself for 1 h when using microwave heating and the maximum density of 98% T.D was achieved at 1150°C for 1 h.

Table 4.17: Sintered densities of n-S-BT with different amount of dopants

Dopants, wt %	Conventional heating, % T.D			Microwave heating, % T.D	
	1200°C/ 2 h	1205°C/2 h	1225°C/2 h	1120°C/1 h	1150°C/ 1 h
0	82	82	93	72	76
1	90	91	87	91	93
1.5	90	91	87	92	93
2	92	94	93	93	93
2.5	92	94	94	94	>98



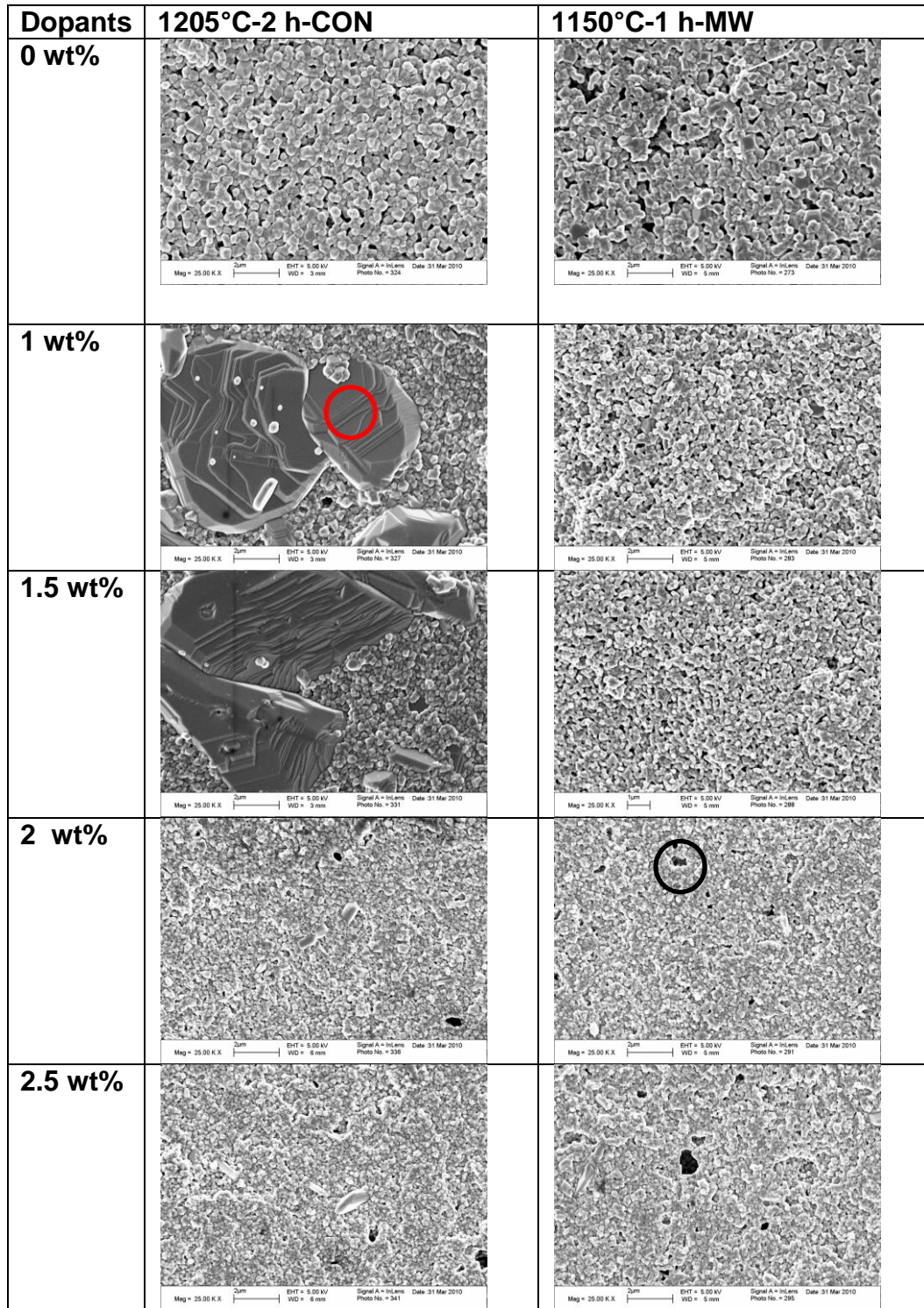


Figure 4.59: Microstructures of the surface of n-S-BT sintered with varying amount of dopants using different type of heating

○ Abnormal grains      ○ Porosity

Some of the dopant elements such as Nb, Y can also act as grain growth inhibitors<sup>224</sup>. At lower concentrations the distribution of dopants was not found to be uniform and this resulted in abnormal grain growth, as shown in Figure 4.59. With increasing the dopant concentration, the dopants were found to be uniformly distributed. With 2.5 wt% of dopants addition a density of >98% T.D was achieved at 1120°C using microwave heating.

However, the critical aspect for that finalises the dopant amount required for n-S-BT is the electrical performance, see Table 4.18. At lower dopant concentration, the amount of grain boundary phase formed was very low which resulted in poor insulation resistance. At higher dopant concentration ( $\geq 1.5$  wt%) the dopants may be uniformly distributed at the grain boundaries, forming a better grain boundary microstructure and hence resulted in good insulation resistance. In addition, with increasing dopant concentration the TCC characteristics were also found to improve and the required X7R characteristics was achieved at  $\geq 2$  wt% dopant addition, Figure 4.60. As discussed earlier in section, the dopants reacted with n-S-BT grains, partially replace the Ba and Ti cation forming a pseudo cubic structure at the grain boundary<sup>50</sup>. Hence the usage of optimum amount of dopants was critical to achieve the commercial level of acceptable electrical performance. This was achieved at 2.5 wt% dopants addition for n-S-BT. Notably the amount of dopant required for n-S-BT (2.5 wt%) is less than the  $\mu$ -BT ( $\geq 3$  wt%). Although n-S-BT has more grain boundaries the grain boundary phase may be thinner compared to  $\mu$ -BT. Though the grain boundary phase increases the insulation resistance it tends to decrease the dielectric permittivity and dissipation factor. The specific composition to improve all the relevant electrical properties is a subject of an ongoing patent application.

**Table 4.18: The room temperature electrical performance of the n-S-BT with different dopants concentration sintered at 1120°C for 1 h using microwave heating at 1 kHz and 1 V**

Dopants	Conditions	Cap, pF	Dissipation Factor, %	IR GOhms	Dielectric permittivity
<b>Target</b>		<b>808</b>	<b>0.5</b>	<b>3000</b>	<b>3800</b>
0 wt%	1120°C/1 h/MW	771	13.4	3	3907
0.5 wt%	1120°C/1 h/MW	659	17.1	6	3275
1 wt%	1120°C/1 h/MW	554	9.3	7	3273
1.5 wt%	1120°C/1 h/MW	633	0.7	2000	3208
2 wt%	1120°C/1 h/MW	413	0.4	2000	2116
2.5 wt%	1120°C/1 h/MW	516	0.4	3000	2760

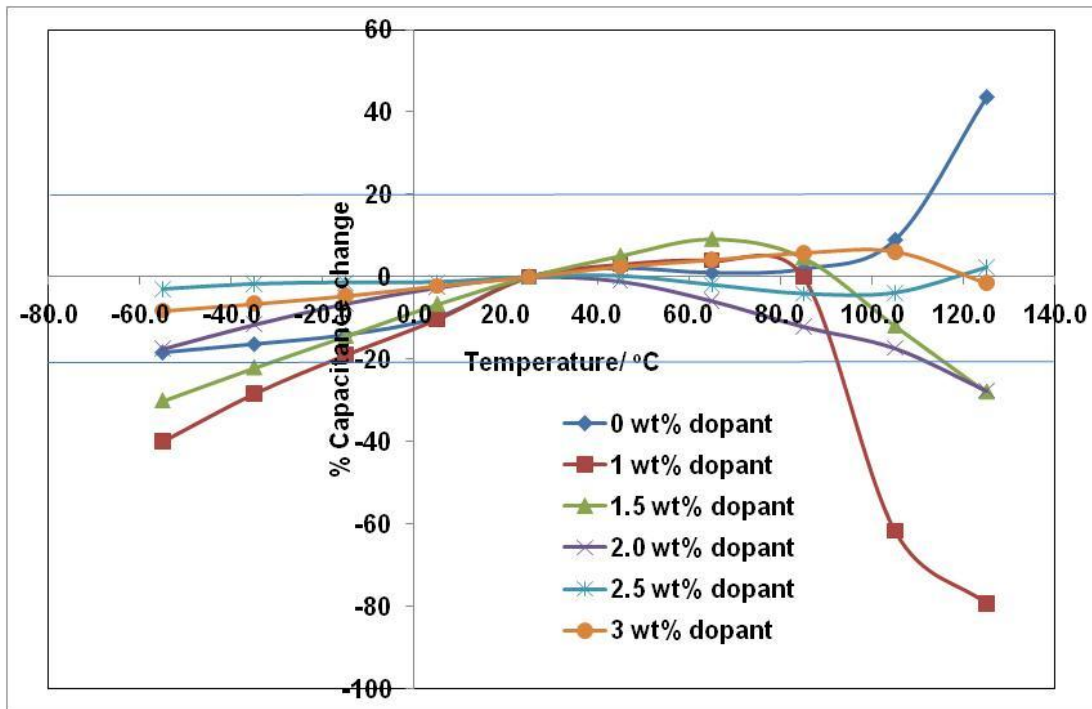


**Figure 4.60: Temperature change of capacitance (with reference to room temperature) of the n-S-BT with different dopant concentrations sintered at 1120°C for 1 h using microwave heating**

*The optimised dopant level for n-BT was identified to be 2.5 wt% to achieve the required insulation resistance and X7R characteristics.*



4.4.4. Sintering of nano MLCCs

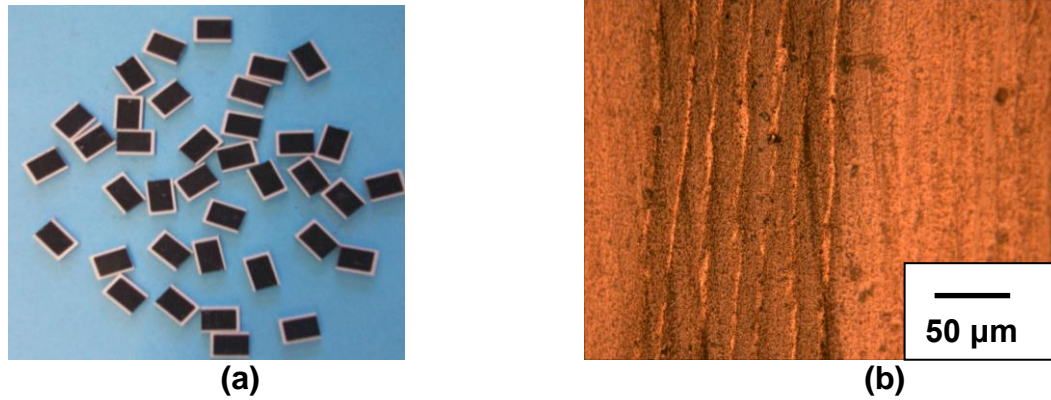


Figure 4.61: (a) Picture of nano MLCCs made (b) Optical micrograph of the nano MLCCs

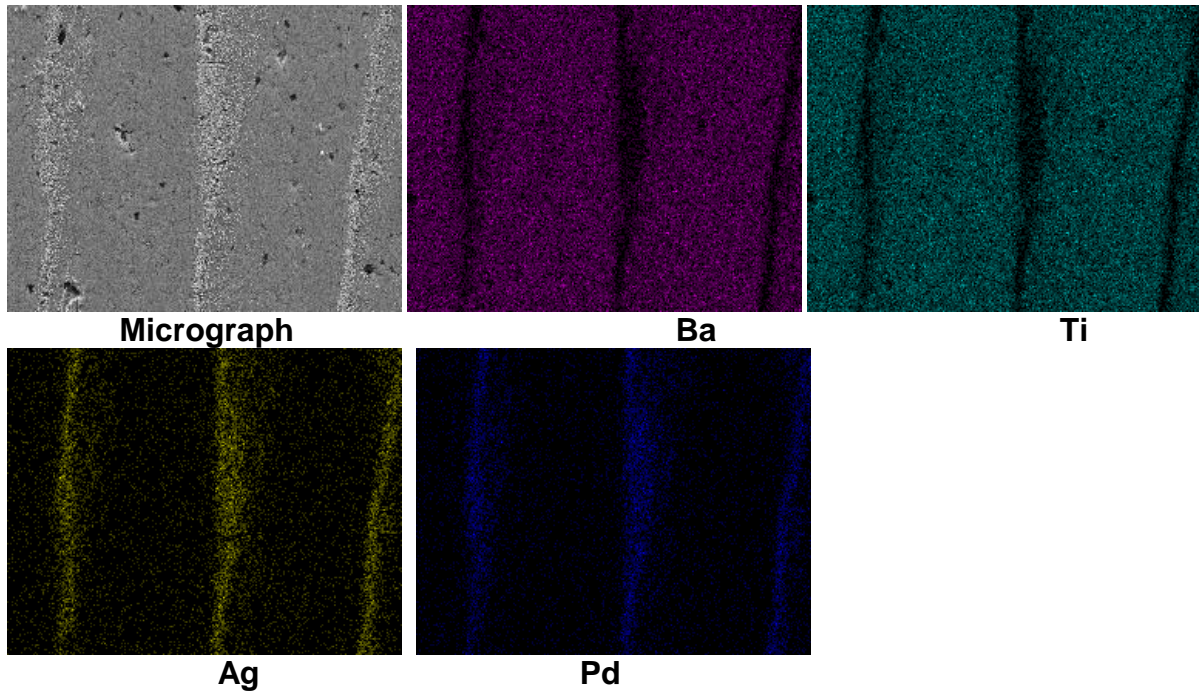


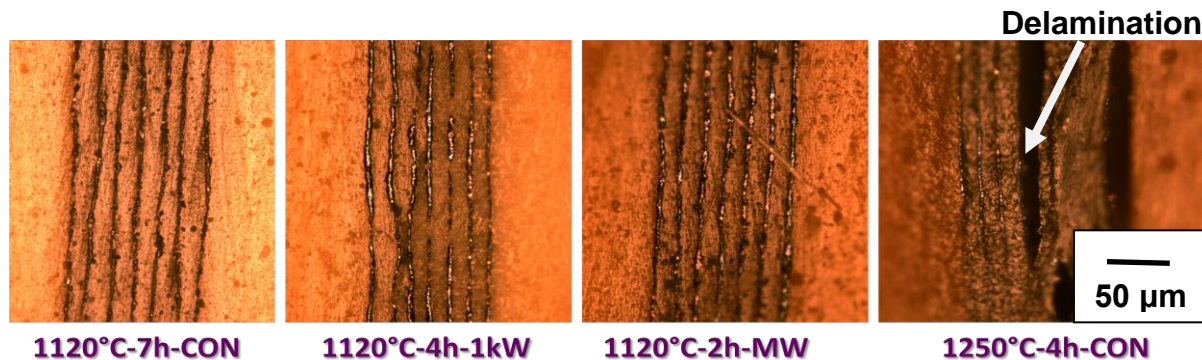
Figure 4.62: Elemental mapping of the binder removed nano MLCCs

Table 4.19: The densities of the nano MLCC sintered at different conditions (For MLCCs the exact value of theoretical density was unknown. Hence absolute values were given)

Heating method	1120°C		1150°C	
	Time, h	Density, g/cc	Time, h	Density, g/cc
Conventional	7 h	5.5	4 h	5.6
Hybrid-1kW	4 h	5.6	2 h	5.7
Microwave	2 h	5.7	1 h	5.7



The n-S-BT with 2.5 wt% dopants ink was used to make a multilayer ceramic capacitor device (nano MLCC) of 5.28 x 3.82 x 0.98 mm dimension with 10-20  $\mu\text{m}$  ceramic layer thickness. The green density of the chip was found to be 3.5 g/cc (Figure 4.61) through screen printing process at Syfer Technology Ltd. 30:70 Ag-Pd alloys were used as an electrode material. The nano MLCC consisted of 14 electrode layers. The electrodes were found to be intact without any delamination (Figure 4.62). There was no electrode migration into the ceramic layers noticed – which is a common problem in MLCCs manufacturing involving Ag electrodes<sup>226</sup>. Thus, in the green samples optimised doped n-S-BT ink formulation prepared at a laboratory was successfully translated to the factory floor to fabricate MLCCs devices.



**Figure 4.63: Optical micrographs (at the same magnification) of the nano MLCCs sintered using different types of heating at 1120°C and 1150°C**

The nano MLCCs were sintered at different conditions using conventional, microwave, and hybrid heating and the densities are tabulated, Table 4.19. In all the heating methods, the nano MLCCs started to sinter at 1120°C itself. The nano MLCCs was sintered to a maximum density of 5.7 g/cc using microwave assisted heating.

In conventional heating, at higher temperatures ( $>1200^\circ\text{C}$ ), the electrodes were found to be delaminated and buckled due to the differential shrinkage of the electrode and ceramic materials<sup>227</sup>. At lower temperatures ( $<1200^\circ\text{C}$ ), there was no necking of the electrode particles noticed, Figure 4.63.

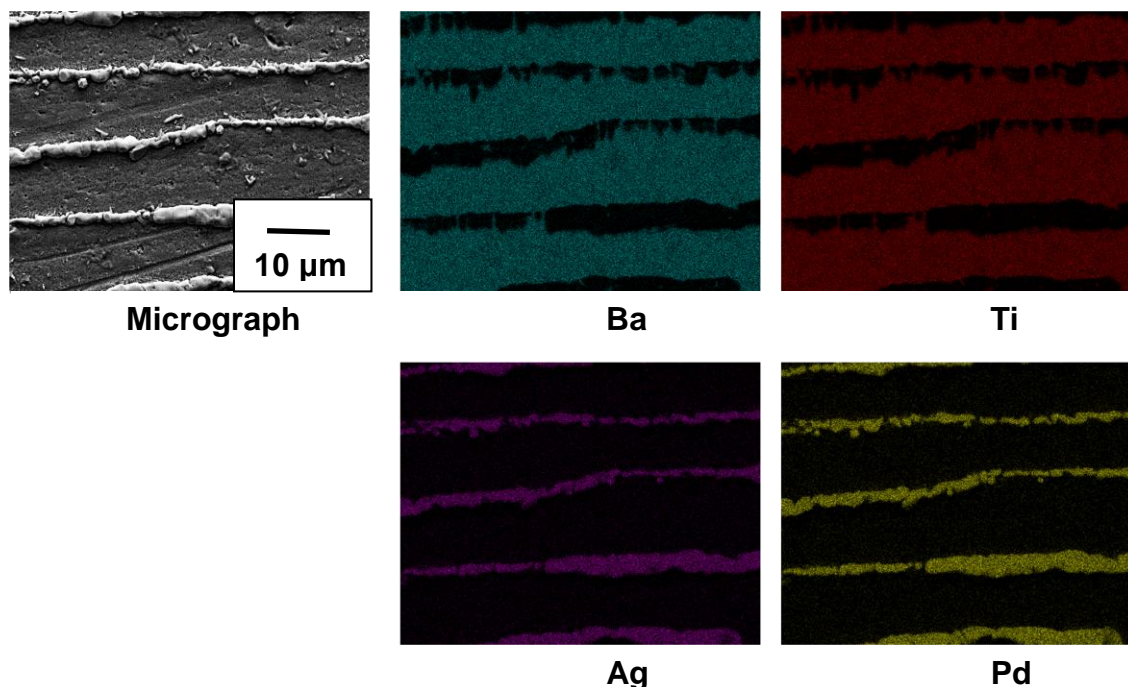


**Figure 4.64: Elemental mapping of the nano MLCC sintered at 1120°C for 1 h using microwave heating**

The microwave assisted heating resulted in higher density and up to 1150°C the samples do not show any electrode delamination or buckling. Further microwaves were found to enhance the necking of electrode particles at 1120°C itself. The elemental mapping shown in Figure 4.64, clearly proves that there is no electrode metal diffusion into the ceramic layer and the electrodes were intact.

#### 4.4.5. Electrical properties of the n-S-BT powder with dopants

**Table 4.20: Room temperature electrical properties of the nano MLCCs with 2.5 wt% dopant sintered using different heating method at 1 kHz & 1 V**

Conditions	Dissipation Factor, %	Dielectric permittivity
1150°C/1 h/MW	0.65	1800
1150°C/2 h/ 1kW	0.6	1665
1150°C/4 h/ CON	0.5	1540

The electrical performance of the nano MLCCs sintered at 1150°C using different heating methods were given in Table 4.20 and the TCC characteristics shown in Figure 4.65. It is evident that at the same temperature, the microwave-sintered nano MLCCs were found to have higher dielectric permittivity with less

dissipation factor and better thermal stability than conventionally sintered samples.

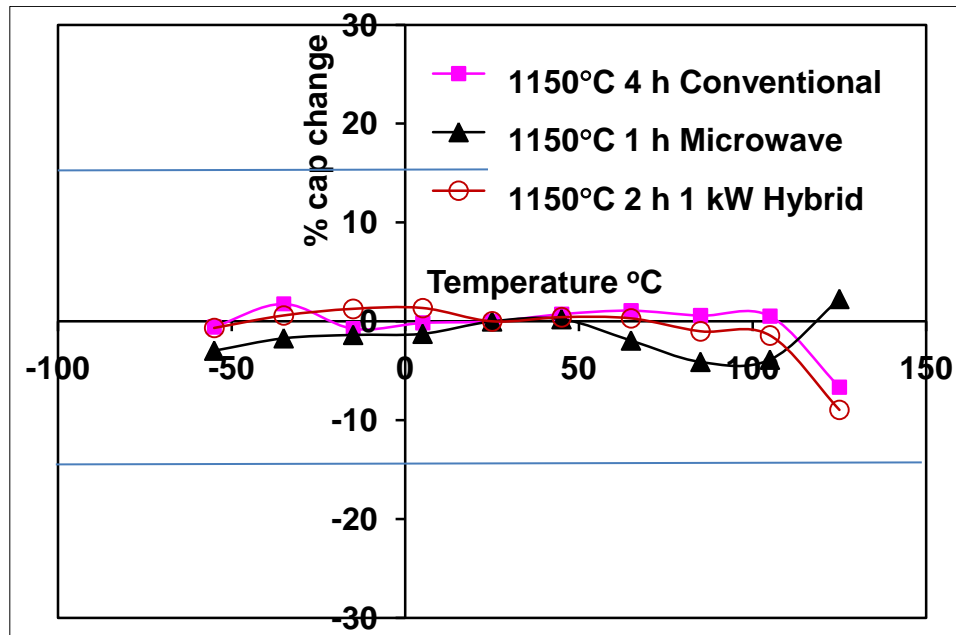


**Figure 4.65: Temperature change of capacitance (TCC) for nano MLCCs sintered using different heating methods**

*Electrical performance of microwave sintered nano MLCCs sintered at 1150°C was found to match with the expected electrical performance and X7R characteristics.*

#### 4.5. Effect of glass frits addition

As mentioned earlier in section 2.8.1, the sintering conditions can be further reduced by using glass frit as sintering aid. Six different glass frit compositions were selected based on their suitability to use with MLCCs. The glass properties such as softening temperature, density, coefficient of thermal expansion, dielectric permittivity were used as pointers during down selection. The details of the composition and properties of the six glass frits were tabulated in Table 4.21

Table 4.21: List of glass frits chosen for the present study

Glass frit	Composition	Content	Softening temperature	Crystallization temperature	Density, g/cc
GF1	B <sub>2</sub> O <sub>3</sub>	15%	520-528 °C	NA	5.4
	ZnO	1-10%			
	Al <sub>2</sub> O <sub>3</sub>	1-10%			
	TiO <sub>2</sub>	1-10%			
	SiO <sub>2</sub>	2-15%			
	Bi <sub>2</sub> O <sub>3</sub>	>70%			
GF2	B <sub>2</sub> O <sub>3</sub>	19%	537-540 °C	NA	5.1
	ZnO	15-35%			
	Al <sub>2</sub> O <sub>3</sub>	1-10%			
	SiO <sub>2</sub>	1-10%			
	Bi <sub>2</sub> O <sub>3</sub>	30-50%			
	Sn <sub>2</sub> O <sub>3</sub>	<1%			
	Cr <sub>2</sub> O <sub>3</sub>	1.5%			
GF3	ZnO	5-25%	805 °C	885 °C	3.7
	Al <sub>2</sub> O <sub>3</sub>	2-15%			
	SiO <sub>2</sub>	30-50%			
	Sn <sub>2</sub> O <sub>3</sub>	<1%			
	BaO	30-50%			
	ZrO <sub>2</sub>	1-10%			
	CaO	1-10%			
GF4	B <sub>2</sub> O <sub>3</sub>	23%	720 °C	NA	3.7
	Al <sub>2</sub> O <sub>3</sub>	2-15%			
	SiO <sub>2</sub>	15-35%			
	BaO	30-50%			
GF5	B <sub>2</sub> O <sub>3</sub>	16%	725 °C	NA	3.6
	Al <sub>2</sub> O <sub>3</sub>	1-10%			
	SiO <sub>2</sub>	30-50%			
	BaO	30-50%			
GF6	B <sub>2</sub> O <sub>3</sub>	7.2%	730 °C	NA	5.1
	ZnO	2-15%			
	Al <sub>2</sub> O <sub>3</sub>	30-50%			
	SiO <sub>2</sub>	5-25%			
	Sn <sub>2</sub> O <sub>3</sub>	<1%			
	Cr <sub>2</sub> O <sub>3</sub>	0.5%			
	BaO	2-15%			
	CuO	<1%			
	Mn <sub>2</sub> O <sub>3</sub>	<1%			

#### 4.5.1. Glass frit composition and properties

To understand the effect of glass frit addition on the sintering conditions, dilatometry experiments were conducted in a hybrid furnace. The typical time temperature profile used is shown in Figure 4.66. The shrinkage curves of the doped n-S-BT with 1.5 wt% of 6 different glass frit compositions are plotted in Figure 4.67. The salient results were provided in Table 4.22.

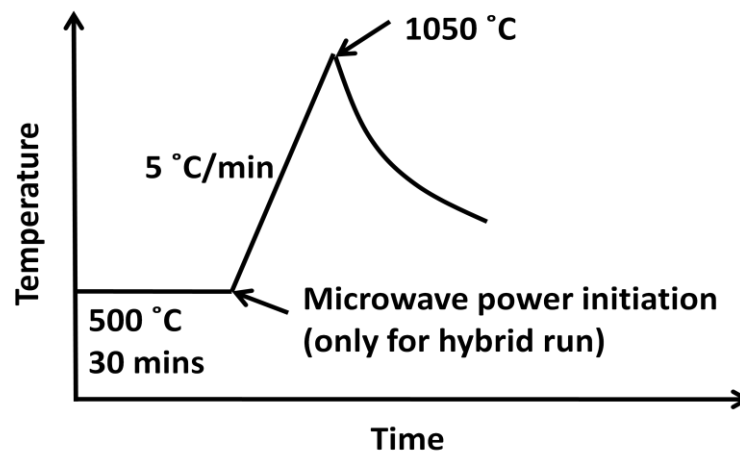


Figure 4.66: Time-Temperature profile used for dilatometer studies of the doped n-S-BT with 1.5 wt% of six different glass frits compositions

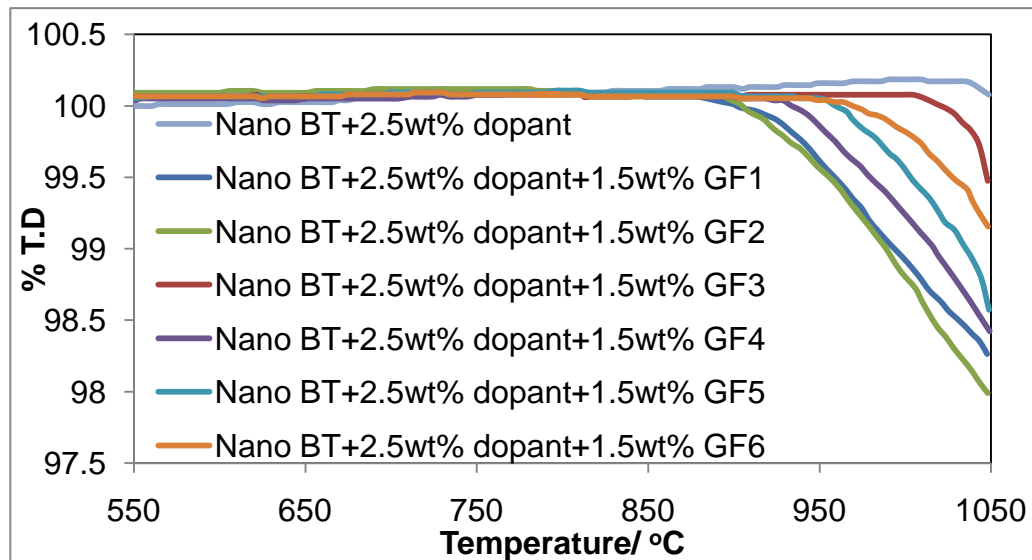


Figure 4.67: Linear shrinkage Vs Temperature of the doped n-S-BT with 1.5wt% of six different glass frit compositions

**Table 4.22: Onset sintering temperature, density and weight loss of the doped n-S-BT with 1.5 wt% of six different glass frits using conventional sintering**

Sample	Onset sintering temperature ( $^{\circ}\text{C}$ ) $\pm 5^{\circ}\text{C}$	Density ( $\text{g}/\text{cm}^3$ ) $\pm 0.5\%$
GF0	1080	3.40
GF1	915	5.10
GF2	905	5.30
GF3	1023	3.53
GF4	948	4.64
GF5	970	4.41
GF6	990	3.98

It is evident from the dilatometer curves that the addition of GF1 and GF2 glass frits lowered the sintering onset temperature to a minimum of 905-915 $^{\circ}\text{C}$ . The use of GF4 resulted in an onset sintering temperature of 948 $^{\circ}\text{C}$ . The remaining glass frits GF5, 6 and 3 showed higher onset sintering temperatures 970, 990 & 1023 $^{\circ}\text{C}$  respectively. The sample with no glass frits (GF0) showed the highest onset temperature of 1080 $^{\circ}\text{C}$ . The samples with GF1 and GF2 glass frits addition also resulted in high density while the addition of GF3 resulted in a low density samples. With GF1 and GF2 additions, glassy phase was formed at early stages of sintering due to lower softening temperature of these materials. On the other hand, since GF3 has a high softening temperature of 1023 $^{\circ}\text{C}$  and the liquid phase movement were also obstructed due to its recrystallising behaviour, it showed less reduction in onset sintering temperature and the resulted in lower sintered density.

From the dilatometer studies of doped n-S-BT with glass frits addition, it is clear that the glass frits addition has resulted in lower onset sintering temperatures as well as densification compared to the sample without any glass frit (GF0). Hence, GF1, GF2 and GF4 were found to be promising glass frits for doped n-S-BT sintering and was chosen for further optimising the sintering condition optimization of sintering conditions.

A close look at the glass frit composition from Table 4.20, GF2 was found to have microwave absorbing oxides such as ZnO. Hence, further dilatometer studies were continued on the doped n-S-BT with 1.5 wt% GF2 glass frit in a hybrid heating

situation using the identical time temperature profiles (Figure 4.66) with varying levels of microwave power viz., 0, 600 and 800 W.

**Table 4.23: Onset sintering temperature, density and weight loss in hybrid heating for doped n-S-BT with 1.5 wt% GF2 glass frits**

Samples	Onset sintering temperature ( $^{\circ}\text{C}$ ) $\pm 5$ $^{\circ}\text{C}$	Density ( $\text{g}/\text{cm}^3$ ) $\pm 0.5\%$	Weight loss (%) $\pm 0.1\%$
GF2-0 W	905	5.30	1.1
GF2-600 W	885	5.54	1.2
GF2-800 W	872	5.61	1.2

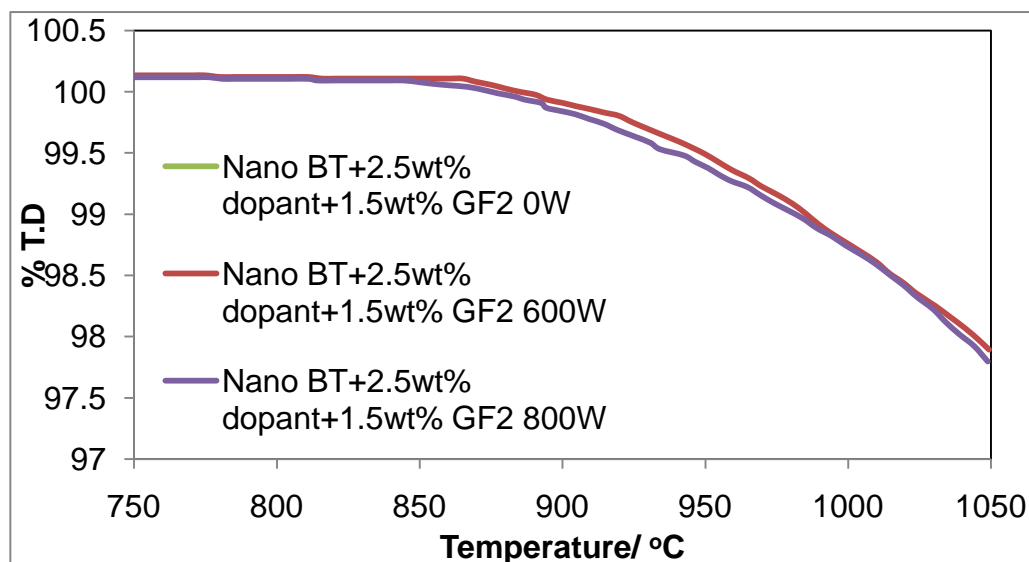


**Figure 4.68: Linear shrinkage Vs Temperature of the doped n-S-BT with 1.5 wt% GF2 using different microwave power.**

From Figure 4.68 and Table 4.22, it was evident that the onset temperature was further decreased by 20-25 $^{\circ}\text{C}$  by the use of microwaves. Although there is no significant shift in the shrinkage curves with different microwave power levels, their sintered densities were found to be increased with the additional microwave power used. As mentioned earlier, the dilatometer only measures, the linear shrinkage along one direction were the sintered density was calculated using volume shrinkage.

#### 4.5.2. Optimization of glass frit amount

As discussed before based on the dilatometer results, three glass frits (GF1, GF2 and GF4) were chosen. The ink derived doped n-S-BT compact with varying amounts of glass frits were sintered at 1050°C for 1 hour using conventional and microwave heating.

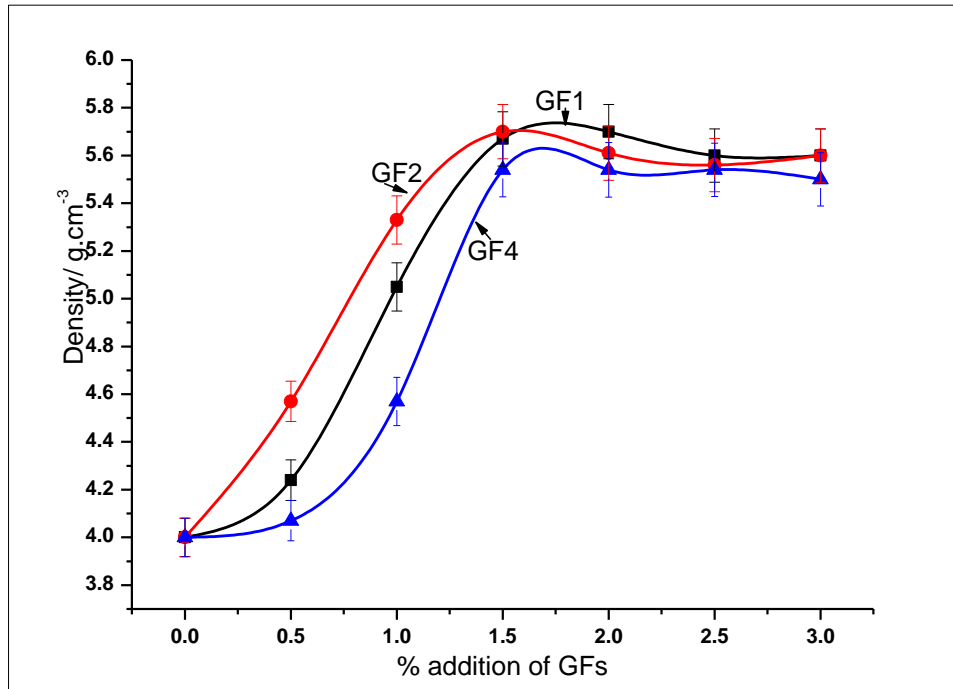


**Figure 4.69: Variation of sintered density with different amount of glass frits (GF1, GF2 and GF4), sintered at 1050°C for 1 hour using microwave heating.**

Figure 4.69, it was observed that all three glass frits showed a similar trend of densification with increasing amounts of glass frits. The sintered density was found to be enhanced with the increasing amount of glass frit content and the density values showed a plateau above 1.5 wt%. No further improvement was observed above 2.0 wt% of glass frit addition. GF1 and GF2 resulted in higher density compared to GF4. The presence of small amount of glass which softens above its softening temperature helps to rearrange the particle and fills the pores. Thus addition of glass frits was found to enhance mass transport and results in high densification. A maximum density of 5.65 g/cc was achieved with 1.5-2.0 wt% GF1



and GF2 glass frit addition. Also as the glassy phases tend to have low dielectric permittivity, it is preferred to have a minimum amount of glass frit addition.

#### 4.5.3. Sintering of n-S-BT with glass frits

The ink derived doped n-S-BT compacts with 1.5 wt% of GF1, GF2 and GF4 glass frits were sintered at 1050°C for 1 hour using conventional and microwave heating, the sintered densities were given in Table 4.24. From Figure 4.70, it was found that both conventional and microwave sintered samples retains the nanostructure, however the microwave sintered samples resulted in better densification. Notably, the soaking time for microwave sintering was found to be halved.

**Table 4.24: Densities of the doped n-S-BT with 1.5 wt% glass frits sintered at 1050°C for 2 h using conventional and 1 h using microwave heating**

Sample	Conventional sintering	Microwave sintering
	Density ( $\text{g/cm}^3$ ) $\pm$ 0.5%	Density ( $\text{g/cm}^3$ ) $\pm$ 0.5%
GF1	5.20	5.67
GF2	5.40	5.70
GF4	4.80	5.54

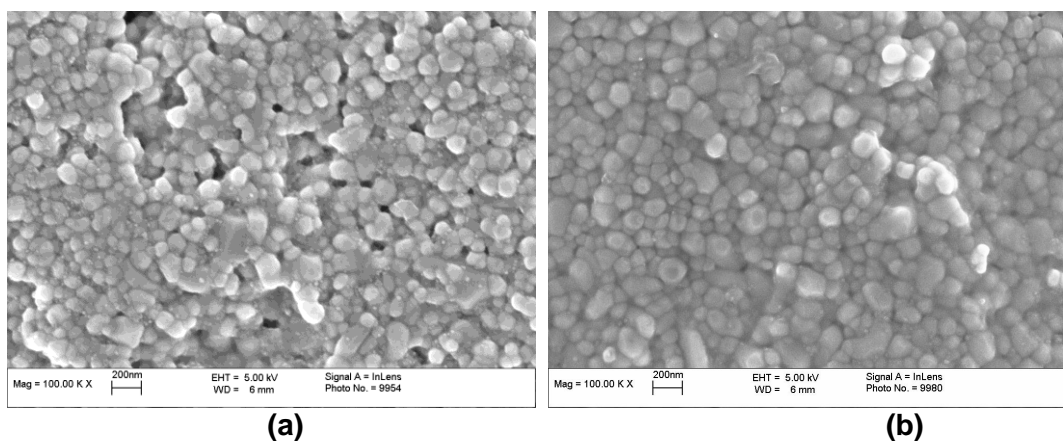


**Figure 4.70: Microstructures of the doped n-S-BT with 1.5 wt% GF2 glass frit, sintered surface at (a) 1050°C for 2 h using conventional heating and (b) 1050°C for 1 h using microwave heating**

#### 4.5.4. Electrical properties of the n-S-BT with glass frits addition

Table 4.25 consolidates the relevant electrical properties (Capacitance, dissipation factor, dielectric permittivity and insulation resistance) of the doped n-S-BT with 1.5 wt% glass frits sintered at 1050°C for 1 hour using microwave heating.

**Table 4.25: Electrical properties of selected samples**

1.5 wt% GFs	Sintering condition	Density, g/cm <sup>3</sup>	Cap, pF	Dissipation factor, %	IR (Gohms)	Dielectric permittivity
GF0	1050 °C-MW-1 h	4.00	516	0.4	3000	2760
GF1	1050 °C-MW-1 h	5.67	319	0.38	600	1675
GF2	1050 °C-MW-1 h	5.70	281	0.47	500	1436
GF4	1050 °C-MW-1 h	5.54	303	0.31	>1000	1527

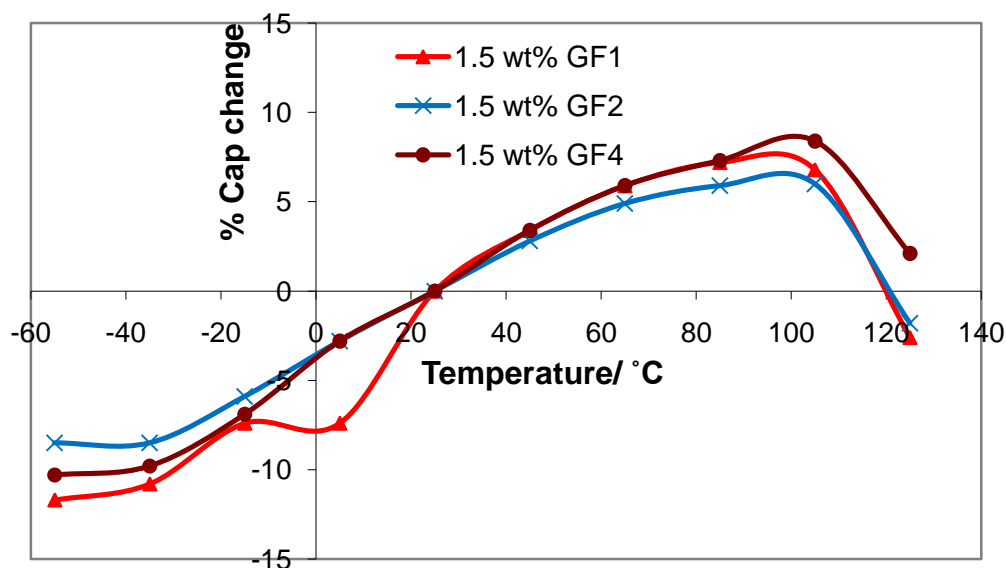


**Figure 4.71: Temperature change in capacitance (TCC) (with reference to room temperature) of the n-S-BT with 2.5 wt% dopants and 1.5 wt% of different glass frits.**

The capacitance of the samples was reduced by the addition of glass frits. As mentioned before, the glasses are low dielectric materials and hence addition of glass frits lowers the overall dielectric permittivity and in turn capacitance. There is

no significant change observed in the dissipation factor with the addition of glass frits. The glass addition makes the grain boundary phase impure and hence with addition of glass frits, insulation resistance was slightly decreased. From Figure 4.71, it was found that all the samples showed  $\pm 15\%$  change in capacitance between  $-55^{\circ}\text{C}$  to  $125^{\circ}\text{C}$ , satisfying the requirements of X7R specification. Thus the addition of glass frits does not deleteriously affect the TCC characteristics.

Using the optimised amount of glass frit and dopant a nano MLCCs device has been fabricated using screen printing technique as mentioned before. This further confirms the translatable nature of the nano BT ink formulation from lab scale to pilot scale. The sintering characteristics and performance evaluation of these newly developed MLCCs will be dealt through future projects in this area.

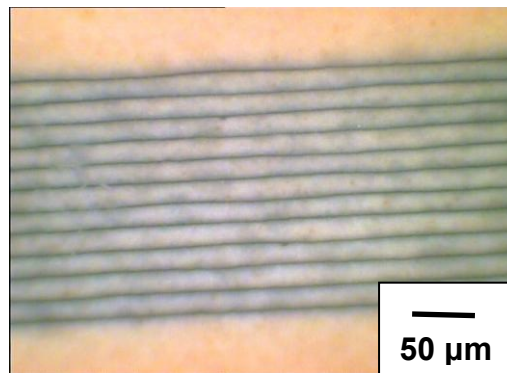


**Figure 4.72: Optical micrograph of the new n-S-BT doped capacitor device**

Thus a new n-S-BT doped capacitor formulation suitable for X7R MLCCs application has been identified, the results are a subject of a patent application.

## Chapter 5

### 5. CONCLUSIONS

#### 5.1. Over all conclusions based on the present work

BT nano powder was synthesized using a microwave assisted polymeric precursor method and the effect of conventional, microwave and hybrid heating methods on the formation of nanocrystalline BT was investigated. Single phase tetragonal (t-BT) nano powder of ~ 20 nm particle size was synthesized using microwave assisted polymeric precursor method. Microwave assisted heating required lower processing temperature and a shorter processing time (700°C/ 30 min) compared to conventional heating (900°C/ 5 hrs), leading to significant energy savings. The nano BT powders synthesized using microwave heating resulted in fine particle size, with less agglomeration, compared to the conventionally calcined powders.

The role played by microwaves during the rapid nano BT synthesis was investigated using hybrid heating conditions. The tetragonal phase nucleation was found to increase, with increasing microwave power levels, under identical thermal history (viz., same time-temperature profiles; 700°C/1 h/1 kW). A significant reduction in activation energy for tetragonal BT formation was noticed as a function of microwave power in hybrid heating condition. The activation energy was found to be  $40 \pm 2$  kJ/mol for microwave assisted synthesis with 1000 W of microwave power in hybrid condition, compared to  $92 \pm 1$  kJ/mol in conventional method. Thus, the activation energy has been reduced by more than half when 1000 W of microwave power was used during nano BT synthesis. In addition, co-existence of hexagonal BT phase at power levels of < 200 W, initiation of tetragonal phase nucleation at  $\geq 200$  W and single phase t-BT formation with  $\geq 1200$  W were observed at the same thermodynamic conditions of temperature-time-pressure. This provided an entirely new possibility of controlling/altering phase evolution during nanoceramics synthesis with microwave power.

Single phase crystalline BZT nano powders with less agglomeration were also synthesized using microwave assisted heating at 700°C/30 min. The crystallinity, surface area and the dielectric permittivity of the microwave synthesized BZT nanopowders were assessed to be better than the conventionally calcined powders.

The microwave technique was also found to be generically applicable for the rapid preparation of nanocrystalline BSZT ( $\text{Ba}_{1-x}\text{Sr}_x\text{Zr}_{0.1}\text{Ti}_{0.9}\text{O}_3$ ) formulations. The less demanding processing conditions resulted in fine grained nanopowders making it an attractive synthesis methodology.

The synthesized nano BT powders (n-LU-BT) of 20 nm particle size were found not to be suitable for wet processing because of its poor wetting and dispersion characteristics. However, the commercially procured nano t-BT (n-S-BT) powders of 100 nm particle size resulted in well dispersed suspension and tangible rheological behaviour was achieved.

The nano powder (n-S-BT) was found to require double the amount of dispersant than that of  $\mu$ -BT suspension due to the high surface area of the ceramic particles. Again, due to the high surface to volume ratio of nanopowders, even with the maximum achievable solid loading of 62 wt%, the resulted nano ink had a very high viscosity compared to  $\mu$ -BT powder ink ( $\geq 70$  wt%).

Further, the nano BT ink was found to be screen printable at 40°C substrate temperature, 90°C blow air temperature,  $10 \pm 0.5$  Kg squeegee pressure, 200 mm/sec squeegee speed at 1.5 mm snap off distance to form multilayer ceramic capacitor chips with and without internal electrodes.

Though, the nano BT ink flow behaviour was poor compared to the  $\mu$ -BT inks, this could produce thin flat prints without any major defects (but with some meshmarks). The thickness of the nano BT screen printed layers was less (10  $\mu\text{m}$ ) compared to the  $\mu$ -BT (20  $\mu\text{m}$ ), which is helped for miniaturization.

Combining the benefits of nano BT with microwave assisted heating, a  $\sim 150^{\circ}\text{C}$ , reduction in onset sintering temperature was achieved compared to the  $\mu$ -BT MLCCs. Microwave assisted sintering of the n-S-BT chips at  $1150^{\circ}\text{C}$  for 1 h resulted in 97% densification without any abnormal grain growth.

The core shell structure responsible for temperature stable characteristics of the capacitors (X7R) was developed by adding proprietary dopants in the n-S-BT ink formulations. The optimized amount of dopants required for nano BT ink was identified as 2.5 wt% based on the electrical performance of the sintered n-S-BT samples. The addition of dopants further reduced the onset sintering temperature by  $100^{\circ}\text{C}$  whilst a maximum density of 98% T.D was achieved at  $1120^{\circ}\text{C}$  using microwave heating. In addition, the microwave sintered MLCCs fabricated using the doped nano BT ink formulation resulted in superior electrical performance compared to conventionally sintered n-S-BT MLCCs and  $\mu$ -BT MLCCs.

With the suitable glass frits addition to the nano ink formulation, sintering temperature was further lowered to  $1050^{\circ}\text{C}$  using microwave sintering resulting in high density samples. Thus the final nano BT ink formulation with dopant and glass frit decreased the sintering temperature by  $\sim 300^{\circ}\text{C}$ . This significant reduction in processing temperature enabled the use of low Pd containing electrode materials.

## Chapter 6

### 6. FUTURE WORK

#### 6.1. Synthesis:

Using the present synthesis methodology, 20-30 nm particle size nano BT was produced at the lab scale. If the methodology for synthesizing the nano BT powders using the polymeric precursor method and microwave heating can be developed for large scale production, this would open up useful research/exploitation opportunity.

The reduction in activation energy was noticed as a genuine microwave effect in the present work. Further detailed study on the possible reasons for activation energy during nano BT synthesis can be carried out as a future project.

The present work used nano BT powder of ~ 100 nm particle size procured from Sakai Chemicals Ltd., for MLCCs fabrication and sintering. It would be beneficial to explore the fabrication of devices with 20-30 nm primary particles for further understandings on the nanostructured BT ceramics.

The development of core shell structure is very important to achieve high insulation resistance and X7R characteristics in BT based capacitors. There are many coatings methodologies of necessary dopants on the BT powder particles have been attempted on micron sized particles using metal organic / inorganic precursors. There is more scope for further research on coating dopant materials on the nano BT powder particles. In addition, coated n-BT powders using an *insitu* synthesis procedure such as sol gel, co-precipitation can also be attempted. This can also lead to new IP opportunities.

Reducing the agglomerates in synthesized nano BT powders is another important parameter. Therefore, capping agents such as ammonium sulphate can be used as coating materials on the nano BT powder particles, to reduce agglomeration further.

The microwave assisted synthesis procedure can be extended to other nano electro ceramic systems such as ferroelectric titanates, zirconates, niobates, ferrites, yttria stabilized zirconia (YSZ), yttrium aluminium garnet (YAG) etc

## **6.2. Green processing**

1. **Milling technique:** The basic criterion to form good homogeneous nano inks is to achieve well dispersed nano particles in the solvent medium prior to the binder addition. In the present study ball milling technique was used to replicate the present production methodology. For achieving better homogenous dispersion of the nano BT powders with dopants and glass frits, a very vigorous (energy intensive) technique such as high shear bead milling can be used.
2. **Lowering surface tension:** The inks with high surface tension does not flow, spread and wet the substrate very well. As the nano particles have high surface area, it's believed that the nanopowders tend to increase the surface tension of the inks. The surface tension of the nano BT inks can be lowered using organic solvents with low surface tension such as Dipentene.
3. **Screen printing conditions:** More detailed study and understanding on the screen printing conditions for nano BT inks is needed, (a) reducing the squeegee pressure can reduce the mesh marks. (b) The off contact distance can be varied. Increasing the off contact distance leaves very less time for the screen in contact with the substrate, hence gives less time for the mesh mark formation and more time for the ink to level. (c) As the nano particles have high surface area, the print layer dries very quickly than the micron particle inks layers, leaving less time for the ink to flow and level. By lowering the substrate temperature and allowing more time for the ink to flow, spread and level this can be sorted. But this may affect the production time involved (d) Thin wired screens can be used that have been proven to reduce the mesh marks.



4. Improving nano particle packing: The particle packing in the screen printed layers can be improved by blending the nano BT with some amount of micron BT particles. This may improve the ink flow behavior, alter the drying rate of the screen printed layer and helps to achieve better packing densities which can lead to higher green densities.
5. Use of nano metal inks: The use of nano metal electrode inks during MLCCs manufacturing may provide further improvements in print conformity, sinterability, and electrical performance.

Fabrication of nano MLCCs can also be attempted using BZT, BSZT ink formulations.

The use of other printing procedures such as ink jet printing is also worth investigating.

### **6.3. Sintering**

Further reduction in microwave sintering temperatures can be sought by using microwave absorbing dopants and glass frit additions. Reduction of processing temperature to  $<1000^{\circ}\text{C}$  could enable the use of even cheaper base metal electrodes.

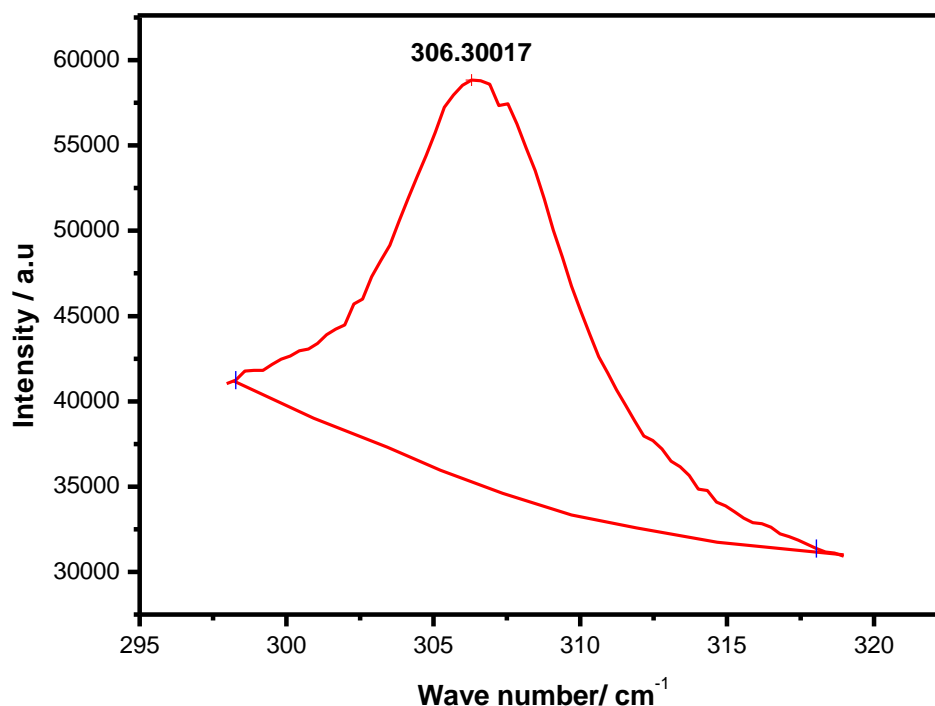
More detailed investigations on the shrinkage behaviour of MLCCs in hybrid heating environment is warranted where the effect of heating rate, microwave power and component dielectric properties on microwave absorption can be helpful to optimize the energy usage during sintering.

The pilot scale microwave assisted sintering of MLCCs can be explored in future that will provide more industrial confidence on the use of this technology. This will also help to understand real time difficulties associated with scale up.

## Appendix-1

### Amount of tetragonal phase calculation

The BT precursors were calcined at three different temperatures of 600, 700 and 800°C for different durations (5-200 min) at different microwave power levels (0-1000 W) using the hybrid furnace. The % tetragonality of the calcined BT powders was calculated using Raman spectra peak area analysis. First the Raman curves were normalised to 100. The characteristics tetragonal peak at 307  $\text{cm}^{-1}$  was used for the tetragonal phase nucleation. The curve from 295 to 315  $\text{cm}^{-1}$  was smoothed through Gaussian method using Sigma plot software and the base line was created. The maximum peak and the integrated area of the peak were calculated by integration method using originPro 7.5. A representative graph and area result of the BT precursor calcined at 700°C for 30 min using microwave heating is shown below.



Area	Peak	Height
182021.56014	306.60901	23703.78781

The peak area of the single phase tetragonal BT calcined at 700°C/ 30 min for microwave heating and 900°C/ 5 h for conventional heating was taken as reference for microwave and conventional heating respectively. The % t-BT nucleation of all other calcination condition was calculated with respect to the reference in conventional and microwave heating.

## Appendix-2

### Two stage sintering: T1 optimization

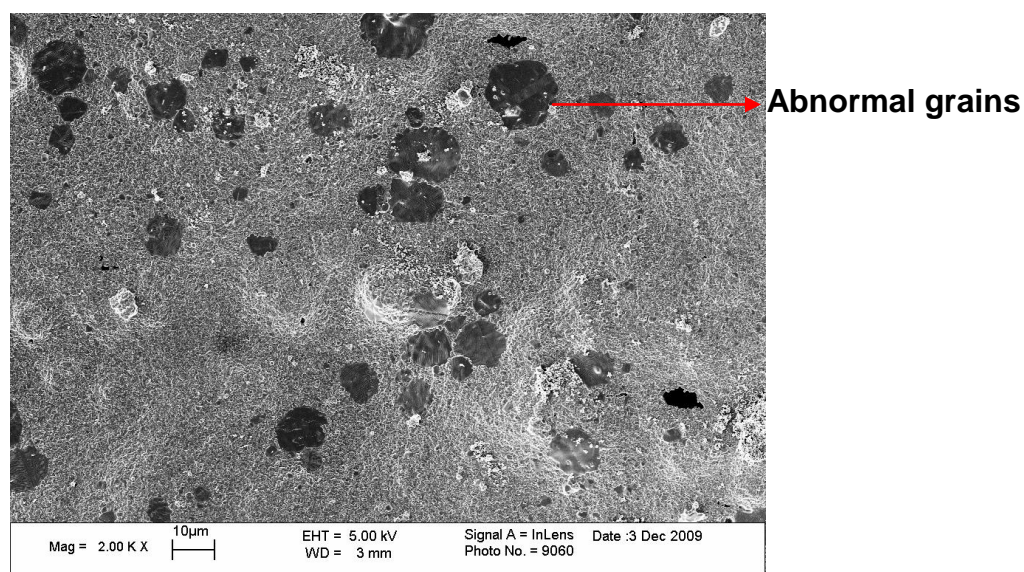
For nano BT samples the temperatures between 1200°C and 1300°C (refer Figure 4.52, dilatometer measurements in section 4.3.1) at intervals of 25°C was chosen as T1 to achieve ~75-80% T.D. A 10°C/min heating rate was used for 0.1 min and furnace cooled. The densities and the grain sizes at various temperatures were measured and provided in the table below.

#### Densities of the n-S-BT at different T1 conditions

Sample	1200°C	1225°C	1250°C	1275°C	1300°C
n-S-BT	61.0%	62.4%	<b>67.2%</b>	79.0%	94.6%
	0.3 $\mu\text{m}$	0.3 $\mu\text{m}$	0.3-0.5 $\mu\text{m}$ Ab	~0.5 $\mu\text{m}$ Ab	0.3 $\mu\text{m}$

Ab-Abnormal grain growth

#### SEM micrograph of the BT samples at 1250°C for 0.1 min



As can be seen from the above table and microstructural analysis, even at a densification of ~67% at 1250°C there was evidence for abnormal grain growth. This could be due to the presence of phosphate based (from the dispersant) liquid phase during sintering. This negates the use of two stage sintering for this material.

## References

---

- 1 A.J. Moulson, J.M. Herbert, "Electroceramics: Materials, properties, and applications", Chapman and Hall, 1990.
- 2 [www.intel.com](http://www.intel.com), Accessed on 10<sup>th</sup> December 2010
- 3 Y.B. Kholam, H.S. Potdar, S.B. Deshpande, A.B. Gaikwad, *Mater. Chem. Phys.*, 97 (2006) p295
- 4 B. Vaidhyanathan, J.G.P Binner, *J. Mater. Sci.*, 41(2006) p5954-5957
- 5 J.G.P.Binner, K.Annapoorani, A.Paul, I.Santacruz, B.Vaidhyanathan, *J. Eur. Ceram. Soc.*, 28 (2008) p973
- 6 A.B. McInroy, A.T. Rowley, R. Freer, *Ceram. Int.* 36 (2010) p2007-2010
- 7 <http://www.kpsec.freeuk.com/components/capac.htm>, Accessed on 25<sup>th</sup> June 2008
- 8 <http://en.wikipedia.org/wiki/capacitors>, Anonymous, Accessed on 9<sup>th</sup> August 2010
- 9 [www.radioelectronics.com](http://www.radioelectronics.com), Accessed on 9<sup>th</sup> August 2010
- 10 [http://en.wikipedia.org/wiki/Surface-mount\\_technology](http://en.wikipedia.org/wiki/Surface-mount_technology), Accessed on 8<sup>th</sup> August 2010
- 11 "Multilayer ceramic capacitors", EPCOS General technical information, Oct 2006
- 12 <http://en.wikipedia.org/wiki/EEStor>, Accessed on 25<sup>th</sup> June 2008
- 13 R.D. Weir, C.W. Nelson, U.S.Patent no: 7595109, 2009
- 14 R.B. William, Hans, Piezoelectric ceramics, Academic Press, 1981
- 15 <http://theeestory.com/topics/317>, Accessed on 9<sup>th</sup> Jan 2011
- 16 H.T. Kim, Y.H.Han, *Ceram. Int.*, 30 (2004) p1719–1723
- 17 J. Wang, J. Fang, L.M. Gan, C.H. Chew, X. Wang, Z. Shen, *J. Am. Ceram. Soc.*, 82 (1999) p873
- 18 Y.J. Jung, D.Y. Lim, J.S Nho, S.B. Cho, R.E. Riman, B.W. Lee, *J. Cryst. Growth*, 274 (2005) p638
- 19 M.H. Frey, D.A. Payne, *Physical Review B*, 54 (1996) p3158
- 20 T. Takeuchi, M. Tabuchi, K. Ado, K. Honjo, O. Nakamura, H. Kageyama, Y. Suyama, N. Ohtori, M. Nagasawa, *J. Mater. Sci.*, 32 (1997) p4053
- 21 G. Busca, V. Buscaglia, M. Leoni, P. Nanni, *Chem. Mater.*, 6 (1994) p955.

- 
- 22 Y.I. Kim, J.K. Jung, K.S. Ryu, *Mater. Res. Bull.*, 39 (2004) p1045
- 23 J. Wang, J. Fang, N.G. Ser-Choon, L.M. Gan, C. H. Chew, X. Wang, Z. Shen, *J. Am. Ceram. Soc.*, 82 [4] (1999) p873-881
- 24 R.S. Roth, *J. Res. Natl. Bur. Std.*, 58 (1957) p75
- 25 R.D. Shannon, *Inorg. Chem.*, 6 (1967) p1474
- 26 Y. Tsur, T. D. Dunbar, C.A. Randall, *J. Electro. Ceram.*, 7 (2001) p25-34
- 27 H. Abdelkefi, H. Khemakhem, G. Velu, J. Claude, R.V. Muhl, *J. Alloys Compd.*, 399 (2005) p1
- 28 V. Vinothini, M.S Thesis, Indian Institute of Technology, Madras, India, 2005
- 29 P.R. Arya, P. Jha, G.N. Subbanna, A.K. Ganguli, *Mater. Res. Bull.* 38 [4] (2003) p617
- 30 F. Moura, A.Z. Simoes, B.D. Stojanovic, M.A. Zaghete, E. Longoa, J.A. Varela, , *J. Alloys Compd.*, 462 [1-2] (2007) p129-134
- 31 C. Mao, X. Dong, T. Zeng, *Mater. Lett.*, 61 (2007) p1633
- 32 Springer-Verlag, Landolt-Bornstein Numerical Data and Functional Relationship in Science and Technology, Berlin (1981) III/28a: p268; III/16a: p422
- 33 D. Hennings, A. Schnell, *J. Am. Ceram. Soc.*, 65 [11] (1982) p539
- 34 S.M. Neirman, *J. Mater. Sci.*, 23 (1988) p3973-3980
- 35 D. McCauley, R.E. Newnham, C.A. Randall, *J. Am. Ceram. Soc.*, 81 (1998) p979–87
- 36 J.N. Li, T.B. Wu, *J. Appl. Phys.*, 68 [3] (1990) p985
- 37 R. Farhi, M.E. Marssi, A. Simon, J. Ravez, *J. Euro. Phys. B*, 18 (2000) p605
- 38 Z. Jing, C. Ang, Z. Yu, P.M. Vilarinho, J.L. Baptista, *J. Appl. Phys.*, 84 [2] (1998) p15
- 39 W. Xiaoyong, F. Yujun, Y. Xi, *Appl. Phys. Lett.*, 83 (2003) p2031
- 40 S.G. Lu, Z.K. Xu, H. Chen, *Appl. Phys. Lett.*, 85 (2004) p5319
- 41 W. Xiaoyong, F. Yujun, Y. Xi, *Appl. Phys. Lett.*, 83 (2003) p2031
- 42 V. Kumar, J. Joseph, I.P. Selvam, *Jpn. J. Ceram. Soc.*, 113 [12] (2005) p784
- 43 V.S. Tiwari, N. Singh, D. Pandey, *Phys: Condensed Matter* 7 (1995) p1441

- 
- 44 T.R.N. Kutty, R. Vivekanadan , *Mater. Res. Bull.*, 22 (1987) p1457
- 45 R. Newnham, *Rep. Prog. Phys*, 52 (1989) p123
- 46 J. Daniels, K.H. Härdtl, D. Hennings, R. Wernicke, *Philips Res. Rep.* 31 (1976) p487-566
- 47 S.R.B. Reddy, K.P. Rao, M.S.R. Rao, *Appl. Phys. A*, 89 (2007) p1011
- 48 I.C. Ho, S.L. Fu, *J. Mater. Sci.*, 25 (1990) p4699
- 49 R. Waser, in: *Third Euro-Ceramics*, P. Duran, J. F. Fernandes (eds.), 2 (1998) p23-28
- 50 C.A. Randall, S.F. Wang, J.P. Dougherty, W. Huebner, *J. Mater. Res.*, 8 [4] (1993) p871-79
- 51 J.M. Herbert, "Ceramic Dielectrics and Capacitors" OPA Amsterdam, 1985, p194
- 52 T.R. Shrout, D.K. Agarwal, B. Vaidhyanathan, U.S.Patent no 6, 610, 241 B2 (2003)
- 53 H. Hahn, R. S. Averbach, *J. Am. Ceram. Soc.*, 74, 2918-2921, 1991
- 54 C. Pithan, D. Hennings, R. Waser, *Int. J. Appl. Ceram. Tech.*, 2 [1] (2005) p1
- 55 K.S. Mazdiyasi, R.T. Dolloff, J.S. Smith, *J. Am. Ceram. Soc.*, 52 [10] (1969) p523
- 56 F. Chatput, J.P. Boilot, "High Tech Ceramics Part B: Materials science Monograph" 38 B edited by P. Vincenzini, Elsevier publications, Amsterdam (1987) p1459
- 57 P.P. Phule, S.H. Risbud, "Better ceramics through Chemistry III" edited by J. Brinker, D.R. Clark, D.R. Ulrich, Materials research society, Pittsburgh (1988) p275
- 58 P.P. Phule, S.H. Risbud, *J. Mater. Sci.*, 25 (1990) p1169
- 59 S. Yoon, S. Baik, M.G. Kim, N. Shin, *J. Am. Ceram. Soc.*, 89 [6] (2006) p1816
- 60 A.N. Virkar, K. Bandyopadhyay, A. Paul, *Trans. Ind Ceram. Soc.*, 44 (1985) p78
- 61 S. Wada, M. Nishiyama, A. Yazawa, T. Hoshina, H. Kakemoto, T. Tsurumi, *Key Engg. Mater.*, 350 (2007) p39
- 62 L.S. Seveyrat, A. Hajjaji, Y. Emziane, B. Guiffard, D. Guyomar, *Ceram. Int.*, 33 (2007) p35
- 63 H. Okada, S.H. Matsubayashi, F.Goto, Japanese patent JP 6272525 A2, 1987
- 64 Y. Kobayashi, A. Nishikata, T. Tanase, M. Konno, 29 [1] (2004) p49
- 65 M.P. Pechini, US patent 3 330 697, 11 July 1967

- 
- 66 S.K. Mazdiyasi, T.R. Dolloff, S.J. Smith, *U.S. Patent Number. 3647364*, 1972
- 67 S.G. Cho, P.F. Johnson, R.A. Condrate, *J. Mater. Sci.*, 25 (1990) p4788
- 68 P. Duran, F. Capel, J. Tartaj, D. Gutierrez, C. Moure, *Solid state Ionics*, 141-142 (2001) p529
- 69 S. Gablenz, H.P. Abicht, E. Pippel, O. Lichtenberger, J. Woltersdorf, *J. Euro. Ceram. Soc.*, 20 (2000) p1053
- 70 .P. Coutures, P. Odier, C. Proust, *J. Mater. Sci.*, 27 (1992) p1849
- 71 K. Chaitanya, "Ceramic Precursor Technology and its applications", Marcel Dekker Inc., New York 1995
- 72 C. L. Robert, F. Ansart, C. Deloget, M. Gaudon, A. Rousset, *Mater. Res. Bull.*, 36 (2001) p2083-2107
- 73 J.D. Tsay, T.T. Fang, T.A. Gubiotti, J.Y. Ying, *J. Mater. Sci.*, 33 (1998) p3721-3727
- 74 P. Durana, D. Gutierrez, J. Tartaja, M.A. Banaresb, C. Mourea, *J. Euro. Ceram. Soc.*, 22 (2002) p797-807
- 75 H.S. Gopalakrishnamurthy, M.S. Rao, T.R.N. Kutty, *J. Inorg. Nucl. Chem.*, 37 (1975) p891
- 76 S. Kumar, G.L. Messing, W.B.White, *J. Am. Ceram. Soc.*, 76 (1993) p617
- 77 J.D. Tsay, T.T. Fang, T.A. Gubiotti, J.Y. Ying, *J. Mater. Sci.*, 33 (1998) p3721
- 78 O.O. Vasyl'kiv, A.V. Ragulya, V.V. Skorokhod, *Powder Metall. Met. Ceram.*, 36 (1997) p277
- 79 D. Hennings, W. Mayr, *J. Solid State Chem.*, 26 (1978) p329
- 80 W.S. Cho, *J. Phys. Chem. Solids*, 59 (1998) p659
- 81 C. Fu, C. Yang, H. Chen, Y. Wang, L. Hu, *Mater. Sci. Engg. B*, 119 (2005) p185
- 82 T. Hu, H. Jantunen, A. Uusimaki, S.L. Vuori, *J. Euro. Ceram. Soc.*, 24 (2004) p1111
- 83 Y.B. Khollam, H.S. Potdar, S.B. Deshpande, A.B. Gaikwad, *Mater. Chem. Phys.*, 97 (2006) p295
- 84 A. Ries, A.Z. Simoes, M. Cilense, M.A. Zaghete, J.A. Varela, *Mater. Character.*, 50 (2003) p217
- 85 C. Mao, X. Dong, T. Zeng, G. Wang, S. Chen, *Mater. Res. Bull.*, 42 (2007) p1602
- 86 X.G. Tang, J. Wang, X.X. Wang, H.L. W.Chan , *Solid State Communications*, 131 (2004) p163



- 
- 87 J.Q. Qi, Y. Wang, W.P. Chen, L.T. Li, H.L. W.Chan, *J Nanoparticle Res.*, 8 (2006) p959
- 88 J.N. Li, T.B. Wu, *J Appl. Phys.*, 68 [3] (1990) p985
- 89 M.L.B. Bernadi, E. Antoneli, A.B. Lourenco, C.A.C Feitosa, L.J.Q. Maia, A.C. Hernades, *J. Therm. Anal. Calorim.*, 87 (2007) p725-730
- 90 R. Birringer, H. Gleiter, H. P. Klein, P. Marquardt, *Phy. Lett.*, 102A (1984) p365-369
- 91 M. J. Mayo, R. W. Seigel, Y. X. Liao, W. D Nix, *J. Mater. Res.*, 7 [4] (1992) p973-979
- 92 J. Eastman, R. W. Seigel, *Res. Dev.*, 31 (1989) p56-60
- 93 R. W. Seigel, S. Ramasamy, H. Hahn, Z. Zonghuan, L. Ting., *J. Mater. Res.*, 3 (1988) p1367
- 94 H. Hahn, J. Logas, R. S. Averbach., *J. Mater. Res.*, 5 (1990) p609-614
- 95 J.Binner, B.Vaidhyathan, *J. Euro. Ceram. Soc.*, 28 (2008) p1329-1339
- 96 B.P.C. Ragupathy, "Spray freeze drying of Zirconia nanopowders", Ph.D Thesis, Loughborough university, 2007
- 97 J R Groza "Nanostructured Materials", edited by C C Koch, Noyes Publications (2002) p115 – 178.
- 98 J. A. Lewis, *J. Am. Ceram. Soc.*, 83 [10] (2000) p2341-2359
- 99 M. C. Blanco-Lopez, B. Rand, F. L. Riley, *J. Euro. Ceram. Soc.*, 17 (1997) p281-287
- 100 J. H. Jean, H. R. Wang, *J. Am. Ceram. Soc.*, 83 [2] (2000) p277–80
- 101 J. H. Jean, H. R. Wang, *J. Am. Ceram. Soc.*, 81 [6] (1998) p1589–99
- 102 M. Lopez, B. Rand, B., F. Riley, *J. Eur. Ceram. Soc.*, 20 (2000) p107, p1579, p1587.
- 103 Z.G. Shen, J.F. Chen, H.K. Zou, J. Yun, *J. Colloid Interface Sci.*, 275 (2004) p158–164.
- 104 C.W. Chiang, J.H. Jean, *Mater. Chem. Phys.*, 80 (2003) p647–655
- 105 J. Cesarano, A. Aksay, A.J. Blier, *J. Am. Ceram. Soc.*, 71 [4] (1988) p250-255.
- 106 U. Paik, V.A. Hackley, *J. Am. Ceram. Soc.*, 83 ([10] (2000) p2381–84
- 107 W.J. Tseng, S.Y. Li, *Mater. Sci. Engineer.*, A333 (2002) p314–319

- 
- 108 C.C. Li, J.H. Jean, *J. Am. Ceram. Soc.*, 85 [6] (2002) p1441–48
- 109 K.C. Hsu, K.L. Ying, L.P. Chen, B.Y. Yu, W.C.J. Wei, *J. Am. Ceram. Soc.*, 88 [3] (2005) p524–529
- 110 X. Wang, B.I. Lee, M. Larry, 202 (2002) p71–80.
- 111 H. Kamiya, H. Gomi, Y. Iida, K. Tanaka, T. Yoshiyasu & T. Kakiuchi, T, (2003) *J. Am. Ceram. Soc.*, 86 (12): 2011–18.
- 112 A. Neubrand, R. Lindner, P. Hoffmann, *J. Am. Ceram. Soc.*, 83 [4] (2000) p860–64
- 113 R.E.Mistler, E.R. Twiname, “Tape casting” American Ceramic Society, 2000
- 114 T.G. Mezger, *The Rheology Handbook*, 2nd Edition, Vincentz Network, 2006
- 115 P.O. Abbe, “The handbook of ball and pebble mill operation”, Little Falls, 1964
- 116 H. A. Barnes, J. F. Hutton, K. Walters, *An Introduction to Rheology*, Elsevier Science, 1989
- 117 M.N.Tong, Ph.D first year report, Loughborough university, U.K
- 118 S.B. Hoff, “Screen printing: A contemporary approach” Delmar Publishers, U.K 1997
- 119 Y. Zhang, X. Huang, Z. Liu, X. Ge, J. Xu, X. Xin, X. Xha, W. Sha, *J. Power Sources*, 160 (2006) p1065-1073
- 120 S. Hoskins, “Water-based screen printing” A & C Black, London, 103 (2001) p41-63.
- 121 R. Adam, C. Robertson, “Screen printing: The complete water based system” Thames & Hudson, London, 65-74 (2003) p10-14
- 122 S. Reiss, “Practical screen printing”, Studio vista Ltd., London, (1969) p7-16.
- 123 W.D. Kingery, “Introduction to Ceramics”, John & Wiley Sons, New York 1967.
- 124 D.W. Richerson, “Modern ceramic engineering: properties, processing, and use in design”, Taylor & Francis, 2005.
- 125 M.N. Rahaman, *Ceramic processing and Sintering*, Marcel & Dekker Inc, New York, 1995
- 126 J.R. Groza, *Nanostructured Materials*, 12 (1999) p987
- 127 I.J. Colm, N.J. Clark, “Forming, Shaping and Working of high Performance Ceramics”, Blackie, London, U.K, (1988) p244

- 
- 128 M. Mayo, *Int. Mater. Rev.*, 41, No. 3, (1990) p85
- 129 M. H. Lin, J. F. Chou, H. Y. Lu, *J. Euro. Ceram. Soc.*, 20 (2000) p517-526
- 130 S. Y. Choi, S. J. Kang, *Acta Mater.*, 52 (2004) p2937–43
- 131 T. Gladman, *Proc. Roy. Soc. London, Ser. A*, A294 (1966) p298-309
- 132 B.K. Lee, S.Y. Chung, *Acta Mater.*, 48 (2000) p1575-1580
- 133 M.H. Lin, J.H. Chou, H.Y. Lu, *J. Euro. Ceram. Soc.*, 20 (2000) p517-526
- 134 R.T. DeHoff, in *Quantitative Microscopy*, ed. R. T. DeHoff, F. N. Rhines. McGraw Hill, New York, (1968) p134
- 135 P.R. Rios, T.Yamamoto, T. Kondo, T. Sakuma, *Acta mater.*, 46 [5] (1998) p1617-1623
- 136 A.C. Caballero, J.F. Fernhdez, C. Moure, P. Duran, *Mater. Res. Bull.*, 32 (1997) p221-229
- 137 Y.I. Jung, S.Y. Choi, S.J. Kang, *J. Am. Ceram. Soc.*, 86 [12] (2003) p2228
- 138 M. J. Mayo, *Int. Mater. Rev.*, 41 [3] (1996) p85–115
- 139 A. V. Ragulya, V. V. Skorokhod, *Nanostruct. Mater.*, 5 [7/8] (1995) p835–43
- 140 I. W. Chen, X. H. Wang, *Nature*, 404 (2000) p168–71
- 141 B. E. Walker Jr., R. W. Rice, R. C. Pohanka, J. R. Spann, *Am. Ceram. Soc. Bull.*, 55 (1976) p274
- 142 R. B. Amin, H. U. Anderson, C. E. Hodgkins, US Patent No. 4082906, 1978
- 143 H. U. Anderson, K. Atteberry, R. Amin, C. Hodgkins, *Am. Ceram. Soc. Bull.*, 58 (1979) p368
- 144 J. M. Haussonne, G. Desgardin, P. H. Bajolet, B. Raveau, *J. Am. Ceram. Soc.*, 66 (1983) p801
- 145 G. Desgardin, I. May, B. Raveau, *Am. Ceram. Soc. Bull.*, 64 (1985) p563
- 146 J. P. Guha, H. U. Anderson, *J. Am. Ceram. Soc.*, 69 (1986) p6192
- 147 R. C. F. Hanold, U.S.Patent No. 4081857. 1978
- 148 D. Hennings, G. Rosenstein, *J. Am. Ceram. Soc.*, 67 (1984) p249
- 149 Y. Kuromitsu, S. F. Wang, S. Yashikawa, R. E. Newnham, *J. Am. Ceram. Soc.*, 77 (1994) p493

- 
- 150 L. M. Castelliz, R. J. Routil, *Can. J. Ceram. Soc.*, 38 (1969) p69
- 151 I. Burn, *J. Mater. Sci.*, 17 (1982) p1398
- 152 S. K. Sarkar, M. L. Sharma, *Mater. Res. Bull.*, 24 (1989) p773
- 153 T. R. Armstrong, K. A. Young, R. C. Buchanan, *J. Am. Ceram. Soc.*, 73 (1990) p700
- 154 D. Hennings, H. Schreinemacher, U.S.Patent No. 4222885. 1980
- 155 C.F. Yang, *Ceram. Int.*, 24 (1998) p341-346
- 156 I. Burn, U.S.Patent No. 4101952, 1978
- 157 G. H. Maher, U.S.Patent No. 4066426, 1978
- 158 I. Burn, U.S.Patent No. 4120677, 1978
- 159 I. Burn, U.S.Patent No. 4283753, 1981
- 160 D. A. Payne, S. M. Park, U.S.Patent No. 4218723, 1979
- 161 Y. Kuromitsu, S. F. Wang, S. Yashikawa, R. E. Newnham, *J. Am. Ceram. Soc.*, 77(1994) p852
- 162 S.F. Wang, T.C.K. Yang, Y.R. Wang, Y. Kuromitsu, *Ceram. Int.*, 27 (2000) p157-162
- 163 C.S. Hsi, Y.C. Chen, H. Jantunen, M.J. Wu, T.C. Lin, *J. Euro. Ceram. Soc.*, 28 (2008) p2581-2588
- 164 H. Mostaghaci, R. J. Brook, *J. Mater. Sci.*, 21 (1986) p3575-3580
- 165 A. Polotai, K. Breece, E. Dickey, C. Randall, A. Ragulya, *J. Am. Ceram. Soc.*, 88 [11] (2005) p3008–3012
- 166 M.H. Frey, Z. Xu, P. Han, D.A. Payne, *Ferroelectrics*, 206-207 (1998) p337-353
- 167 W. Luan, L. Gao, H. Kawaoka, T. Sekino, K. Niihara, *Ceram. Int.*, 30 (2004) p405–10
- 168 Y.V. Bykov, K.I. Rybakov, V.E. Semenov, *J. Phys. D: Appl. Phys.*, 34 (2001) p55
- 169 H. Zhang, S. Ouyang, H. Liu, Y. Li, *Proc. Mater. Res. Soc. Symp.*, 430 (1996) p447
- 170 A. Paul, “Processing and Properties of Nanostructured Zirconia Ceramics”, Ph.D Thesis, Loughborough University, U.K, 2009

- 
- 171 M.A. Janney, H.D. Kimrey, in "Microwave Processing of Materials II". Edited by W.B. Snyder Jr, W.H. Sutton, M.F. Iskander, D.L. Johnson, *Mater. Res. Soc. Symp. Proc.*, 189, Pittsburgh, PA, (1991) p215
- 172 R. Dagani, *Chemical & Engineering, News*, 1997, p26
- 173 W.H. Sutton in "Microwave Processing of Materials III". Edited by R.L. Beatty, W.H. Sutton, M.F. Iskander. *Mater. Res. Soc. Symp. Proc.*, 269, Pittsburgh, Pennsylvania. Materials Research Society (1992) p3
- 174 D.E. Clark, "Microwaves: Theory and Application in Materials Processing IV". Edited by D. Clark W.H. Sutton, and D.A. Lewis. *Ceram. Trans.*, 80, Westerville, OH. The American Ceramic Society, (1997) p61.
- 175 G.R. Robb, A. Harrison, A.G. Whittaker, *Phys. Chem. Comm.*, 19 [5] (2002) p135
- 176 M.A. Janney, H.D. Kimrey, W.R. Allen, *J. Mater. Sci.*, 32 [5] (1997) p1347
- 177 R. Wroe, A.T. Rowley, *J. Mater. Sci.*, 31 (1996) p2019
- 178 K.J. Rao, B. Vaidhyanathan, M. Ganguli, P.A. Ramakrishnan, *Chem. Mater.* 11 (1999) p882
- 179 A.T. Rowley, R. Wroe, D. Vazqueznavarro, W. Lo, D.A. Cardwell, *J. Mater. Sci.*, 32 (1997) p4541
- 180 M.W. Porada, "Microwave Processing of Materials V", Edited by M.F. Iskander, J.O. Kiggans, J.C. Bolomey. *Mater. Res. Soc. Symp. Proc.*, 430, Pittsburgh, Pennsylvania. Materials Research Society (1996) p403
- 181 Y.V. Bykov, S.V. Egorov, A.G. Ereemeev, K.I. Rybakov, V.E. Semenov, A.A. Sorokin, S.A. Gusev, *J. Mater. Sci.*, 36 (2001) p131
- 182 J.H. Booske, R.F. Cooper, I.J. Dobson, *J. Mater. Res.*, 7 (1992) p495
- 183 J. Wang, "Evidence for the microwave effect during hybrid sintering and annealing of ceramics", Ph.D Thesis, Loughborough University, U.K, 2005
- 184 V.L. Gurevich. Transport in phonon systems, North-Holland, Amsterdam, 1986
- 185 G.A. Dimitrakis, "High Temperature Dielectric properties of Micro and Nano-scale Yttria doped Zirconia at Microwave Frequencies", Ph.D Thesis, The university of Nottingham, December 2005
- 186 Z. Fathi, I. Ahmed, J.H. Simmons, D.E. Clark, A.R. Lodding, in "Microwaves: Theory and Application in Materials Processing", *Ceram. Trans.*, edited by D.E. Clark, F.D. Gac, W.H. Sutton, 21 (1991) p623
- 187 J.G.P. Binner, N.A. Hassine, T.E. Cross, *J. Mater. Sci.*, 30 (1995) p5389

- 
- 188 N.A. Hassine, J.G.P. Binner, T.E. Cross, *Int. J. Refractory Met. Hard Mater.*, 13 (1995) p353
- 189 K.I. Rybakov, V.E. Semenov, *Phys. Rev. B*, 49 [1] (1994) p64
- 190 K.I. Rybakov, V.E. Semenov, *Phys. Rev. B*, 52 [5] (1995) p3032
- 191 J.G.P Binner, B. Vaidhyanathan, J. Wang, *9th International Conference on Microwave and High Frequency Heating*, Loughborough, UK (2003) p477-480
- 192 R. Wroe, EA Technology, U.K, International Patent WO 95/05058, 1995
- 193 K.H. Felgnera, T. Mullerb, H.T. Langhammera, H.P. Abicht, *Mater. Lett.*, 58 (2004) p1943
- 194 Y. Ma, E. Vilen, S.L. Suib, P.K. Dutta, *Chem. Mater.*, 9 (1997) p3023
- 195 Y.S. Maigne, A.V. Gurjar, S.R. Dharwadkar, *Bull. Mater. Sci.*, 27 [3] (2004) p217
- 196 J.M. Amalnerkar, P. Dinesh, H.Y. Kyu, J.S. Hwa, H.J. Soo, C.J. San, *J. Nanosci. Nanotech.*, 7 [3] (2007) p952
- 197 L. Guo, H. Luo, J. Gao, L. Guo, J. Yang, *Mater. Lett.*, 60 (2006) p3011
- 198 O.P. Thakur, C. Prakash, D.K. Agarwal, *J. Ceram. Processing Res.*, 3 [2] (2002) p75
- 199 M. Yasuoka, Y. Nishimura, T. Nagaoka, K. Watari, *Advances in Technology of Material and Processing (ATM).*, 6 (2004) p270-75
- 200 K. Sadhana, T. Krishnaveni, K. Praveena, S. Bharadwaj, S.R. Murthy, *Scripta Materialia*, 59 [5] (2008) p495-498
- 201 W. Yang, A. Chang, B. Yang, *J. Mater. Synth. Process.*, 10 [6] (2002) p303-309
- 202 B. Vaidhyanathan, A.P. Singh, D.K. Agarwal, T.R. Shrout, R. Roy, *J. Am. Ceram. Soc.*, 84 [6] (2001) p1197
- 203 J. Cheng, X. Liu, J. Qiu, J. Zhou, N. Ye, *Advanced Structural Materials. Proc.C-MRS Int.1990 Conf. Beijing; 18-22 June 1990*
- 204 C.Y. Fang, C. Wang, A.V. Polotai, D.K. Agrawal, M.T. Lanagan, *Mater. Lett.*, 62 (2008) p2551-2553
- 205 S. Mahbooba, A.B. Dutta, C. Prakash, G. Swaminathan, S.V. Suryanarayana, G. Prasad, G.S. Kumar, *Mater. Sci. Engg. B*, 134 (2006) p36
- 206 A. Changa, J. Jian, *J. Mater. Process. Tech.*, 137 (2003) p100
- 207 D.K. Agarwal, *Current opinion in solid state and material science*, 3 [5] (1998) p480

- 
- 208 B. Vaidhyanathan, P. Raizada, K.J. Rao , *J. Mater. Sci. Lett.*, 16 [24] (1997) p2022
- 209 B. Vaidhyanathan, D.K. Agarwal, T.R. Shrout, Y. Fang, *Mater. Lett.*, 42 [3] (2000) p207
- 210 B. Vaidhyanathan, D.K. Agrawal, R. Roy, *J. Am. Ceram. Soc.*, 87 [5] (2004) p834
- 211 B. Vaidhyanathan, K. Annapoorani, J.G.P. Binner and R. Raghavendra, *Ceram. Engg. Sci. Proc.*, 30 (2009) p11-18
- 212 J. Wang, J.G.P. Binner, B. Vaidhyanathan, N. Joomun, J. Kilner, G. Dimitrakis, T.E. Cross, *J. Am. Ceram. Soc.*, 89 [6] (2006) p1977–1984
- 213 Micromeritics Tristar 3000, Operator's manual.
- 214 D. Hennings, G. Rosenstein, H. Schreinemacher, *J. Euro. Ceram. Soc.*, 8 (1991) p107-115
- 215 Y.A. Plonskii, G.A. Pavlova, V.N. Savel'ev, T.V. Milovidova, V.B. Vinogradov, *Glass and Ceramics*, 28 (1971) p182-184
- 216 W. Cho, *J. Phys. Chem. Solids.*, 59 [5] (1998) p659-666
- 217A. Amin, M.A. Spears, B.M. Kulwicki, *J. Am. Ceram. Soc.*, 66 (1983) p733
- 218 W.Hertl, *J. Am. Ceram. Soc.*, 71 [10] (1988) p879-83
- 219 J. Bera, S.K. Rout, *Mater. Lett.*, 59 (2005) p135-138
- 220 V. Vinothini, B.Vaidhyanathan, J.Binner, *J. Mat. Sci.*, 46 (2011) p2155-2161
- 221 M.G. Randall, *Liquid phase sintering, Technology & Engineering*, Plenum press, 1985
- 222 I.W. Chen, X.J. Wang, *Nature*, 404 (2000) p168-171
- 223 F. Azough, R. Al-Saffar, R. Freer, *J. Euro. Ceram. Soc.*, 18 (1998) p75 l-758
- 224 V.V. Mitic, Z. S. Nikolic, V. B. Pavlovic, V. Paunovic, M. Miljkovic, B. Jordovic, and L. Zivkovic, *J. Am. Ceram. Soc.*, 93 (2010) p132–137
- 225 N. Hirose, J.M.S. Skakle, A.R. West, *J. Electroceram.*, 3 (1999) p233-238
- 226 Z. Ruzhong, L. Longtu, G. Zhilun, *Ceram. Int.*, 27 [8] (2001) p889-893
- 227 J.G. Pepin, W. Borland, P. Callaghan, R.J.S. Young *J. Am. Ceram. Soc.*, 72 [12] (1989) 2287-91